

THE WORLDLINE METHOD FOR ELECTROMAGNETIC CASIMIR
ENERGIES

by

JONATHAN B. MACKRORY

A DISSERTATION

Presented to the Department of Physics
and the Graduate School of the University of Oregon
in partial fulfillment of the requirements
for the degree of
Doctor of Philosophy

June 2017

DISSERTATION APPROVAL PAGE

Student: Jonathan B. Mackrory

Title: The Worldline Method for Electromagnetic Casimir Energies

This dissertation has been accepted and approved in partial fulfillment of the requirements for the Doctor of Philosophy degree in the Department of Physics by:

Michael Raymer	Chair
Daniel Steck	Advisor
Steven van Enk	Core Member
John Toner	Core Member
Michael Kellman	Institutional Representative

and

Scott L. Pratt	Dean of the Graduate School
----------------	-----------------------------

Original approval signatures are on file with the University of Oregon Graduate School.

Degree awarded June 2017

DISSERTATION ABSTRACT

Jonathan B. Mackrory

Doctor of Philosophy

Department of Physics

June 2017

Title: The Worldline Method for Electromagnetic Casimir Energies

The Casimir effect refers to the primarily attractive force between material bodies due to quantum fluctuations in the electromagnetic field. The Casimir effect is difficult to calculate in general, since it is sensitive to the exact shapes of the bodies and involves contributions from all frequencies. As a result, calculating the Casimir effect between general bodies usually requires a numerical approach. The worldline method computes Casimir energies by creating an ensemble of space-time paths corresponding to a virtual particle interacting with the bodies. This method was originally developed for a scalar field coupled to an idealized background potential, rather than the vector electromagnetic field interacting with media.

This thesis presents work on extending the worldline method to account for the material properties of the interacting bodies, and the polarizations of electromagnetism. This thesis starts by covering background material on path integrals, and quantizing the electromagnetic field in media. The electromagnetic field is decomposed in terms of two scalar fields for planar bodies, where these scalar fields correspond to the transverse-electric and transverse-magnetic polarizations of the electromagnetic field. The worldline path integrals are developed for both polarizations, and solved analytically. Next, numerical methods are developed and

tested in the context of planar bodies. The starting positions, and scale of the paths, and shape of the paths are sampled via Monte Carlo methods. The transverse-magnetic path integral also requires specialized methods for estimating derivatives, and path construction. The analytical and numerical results for both worldline path integrals are in agreement with known solutions. Finally, specialized methods are developed for computing derivatives of the worldline Casimir-energy path integrals, allowing for efficient numerical computations of Casimir forces and torques.

CURRICULUM VITAE

NAME OF AUTHOR: Jonathan B. Mackrory

GRADUATE AND UNDERGRADUATE SCHOOLS ATTENDED:

University of Oregon, Eugene
University of Auckland, Auckland

DEGREES AWARDED:

Doctor of Philosophy, Physics, 2017, University of Oregon
Master of Science, Physics, 2008, University of Auckland
Bachelor of Science Honours, Physics, 2007, University of Auckland

AREAS OF SPECIAL INTEREST:

Monte Carlo Simulation
Quantum Measurement
Casimir Effect

PROFESSIONAL EXPERIENCE:

Graduate Teaching Fellow, University of Oregon, Department of Physics, 2008–2017

PUBLICATIONS:

Mackrory, J. B., Bhattacharya, T. and Steck, D. A. (2016), “Worldline approach for numerical computation of electromagnetic Casimir energies. I. scalar field coupled to magnetodielectric media”. *Phys. Rev. A* **94**, 042508.

Mackrory, J. B., Jacobs, K. and Steck, D. A. (2010), “Reflection of a particle from a quantum measurement”. *New J. Phys.* **12**, 113023.

ACKNOWLEDGEMENTS

First, I would like to acknowledge my advisor, Daniel Steck. All of the work in this thesis was undertaken in very close collaboration with him, and it has been a pleasure bouncing ideas around with him over the years. Dan’s indefatigable optimism kept me from giving up on this approach, and any time I thought we were permanently stuck Dan would find another way of looking at the problem. Dan also came up with main ideas that allowed the numerical methods for the TM polarization to work at all. Much of my understanding of stochastic processes, quantum trajectories and the Casimir effect has come from studying his notes on “Quantum and Atom Optics”, which is reflected in the number of times they are referenced.

Next I would like to acknowledge our collaborators, Tanmoy Bhattacharya and Kurt Jacobs. Tanmoy provided the basic grounding that let us start on the worldline Casimir project, by explaining path integrals and the novel techniques involved in the worldline path integrals. In addition he has proven a great oracle for new ideas in Monte Carlo methods, and skeptical tests of some of our more outlandish ideas. Kurt collaborated with us on a paper on non-uniform quantum position measurements, which was left out of this thesis.

I would like to thank my lab-mates, Jeremy Thorn, Elizabeth Schoene, Eryn Cook, Paul Martin, Wes Erickson, and Richard Wagner. We have had many discussions about my work over the years, and I’ve appreciated learning a little about how much work goes into a building a cold atom experiment. I also appreciate the hours of companionship we’ve spent together outside the lab, be it hiking, gaming, or watching terrible movies.

Finally, I would like to thank my wife Erin Mondloch for her emotional support throughout this project and particularly during the writing phase.

I would also like to acknowledge the financial support of the University of Oregon Physics Department throughout the years.

TABLE OF CONTENTS

Chapter	Page
I. INTRODUCTION	1
1.1. Casimir Effect	5
1.1.1. Casimir–Polder Forces	6
1.1.1.1. Derivation of the Atom-Perfect Conductor Potential	7
1.1.2. Forces between Bodies: Casimir Energy	13
1.1.2.1. Derivation of Lifshitz Formula	14
1.1.2.2. Physical Interpretation	18
1.1.2.3. Different Distance Scaling Regimes	19
1.2. Overview of Casimir Experiments	21
1.2.1. Experiments on Casimir Forces	21
1.2.2. Experiments on Casimir–Polder Forces	23
1.2.3. Current Experimental Directions	25
1.2.3.1. Repulsive Casimir Effects	25
1.2.3.2. Searches for New Physics	27
1.3. Computational Methods for Casimir Effects	28
1.3.1. Proximity Force Approximation	28
1.3.2. Scattering Approach	29
1.4. Path Integrals	32
1.4.1. Derivation of Feynman’s Path Integral	33
1.5. Scalar Worldline Casimir Energies	37

Chapter	Page
1.5.1. Derivation of the Scalar Casimir Worldline Path Integral	39
1.5.2. Worldline Distance Dependence	46
1.5.3. Numerical Method	48
1.5.4. Advantages and Shortcomings of the Scalar Method	49
1.5.5. Motivation and Goal for Thesis Project	50
1.6. Thesis outline	51
 II. ELECTROMAGNETIC FIELD QUANTIZATION AND ELECTROMAGNETIC WORLDFINES	 57
 2.1. Approaches to Quantizing Electromagnetism in Media	 58
2.2. Classical Electromagnetic Field Theory	61
2.3. Quantum Theory	65
2.4. Electromagnetic Partition Function	67
2.4.1. Faddeev–Popov Gauge Fixing	69
2.4.2. Gauge Choices	71
2.5. Gauge-Fixing: Generalized Lorenz Gauge	73
2.6. Scalar Decomposition for Planar Geometries	79
2.6.1. Scalar-Polarization Partition Functions	80
2.6.2. TE Polarization Worldline	82
2.7. Nonzero Temperature Worldline Path Integrals	86

Chapter	Page
III. PATH INTEGRALS AND FEYNMAN–KAC FORMULAE	90
3.1. Derivation of the Feynman–Kac formula	91
3.1.1. Steady-State Brownian Bridge Path Integral	95
3.2. Single Step Potential	97
3.2.1. Planar Dirichlet Conditions	99
3.3. Two Step Potentials	101
3.4. Feynman–Kac Formula for Singular Potentials	102
3.4.1. Transfer Layer Boundary Conditions for the TM Potential	104
3.4.2. Finding the Path Integral Solution for the TM Potential	107
3.5. Single TM potential and Step	110
3.6. Two TM Step Potentials	111
IV. ELECTROMAGNETIC WORLDLINES: ANALYTICAL RESULTS . . .	114
4.1. Extracting Casimir–Polder Energies	114
4.2. Rearranging Worldline Casimir Energies	119
4.2.1. Laplace–Mellin Transforms	119
4.2.2. Inverse Moment Theorem	121
4.2.3. Rewriting the Worldline in Analytical Form	121
4.3. Analytical TE Casimir–Polder Energy for an Atom and a Dielectric Plane	122
4.4. Analytical TM Casimir–Polder Energy for an Atom and a Dielectric Plane	124

Chapter	Page
4.5. Analytical TE Casimir Energy between Two Dielectric Planes	126
4.6. Analytical TM Casimir Energy between Two Dielectric Planes	130
4.7. Nonzero Temperature and Dispersion	133
4.7.1. Thermal TE Casimir–Polder Energy	136
4.7.2. Thermal TM Casimir-Polder Energy	138
4.7.2.1. The Zero Temperature, Near-Field Limit	139
4.7.2.2. The High Temperature, Far Field Limit	140
 V. ELECTROMAGNETIC WORLDSLINES: NUMERICAL METHODS AND RESULTS	 142
 5.1. TE Casimir Numerics	 144
5.1.1. Path Generation	144
5.1.1.1. Open Brownian Bridges: V-loop Construction	144
5.1.2. Monte Carlo Sampling	148
5.1.2.1. Sampling Path-Times from a Power Law	149
5.1.2.2. Sampling Starting Positions	150
5.1.2.3. Evaluating the Dielectric Path Average	151
5.1.3. Results: TE Casimir and Casimir–Polder Energies for Planar Geometries	152
5.1.3.1. Error Scaling with Path Length N	156
 5.2. TM Casimir Numerics	 158
5.2.1. Scaling of the Averaged TM Potential with Path Length N	160
5.2.1.1. TM-Gaussian Paths	162

Chapter	Page
5.2.1.2. Birth-Death Path Swarm	165
5.2.2. Monte Carlo Sampling for the Path Time	169
5.2.3. Gradient Estimation	172
5.2.3.1. Finite Differences	172
5.2.3.2. Malliavin Calculus	174
5.2.3.3. Partial Averaging Gaussian Paths	175
5.2.3.4. General Method Near Surfaces	179
5.2.4. Results: TM Casimir and Casimir–Polder Energies for Planar Geometries	182
5.3. Frequency Sampling	186
 VI. ELECTROMAGNETIC WORLDFINES: NUMERICAL FORCES AND CURVATURES FOR THE TE POLARIZATION	 188
 6.1. Surface Pinned Paths	 190
6.1.1. Force	191
6.1.2. Potential Curvature	193
6.1.3. Torque	195
6.1.4. Casimir–Polder Force	196
6.2. Occupation Number	198
6.3. Force and Curvature Numerics	203
6.3.1. Direct Path Construction for General- χ Coupling Method for Potential Curvature	206
6.3.2. Softened Delta Function Pinning for Strong-Coupling Limit for Potential Curvature	207
6.3.2.1. Softened Delta Function Pinning	208
6.3.2.2. Splitting the Potential Curvature	210

Chapter	Page
VII. CONCLUSION	216
APPENDIX: DETAILED CALCULATIONS	218
A.1. Integrated Renormalized Two-Body Feynman-Kac Formula . . .	218
A.1.1. TE Reflection Coefficients	221
A.1.2. TM Reflection Coefficients	221
REFERENCES CITED	222

LIST OF FIGURES

Figure	Page
1.1. Allowed modes between parallel plates	2
1.2. Feynman diagram for Casimir–Polder energy	10
1.3. Sketch of two planar dielectric slabs	15
1.4. Casimir energy in terms of fundamental QED processes.	19
1.5. Schematic of worldline paths interacting with plane and sphere	47
2.1. Scalar polarizations at planar interface	80
3.1. Regularized TM potential	104
3.2. Plot of TM solution	109
5.1. Planar Casimir–Polder TE energy as function of χ	154
5.2. Planar TE Casimir energy as function of χ	155
5.3. Convergence of planar TE Casimir–Polder energy as function of N	157
5.4. Convergence of planar TE Casimir energy as function of N	157
5.5. Histogram of accumulated numerical TM estimates	161
5.6. Combined TM-Gaussian probability distribution.	162
5.7. (Preliminary data) Scaling of standard deviation for estimated TM potential as function of N for four methods.	168
5.8. Partial averaging along a path	177
5.9. Thresholds for partial averaging for atom between two bodies	180
5.10. Numerical TM Casimir–Polder efficiency	183
5.11. Numerical TM Casimir efficiency	183
6.1. Sketch of geometry for interacting bodies	191
6.2. Numerically computed TE force	204

6.3. Numerical TE potential curvature for two planar surfaces, evaluated with occupation method	208
6.4. (Preliminary data) Numerical TE potential curvature for two planar surfaces, evaluated with strong-coupling methods	214

CHAPTER I

INTRODUCTION

The Casimir effect is one of the more surprising consequences of quantum electrodynamics (QED), the quantum theory describing the interaction of matter and photons. Casimir (1948) showed that according to QED a pair of electrically neutral, conducting bodies will be attracted to one another due to their mutual interaction with the quantized electromagnetic (EM) field, even if the EM field is in its vacuum state. In brief, the total energy of in the field is the sum of the energies of each of the field modes, where each mode has vacuum energy proportional to its frequency. The presence of the conducting bodies restricts the electric field on the plates, as illustrated in Figure 1.1. The allowed modes must have a half-integer number of wavelengths fit between the plates. Changing the plates separation changes the allowed modes, and thus the total energy. While the total vacuum energy is a divergent quantity, the difference in energy for two configurations is well defined. The vacuum energy is compared between the cases when the plates are a finite distance apart, and when they are removed to arbitrarily far apart. As the plates are brought closer together, this vacuum energy difference is reduced, leading to an attractive force between the plates.

While the Casimir effect is a generic consequence of quantum field theory subject to boundary conditions, the electromagnetic Casimir effect is the most important example. This is because photons (the quanta of the EM field) are massless which makes their interaction long-ranged, and the coupling of electromagnetism to matter is much stronger than gravity, the only other long-ranged fundamental force. In the electromagnetic Casimir effect, one can think of the electrons in a body emitting and

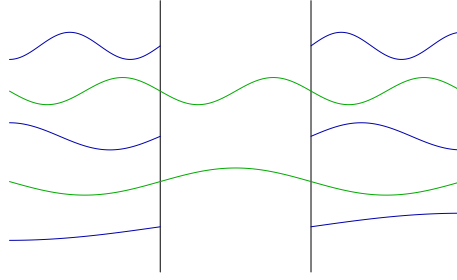


FIGURE 1.1. Sketch of allowed modes between perfectly conducting parallel plates. Only waves with a half-integer number of wavelengths are allowed between the plates. The blue modes are only allowed outside the plates, while green modes are allowed inside and outside. The modes have been vertically offset for clarity.

absorbing virtual photons that can in turn interact with electrons in other bodies. The interacting bodies can be pairs of atoms (Casimir and Polder, 1948), macroscopic bodies such as metallic planes and dielectric slabs (Lifshitz, 1956), or any combination.

Alternatively, the Casimir effect can be attributed to the attraction between instantaneous dipoles forming in the bodies. This interpretation is intimately related to the van der Waals force, where molecules with fluctuating dipole moments are attracted to one another (van der Waals, 1873). While the emphasis on fluctuating EM fields or fluctuating dipoles may differ between Casimir and van der Waals forces, they ultimately describe the same phenomenon.

Despite the prediction of the Casimir force in 1948, precise measurements of the Casimir force were only carried out in the late 1990s (Lamoreaux, 1997; Mohideen and Roy, 1998). These first modern experiments measured the Casimir force between conducting spheres and plates, rather than between parallel conducting plates, since a sphere and plate are easier to align and control. Experiments have also been carried out to measure the forces between atoms and surfaces (Harber *et al.*, 2005; Perreault and Cronin, 2005; Sukenik *et al.*, 1993).

Beyond their importance as observable consequences of quantum field theory, Casimir effects are also important to a range of modern experiments and developing technologies. They are important for microelectromechanical systems (MEMS), where the Casimir attraction between components leads to stiction, which causes the pieces to be permanently stuck together (Buks and Roukes, 2001). Casimir forces are also important for technologies using atoms near dielectric surfaces (Alton *et al.*, 2011; Folman *et al.*, 2000; Hung *et al.*, 2013). In these experiments, the attractive Casimir potential sets a lower bound for how close the atoms can be brought to the surface. Consequently, the Casimir effect must be considered in the engineering of these devices.

The advent of these experiments in complicated arrangements of bodies, has spurred the development of a number of theoretical and computational methods for computing Casimir effects (Bordag *et al.*, 2009; Dalvit *et al.*, 2011). To model these experiments, it is necessary to be able to compute the Casimir effect between arbitrarily shaped bodies, with realistic material properties—which in general requires a numerical approach (Johnson, 2011). The most important of these modern methods are the so-called “scattering method” (Lambrecht *et al.*, 2006; Rahi *et al.*, 2009; Reid *et al.*, 2009) and “worldline methods” (Gies *et al.*, 2003). To date, the scattering method is the only general purpose numerical method available for computing Casimir forces in arbitrary arrangements of bodies (Reid *et al.*, 2009, 2011, 2013). This method considers fluctuating currents confined to the surfaces of the interacting bodies, where the currents at each patch of surface interact with one another by emitting and reabsorbing photons. The Casimir energy is calculated by evaluating the determinant of the (large) scattering matrix for all of these patches (Reid *et al.*, 2011). The worldline method is another promising method for calculating Casimir

energies (Gies *et al.*, 2003), which considers an ensemble of closed Brownian paths propagating through space. These paths can be intuitively thought of as the space-time trajectory of a virtual particle. As the paths propagate, they accumulate a weight based on whether the path intersects any of the bodies. The Casimir energy is found by summing up the contributions from paths at all starting points and sizes. The worldline method has only been developed for scalar fields interacting with idealized surfaces. In contrast to the scattering method, the worldline method is a Monte Carlo method, which makes it easy to parallelize.

It is the goal of this thesis to extend the worldline method to computing electromagnetic Casimir effects. This requires accounting for the vector nature of the EM field, and including realistic coupling to material properties, while attempting to retain as many of its appealing properties as possible. In Chapter II, we will discuss quantization of the EM field, and introduce two versions of the worldline path integral: one in terms of the vector and scalar potentials, and another in terms of two scalar fields. The scalar field description is specialized for planar geometries, but it does account for the magnetic and dielectric properties of the medium. We will develop the necessary analytical methods for evaluating path integrals in Chapter III, and apply them to Casimir worldline path integrals in Chapter IV. In Chapters V and VI, we develop and test numerical methods for evaluating the electromagnetic worldline method. In both analytical and numerical cases the results show agreement with known electromagnetic Casimir results. (A longer outline of the thesis, and some key analytical results is presented in Section 1.6.)

The rest of this chapter will cover simple examples of Casimir effects, and expand on some necessary background material. In Section 1.1, we will introduce some simple calculations for Casimir effects such as the Casimir–Polder potential

between an atom and a conducting wall, and the Lifshitz formula for the Casimir effect between dielectric half-spaces (both of which we will use as checks on our later work). In Section 1.2 we will briefly survey recent experiments on the Casimir effect. In Section 1.3 we will cover the most prominent numerical methods for computing the Casimir effect, such as the proximity force approximation, the scattering method and the worldline method. In particular we will introduce the Feynman path integral and the scalar worldline method at length. Finally, in Section 1.6 we will review the rest of the thesis, and present some of the key equations.

1.1. Casimir Effect

Casimir and van der Waals forces are intimately related, and describe the same basic quantum mechanical force. Van der Waals forces were first discovered as deviations from ideal gas behavior, which can be attributed to the atoms possessing a finite size and inter-atomic forces (Parsegian, 2006; van der Waals, 1873). London (1930) gave these interatomic forces a theoretical underpinning in terms of fluctuating, induced dipoles using quantum mechanical perturbation theory. This work leads to an interatomic potential with a characteristic d^{-6} scaling. While this scaling is similar to the other possible dipole-dipole interactions, these dispersion forces are often the dominant contribution to inter-molecular forces (Israelachvili, 2011).

London's perturbation theory assumes that the dipole interact with another instantaneously, which ignores the finite speed of light. Casimir and Polder (1948) extended this calculation to quantum electrodynamics, where they accounted for the retardation due to the finite speed of light. The retardation causes the potential to decay more quickly at larger distances.

Casimir (1948) then showed that uncharged, conducting plates would be attracted by their mutual interaction with the quantized EM field. This calculation emphasizes the role played by the fields, and suggests a global interaction due to the effective boundary conditions imposed by the plates. This interpretation stands in contrast to the van der Waals picture which emphasizes the pair-wise interactions between induced dipoles.

This was followed by later work by Lifshitz and co-workers on the Casimir effect between dielectric bodies (Dzyaloshinskii *et al.*, 1961; Lifshitz, 1956). This is particularly relevant since some of their later work showed that the Casimir effect can be derived from the pair-wise van der Waals interactions of all of the constituent parts (Dzyaloshinskii *et al.*, 1961).

In this thesis, we will follow the quantum optics convention and use “Casimir effect” as an umbrella term for all of these vacuum fluctuation forces. Near-field forces where the dipole interactions can be considered as instantaneous will be referred to as “van der Waals forces”. The forces between atoms and microscopic bodies will be referred to as “Casimir–Polder forces”, in distinction to the Casimir forces between macroscopic bodies.

We will start our development from Casimir and Polder’s work, since that was framed in the more modern language of quantum field theory, and naturally encompasses all of the limiting cases.

1.1.1. Casimir–Polder Forces

Casimir and Polder (1948) computed the energy between pairs of atoms, and for atoms and conducting walls using non-relativistic quantum electrodynamics to account for the retardation due to the finite speed of light. They found that in

the far-field (where the transition wavelengths $\lambda = 2\pi c/\omega_A$ exceed the separation of the atoms d , $d \gg 2\pi c/\omega_A$) the inter-atomic potential decays more rapidly as d^{-7} , instead of the typical d^{-6} scaling for London forces. The change in power law can be attributed to the induced dipoles decorrelating over the time of flight of the virtual photon, and thus having a weaker effective interaction.

They also found an attractive force between an atom and perfectly conducting wall, with a d^{-3} scaling in the near field regime, that passes over to d^{-4} scaling in the far field. In this case the atom can be thought of as interacting with its negative image in the wall, which leads to an attractive potential for the atom,

$$V_{\text{CP}}(d) = -\frac{3\hbar c\alpha_0}{32\pi^2\epsilon_0 d^4}, \quad (1.1)$$

where \hbar is the reduced Planck's constant, c is the speed of light, α_0 is the atom's static polarizability, and ϵ_0 is the permittivity of free space.

1.1.1.1. Derivation of the Atom-Perfect Conductor Potential

The Casimir–Polder potential between an atom in its ground state and a surface can be derived via perturbation theory in the coupling of the atom to the EM field. We will consider the attraction between an atom and a perfectly conducting wall.¹ The Hamiltonian for the whole atom-field system is

$$H = H_{\text{atom}} + H_{\text{field}} + H_{\text{int}} \quad (1.2)$$

¹ This derivation is adapted from Chapter 13 and Section 14.3 of Steck (2015) and Section 3.12 of Milonni (1994).

where we have split the energy into energy for atom, the EM field, and a term describing their interaction. The atomic Hamiltonian is

$$H_{\text{atom}} = \frac{\hat{\mathbf{p}}^2}{2m} + \sum_j \hbar\omega_j \hat{\sigma}_j^\dagger \hat{\sigma}_j \quad (1.3)$$

where the first term is the kinetic energy, and the second term gives the atom's internal electronic energy. The atom's quantized energy levels are given by $E_j = \hbar\omega_j$, and $\hat{\sigma}_j = |g\rangle\langle e_j|$ is the lowering operator for the atom's internal state. The field Hamiltonian is

$$H_{\text{field}} = \sum_{\mathbf{k}, \zeta} \hbar\omega_k \left(\hat{a}_{\mathbf{k}, \zeta}^\dagger \hat{a}_{\mathbf{k}, \zeta} + \frac{1}{2} \right), \quad (1.4)$$

where $\hat{a}_{\mathbf{k}, \zeta}$ is the annihilation operator for the EM field mode with wavenumber k , and polarization ζ , which has spatial mode function $\mathbf{f}_{\mathbf{k}, \zeta}(\hat{\mathbf{x}})$. This field energy also includes the zero-point energy, $\sum_k \hbar\omega_k/2$, which will be important in the Casimir effect. For the Casimir–Polder calculation, this zero-point-energy is a divergent constant which drops out when considering the energy differences when the atom is moved close to the surface from arbitrarily far away. Finally, the interaction Hamiltonian couples the internal state of the atom to the quantized light field,

$$H_{\text{int}} = -\hat{\mathbf{d}} \cdot \hat{\mathbf{E}} = \sum_j \sum_{\mathbf{k}, \zeta} \sqrt{\frac{\hbar\omega_k}{2\epsilon_0}} (\hat{\sigma}_j + \hat{\sigma}_j^\dagger) \mathbf{d}_j \cdot [\hat{a}_{\mathbf{k}, \zeta} \mathbf{f}_k^*(\hat{\mathbf{x}}) + \hat{a}_{\mathbf{k}, \zeta}^\dagger \mathbf{f}_{\mathbf{k}, \zeta}(\hat{\mathbf{x}})], \quad (1.5)$$

where $\mathbf{d}_j = -e\langle g|\hat{\mathbf{x}}|e_j\rangle$. The interaction Hamiltonian is written in the dipole approximation, which assumes that the atom is much smaller than the relevant wavelengths. In this case, the dominant wavelengths are typically on the order of the separation between the atom and the wall. In this calculation the mode functions $\mathbf{f}_{\mathbf{k}, \zeta}$ must satisfy the EM boundary conditions on the surfaces of the bodies. The resulting

EM mode functions (and thus the potential) are then sensitive to the arrangements of the bodies.

Note that some of the terms in the interaction Hamiltonian violate energy conservation, in the sense that $[H_{\text{atom}} + H_{\text{field}}, H_{\text{int}}] \neq 0$, so H_{int} causes transitions between the eigenstates of the non-interacting Hamiltonians $H_{\text{atom}} + H_{\text{field}}$. For example, $\hat{\sigma}_j^\dagger \hat{a}_{\mathbf{k}, \zeta}^\dagger$ creates a photon with energy $\hbar\omega_k$ and raises the atom from the ground state to an excited state with energy $\hbar\omega_j$. These terms are normally dropped in the rotating-wave-approximation, since they oscillate quickly in time as $e^{i(\omega_j + \omega_k)t}$, and average down to zero on typical atomic timescales. However, these energy non-conserving terms lead to observable effects at higher order in perturbation theory. The first order energy shift $\langle E_n | H_{\text{int}} | E_n \rangle = 0$, since the mean value of the electric field in vacuum is zero. The Casimir–Polder potential emerges when computing the energy shift for the atom from H_{int} to second order. For an atom in its ground state, the Casimir–Polder potential is given by

$$V_{\text{CP}} = - \sum_{n \neq 0, \mathbf{k}, \zeta} \frac{\langle E_0, 0 | H_{\text{int}} | E_n, 1_{\mathbf{k}, \zeta} \rangle \langle E_n, 1_{\mathbf{k}, \zeta} | H_{\text{int}} | E_0, 0 \rangle}{\hbar(\omega_k + \omega_{n0})}, \quad (1.6)$$

where $|E_n, 1_{\mathbf{k}, \zeta}\rangle$ denotes the state with the atom in energy level n and one photon in mode \mathbf{k} , $|0\rangle$ denotes the vacuum state of the EM field, and the transition frequency $\omega_{n0} = (E_n - E_0)/\hbar$. The shift V_{CP} can be understood as two virtual transitions—one from the atomic ground state with no photons to an atomic excited state with one photon, followed by a return transition. The total energy shift is found by summing over all possible intermediate states. This process is represented schematically via the Feynman diagram in Figure 1.2, where an atom in the ground-state emits a virtual photon, and re-absorbs it. This transition is a “virtual” one, since these intermediate

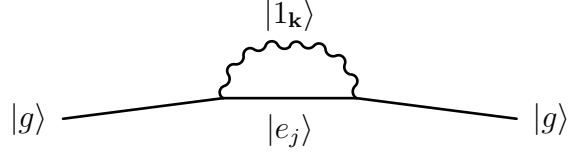


FIGURE 1.2. Feynman diagram representing an atom interacting with EM field via emitting and absorbing photons. The wavy line represents the EM Green function in the presence of boundaries—as opposed to the usual plane waves exploited in field theory computations. The atom is excited into intermediate states.

transitions violate energy conservation, and these intermediate states are not directly physically observable on a detector.

After substituting in H_{int} , the Casimir–Polder energy can be written as

$$V_{\text{CP}}(\mathbf{r}) = - \sum_{n \neq 0, \mathbf{k}, \zeta} \frac{\hbar \omega_k}{6\epsilon_0} \frac{|\langle E_0 | \mathbf{d} | E_n \rangle|^2 |\mathbf{f}_{\mathbf{k}, \zeta, i}(\mathbf{r})|^2}{\hbar(\omega_k + \omega_{n0})}, \quad (1.7)$$

where we substituted the form of H_{int} and assumed a spherically symmetric atom, $|\langle E_0 | d_i | E_n \rangle|^2 = |\langle E_0 | \mathbf{d} | E_n \rangle|^2 / 3$, which corresponds to assuming that all components of dipole matrix elements are equal.

The mode functions for the electric field near a perfectly conducting plane can be substituted into the energy. Following Milonni (1994, Section 3.12), we assume the atom is close to one wall of a perfectly conducting box, but far from all other walls. The box is formed by conducting planes at $x = 0, L$, $y = 0, L$, and $z = 0, L$. The EM mode functions for a perfectly conducting box are given by

$$\begin{aligned} \mathbf{f}_{\mathbf{k}, \zeta}(\mathbf{r}) = \sqrt{\frac{8}{V}} \left(\hat{x}(\hat{\epsilon}_{\mathbf{k}, \zeta} \cdot \hat{x}) \cos(k_x x) \sin(k_y y) \sin(k_z z) \right. \\ + \hat{y}(\hat{\epsilon}_{\mathbf{k}, \zeta} \cdot \hat{y}) \sin(k_x x) \cos(k_y y) \sin(k_z z) \\ \left. + \hat{z}(\hat{\epsilon}_{\mathbf{k}, \zeta} \cdot \hat{z}) \sin(k_x x) \sin(k_y y) \cos(k_z z) \right), \quad (1.8) \end{aligned}$$

where $\hat{\mathbf{e}}_{\mathbf{k},\zeta}$ are the polarization unit vectors, and the wavenumbers are given by $k_i = n_i\pi/L$, with n_i integers (Steck, 2015, Section 8.4.1). The square-modulus $|\mathbf{f}_{\mathbf{k},\zeta}(\mathbf{r})|^2$ can be simplified under a couple limits. If the atom is close to the $z = 0$ plane, but very far from the other walls, the squared-sinusoids in x and y can be replaced by their average value of $1/2$, since they will be quickly oscillating. In addition, the polarization vectors form a resolution of the transverse identity (since Gauss's law implies that the electric field is transverse, $\nabla \cdot \mathbf{E} = 0$),

$$\sum_{\zeta} \hat{\mathbf{e}}_{\mathbf{k},\zeta}^i \hat{\mathbf{e}}_{\mathbf{k},\zeta}^j = \delta_{ij} - \frac{k_i k_j}{k^2}. \quad (1.9)$$

The sum over dipole matrix elements can also be rewritten in terms of the atom's ground-state polarizability,

$$\alpha_{ij}(\omega) = \sum_n \frac{2\omega_{n0} \langle E_0 | d_i | E_n \rangle \langle E_n | d_j | E_0 \rangle}{\hbar(\omega_{n0}^2 - \omega^2)}. \quad (1.10)$$

If we assume the atom's distance from the surface d is larger than the atom's dominant emission wavelength, ω_{n0} then the dominant contribution to the sum will come from frequencies for which $\omega_k \sim c/d \ll \omega_{n0}$. In that limit, the atomic polarizability can be replaced by the atom's static (zero frequency) polarizability

$$\alpha_0 = \lim_{\omega \rightarrow 0} \alpha(\omega) = \sum_n \frac{2|\langle E_0 | \mathbf{d} | E_n \rangle|^2}{3\hbar\omega_{n0}}. \quad (1.11)$$

In this far-field limit, the Casimir–Polder energy can be approximated as

$$V_{\text{CP}}(\mathbf{r}) = -\frac{\hbar}{4\epsilon_0} \alpha_0 \sum_{\mathbf{k},\zeta} \omega_k |\mathbf{f}_{\mathbf{k},\zeta}(\mathbf{r})|^2. \quad (1.12)$$

With these simplifications, and taking the limit of a large box to convert the sum over wavevectors into an integral, the Casimir–Polder potential is given by

$$V_{\text{CP}}(\mathbf{r}) = -\frac{\hbar\alpha_0}{8\pi^3\epsilon_0} \int_{k_z>0} d^3k \omega_k \left[\left(1 - \frac{k_x^2}{k^2}\right) [1 - \cos(2k_z z)] + \left(1 - \frac{k_y^2}{k^2}\right) [1 - \cos(2k_z z)] + \left(1 - \frac{k_z^2}{k^2}\right) [1 + \cos(2k_z z)] \right], \quad (1.13)$$

where the sinusoids have been rewritten using double-angle formulae. The z -independent parts lead to a constant, divergent contribution to the energy. In order to extract a finite energy shift it is essential to renormalize the energy by subtracting off this constant energy. This corresponds to considering the energy change as the atom is brought close to the surface from arbitrarily far away. Throughout this thesis, this simple energy subtraction is the only renormalization that will be required.

The renormalized Casimir–Polder energy between an atom and a conducting plane can be evaluated in spherical coordinates, although some care is required to regularize these oscillatory integrals—this can be done by introducing an exponential convergence factor e^{-ak} and taking the limit $a \rightarrow 0$ at the end of the computation:

$$V_{\text{CP}}(\mathbf{r}) - V^{(0)} = \lim_{a \rightarrow 0} \frac{\hbar\alpha_0}{8\pi^3\epsilon_0} \int d^3k \omega_k \frac{2k_z^2}{k^2} \cos(2k_z z) e^{-ka} \quad (1.14)$$

$$= \lim_{a \rightarrow 0} \frac{\hbar c\alpha_0}{4\pi^2\epsilon_0} \int_0^\infty dk \int_0^{\pi/2} d\theta k^3 \sin\theta \cos^2\theta \cos(2kz \cos\theta) e^{-ka} \quad (1.15)$$

$$= -\frac{3\hbar c\alpha_0}{32\pi^2\epsilon_0 z^4}. \quad (1.16)$$

While we have carried out the calculation for the case of perfectly-conducting planar interfaces, similar computations can be carried out for dielectric interfaces and more general shapes of macroscopic bodies. In the case of an atom near a planar, dielectric

interface the Casimir–Polder potential is

$$V_{\text{CP}}(\mathbf{r}) - V^{(0)} = -\frac{3\hbar c\alpha_0}{32\pi^2\epsilon_0 z^4}\eta(\chi), \quad (1.17)$$

where χ is the static susceptibility of the medium, and the efficiency factor η approaches zero as $\chi \rightarrow 0$ and unity as $\chi \rightarrow \infty$. Note that this type of calculation relies on having analytical expressions available for the mode functions, which limits this approach to simple geometries.

1.1.2. Forces between Bodies: Casimir Energy

We now turn our attention to the Casimir effect where macroscopic bodies are attracted to one another via their interaction with the quantized EM field (Casimir, 1948). The presence of the bodies restricts the allowed modes of the electric field, which is illustrated for perfectly conducting planes in Figure 1.1. Each quantized mode of the EM field contributes to the energy, even in the ground state with zero photons. The total ground state energy in the EM field is

$$E = \sum_{\alpha} \frac{\hbar\omega_{\alpha}}{2}, \quad (1.18)$$

where α indexes all possible modes. While the total energy is divergent, a finite answer can be found by considering the energy difference between two different configurations of bodies. In this case, the energy is renormalized by subtracting the energy when the bodies are moved arbitrarily far apart from one another. For example, the renormalized energy between two perfectly conducting plates is

$$E - E_0 = -\frac{\pi^2\hbar c}{720d^3}, \quad (1.19)$$

where d is the distance between the plates.

The theory was extended by Lifshitz and coworkers to describe forces between dielectric half-spaces (Dzyaloshinskii *et al.*, 1961; Dzyaloshinskii and Pitaevskii, 1959; Lifshitz, 1956). The Lifshitz calculation can also recover the Casimir force between perfect conductors, and Casimir–Polder forces between atom’s and dielectric surfaces. We will sketch the derivation of the Lifshitz formula (which will be used later), since this can naturally also compute the Casimir energy.

1.1.2.1. Derivation of Lifshitz Formula

The Lifshitz formula for the Casimir energy can be found with an argument due to van Kampen *et al.* (1968). In its full generality, the Lifshitz formula gives the total energy for two planar dielectric bodies with dielectric constants ϵ_1 and ϵ_2 , separated by a medium with dielectric constant ϵ_3 .² This geometry is illustrated in Figure 1.3. The energy for the EM field in its ground state is

$$E = \sum_{\zeta} \sum_{k_x, k_y, \omega} \frac{\hbar \omega_k}{2}, \quad (1.20)$$

where the sum runs over all of the allowed modes for the particular arrangement of bodies. In this case, the non-zero contribution to the Casimir effect comes from surface plasmon modes, which propagate along the interfaces and decay exponentially away from the bodies. The mode sum can be converted into an integral with respect to the transverse wavenumber $k_T := \sqrt{k_x^2 + k_y^2}$. The sum over frequencies can be recast as a contour integral over complex frequency ξ , against a function $\Delta^{(\zeta)}$, whose

²This derivation parallels those in Milonni (1994, Section 7.2), and Bordag *et al.* (2009, Ch. 12). A similar result emerges from the scattering approach as discussed by Lambrecht *et al.* (2011).

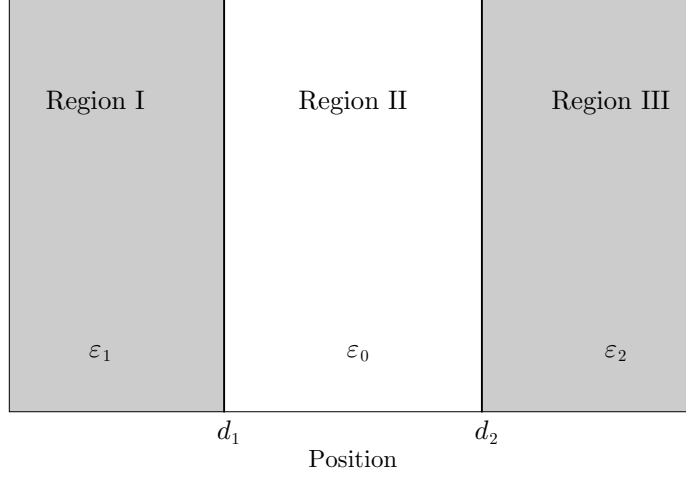


FIGURE 1.3. Sketch of two planar dielectric slabs, with dielectrics ϵ_1 and ϵ_2 , with interfaces at $x = d_1$ and $x = d_2$. The slabs are separated by vacuum.

poles occur at the allowed frequencies, with residue ω_k

$$E = \frac{L^2}{(2\pi)^2} \sum_{\zeta} \int_0^{\infty} dk_T k_T \oint d\xi \frac{\hbar\xi}{2} \frac{1}{(2\pi i)\Delta^{(\zeta)}(\xi)} \frac{d\Delta^{(\zeta)}(\xi)}{d\xi}. \quad (1.21)$$

The function $[2\pi i\Delta(\xi)]^{-1}d\Delta(\xi)/d\xi$ is designed to have unit residue at the zeroes of $\Delta(\xi)$. The factor of L^2 is accounted for by considering the energy per unit area. The energy can be simplified by integrating by parts, leading to

$$\frac{E}{A} = \frac{\hbar}{16\pi^3 i} \sum_{\zeta} \int_0^{\infty} dk_T k_T \oint d\xi \ln \Delta^{(\zeta)}(\xi). \quad (1.22)$$

The most important modes are the surface modes, since these modes are sensitive to the position of the other body, where these modes exponentially decay between the bodies. The allowed frequencies for these modes must satisfy

$$r_{13}^{(\zeta)} r_{23}^{(\zeta)} e^{-2k_z d} = 1, \quad (1.23)$$

where $r_i^{(\zeta)}$ are the reflection coefficients for surface i and polarization ζ , and the wavenumber is given by $k_z = \sqrt{k_T^2 - \epsilon(\omega)\omega^2/c^2}$. The reflection coefficients are given by

$$r_{13}^{(\text{TE})} = \frac{k_{z,1} - k_{z,3}}{k_{z,1} + k_{z,3}} \quad r_{13}^{(\text{TM})} = \frac{\epsilon_3 k_{z,1} - \epsilon_1 k_{z,3}}{\epsilon_3 k_{z,1} + \epsilon_1 k_{z,3}}. \quad (1.24)$$

The frequency condition is suggestive of the requirement that accumulated round-trip phase including reflections from both walls, is unity for allowed modes [this interpretation is bolstered by considering the Casimir force between realistic mirrors (Genet *et al.*, 2003)]. The condition (1.23) suggests choosing $\Delta(\xi) = 1 - r_{13}^{(\zeta)} r_{23}^{(\zeta)} e^{-2k_z d}$, where the wavenumber k_z and the reflection coefficients are functions of ξ .

The contour integral (1.22) can be split into two pieces. The integral over the right semi-circle is independent of d , and decays to zero when the semicircular contour is taken to infinity. This leaves the integral along the imaginary frequency axis, $\xi = is$ where s is real. Casimir effects are most naturally discussed along the imaginary frequency axis. Due to the causal nature of the dielectric response functions, the dielectric function is a smooth, real function on the imaginary axis. This also means that the z -wavenumber is also real, with $k_z = \sqrt{k_T^2 + \epsilon(is)s^2/c^2}$, and that oscillatory functions like plane wave factors are replaced with real, decaying exponentials. Both of these features are extremely attractive for numerical methods, and so numerical methods also work with imaginary frequency (Johnson, 2011).

The Casimir energy between two dielectric half-spaces of permittivities ϵ_1 and ϵ_2 separated by a gap of thickness filled with permittivity ϵ_3 is given by

$$\frac{E}{L^2} = -\frac{\hbar}{2\pi^2 c^3} \int_0^\infty ds s^2 \epsilon_3 \int_1^\infty dp p \sum_{\zeta=\text{TE, TM}} \log \left(1 - r_{13}^{(\zeta)} r_{23}^{(\zeta)} e^{-2\sqrt{\epsilon_3} p s d / c} \right), \quad (1.25)$$

where the EM reflection coefficients are given by

$$r_{ij}^{(\text{TE})} = \frac{\kappa_i - \kappa_j}{\kappa_i + \kappa_j} \quad r_{ij}^{(\text{TM})} = \frac{\epsilon_j \kappa_i - \epsilon_i \kappa_j}{\epsilon_j \kappa_i + \epsilon_i \kappa_j}, \quad (1.26)$$

and

$$\kappa_i = \sqrt{p^2 + \epsilon_i/\epsilon_3 - 1}, \quad (1.27)$$

following Zhou and Spruch (1995). The variables have been adjusted to agree with the Lifshitz calculation, by defining $k_T = s\sqrt{\epsilon_3(p^2 - 1)}/c$. In general, this integral form (1.25) is the simplest expression for the Casimir energy between two dielectrics planes. The perfect-conductor Casimir energy result (1.19) can be found by taking the strong-coupling limit, $r_i^{(\zeta)} \rightarrow 1$, setting $\epsilon_3 = 1$, and evaluating the integrals using

$$\int_0^\infty ds s^2 \int_1^\infty dp p \log(1 - e^{-2spd/c}) = -\frac{c^3 \pi^4}{360d^3}. \quad (1.28)$$

The Casimir–Polder results for interacting atoms can be recovered from the Lifshitz formula by taking the limit of dilute bodies, $\epsilon \approx 1 + \alpha_0 n$, where $n \ll 1$ is the density, and α_0 is the static polarizability.

The Lifshitz theory can be extended to account for dispersion and finite temperature. Some care is required in quantizing the EM field within dielectric media, since according to the Kramers-Krönig relations, the presence of dispersion implies dissipation. However, it has been observed that one gets the correct answers by a direct substitution $\epsilon(\mathbf{x}) \rightarrow \epsilon(\omega, \mathbf{x})$. Barash and Ginzburg (1975) and Rosa *et al.* (2010) investigated this more carefully by in terms of the total thermodynamic energy and the work done on the microscopic details of the medium.

At non-zero temperature it is necessary to also include the effects of real, thermally excited photons. At inverse temperature $\beta = (k_B T)^{-1}$, for a frequency ω , the mean number of photons is $\bar{n}(\omega) = \coth(\beta\hbar\omega/2)$. Note that $\coth(ix)$ has simple poles at $x = \pm n\pi$ for n integer. Exactly the same style of argument that used to derive Eq. (1.25), can be used to find the thermal Casimir energy between dielectrics. But due to the presence of $\coth(is)$, the integral over imaginary frequency picks up the residues of the integrand at the Matsubara frequencies $s_n := 2\pi n/(\beta\hbar)$. The resulting free energy per unit area is

$$\frac{\mathcal{F}}{L^2} = \frac{k_B T}{2\pi} \sum_{n=0}^{\infty \prime} s_n^2 \epsilon_3 \int_1^{\infty} dp p \sum_{\zeta=\text{TE, TM}} \log \left[1 - r_{13}^{(\zeta)}(is_n) r_{23}^{(\zeta)}(is_n) e^{-2\sqrt{\epsilon_3} p s_n d/c} \right], \quad (1.29)$$

where the primed sum weights the $n = 0$ term by $1/2$, and all functions of frequency are evaluated at s_n . At zero temperature, this result passes over to the previous one, by transforming the sum over frequencies into an integral. Eq. (1.1.2.3) is the most general form of the Lifshitz formula, and can recover all of the limiting behaviors in the near and far field, and perfect conducting media, and rarefied media.

1.1.2.2. Physical Interpretation

Casimir's original calculation vividly shows the importance of vacuum fields, and is said to show the reality of the vacuum field (Jaffe, 2005). This is due to the emphasis given to the imposed boundary conditions, which are emphasized over the matter that created the boundary conditions. The Casimir effect is best thought of as a long-ranged interaction between dielectric bodies mediated via the EM field (Jaffe, 2005; Rahi *et al.*, 2009). This picture is also analogous to the intuitive photon exchange picture used to explain the Casimir–Polder potential. Figure 1.4 shows

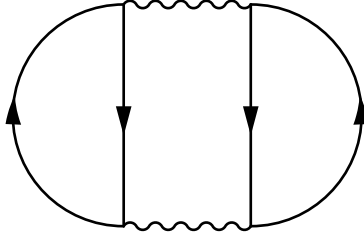


FIGURE 1.4. Casimir Energy in terms of fundamental QED processes. The electrons are considered bound within their respective media, but still interact with electrons on other bodies by exchanging photons. Any self-interactions are removed by renormalization via considering energy differences. The effective interaction of the electron current with the field is described by the dielectric constant.

a term contributing to the Casimir effect where electrons on different bodies interact with one another via the EM field. The solid lines should be understood as the current operators \hat{j}_μ for the electrons bound to a particular, separate media, while the wavy lines are the EM Green functions describing the photon. In fact, if summed over all such dipole “bubbles,” one can recover the full Casimir force results—as was done by Dzyaloshinskii *et al.* (1961) in re-summing a field theoretic expansion. In that case the closed electron loops should be understood as current-current correlation functions, $\langle j_\mu j_\nu \rangle$, where under linear response theory, this correlation function is related to the conductivity tensor $\sigma_{\mu\nu}$ (Altland and Simons, 2011; Kubo, 1957). The conductivity tensor is in turn related to the dielectric tensor, ϵ_{ij} via Ohm’s Law $j_i = \sigma_{ij} E_j$, which makes the connection between the underlying fundamental physics, and the material functions used in the Casimir effect.³

1.1.2.3. Different Distance Scaling Regimes

The Casimir effect is important at distances around the resonant wavelengths of the atom or medium, which are typically on the order of a micron for optical

³ This relationship was pointed out by Rahi *et al.* (2009), as a justification for their starting point in quantizing the EM field in media.

transitions. The Casimir effect is typically computed in a long-wavelength or low energy limit where the constituents of the bodies can be treated as a continuum. This approximation starts to break down when the distances between bodies approach an angstrom. That is the separation of the constituent atoms of the bodies, the distance scale where exchange effects and other quantum physics becomes important. At the other extreme, for distances beyond a hundred microns, the Casimir effect becomes too weak to detect.

The distance scaling of the Casimir energy for bodies separated by a distance d , can be found by approximating the Lifshitz integral (1.1.2.3) in certain limits. In particular, one must compare the separation of the bodies d to the resonant wavelengths or frequencies of the interacting media. This requires some knowledge of the peak frequencies ω_A of the atomic polarizabilities $\alpha(\omega)$ or the dielectric function $\epsilon(\omega)$. At nonzero temperature, there is another distance scale given by the thermal wavelength, $\omega_T = k_B T / \hbar$. One can estimate the most important frequencies by examining $\alpha(is)$, $\epsilon(is)$, $e^{-2pd\xi/c}$ and approximating the integral () in various limits.

In the near field or van der Waals regime, the separation of the bodies is less than any of the resonant wavelengths for the bodies $d \ll \omega_A/c$. In that limit all of the frequencies contribute, weighted by $\alpha(i\omega)$ and $\epsilon(i\omega)$. The exponential factor $e^{-2pd\xi/c}$ is also constant for all relevant frequencies. In essence, the interaction is an instantaneous dipole interaction between the bodies. For example the atom-wall potential shows a d^{-3} scaling.

In the retarded or Casimir–Polder regime, the atoms are much further than a resonant wavelength $d \gg \omega_A/c$. In that case the dominant contributions come at zero frequency, and the functions can be approximated with their static limit. This typically occurs for distances greater than a micron. In this far field regime, the

potential typically decays more quickly. For example, the atom-wall potentials shows a d^{-4} scaling in this limit.

At even greater separations between the bodies is the thermal regime $d \sim \omega_T/c$, where the real photons excited by the thermal field contribute significantly to polarizing the atom. At room temperature, the thermal wavelength is $\lambda_T \sim 10\mu\text{m}$. In this regime the potential falls off more slowly as $E \sim d^{-3}$, the same as the near-field van der Waals regime.

1.2. Overview of Casimir Experiments

The Casimir effect has been measured in experiments, both for macroscopic bodies and atoms. This section provides a brief overview of the broad categories of experiments where the Casimir effect is relevant, and the challenges these experiments provide to theoretical and computational methods. The following is intended as a broad survey, since the full literature on the Casimir and Casimir–Polder effects is quite large.

1.2.1. Experiments on Casimir Forces

Despite its prediction in 1948, the Casimir effect proved quite difficult to directly measure. Some early confirmations used the Casimir effect to explain the thickness of liquid helium film on the wall of its container (Dzyaloshinskii *et al.*, 1961; Sabisky and Anderson, 1973). In that case, helium satisfies the repulsive Casimir criterion and it is energetically favorable to have a thin film of helium between the vacuum and the walls.

The first precise measurement of the Casimir effect was carried out by Lamoreaux (1997). This experiment measured the Casimir force between a sphere above a metal

plate via a torsion pendulum. This landmark experiment was closely followed by Mohideen and Roy (1998), who used an atomic force microscope in a closer distance regime to measure the force in a sphere-plate geometry. The Casimir force has also been directly measured in a nanoelectromechanical (NEMS) system by Chan *et al.* (2001). In this case, the Casimir force is detected by the modification it makes to the frequency of a torsional oscillator suspended above a plate. The sphere-plate and oscillator geometries have the experimental advantage of removing the need to carefully align the parallel metal plates. Despite the aforementioned difficulties, the Casimir force between parallel plates was measured precisely by Bressi *et al.* (2002).

The Casimir force is also important in applications of microelectromechanical systems (MEMS), as a source of stiction (Buks and Roukes, 2001; Serry *et al.*, 1998; Tas *et al.*, 1996). This is particularly important in free standing structures such as nano-oscillators. Given that the Casimir force is an attractive potential, if parts of the device get too close to the substrate they will permanently stick to one another, leading to device failure.

Precisely measuring such a small force requires careful calibration of the measurements and removing systematic effects. Reviews of these and other difficulties are available (Bordag *et al.*, 2009; Lamoreaux, 2011; van Zwol *et al.*, 2011). Two of the primary experimental errors are due to patch potentials, and surface roughness. The patch potentials are randomly distributed, localized surface charge distributions on the surface of a conductor. Their Coulombic interaction leads to a d^{-1} power law contribution to the total force, which must be subtracted off to extract the weaker Casimir force, which decays as d^{-3} or d^{-4} (Sushkov *et al.*, 2011b).

While these electrostatic forces can be mitigated and in principle removed, the Casimir effect is a fundamental effect and must be taken into account in engineering applications.

The fact that the thin metallic films and surfaces used in these experiments are not perfectly smooth is referred to as surface roughness, and is one of the main theoretical sources of error in these experiments. In addition, the optical properties of the surface must also be carefully characterized, since the optical properties of a coating can vary significantly. Another difficulty in predicting the size of the Casimir effect is that the optical properties must be interpolated from data for other experiments (van Zwol *et al.*, 2011).

1.2.2. Experiments on Casimir–Polder Forces

Van der Waals and Casimir–Polder forces were first observed experimentally in molecules, which prompted the further development of theory to explain the effects. Beyond those early experiments, Casimir–Polder forces have also been measured precisely in more modern experiments using isolated atoms in experiments using atomic beams, cavity QED, and Bose-Einstein condensates.

The first modern attempts at directly measuring the Casimir–Polder force used atomic beams near surfaces. Sukenik *et al.* (1993) made the first modern measurement of the Casimir–Polder force. Their experiment passed a hot beam of atoms through an optical cavity and detected the Casimir–Polder force by measuring the fraction of the atoms that passed through the cavity undeflected. More recent experiments by Perreault and Cronin (2005), and Lonij *et al.* (2009) measured the Casimir–Polder force by passing an atomic beam through a grating and detecting the phase-shift via atom interferometry.

The Casimir–Polder effect has also been observed in the context of a Bose–Einstein Condensate (BEC) of ultra-cold atoms (Harber *et al.*, 2005; Obrecht *et al.*, 2007). The atoms are confined to a harmonic trap, and can be brought near to a surface to probe the Casimir force, where the Casimir–Polder force shifts the oscillation frequency of the harmonic trap.

The Casimir–Polder force is also important in developing atomic technologies. Atoms are an attractive platform for a number of reasons: Each atom of the same species is identical; atoms have readily accessible, well-defined transitions that can be used to control their motion, internal state and interactions; and atoms have internal states that are long-lived, which would be important in storing information.

In recent years there has been a concerted push to develop technology that retains the appealing features of cold atoms in an architecture that can be scaled up to having large numbers of addressable atoms (Kimble, 2008). The desire to get strong coupling between the atom and light fields, addressable qubits, and a scalable architecture has pushed groups towards developing traps that hold atoms close to dielectric surfaces. In this regime, the Casimir–Polder force is the dominant force, which can only be partially mitigated by using laser fields to generate repulsive potentials. In designing these new devices it is essential to compute and account for the Casimir–Polder force the atoms experience when brought close to the dielectric surface.

One direction that has been pursued is the atom chip (Folman *et al.*, 2000; Salem *et al.*, 2010; Schneider *et al.*, 2003), where atoms are trapped within a few microns of the surface via a combination of lasers and magnetic fields from wires embedded in the surface. In most applications the Casimir effect imposes a lower bound on how close bodies can be brought to each other, which in turn limits the coupling strength, as well as how small devices can be made. In the atom-chip example, bringing the

atoms closer than a micron lead to most of the atoms escaping the trap (Lin *et al.*, 2004).

Another direction that has been pursued is strong coupling of atoms to light via cavity QED. Kimble’s group is developing microscopic dielectric waveguides to allow trapping, addressing and strongly interacting with single atoms in a scalable manner (Alton *et al.*, 2011; Goban *et al.*, 2014; Hung *et al.*, 2013). In more recent work, the Casimir–Polder potential is explicitly accounted for as part of the trapping potential (Goban *et al.*, 2014), and must be precisely computed.

1.2.3. Current Experimental Directions

Beyond directly detecting the Casimir effect, experiments are also moving in some directions worth highlighting, since they are quite challenging for the theory to handle. There is a continued effort to find repulsive Casimir effects, via material properties or geometric efforts. In addition, some experiments search for new forces on the micron scale, where any deviation from the predicted Casimir effect may be a new force. In that case it is essential to be able to precisely calculate Casimir forces, and carefully remove all known backgrounds.

1.2.3.1. Repulsive Casimir Effects

Given that Casimir effects tend to enforce lower bounds for how close bodies can approach each other without stiction, there has been a search for repulsive Casimir effects. This would open the possibility of trapping particles, and potentially allow smaller devices to be constructed. Unfortunately, these prospects are somewhat limited, due to requiring unusual material properties. From the Lifshitz formula (1.1.2.3), the Casimir force is repulsive if $r_{12}r_{23} < 0$. This implies Casimir

repulsion should be possible if $\epsilon_1 < \epsilon_3 < \epsilon_2$ over a broad range of frequencies. This was experimentally demonstrated for a gold sphere immersed in bromobenzene above a silica plate by Munday *et al.* (2009). However, this method is little help for Casimir forces between identical materials or cold atoms in vacuum.

Alternatively, the Casimir force is also repulsive for combinations of dielectric and magnetic materials (Boyer, 1974). Given the strength of electric interactions over magnetic interactions in atoms, this spurred interest in exploiting materials with strong magnetic responses (Kenneth *et al.*, 2002). Since these materials are relatively rare, there was some interest in exploiting metamaterials [arrays of micropatterned circuits with large effective magnetic response at certain wavelengths (Pendry *et al.*, 1999)]. However, this was shown to be ineffective for Casimir applications since the underlying metallic dielectric response of the metamaterial dominates for the most important long wavelengths. Since the metallic response implies an attractive potential, the overall Casimir effect is attractive (Iannuzzi and Capasso, 2003; Pirozhenko and Lambrecht, 2008; Rosa *et al.*, 2008; Yannopapas and Vitinov, 2009).

While the preceding discussion emphasized varying materials for Casimir applications, it may be possible to exploit similar ideas for repulsive Casimir–Polder effects (Milton *et al.*, 2011, 2012), since the atom responds to a narrower range of frequencies. In the far field, the attractive dielectric response would dominate over any repulsive response, so it might be possible to engineer a trap. These proposals require an anisotropic response from the atom, which might be possible in the excited state.

Another method of generating repulsive Casimir effects is by varying the geometry of the bodies. For example, the Casimir effect is repulsive in certain regimes for an elongated needle above a hole in a conducting plate (Levin *et al.*,

2010; Rodriguez *et al.*, 2013). However, in this example the repulsion is unstable. A stability criterion can be derived for the Casimir energy from within the scattering approach to Casimir theory (Rahi *et al.*, 2011, 2010).⁴ Only bodies composed of media for which the planar Casimir force is repulsive can be stably levitated (Rahi *et al.*, 2011).

Boyer (1968) found that the renormalized Casimir self-stress of a conducting shell is repulsive. In this case, a great deal of care is required in isolating divergent terms to find a finite result. This surprising result has been verified multiple times [the issue of self-stresses is reviewed in Milton *et al.* (2011), and chapters 5 and 6 of Milton (2001)]. There is also a similar repulsive Casimir effect for a dielectric sphere. While the self stress on a spherical shell is repulsive, the force between two separated halves of a sphere is attractive. Thus it is not clear how this self-stress could be measured.

1.2.3.2. Searches for New Physics

The Casimir force is also important for speculative searches for new physics on the millimeter to micron scale (Bezerra *et al.*, 2011; Dimopoulos and Geraci, 2003). Since the new physics must be relatively short-ranged, it is typically modeled with a Yukawa potential, $V_{\text{Yuk}} = \alpha e^{-\lambda r}/r$, which models the interaction with a new massive particle. On the micron scale however, the Casimir effect is the dominant interaction between neutral bodies, and must be carefully subtracted in any experimental procedure. Experiments then look for deviations from the expected Casimir effect, which means that the theory and experiment must be in good agreement with one another. This approach has already been used to exclude regions of the parameter space for the

⁴The scattering approach which will be briefly discussed in Section 1.3.2.

hypothetical Yukawa interaction (Bezerra *et al.*, 2011; Chen *et al.*, 2016; Obrecht *et al.*, 2007; Sushkov *et al.*, 2011a). Experiments searching for modifications of gravity typically employ a thin gold layer over a density modulation. The gold layer provides a common short-ranged Casimir interaction, while the a density modulation allows measuring variations due to gravity (Geraci and Goldman, 2015; Sorrentino *et al.*, 2009). Given the difficulties in cleanly measuring the Casimir force, this even more ambitious program has yet to yield results.

1.3. Computational Methods for Casimir Effects

Modern experiments require theoretical and computational methods for the Casimir force that can account for a wide variety of material responses, anisotropies and the ability to handle arbitrary shapes. For a simple, symmetric geometry (like the perfectly conducting planes we used in Section 1.1.1.1) it is possible to write down tractable analytical expressions for the Casimir energy based on expanding the field in mode functions. However, for completely general geometries these requirements force one to adopt a numerical approach to computing Casimir forces (Johnson, 2011). We will discuss three of these methods: the proximity-force approximation (PFA), the scattering or fluctuating surface current approach, and the worldline method.

1.3.1. Proximity Force Approximation

The proximity force approximation (PFA) or Derjaguin approximation, is an uncontrolled approximation to the Casimir force between arbitrarily shaped objects (Blocki *et al.*, 1977; Derjaguin, 1934). The PFA treats each infinitesimal patch of the surfaces as if they were planar bodies, and sums up the pairwise interactions between different patches. The PFA is assumed to be valid if the radius of curvature

of the bodies R is large relative to their separation d . For many years the PFA was the only practical general method of estimating Casimir forces in arbitrary geometries. The PFA has the advantage of being straightforward to implement, and functions as an order of magnitude estimate for the Casimir force for arbitrary geometries.

However, it has some prominent limitations. First, it is only valid for vanishing curvature. Second, the PFA assumes that the force can be found by integrating up the pair-wise Casimir forces between each pair of surface patches. This ignores the non-additivity of the Casimir force. Unlike the potential between electric charges where the total potential is the sum of the pair wise potential energies, the Casimir force for an arrangement of bodies is not just the sum of the pair wise energies. [This is discussed further in Section 8.2 and Section 8.4 by Milonni (1994).] As a crude justification, the Casimir energy involves a sum over the frequencies for mode functions of the systems. Since the mode functions are changed in a global, nonlinear fashion by introducing another body, the sum over frequencies also changes in a nonlinear fashion as more bodies are added.

1.3.2. Scattering Approach

The scattering approach is currently the only general method of computing EM Casimir forces between media.⁵ The scattering method is based on techniques from classical EM theory and quantum mechanics. This method has been developed by a number of groups as an analytical method for general geometries (Canaguier-Durand *et al.*, 2012; Emig and Büscher, 2004; Emig *et al.*, 2007; Kenneth and Klich, 2006; Lambrecht *et al.*, 2006; Maia Neto *et al.*, 2008; Rahi *et al.*, 2009). The Casimir energy

⁵The following is an extremely short introduction to the scattering method. The book chapters by Lambrecht *et al.* (2011), Rahi *et al.* (2011) and Johnson (2011) provide a varied introduction to the topic from some of the main contributors.

can be written as

$$E = \frac{\hbar c}{2\pi} \int_0^\infty d\xi \log \det[\mathbb{M}\mathbb{M}_\infty^{-1}] \quad (1.30)$$

where \mathbb{M} is the scattering matrix describing scattering between the free modes of the EM field induced by the presence of bodies, and ξ is the imaginary frequency (Rahi *et al.*, 2009). The energy is renormalized via \mathbb{M}_∞^{-1} , which is the scattering matrix as the bodies are moved arbitrarily far apart; this renormalization removes any self-coupling of the bodies to themselves. The indices of these matrices run over the labels of the possible modes (such as wavelength, polarization, mode origin for different bodies). Derivations similar to the argument principle used in Section 1.1.2.1 can be applied to describe the scattering between modes—instead of reflection coefficients for a surface, one considers the full scattering matrix for each body. This version of the scattering method has been applied to two-body systems such as realistic mirrors (Lambrecht *et al.*, 2006), and spheres and planes with investigations of surface roughness (Canaguier-Durand *et al.*, 2012). This subclass of these methods rely on scattering between mode functions suited to analytical expansions, and while they in principle offer a general purpose numerical method, the simulations may be slow to converge if the choice of basis functions is poorly suited to the actual geometry required.

The Johnson group at MIT has developed a formulation of the scattering method that is better suited to numerical applications for piecewise constant media (Reid *et al.*, 2009, 2011, 2013; Rodriguez *et al.*, 2007a,b, 2009). In particular, Reid *et al.* (2009, 2011, 2013) developed the fluctuating-surface-current formulation as a general method for computing Casimir energies for piecewise continuous linear dielectric and magnetic media. In essence the method calculates the interaction between electric and magnetic surface currents on different bodies, mediated by the EM

field. Mathematically this is derived from a path integral for the EM field, where the fields are restricted to obeying EM boundary conditions at the surfaces via functional delta functions [simpler boundary conditions were handled in this fashion by Bordag *et al.* (1985) and Li and Kardar (1991)]. The delta functions introduce fields bound to the surfaces, which can be interpreted as surface currents flowing to enforce boundary conditions. After integrating out the EM field in the interior and exterior regions, these surface currents interact with one another via the EM Green functions. Since the method assumes piecewise, homogeneous media and enforces EM boundary conditions, it is the relatively simple homogeneous EM Green function that appears in these expressions. These surface integrals are then discretized by splitting the surface into a finite number of patches. All of the surface currents can then be integrated over, leaving a functional determinant analogous to Eq. (1.30) where now the matrix elements \mathbb{M} describe the coupling between different surface-patches induced by the EM Green functions.

Numerically, this method comes down to computing the determinant of a large matrix, which is an intensive operation. If a matrix has N non-zero entries, the determinant for a dense matrix requires $\mathcal{O}(N^3)$ operations. While it is possible to parallelize computing the determinant (Beliakov and Matiyasevich, 2013), this is difficult. However, for a sparse matrix system, it may be possible to make this relatively efficient and only require $\mathcal{O}(N \log N)$ operations (Reid *et al.*, 2009). Since each frequency ξ contributes independently, the integral over ξ could be trivially parallelized, but this may only offer relatively little parallelization for some problems.

The fluctuating-surface-current method has been used to describe the energy dependence of tetrahedral nanoparticles, capsules, and other geometries (Reid *et al.*, 2009, 2011; Rodriguez *et al.*, 2010). It has also been used to find cases where the

Casimir force is repulsive due to geometric effects (Levin *et al.*, 2010; Rodriguez *et al.*, 2013). The scattering method has also been used in the design of atomic traps near dielectric waveguides, where the Casimir–Polder force is an essential component of the trap (Hung *et al.*, 2013).

As we noted, the scattering method is the only available general method for computing Casimir effects. However, it is useful to have multiple methods with different computational properties and biases, particularly when extending calculations to unexplored domains. We now turn to the worldline method, which offers a very different picture and numerical method.

1.4. Path Integrals

In order to discuss the modern methods of computing the Casimir effect it is necessary to introduce the path integral. The path integral was originally developed by Feynman (1948) as an alternative formulation of quantum mechanics (Feynman and Hibbs, 1965). In the path integral, the probability amplitude for a particle to propagate from one position to another, is given by the sum over *all* possible paths between the points. [In fact the path integral can be derived as the propagator from more traditional operator quantum mechanics (Sakurai, 1994).] Each path is weighted with a phase $e^{iS[x(t)]/\hbar}$ where $S[x(t)]$ is the classical action for the path.

Path integrals have been used extensively in a wide range of theoretical physics (Kleinert, 2012). While offering an intuitive picture of quantum mechanics, they are much harder to use than typical operator mechanics for anything other than the simplest problems (Feynman and Hibbs, 1965). However, path integrals form a natural basis for quantum field theories, where they offer a relativistically covariant

quantization procedure that naturally accounts for the gauge symmetries that underlie the Standard Model of particle physics (Brown, 1994; Srednicki, 2008).

Path integrals have also been used in mathematics and statistics to describe stochastic processes (Durrett, 1996; Kac, 1949; Karatzas and Shreve, 1991). Rather than solving the Schrödinger equation, this path integral solves a diffusion equation—this effectively passes over to “imaginary time,” since after the Wick rotation $t \rightarrow -i\tau$, the Schrödinger equation is a diffusion equation. This mathematical path integral weights each path by $e^{-S_E[x]}$, where S_E is the real-valued, imaginary time action for the path. In this form the path integral has clearer convergence properties, since the paths are weighted by real, decaying exponentials, as opposed to the oscillatory integrals in Feynman’s path integral.

Path integrals underlie most of the work carried out in this thesis: we will use path integrals to quantize the EM field, and the worldline method relies heavily on path integrals. In addition, we will use the connection between path integrals and diffusion equations to verify analytically that the worldline path integral gives the correct results, and enhance our numerical calculations. Considering their importance to this thesis, we will now derive Feynman’s path integral, which will serve as a prototype for all of the path integrals that follow. [Our derivation follows the simple one given in Sakurai (1994).]

1.4.1. Derivation of Feynman’s Path Integral

Let us consider the quantum mechanical treatment of a particle moving in a D -dimensional space time, in a time-independent potential $V(\mathbf{x})$. The particle is

described by the following Hamiltonian:

$$\hat{H} = \frac{\hat{\mathbf{p}}^2}{2m} + V(\hat{\mathbf{x}}). \quad (1.31)$$

The position and momentum operators obey the following commutation relations,

$$[\hat{x}_i, \hat{p}_j] = i\hbar\delta_{ij} \quad [\hat{x}_i, \hat{x}_j] = [\hat{p}_i, \hat{p}_j] = 0, \quad (1.32)$$

and have the following resolutions of the identity,

$$I = \int d\mathbf{x} |\mathbf{x}\rangle \langle \mathbf{x}| = \int \frac{d\mathbf{p}}{(2\pi\hbar)^D} |\mathbf{p}\rangle \langle \mathbf{p}|. \quad (1.33)$$

The overlap between position and momentum eigenstates is

$$\langle \mathbf{x} | \mathbf{p} \rangle = e^{i\mathbf{p} \cdot \mathbf{x} / \hbar}. \quad (1.34)$$

In quantum mechanics, the amplitude for a particle starting at \mathbf{x}_0 at time $t_0 = 0$, and propagating to \mathbf{x}_N at time t is given by

$$\langle \mathbf{x}_N, t | \mathbf{x}_0, t_0 \rangle = \langle \mathbf{x}_N | e^{-i\hat{H}t/\hbar} | \mathbf{x}_0 \rangle. \quad (1.35)$$

The amplitude to propagate from \mathbf{x}_0 to \mathbf{x}_N can be developed into a path integral in a number of steps. First, the evolution operator is split into N pieces, and $(N - 1)$ resolutions of the \mathbf{x} -identity and N resolutions of the \mathbf{p} -identity are inserted between

the pieces

$$\begin{aligned}
\langle \mathbf{x}_N, t | \mathbf{x}_0, t_0 \rangle &= \int \prod_{k=1}^{N-1} d\mathbf{x}_k \prod_{j=1}^{N-1} \frac{d\mathbf{p}_j}{(2\pi\hbar)^D} \langle \mathbf{x}_N | \mathbf{p}_N \rangle \langle \mathbf{p}_N | e^{-i\hat{H}\Delta t/\hbar} | \mathbf{x}_{N-1} \rangle \\
&\times \langle \mathbf{x}_{N-1} | \mathbf{p}_{N-1} \rangle \langle \mathbf{p}_{N-1} | e^{-i\hat{H}\Delta t/\hbar} | \mathbf{x}_{N-2} \rangle \cdots \langle \mathbf{x}_1 | \mathbf{p}_1 \rangle \langle \mathbf{p}_1 | e^{-i\hat{H}\Delta t/\hbar} | \mathbf{x}_0 \rangle
\end{aligned} \tag{1.36}$$

where $\Delta t := t/N$. At this point we can note the basic structure: The total amplitude for the particle to propagate from \mathbf{x}_0 to \mathbf{x}_N is the product of the amplitudes to propagate from one point \mathbf{x}_k to the next \mathbf{x}_{k+1} , with the total amplitude being the sum over all such paths. Each infinitesimal time evolution operator can be factored into a kinetic and potential piece,

$$e^{-i\hat{H}\Delta t/\hbar} = \exp\left(-i\frac{\hat{\mathbf{p}}^2}{2m\hbar}\Delta t\right) \exp\left(-\frac{i}{\hbar}V(\hat{\mathbf{x}})\Delta t\right) + \mathcal{O}(\Delta t^2), \tag{1.37}$$

where the corrections due to splitting and factorizing the exponential operator contribute at $\mathcal{O}(\Delta t^2)$. [In general, it is crucial to consistently carry out all expansions in path integrals to $\mathcal{O}(\Delta t)$.] The position and momentum operators can then be replaced by their eigenvalues, and the state-overlap can be used to write,

$$\langle \mathbf{x}_N, t | \mathbf{x}_0, t_0 \rangle = \int \prod_{k=1}^{N-1} \frac{d\mathbf{x}_k d\mathbf{p}_k}{(2\pi\hbar)^D} \left(\prod_{n=0}^{N-1} e^{-i\mathbf{p}_{n+1}^2 \Delta t / (2m\hbar) - iV(\mathbf{x}_n) \Delta t / \hbar + i(\mathbf{x}_{n+1} - \mathbf{x}_n) \cdot \mathbf{p}_{n+1} / \hbar} \right). \tag{1.38}$$

Since the momentum integrals are Gaussian, they can be straightforwardly evaluated, with the result

$$\langle \mathbf{x}_N, t | \mathbf{x}_i, t_0 \rangle = \int \prod_{k=1}^{N-1} d\mathbf{x}_k \prod_{n=0}^{N-1} \left[\left(\frac{m}{2\pi i \hbar \Delta t} \right)^{D/2} e^{im(\mathbf{x}_{n+1} - \mathbf{x}_n)^2 / (2\Delta t)} e^{-iV(\mathbf{x}_n)\Delta t / \hbar} \right] \quad (1.39)$$

$$= \int D\mathbf{x} \exp \left[\frac{i}{\hbar} \int_0^t dt' \left(\frac{m}{2} \dot{\mathbf{x}}^2 - V[\mathbf{x}(t')] \right) \right]. \quad (1.40)$$

In the final line we have taken the continuum limit, replacing $(\mathbf{x}_{n+1} - \mathbf{x}_n)/\Delta t \rightarrow \dot{\mathbf{x}}$, $\sum_n \Delta t f(n\Delta t) \rightarrow \int dt f(t)$, and introducing $D\mathbf{x} = \prod_{k=1}^{N-1} d\mathbf{x}_k \left[m / (2\pi i \hbar \Delta t) \right]^{D/2}$. The phase in exponent is the classical action for a particle in a potential. Paths with the same phase will add together constructively, while paths in regions where the phase is quickly varying will cancel. This leads to a natural description for the classical limit ($\hbar \rightarrow 0$) where only the paths of stationary phase where $\delta S[x(t)] = 0$ contribute. Quantizing field theories via the path integral is seen as a more relativistically covariant process than the canonical quantization procedure, which must single out a particular time. The symmetries of the field are also naturally taken into account due to the presence of the action.

In this thesis, this simple type of derivation will be all that is required. We will often work with the imaginary time version, which replaces the oscillating exponentials with decaying exponentials. The extension to field path integrals over fields is straightforward: the field $\phi(\mathbf{x})$ is described by its value at finitely many points $\phi(\mathbf{x}_k)$, where the field at each point varies independently. The field path integral involves an integral over the field values at all of these points. At the end of the calculation, the spacing between grid points goes to zero, and the size of the grid is taken to be arbitrarily large. We will also only need to consider Gaussian

path integrals, of the type considered here. This derivation will be extended to include sources in Chapter III.

1.5. Scalar Worldline Casimir Energies

The worldline method is an alternative method for computing Casimir energies (Gies *et al.*, 2003). The worldline method is a descendant of the scalar electrodynamics discussed by Feynman (1950), where the dynamics of a scalar field is described in terms of a particle propagating in an artificial proper-time through a fixed background potential. The worldline method was later developed as an alternative method for carrying out general quantum field theory calculations in terms of single particle quantum mechanics (McKeon and Rebhan, 1993; Schubert, 2001; Strassler, 1992). The basic insight of the worldline method is that for one-loop effective actions⁶, the field path integral calculation can be recast in terms of the path integral for particles traveling in closed space-time paths. Higher order loop calculations can also be carried out with more particles, and gauge fields can also be treated (Schubert, 2001). For example, the worldline method has been used to compute relativistic field effects for QED such as the Lamb shift (Schmidt and Schubert, 1995). It has also been used as a numerical algorithm for computing these relativistic QED effects (Mazur and Heyl, 2014)—however, these methods were developed for free-space interactions at high energy, rather than the low energy Casimir phenomena we seek to describe. The worldline method is also closely related to the Heat Kernel [which is reviewed

⁶ One loop order in quantum field theory corresponds to processes such as the Casimir effect, where the field emits and absorbs a virtual particle, such as in Figure 1.2. These are the first correction from quantum effects. For example, the Lamb shift and Casimir–Polder effect involve one loop, since the electron emits and reabsorbs a photon. Higher loop orders correspond to more virtual processes. The effective action, gives the equations of motion in the absence of any external driving on the system (Weinberg, 1996, Ch. 16). The one-loop effective action then gives calculates action accounting for the lowest order contributions from quantum fluctuations around the classical solution.

in Vassilevich (2003)]. The Heat Kernel examines the divergence structure of a field theory by examining the short time behavior of the worldline.

The worldline method was first used to compute scalar Casimir energies by Gies *et. al* (Gies and Klingmüller, 2006a,b; Gies *et al.*, 2003). The scalar worldline method has been extended to nonzero temperatures (Klingmüller and Gies, 2008), used to study the torsion of inclined planes (Weber and Gies, 2009), and forces in the sphere-plane and cylinder-plane geometries (Weber and Gies, 2010a,b). In these nontrivial geometries the worldline method has also been used to examine the failure of the proximity force approximation. More recent work has focused on computing the stress-energy tensor (Schäfer *et al.*, 2012, 2016), with a view to exploring how the Casimir energy violates certain energy conditions (violations of which are required for certain exotic physics).

The scalar worldline is also related to some semiclassical expansions for the Casimir energy. In particular, it is a direct numerical method for computing the so-called optical path integral discussed by Scardicchio and Jaffe (2005, 2006). The sum over intersecting paths is also reminiscent of the semiclassical approach to the Casimir force by Schaden and Spruch (1998), which evaluates the Casimir energy by summing over all periodic orbits of light around the interacting bodies. This latter work is particularly related to other work on the semiclassical limits of path integrals involving chaos (Gutzwiller, 1990). Both of these approximate techniques rely on a path integral expression for the Casimir energy that models electromagnetism as a scalar field. The worldline provides a general way of evaluating those path integrals.

The worldline method has also been applied to the Casimir piston, where there are interesting geometric effects based on the geometry of the piston (Schaden, 2009a,b). Most of this work is for idealized surfaces that imposed Dirichlet boundary

conditions, but there has also been some effort to extend the worldline method to account for Neumann boundary conditions (Fosco *et al.*, 2010). To date there has only been speculation on how to extend the worldline method to electromagnetism (Aehlig *et al.*, 2011), which only considered perfect conductors, and did not have concrete, correct results.

1.5.1. Derivation of the Scalar Casimir Worldline Path Integral

We now introduce the basic scalar worldline method, to discuss its positive features and limitations. We will use terminology and scaling of dimensions in common with our later work, rather than the choices used in the original papers by Gies *et al.* (2003). [See also chapter 20 of Steck’s Quantum Optics notes for an alternative perspective on this work, including some of the analytical techniques will be used in later chapters (Steck, 2015).]

Consider a scalar field $\phi(\mathbf{r}, t)$, interacting with a background potential $V(\mathbf{r})$. As a matter of convention we will distinguish between \mathbf{r} , which is a position label or parameter, and the coordinate of a path integral \mathbf{x} . The action for the field ϕ is given by the time integral of the Lagrangian density \mathcal{L} ,

$$S = \int_0^T dt \int d\mathbf{r} \mathcal{L} = \int_0^T dt \int d\mathbf{r} \left(\frac{1}{2c^2} (\partial_t \phi)^2 - \frac{1}{2} |\nabla \phi|^2 - V(\mathbf{r}) \phi^2 \right). \quad (1.41)$$

The potential $V(\mathbf{r})$ defines the surfaces of the interacting objects

$$V(\mathbf{r}) := \lambda \sum_j \delta[\sigma_j(\mathbf{r} - \mathbf{R}_j)], \quad (1.42)$$

where λ is the coupling constant, $\sigma_j(\mathbf{r}) = 0$ defines the surfaces, and \mathbf{R}_j marks the center location of each body. In most work on scalar worldlines, the coupling constant

λ is taken to infinity, which corresponds to imposing Dirichlet boundary conditions on the surfaces. For planar geometries, this recovers electromagnetic Casimir results for idealized perfect conductors.

From the Lagrangian, one can find the Hamiltonian and quantize the theory. The momentum conjugate to ϕ is given by

$$\Pi(\mathbf{r}, t) := \frac{\partial \mathcal{L}}{\partial(\partial_t \phi)} = \frac{1}{c^2} \partial_t \phi(\mathbf{r}, t). \quad (1.43)$$

The Hamiltonian is then given by

$$H := \int d\mathbf{r} (\Pi \partial_t \phi - \mathcal{L}) = \int d\mathbf{r} \left(\frac{\Pi^2}{2} + \frac{1}{2} (\nabla \phi)^2 + V(\mathbf{r}) \phi^2 \right). \quad (1.44)$$

The theory can now be quantized by promoting the classical fields to quantum operators, $\phi \rightarrow \hat{\phi}$, $\Pi \rightarrow \hat{\Pi}$, with equal-time commutation relations

$$[\hat{\phi}(\mathbf{r}, t), \hat{\Pi}(\mathbf{r}', t)] = i\hbar \delta(\mathbf{r} - \mathbf{r}'). \quad (1.45)$$

In exactly analogous fashion to quantum mechanics, the overlap between states is given by

$$\langle \phi | \Pi \rangle = \exp \left(\frac{i}{\hbar} \int d\mathbf{r} \phi(\mathbf{r}) \Pi(\mathbf{r}) \right). \quad (1.46)$$

Physical quantities of interest such as Casimir energies and forces can be computed by taking suitable derivatives of the field partition function. The quantum partition function for the field is

$$Z = \text{tr} \left(e^{-\beta \hat{H}} \right) = \int d\phi \langle \phi | e^{-\beta \hat{H}} | \phi \rangle, \quad (1.47)$$

and the trace is evaluated over the complete set of field states. It is actually more useful to carry out calculations with the free energy $\mathcal{F} = -k_B T \log Z$. As in Section 1.4, the exponential operator can be split into N pieces, and resolutions of the identity in both fields and conjugate-momentum fields can be inserted between each piece. After integrating out the momentum fields, the partition function can be written as a Euclidean path integral

$$Z = \int D\phi \exp \left[- \int_0^{\hbar\beta c} d\tau \int d\mathbf{r} \left(\frac{1}{2} (\partial_\tau \phi)^2 + \frac{1}{2} (\nabla \phi)^2 + V(\mathbf{r}) \phi^2 \right) \right], \quad (1.48)$$

where $\tau = \beta \hbar c$. The partition function can be cast into a more suggestive form by integrating by parts in the exponential integrand,

$$Z = \int D\phi \exp \left[- \int_0^{\hbar\beta c} d\tau \int d\mathbf{r} \phi(\mathbf{r}, \tau) \left(-\frac{1}{2} \partial_\tau^2 - \frac{1}{2} \nabla^2 + V(\mathbf{r}) \right) \phi(\mathbf{r}, \tau) \right]. \quad (1.49)$$

The surface terms from integrating by parts were discarded by assuming the fields tend to zero at spatial (and temporal) infinity.

The functional integral over ϕ is Gaussian and can be formally evaluated as a functional determinant, since the differential operator is positive operator. Some care is required in regularizing such infinite determinants. This is done in analogy with finite dimensional Gaussian integrals. The fields can be considered as only being evaluated on a finite lattice of space-time points, with the lattice also having a finite extent which bounds all bodies. The field ϕ at each point \mathbf{x}_k , is treated as an independent variable from the fields at other positions. The gradient operators can be treated via their finite difference approximations, which can be thought of as sparse matrices. For example, $\partial_x^2 \phi(x_k) \approx [\phi(x_k + \Delta) - 2\phi(x_k) + \phi(x_k - \Delta)]/\Delta^2$. In

that case the partition function is a large, finite Gaussian integral of the form,

$$Z_{\text{reg}} = \int d\phi_k \exp \left(- \sum_{j,k} \Delta\tau (\Delta x)^{D-1} \phi_k A_{jk} \phi_j \right). \quad (1.50)$$

where the fields have been labeled with position indices and the matrix A represents the differential operator. This regularized expression can be integrated, under the assumption that the eigenvectors of A can be found, where $\sum_k A_{jk} \psi_k^{(n)} = \lambda_{(n)} \psi_j^{(n)}$. In that case, each Gaussian integral decouples and the regularized partition function can be written as

$$Z_{\text{reg}} = C \prod_n \lambda_{(n)}^{-1/2} = C \det(A)^{-1/2}, \quad (1.51)$$

where the determinant is understood to be the product of the eigenvalues of the operator A .⁷ The limit of an arbitrarily large volume, and lattice resolution can be taken after integration.

In an analogous fashion, one can formally evaluate the partition function path integral as a functional determinant,

$$Z \propto \det^{-1/2} \left(-\frac{1}{2} \partial_\tau^2 - \frac{1}{2} \nabla^2 + V(\mathbf{r}) \right). \quad (1.52)$$

The proportionality is due to an additional (infinite) normalization constant which will be canceled in the renormalization process. The free energy for the interacting

⁷ In fact, there is an approach to computing van der Waals energies based on directly evaluating a functional determinant for electric fields on a discrete spatial grid (Maggs and Everaers, 2006; Pasquali *et al.*, 2008). This approach omits any time evolution of the fields, but it does offer a direct method of trying to evaluate the field path integral. That work relied on direct spatial discretization to evaluate the functional determinants, which limits the size of medium that can be considered.

field can be written as

$$\mathcal{F} = -k_{\text{B}}T \log Z = \frac{1}{2}k_{\text{B}}T \log \det \left(-\frac{1}{2}\partial_{\tau}^2 - \frac{1}{2}\nabla^2 + V(\mathbf{r}) \right) + C, \quad (1.53)$$

where C is a divergent constant. As it stands this functional determinant is divergent, but finite results can be found by subtracting off the free energy \mathcal{F}_0 when the bodies are removed arbitrarily far apart. The renormalized free energy can now be written in terms of a single-particle path integral via some formal manipulations. First, we will use the identity $\log \det A = \text{tr} \log A$, which can be verified for positive finite matrices,

$$\log \det A = \log \prod_j \alpha_j = \sum_j \log \alpha_j = \text{tr} \log A, \quad (1.54)$$

where we used the facts that the trace and determinant of a matrix A are given by the sum and product of its eigenvalues α_j respectively. Second, the logarithm can be rewritten in an integral representation,

$$\log A - \log B = - \int_0^{\infty} \frac{d\mathcal{T}}{\mathcal{T}} (e^{-A\mathcal{T}} - e^{-B\mathcal{T}}), \quad (1.55)$$

where A and B are positive operators (i.e. A and B have strictly positive eigenvalues). This expression also relies on a difference of terms to cancel out divergent terms at $\mathcal{T} = 0$. The earlier renormalization by subtracting off the vacuum energy when the bodies are far apart provides exactly this subtraction.

By applying Eqs. (1.54) and (1.55) to the free energy (1.53), the renormalized free energy can be rewritten as

$$\mathcal{F} - \mathcal{F}_0 = -\frac{k_{\text{B}}T}{2} \int_0^{\infty} \frac{d\mathcal{T}}{\mathcal{T}} \text{tr} \left(e^{[(\partial_{\tau}^2 + \nabla^2)/2 - V(\mathbf{x})]\mathcal{T}} - e^{(\partial_{\tau}^2 + \nabla^2)\mathcal{T}/2} \right). \quad (1.56)$$

The trace can be evaluated by introducing a D -dimensional auxiliary Hilbert space, where $\langle \mathbf{x}, x_\tau | \hat{p}_i | \psi \rangle = -i \partial_i \langle \mathbf{x}, x_\tau | \psi \rangle$, $[\hat{x}_i, \hat{p}_j] = i \delta_{ij}$. Note that $\hbar = 1$ in this auxiliary Hilbert space. The free energy is then

$$\mathcal{F} - \mathcal{F}_0 = -\frac{k_B T}{2} \int_0^\infty \frac{d\mathcal{T}}{\mathcal{T}} \int d\mathbf{x}_0 d\tau_0 \langle \mathbf{x}_0, \tau_0 | e^{-(\hat{p}_\tau^2 + \hat{\mathbf{p}}^2)\mathcal{T}/2 - V(\hat{\mathbf{x}})\mathcal{T}} - e^{-(\hat{p}_\tau^2 + \hat{\mathbf{p}}^2)\mathcal{T}/2} | \mathbf{x}_0, \tau_0 \rangle. \quad (1.57)$$

The free energy is now in the form of the imaginary-time transition amplitude for a quantum particle in D space-time dimensions, in a potential V . In the same fashion as in Section 1.4, this can be converted into a single-particle path integral, although there are some minor differences. First, the starting and ending points are the same, so the paths form closed loops. Second, the parameter \mathcal{T} has dimension of L^2 . It governs the spatial extent of the path, rather than the proper time between events. The resulting worldline path integral for the free energy at zero temperature is

$$\begin{aligned} \mathcal{F} - \mathcal{F}_0 = & -\frac{k_B T}{2} \int_0^\infty \frac{d\mathcal{T}}{\mathcal{T}} \int d\mathbf{x}_0 d\tau_0 \int \prod_{k=1}^N d\mathbf{x}_k d\tau_k \\ & \times \prod_{k=0}^{N-1} \left(\frac{1}{(2\pi\Delta\mathcal{T})^{D/2}} e^{-(\mathbf{x}_{k+1} - \mathbf{x}_k)^2 / (2\Delta\mathcal{T})} e^{-(\tau_{k+1} - \tau_k)^2 / (2\Delta\mathcal{T})} \right) \\ & \times \left(\prod_{j=1}^N e^{-\Delta\mathcal{T}V(\mathbf{x}_j)} - 1 \right) \delta(\mathbf{x}_N - \mathbf{x}_0) \delta(\tau_N - \tau_0). \end{aligned} \quad (1.58)$$

The intermediate Gaussian integrals over τ_k can be carried out, since the potential is independent of τ . The final integral over τ is $\int d\tau_0 = \beta\hbar c$, since $\tau_0 \in [0, \beta\hbar c]$. There is also a normalization constant of $(2\pi\mathcal{T})^{-1/2}$ for each dimension due to the loop closure condition. This can be thought of as the total normalization for N Gaussian steps of length $\Delta\mathcal{T} = \mathcal{T}/N$, subject to the loop-closure requirement $\mathbf{x}_0 = \mathbf{x}_N$. The free energy can be written in a more intuitive form, better suited to numerical calculations, if

we consider the coupled Gaussians as the probability distribution for paths through space-time. Each path increment $\Delta \mathbf{x}_k = \mathbf{x}_{k+1} - \mathbf{x}_k$ is Gaussian with zero mean and variance $\Delta \mathcal{T}$. In addition, the resulting paths must close on themselves.

The resulting paths are a specific form of Brownian motion. A Brownian motion (or Wiener process) is a continuous random process $W(t)$, that starts at the origin $W(t=0) = 0$, and has increments $\Delta W(t) := W(t + \Delta t) - W(t)$, that are Gaussian random variables with $\langle\langle \Delta W(t) \rangle\rangle = 0$, $\langle\langle \Delta W(t) \Delta W(t') \rangle\rangle = 0$ for $t \neq t'$ and $\langle\langle [\Delta W(t)]^2 \rangle\rangle = \Delta t$ (Gardiner, 2009). (Note that we are using $\langle\langle \dots \rangle\rangle$ to denote the ensemble average.) A Brownian bridge is a Brownian motion with fixed end points at times $t = 0$ and $t = T$, where $B(t=0) = 0$, and $B(t=T) = c$, and its increments obey the same statistics as the Wiener process (Karatzas and Shreve, 1991). Throughout this thesis, we will most often use the discrete form of these processes where $W_j = W(t_j) = W(j\Delta t)$. Brownian motion can be straightforwardly generalized to multiple-dimensions.

The result of these manipulations is

$$\mathcal{F} - \mathcal{F}_0 = -\frac{\hbar c}{2} \int \frac{d\mathcal{T}}{(2\pi\mathcal{T})^{D/2}\mathcal{T}} \int d\mathbf{x}_0 \langle\langle e^{-\mathcal{T}\langle V \rangle} - 1 \rangle\rangle_{\mathbf{x}(t)}, \quad (1.59)$$

where $\langle\langle \dots \rangle\rangle_{\mathbf{x}(t)}$ denotes an ensemble average over closed Brownian bridges $\mathbf{x}(t)$ starting at \mathbf{x}_0 and returning to $\mathbf{x}_N = \mathbf{x}_0$, and

$$\langle V \rangle := \frac{1}{\mathcal{T}} \int_0^{\mathcal{T}} dt V[\mathbf{x}(t)] = \frac{1}{N} \sum_{k=0}^{N-1} V(\mathbf{x}_k) \quad (1.60)$$

is the path-averaged value of the potential. The worldline method relies on generating an ensemble of closed Brownian bridges, and evaluating the path-averaged potential for each path. The total Casimir energy (1.59) then requires further integrals over

the starting point \mathbf{x}_0 of the paths, and the total path time \mathcal{T} . The path time \mathcal{T} governs the spatial extent of the paths, where the typical extent of a path is given by $x \sim \sqrt{\mathcal{T}}$. The renormalization against vacuum ensures that only paths that touch one of the bodies contribute. In order to extract interaction energies between two bodies (such as the two-body Casimir energy), the single body energies for each body must also be subtracted from the total energy. As a result, only paths that touch both bodies contribute. This is depicted in Figure 1.5, where the upper path would contribute to the Casimir energy, while the lower path would not. At small times \mathcal{T} , both paths would shrink down around their starting points, and since the paths would not touch both bodies, neither would contribute. This is a direct result of the energy renormalization—subtracting off the vacuum energy cuts off the divergent \mathcal{T} integral as small \mathcal{T} . At later times \mathcal{T} , these paths would have larger extent, and both would contribute, but due to the $\mathcal{T}^{-(1+D/2)}$ dependence, the lower path would have a smaller contribution.

1.5.2. Worldline Distance Dependence

The distance dependence can also be read off from Eq. (1.59). A typical path will touch a surface a distance d away, at a path time $\mathcal{T} \sim d^2$. Since the integrand (1.59) is either zero or one, depending on whether any points on the path intersect the bodies, the energy density at a point d from the surface is approximately $\int_{d^2}^{\infty} d\mathcal{T} \mathcal{T}^{1+D/2} \sim d^{-D}$. After integration over the starting point \mathbf{x}_0 , the Casimir energy scales as d^{-3} in four dimensions.

The worldline method has also been extended to nonzero temperatures (Klingmüller and Gies, 2008). The generalization is straightforward—in essence the fields must be periodic on $\tau \in [0, \beta\hbar c]$, since $\phi(0) = \phi(\beta\hbar c)$ due to the nature of the

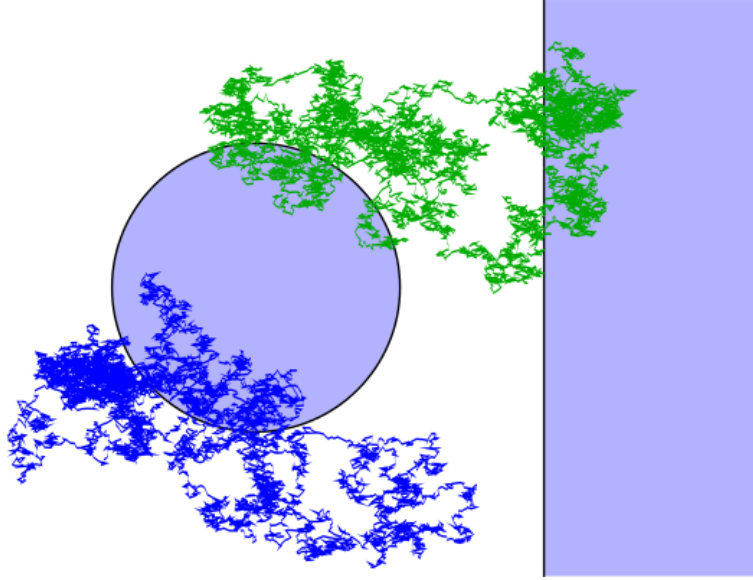


FIGURE 1.5. Schematic of worldline paths interacting with a plane and a sphere. Only paths which touch *both* bodies will contribute at a given path time \mathcal{T} . The upper path touches both objects and will contribute to Casimir energy, while the lower path only touches one body, and does not contribute to Casimir energy.

trace in Eq. (1.47). This motivates expanding the fields in a Fourier series, with the Matsubara frequencies $s_n = (2\pi n)/(\beta\hbar)$, where each Fourier component contributes independently of the others. The same sort of manipulations used to derive the zero temperature worldline (1.59), can be extended to nonzero temperature with the result

$$\mathcal{F} - \mathcal{F}_0 = -k_B T \sum_{n=0}' \int_0^\infty \frac{d\mathcal{T}}{(2\pi\mathcal{T})^{(D-1)/2}\mathcal{T}} \int d\mathbf{x}_0 e^{-s_n^2 \mathcal{T}/(2c^2)} \langle\langle e^{-\mathcal{T}\langle V \rangle} - 1 \rangle\rangle, \quad (1.61)$$

where the prime on the sum means that the $n = 0$ term is multiplied by a $1/2$. Since the \mathcal{T} dependence differs, there is also a different distance dependence. Since the effective dimension has been reduced by one, the energy density now scales as $d^{-(D-1)}$, which means the renormalized energy density scales as d^{-3} , and the total energy scales as d^{-2} in four dimensions.

1.5.3. Numerical Method

In order to numerically evaluate the worldline Casimir energy, it is necessary to generate an ensemble of closed, Brownian paths. Given the probability for a free Brownian motion $W(t)$ to close on itself after N steps is negligible, it is essential to force the closure constraint when constructing the paths.

The simplest method generates a free Brownian motion, and then forces the path to close by subtracting off a pro-rated fraction of the final position from each increment. So if W_k is a random walk,

$$W_k = \sum_{j=1}^k \Delta W_j, \quad (1.62)$$

where $\langle\langle \Delta W_k \rangle\rangle = 0$ and $\langle\langle \Delta W_k \Delta W_j \rangle\rangle = \delta_{jk} \Delta \mathcal{T}$, then a closed Brownian bridge can be constructed as

$$B_k = \sum_{j=1}^k \Delta W_j - \frac{k}{N} W_N. \quad (1.63)$$

This algorithm has the virtue of simplicity, but it does require that knowledge the whole Brownian path in order to construct the closed version. Gies *et al.* (2003) developed an improved algorithm, the so-called “v-loop” algorithm for generating Brownian paths. A Brownian bridge can be constructed as

$$B_k = c_k B_{k-1} + \sqrt{c_k} \Delta W_k, \quad k = 1, \dots, N-1, \quad (1.64)$$

where $B_0 = 0$ and

$$c_k = \frac{N-k}{N-k+1}, \quad k = 1, \dots, N-1. \quad (1.65)$$

Since we will use the v-loop algorithm in our own simulations, we will discuss this algorithm further in Chapter V.

Having constructed a path, it is then necessary to compute the worldline integrand $e^{-\mathcal{T}(V)} - 1$ along that path. If any point along the path intersects one of the surfaces, then in the strong coupling limit the potential $V = \lambda\delta[\sigma(\mathbf{x})]$ is nonzero, and in the $\lambda \rightarrow \infty$ limit, the worldline integrand goes to negative one. If however, no points on the path intersect a surface, then the potential is zero, and the renormalized worldline integrand is also zero.

Once a particular random path has been constructed, it is necessary to integrate the contributions from each starting point \mathbf{x}_0 , and path time \mathcal{T} . Thus the worldline algorithm relies on finding the times \mathcal{T} when at least one path point intersects the bodies, and integrating over those times. This must further be integrated over every possible path starting point. For simple geometries, these touching times can be found analytically for a particular random path, which simplifies the method further (Weber and Gies, 2009, 2010b).

1.5.4. Advantages and Shortcomings of the Scalar Method

The worldline method has a number of attractive features. First, it offers an intuitive picture of Casimir energies emerging from the spatial paths of virtual particles. In this picture, the random paths explore all of space and accumulate a contribution to the Casimir energy based on the potential V they encounter.

Second, it offers a geometry independent method of handling Casimir forces. The paths are created without reference to the underlying body geometry or a spatial discretization, so the method can be easily applied to arbitrarily complicated

arrangements of bodies. The only requirement is that the paths are fine enough to resolve the structure of the surfaces.

Third, since each path is independent, the algorithm is trivially parallelizable: each path can be handled by a separate computing process, without any requirement that the processes communicate with one another, except when accumulating results. This has the advantage of exploiting the growth of computing clusters with many nodes, where that power can be harnessed with minimal effort: once the algorithm works on a single computer, it can be easily extended to arbitrarily many computers to increase the size of the ensemble sampled from, or to reduce the time required to reach a given accuracy.

However, the worldline method has some prominent shortcomings. First of all, it only applies to scalar fields. The most important Casimir effects are due to EM radiation field, which is a transverse vector field. Second, it has only been applied for idealized potentials that effectively impose Dirichlet boundary conditions on the surfaces. As a result it is missing any coupling of the fields to media with realistic properties. Finally, the development has been focused on Casimir energies, with no simple way to extract Casimir–Polder energies for atoms near surfaces (although it may be possible to extract these from the stress-energy tensor). Thus far, there has only been speculation on how to extend the worldline method to electromagnetism, without any concrete results (Aehlig *et al.*, 2011).

1.5.5. Motivation and Goal for Thesis Project

The goal of this thesis is to extend the scalar worldline method to vector electromagnetism. Ideally we would retain the attractive features of the method, such as geometry independence of the paths, and only needing Brownian sample

paths. In addition, we aim to improve the method to account for the two physical polarization states of the EM field, and properly account for the material properties of the medium. Finally, the method must agree with known results in simple geometries.

As later chapters in this thesis will show, we have partially met those goals. We have developed analytical and numerical techniques that can be applied to improving existing worldline algorithms. This thesis focuses primarily on solving the planar problem—although this is well-studied, it is a good platform for exploring and testing worldline methods. The methods we develop here could be used as uncontrolled approximations in general geometries, but with no guarantee of correctness.

1.6. Thesis outline

This section provides an overview of the thesis, and will also present some key results, by referencing where the result appears later in the thesis. The rest of this thesis is laid out as follows: Chapter II formally quantizes the EM field in media characterized by their relative permeability ϵ_r and permittivity μ_r . There are two approaches to developing the worldline expressions for the electromagnetic Casimir energy. The first emphasizes a full vector path integral for the EM field partition function (2.46), which can then be converted into a worldline path integral expression (2.50). Unfortunately, it is not clear how to extract the two physical degrees of freedom from that complicated expression, which involves the cancellation of a number of degrees of freedom. Alternatively, the EM field can be split into two noninteracting scalar polarizations: the transverse-electric (TE) and transverse-magnetic (TM) polarizations. The worldline path integral for the free energy in the

TE polarization at zero temperature in dispersion-free media is [Eq. (2.71)]

$$\mathcal{F}_{\text{TE}} - \mathcal{F}^{(0)} = -\frac{\hbar c}{2} \int_0^\infty \frac{d\mathcal{T}}{(2\pi\mathcal{T})^{D/2}\mathcal{T}} \int d\mathbf{x}_0 \left\langle\left\langle \frac{e^{-\langle V_{\text{TE}}(z) \rangle \mathcal{T}}}{\sqrt{\langle \epsilon_r(z) \mu_r(z) \rangle}} - 1 \right\rangle\right\rangle_{\mathbf{x}(t)}, \quad (1.66)$$

where

$$V_{\text{TE}}(z) := \frac{1}{2} [(\partial_z \log \sqrt{\mu_r})^2 - \partial_z^2 \log \sqrt{\mu_r}]. \quad (1.67)$$

The equivalent TM polarization is recovered by exchanging ϵ_r and μ_r .

Chapter III discusses the analytical methods for solving single-particle path integrals. The central expression underlying this analytical approach is the Feynman-Kac formula, which states the path integral is the solution to a diffusion equation. Section 3.1 considers a diffusion equation (3.1),

$$\partial_t f = \frac{1}{2} \nabla^2 f - [V(\mathbf{x}) + \lambda] f + \delta(\mathbf{x} - \mathbf{c}), \quad (1.68)$$

for a probability distribution $f(\mathbf{x}, t)$, interacting with a space-dependent potential $V(\mathbf{x})$, and a source term $\delta(\mathbf{x} - \mathbf{c})$. In the steady-state ($t \rightarrow \infty$) limit, the solution to Eq. (3.1) can be simplified to the following path integral [Eq. (3.14)],

$$f(\mathbf{x}) = \int_0^\infty ds \left\langle\left\langle \delta[\mathbf{x} + \mathbf{W}(s) - \mathbf{c}] \exp\left(-\lambda s - \int_0^s du V[\mathbf{x} + \mathbf{W}(s-u)]\right) \right\rangle\right\rangle, \quad (1.69)$$

In simple cases, the steady-state diffusion equation (3.1) can be solved directly to find an analytical expression for the path integral. Most importantly, Section 3.4.1 shows that the TM potential [Eq. (3.32)]

$$V_{\text{TM}}(z) := \frac{1}{2} [(\partial_z \log \sqrt{\epsilon_r})^2 - \partial_z^2 \log \sqrt{\epsilon_r}], \quad (1.70)$$

can be regularized leading to an effective boundary condition in the diffusion equation. For a dielectric step characterized by $\epsilon_r = 1 + \chi\Theta(x - d)$, the corresponding effective boundary condition from V_{TM} is given by [Eq. (3.45)],

$$f(d + 0_+) = e^{-\Xi} f(d - 0_+) \quad \partial_x f(d + 0_+) = e^{\Xi} \partial_x f(d - 0_+), \quad (1.71)$$

where $e^{\Xi} = \sqrt{1 + \chi}$. Using that boundary condition, Section 3.4 shows that the path-averaged analytical solution for paths from $x = 0$ to $x = c$ in time t , interacting with potential V_{TM} is [Eq. 3.52]

$$\left\langle\left\langle e^{-\int_0^t dt' V_{\text{TM}}(x-d)} \right\rangle\right\rangle = \begin{cases} 1 + \text{sgn}(d) \tanh \Xi e^{-2d(d-c)/t} & d(d-c) > 0 \\ \text{sech } \Xi & d(d-c) < 0. \end{cases} \quad (1.72)$$

The analytical ensemble average over all paths interacting with V_{TM} has even further smoothed out the singular potential. This result is crucial to regularizing the TM potential and allowing the numerical calculations with the TM polarization to proceed. The path integral solutions for the step potentials $V = \chi\Theta(x - d)$ are given in Eqs. (3.25) and (3.31), and are particularly relevant for TE calculations. The analogous results that include TM boundary conditions in addition to the step potential are given in Eqs. (3.56) and (3.60), and are required for analytical TM calculations.

Chapter IV uses the results from the previous chapter to derive analytical results showing agreement between the worldline method and other calculations. In Section 4.1, the worldline Casimir–Polder energy is derived by treating the atom as a small perturbation to the material functions, where the atom is located at \mathbf{r}_A , with static polarizability α_0 . These expressions can be simplified by assuming that the

media are non-magnetic ($\mu_r = 1$), and the atom's magnetic response can also be neglected. In that case, the worldline expressions for the Casimir–Polder energy are given by [Eqs. (4.14)–(4.15)]:

$$V_{\text{CP}}^{(\text{TE})}(\mathbf{r}_A) = \frac{\hbar c \alpha_0}{4\epsilon_0 (2\pi)^{D/2}} \int_0^\infty \frac{d\mathcal{T}}{\mathcal{T}^{1+D/2}} \left\langle\left\langle \frac{1}{\langle \epsilon_r \rangle^{3/2}} - \frac{1}{[\epsilon_r(\mathbf{r}_A)]^{3/2}} \right\rangle\right\rangle_{\mathbf{x}(t), \mathbf{x}(0)=\mathbf{r}_A} \quad (1.73)$$

$$V_{\text{CP}}^{(\text{TM})}(\mathbf{r}_A) = \frac{\hbar c \alpha_0}{4\epsilon_0 (2\pi)^{D/2}} \int_0^\infty \frac{d\mathcal{T}}{\mathcal{T}^{1+D/2}} \left\langle\left\langle \frac{e^{-(V_{\text{TM}})\mathcal{T}}}{\langle \epsilon_r \rangle^{3/2}} - \frac{1}{[\epsilon_r(\mathbf{r}_A)]^{3/2}} - \frac{\mathcal{T}}{2\epsilon_r(\mathbf{r}_A)} \nabla^2 \frac{e^{-(V_{\text{TM}})\mathcal{T}}}{\langle \epsilon_r \rangle^{1/2}} \right\rangle\right\rangle_{\mathbf{x}(t), \mathbf{x}(0)=\mathbf{r}_A} . \quad (1.74)$$

Note that these Casimir–Polder worldline path integrals only involve paths emanating from the atom's position \mathbf{r}_A . The analytical results from Chapter III can be used in the worldline path integrals after transforming the solutions by using the Laplace–Mellin theorem (4.18) and the inverse moment theorem (4.22). The worldline method then recovers prior results such as the Casimir–Polder energy (1.17), and the Lifshitz expression for the energy (1.25). The chapter ends by discussing the transition between high and low temperature, and the near-field and far-field limits within the worldline context.

Chapter V presents the numerical methods for evaluating worldline path integrals. This involves using Monte Carlo sampling methods for generating paths. The Monte Carlo sampling also extends to the starting positions of the paths \mathbf{x}_0 , and the size of the path, which is governed by path time \mathcal{T} . These methods are discussed for the TE polarization in Section 5.1. Section 5.1.3 presents the numerical results for the TE polarization, and examines the convergence of the TE results as the path resolution is increased. Numerical calculations involving the TM polarization are more challenging than their TE counterparts, even after regularization and analytical averaging. As discussed in Section 5.2.1, the numerically estimated TM path integral

shows rapidly growing statistical errors as the number of steps N increases. The “birth-death path swarm” is introduced in Section 5.2.1.2, and is essential for reducing the statistical errors associated with accumulating the product of the path-averaged potential along the path. The derivatives required for the TM Casimir–Polder energy are estimated using a “partial-averaging method” discussed in Section 5.2.3.3. The numerical results for the TM polarization are presented in Section 5.2.4, where they show some agreement with the analytical results.

Chapter VI develops general expressions for the force, torque, and derivative of the force for the TE worldline path integral. These expressions emphasize that the Casimir force emerges from paths that start on the surfaces of the bodies. For example, the “pinning” expression for the Casimir force on the second body is [Eq. (6.8)]

$$\mathbf{F}_2 = -\frac{a\chi_2\hbar c}{2(2\pi)^{D/2}} \int_0^\infty \frac{d\mathcal{T}}{\mathcal{T}^{1+D/2}} \oint_{\sigma_2(\mathbf{x}_0-\mathbf{R}_2)=0} dS \hat{n}_2(\mathbf{x}_0) \left\langle\left\langle \frac{1}{\langle\epsilon_{r,12}\rangle^{a+1}} - \frac{1}{\langle\epsilon_{r,2}\rangle^{a+1}} \right\rangle\right\rangle_{\mathbf{x}(t)}. \quad (1.75)$$

Here $\sigma_2 = 0$ defines the surface of the second body, \hat{n}_2 is the surface normal of the body, while $\epsilon_{r,12}$ and $\epsilon_{r,2}$ are the dielectric functions involving both bodies, and only the second body, respectively. Unfortunately, the pinning method fails to recover the correct answer for strong-coupling cases where $\chi/N \gg 1$, which prompts the development of the “occupation” method in Section 6.2. Some care is still required when using the occupation method numerically, since in the strong-coupling limit, only rare paths that just touch the surfaces will contribute. A hybrid approach designed to capture the weak coupling and strong-coupling cases is discussed further in Sections 6.3.1 and 6.3.2.

Finally, the findings and directions for future work are summarized in the conclusion. In particular, the planar methods could be generalized to general geometries by suitably coupling the two scalar polarizations together.

CHAPTER II
ELECTROMAGNETIC FIELD QUANTIZATION AND ELECTROMAGNETIC
WORLDLINES

This chapter develops the worldline path integrals for electromagnetism with a space-dependent dielectric function, paralleling the treatment of the Dirichlet scalar worldline method in Section 1.5. First, Section 2.1 reviews the prior work on quantizing the EM field inside media. Following that, Section 2.2 reviews classical EM field theory, and Section 2.3 formally quantizes the EM field. The partition function for the EM field follows from a gauge-fixed path integral in terms of the scalar and vector potentials in Sections 2.4 and 2.5. However, the resulting worldline path integrals (2.50) are unsatisfactory, since it is not clear how the contributions from the two physical degrees of freedom emerge from these complicated expressions, nor how to efficiently numerically evaluate the resulting expressions. In response, Section 2.6 develops scalar models that better capture the features of electromagnetism. In planar geometries the scalar models correspond to the amplitudes of the TE and TM polarizations. Sections 2.6.1 and 2.6.2 develop the worldline path integrals for those scalar fields [the TE worldline path integral is presented in Eq. (2.71), and the equivalent TM path integral follows from EM duality (2.4)]. Those path integrals will form the basis for the analytical and numerical work in Chapters IV and V. Finally, the extension to dispersive materials and nonzero temperature is considered in Section 2.7.

[The decomposition of the EM field into two scalars, and the derivation of the associated worldline path integrals was carried out in Mackrory *et al.* (2016).]

2.1. Approaches to Quantizing Electromagnetism in Media

The quantization of the EM field inside dielectric media provides a number of challenges beyond quantization in vacuum (Bechler, 1999; Bordag *et al.*, 1998; Dung *et al.*, 1998; Huttner and Barnett, 1992; Rahi *et al.*, 2009; Reid *et al.*, 2013). First, in Casimir problems the dielectric varies spatially. The usual procedure for quantizing the EM field decomposes the field into a set of normal modes, and quantizes their amplitudes. While it is possible to write down the wave equations for the modes, and quantize the amplitudes in analogy with free space (Glauber and Lewenstein, 1991), a full development of this method still requires finding those mode functions. For our purposes, an ideal procedure for quantizing the field would not require solving for the mode functions in general geometries, nor would it be adapted to any particular geometry.

Second, the dielectric complicates the choice of gauge-fixing. In brief, EM has a gauge symmetry, or redundant degrees of freedom, which must be excluded from the quantization procedure. The gauge symmetry can be removed by imposing a gauge condition on the fields. In free space this is typically done by fixing Coulomb or Lorenz gauge, which decouple the radiative and static electromagnetic problems, or maintain relativistic invariance, respectively. However for macroscopic EM inside a dielectric, the usual gauge-fixings lose these nice features, and must be replaced by a dielectric-dependent condition. This issue will be discussed further in Section 2.4.1.

Third, since the dielectric has some frequency response or dispersion, the Kramers-Krönig relations require that there is also loss or dissipation. In quantum optics, dissipation is usually handled by coupling the system to a bath, and

then integrating or tracing out the bath degrees of freedom.¹ The light field is linearly coupled to the dielectric medium, which is modeled as a bath of harmonic oscillators (Bechler, 1999; Dung *et al.*, 1998; Huttner and Barnett, 1992). The dielectric medium is in turn coupled to a bath of harmonic oscillators, which provides the damping. Integrating out the bath degrees of freedom yields the required dispersion and dissipation for the medium, while integrating out the medium's degrees of freedom yields a frequency dependent dielectric constant $\epsilon(\omega)$. Huttner and Barnett (1992) were the first to use this harmonic model to quantize the EM field in media. Their work directly diagonalized the whole system of fields and bath in terms of the modes of a single combined harmonic oscillator. Another approach to the same problem directly couples the medium to white noise sources to represent the fluctuations inside the medium that lead to dissipation (Dung *et al.*, 1998; Scheel *et al.*, 1998; Tip *et al.*, 2001). Bechler (1999, 2006) carried out path integral quantization for a harmonic medium including dispersion, and shown agreement with previous results in terms of noise operators and commutators for the fields. It is not strictly necessary to assume that the fields are directly coupled to harmonic oscillators. The dielectric function can be understood in terms of the linear response of the underlying medium (which might not be harmonic) to the EM field (Altland and Simons, 2011). This was used by Rahi *et al.* (2009) to motivate the effective Lagrangian description in terms of macroscopic field in their work on the scattering method. More recently Philbin (2010) carried out a full canonical quantization of EM in media, without explicitly assuming a harmonic medium.

¹If damping is added to the system in an ad hoc manner, the canonical commutation relations between operators would decay away. Adding the bath is necessary to preserve the commutation relations for the system operators. As a result, dissipation in quantum systems is attended by noise, either as decoherence terms in the master equation or as noise terms in the Langevin equations for the operators (Gardiner and Zoller, 2004)

Focusing on Casimir physics, in modern treatments the EM field has been quantized via path integration. Reid *et al.* (2013) quantize the EM field, under the assumption of piecewise constant dielectric media, where the EM boundary conditions are explicitly enforced at the interfaces. Enforcing those boundary conditions allows the remaining computations to proceed as if the media were homogeneous and filled all of space, based on a version of Green’s theorem (Emig and Büscher, 2004). Fixing the boundary conditions also simplifies the algebra, since derivatives and material functions effectively commute with one another. Any commutator terms would arise on the surface, but since the fields are restricted on the surface via functional delta functions, those corrections can be ignored. The resulting derivations proceed in analogy with the case of a homogeneous dielectric, but with the fields in different regions coupled by the currents on the surfaces.

Bordag *et al.* (1998) also carried out path integral quantization of the EM field inside a spatially varying dielectric neglecting dispersion, starting from the effective Lagrangian description for the macroscopic fields. They fix a generalized Lorenz gauge, and set about deriving the heat kernel, which is effectively a small- \mathcal{T} expansion of the worldline path integral. The primary focus here was to explore the divergence structure of the theory (i.e, how does QED in media behave at high frequencies and small wavelengths?). Unfortunately, their results are hard to interpret given that the non-physical degrees of freedom do not cleanly cancel. In particular, the contributions from the unphysical scalar and longitudinal photons do not cancel the gauge-fixing or “ghost” determinant, as happens in vacuum. In later work Bordag *et al.* (1999) considered the quantization for EM in a spherical dielectric ball and found better results by exploiting the dual potentials. In this latter paper they split the EM field into two scalar fields, corresponding to the TE and TM polarizations. Milton *et al.*

(1978); Schwinger (1992); Schwinger *et al.* (1978) also split the EM field into two non-interacting scalars in their works on the Casimir effect in planar and spherical geometries.

Our work on the EM path integral will parallel Bordag *et al.*, with some difference in aims. The primary goal of Bordag *et al.* was to examine the divergence structure of QED in media via purely analytical calculations. Our goal is to develop a numerical method for Casimir energies. Since we will explicitly renormalize the Casimir energy against vacuum, we will have more freedom in rescaling the fields than they did. Further, we will be interested in evaluating the worldline path integrals at all path times \mathcal{T} , rather than just making small- \mathcal{T} expansions.

2.2. Classical Electromagnetic Field Theory

Maxwell's equations govern the classical evolution for the electric and magnetic fields $\mathbf{E}(\mathbf{r}, t)$ and $\mathbf{B}(\mathbf{r}, t)$. In a medium, with permeability $\epsilon(\mathbf{r})$ and permittivity $\mu(\mathbf{r})$, but no external source charges or currents, Maxwell's equations are

$$\nabla \cdot \mathbf{B} = 0 \quad \nabla \times \mathbf{E} = -\partial_t \mathbf{B} \quad (2.1)$$

$$\nabla \cdot \mathbf{D} = 0 \quad \nabla \times \mathbf{H} = \partial_t \mathbf{D}, \quad (2.2)$$

where the electric displacement is $\mathbf{D}(\mathbf{r}, t) := \epsilon(\mathbf{r})\mathbf{E}(\mathbf{r}, t)$, and the magnetic field strength is $\mathbf{H}(\mathbf{r}, t) := \mu(\mathbf{r})\mathbf{B}(\mathbf{r}, t)$. In this initial development, we will ignore any frequency dependence in ϵ and μ . Later, we will extend this work to handle frequency dependence in the medium. The relative permeability and permittivity are defined by $\epsilon_r(\mathbf{r}) := \epsilon(\mathbf{r})/\epsilon_0$, and $\mu_r(\mathbf{r}) := \mu(\mathbf{r})/\mu_0$, where ϵ_0 and μ_0 are the permeability and

permittivity of free space. In Casimir physics we will be interested in the energy of the field alone, without any external free charges or currents.

The \mathbf{E} and \mathbf{B} fields can be rewritten in terms of the scalar $\phi(\mathbf{r}, t)$ and vector potential $\mathbf{A}(\mathbf{r}, t)$ as

$$\mathbf{B} = \nabla \times \mathbf{A} \quad \mathbf{E} = -\nabla\phi - \partial_t\mathbf{A}. \quad (2.3)$$

These are constructed to automatically satisfy two of Maxwell's equations. In the absence of sources, Maxwell's equations are invariant under the duality transformation

$$\mathbf{E} \leftrightarrow \mathbf{H} \quad \mathbf{B} \leftrightarrow -\mathbf{D} \quad \mu \leftrightarrow \epsilon. \quad (2.4)$$

This suggests that instead \mathbf{D} and \mathbf{H} can be written in terms of another set of potentials. In these dual potentials the fields are given by

$$\mathbf{D} = \nabla \times \mathbf{C} \quad \mathbf{H} = -\nabla\Lambda - \partial_t\mathbf{C}. \quad (2.5)$$

The gauge potentials and the dual potentials are connected via a duality transformation on the field tensor $F_{\mu\nu}$. Note that the electric and magnetic fields are unchanged under the following gauge transformation

$$\mathbf{A}' = \mathbf{A} + \nabla g \quad \phi' = \phi - \partial_t g, \quad (2.6)$$

where g is an arbitrary function. Physical results do not depend on the gauge chosen to carry out calculations. However in order to quantize the theory it is necessary to fix this degree of freedom.

The procedure for canonical quantization starts from the classical Lagrangian, and finds the associated Hamiltonian. The theory is quantized by promoting the classical Poisson brackets to quantum commutation relations. However, this procedure must be modified for gauge theory, since there are redundant degrees of freedom. In the Hamiltonian theory, the gauge degrees of freedom are non-dynamical, so they imply constraints. There are a number of ways to confront this. The Gupta-Bleuler formulation restricts the allowed states to obey a gauge condition (Mandl and Shaw, 2010, Section 5.2). Dirac (1950, 1964, 1966) developed another method that instead adjusts the classical bracket to account for the constraints. Some care is required to ensure that the constraints are only enforced after deriving all relations between variables. In the quantum theory, it is the Dirac bracket that is promoted to the equal-time commutation relation. Finally in a path integral, it is necessary to remove the gauge degree of freedom via Faddeev–Popov gauge fixing (Faddeev and Slavnov, 1991).

The classical Lagrangian for EM in non-dispersive media is

$$L_{\text{EM}} = \frac{1}{2} \int d\mathbf{r} (\mathbf{E} \cdot \mathbf{D} - \mathbf{B} \cdot \mathbf{H}) = \frac{\epsilon_0}{2} \int d\mathbf{r} \left(\epsilon_r(\mathbf{r})(\nabla\phi + \partial_t\mathbf{A})^2 - \frac{c^2}{\mu_r(\mathbf{r})}(\nabla \times \mathbf{A})^2 \right). \quad (2.7)$$

The first two Maxwell equations (2.1) are automatically satisfied by the definition of the gauge fields, and the remaining Maxwell equations (2.2) can be derived from this Lagrangian. The momentum fields conjugate to the potential fields $A^\mu = (\phi, \mathbf{A})$ are

$$\Pi_0 = \frac{\delta L_{\text{EM}}}{\delta(\partial_t\phi)} = 0 \quad (2.8)$$

$$\mathbf{\Pi} = \frac{\delta L_{\text{EM}}}{\delta(\partial_t\mathbf{A})} = \epsilon_0\epsilon_r(\mathbf{r})(\nabla\phi + \partial_t\mathbf{A}), \quad (2.9)$$

where $\delta L_{\text{EM}}/\delta f$ is the functional derivative of the Lagrangian with respect to the function f . The functional derivative for a functional $F[f(x)]$ is defined as

$$\frac{\delta F}{\delta f(x')} := \lim_{a \rightarrow 0} \frac{F[f(x) + a\delta(x - x')] - F[f(x)]}{a}. \quad (2.10)$$

From Eq. (2.9), the momentum field $\mathbf{\Pi}$ conjugate to \mathbf{A} is proportional the electric displacement, \mathbf{D} . Since $\Pi_0 = 0$ for all times, there is a constraint on the system. Since the constraint equation must also be preserved at all times, there will be a further constraints imposed on the theory. That next constraint will turn out to be Gauss's law, which enforces conservation of electric charge.

The Hamiltonian for the potentials and their conjugate momenta is given by

$$H_{\text{EM}} = \int d\mathbf{r} (\Pi_0 \partial_t \phi + \mathbf{\Pi} \cdot \partial_t \mathbf{A}) - L_{\text{EM}} \quad (2.11)$$

$$= \int d\mathbf{r} \left(\frac{\mathbf{\Pi}^2}{2\epsilon_0 \epsilon_r(\mathbf{r})} + \frac{\epsilon_0 c^2}{2} (\nabla \times \mathbf{A})^2 - \mathbf{\Pi} \cdot \nabla \phi \right). \quad (2.12)$$

The Poisson bracket in 4-vector notation follows from the choice that $A^\mu = (\phi, \mathbf{A})$.

This implies that the momentum conjugate to A^μ is given by

$$\Pi_\mu = \frac{\delta L_{\text{EM}}}{\delta \partial_t A^\mu}. \quad (2.13)$$

[Note that we are working in a flat spacetime where the metric is $\eta_{\mu\nu} = \text{diag}(-1, 1, 1, 1)$.] The Poisson bracket for fields is

$$\{F_\mu(\mathbf{r}), G_\nu(\mathbf{r}')\}_{\text{PB}} = \sum_\sigma \int d\mathbf{y} \left(\frac{\delta F_\mu(\mathbf{r})}{\delta A^\sigma(\mathbf{y})} \frac{\delta G_\nu(\mathbf{r}')}{\delta \Pi_\sigma(\mathbf{y})} - \frac{\delta G_\nu(\mathbf{r}')}{\delta A^\sigma(\mathbf{y})} \frac{\delta F_\mu(\mathbf{r})}{\delta \Pi_\sigma(\mathbf{y})} \right), \quad (2.14)$$

and the Poisson bracket between the fields and momenta is

$$\{A_\mu(\mathbf{r}), \Pi_\nu(\mathbf{r}')\}_{\text{PB}} = \eta_{\mu\nu}\delta(\mathbf{r} - \mathbf{r}'). \quad (2.15)$$

The equations of motion can be derived from the Hamiltonian, since the time evolution for a quantity is given by its Poisson bracket with the Hamiltonian. In particular, the requirement that the first constraint (2.8) holds for all time implies

$$\partial_t \Pi_0 = \{\Pi_0, H_{\text{EM}}\}_{\text{PB}} = -\frac{\delta H_{\text{EM}}}{\delta \phi} = \nabla \cdot \mathbf{\Pi} = 0. \quad (2.16)$$

Since the momentum $\mathbf{\Pi}$ is proportional to the displacement, this is just Gauss's law. This constraint does not impose any further constraints, since $\{\nabla \cdot \mathbf{\Pi}, H_{\text{EM}}\}_{\text{PB}} = 0$. Since the constraints vanish, they can be added in any amount to the Hamiltonian without changing the dynamics. The Hamiltonian can equally well be written as

$$H_{\text{EM}} = \int d\mathbf{r} \left(\frac{\mathbf{\Pi}^2}{2\epsilon_0\epsilon_r(\mathbf{r})} + \phi(\nabla \cdot \mathbf{\Pi}) + \frac{\epsilon_0 c^2}{2} (\nabla \times \mathbf{A})^2 + f\Pi_0 + g(\nabla \cdot \mathbf{\Pi}) \right) \quad (2.17)$$

where f and g are arbitrary functions. In this case f and g serve as gauge degrees of freedom, with Π_0 and $\nabla \cdot \mathbf{\Pi}$ generating the gauge transformations. [A parallel treatment of the Hamiltonian treatment of EM is given by Steck (2015, Section 8.8).]

2.3. Quantum Theory

The Hamiltonian theory can be quantized by promoting the Poisson bracket to a commutator between field operators. However, there is the matter of the constraints. We will follow the Gupta-Bleuler prescription which restricts the allowed quantum states to those that obey the constraints. In the Gupta-Bleuler formulation, the

equal-time commutation relations are given by

$$[\hat{A}_\mu(\mathbf{r}, t), \hat{\Pi}_\nu(\mathbf{r}', t)] = i\hbar\eta_{\mu\nu}\delta^3(\mathbf{r} - \mathbf{r}'), \quad (2.18)$$

and the allowed states $|\Psi\rangle$ must obey:

$$\hat{\Pi}_0|\Psi\rangle = 0, \quad \nabla \cdot \hat{\boldsymbol{\Pi}}|\Psi\rangle = 0. \quad (2.19)$$

The resolutions of the identity for the fields are

$$1 = \int d^3\mathbf{A} d\phi |\phi, \mathbf{A}\rangle \langle \phi, \mathbf{A}| \quad (2.20)$$

$$1 = \int d^4\Pi |\boldsymbol{\Pi}\rangle \langle \boldsymbol{\Pi}| \delta(\nabla \cdot \boldsymbol{\Pi}) \delta(\Pi_0) = \int d^3\boldsymbol{\Pi} |\boldsymbol{\Pi}\rangle \langle \boldsymbol{\Pi}| \delta(\nabla \cdot \boldsymbol{\Pi}). \quad (2.21)$$

(Strictly speaking, the identity for the potential states is proportional to the volume of the gauge group because the integral runs over equivalent physical states that are related by gauge transformations. Ultimately, this adds an additive constant to the energy, but for EM this can be ignored.) The delta functions restrict the momentum states to those that satisfy the constraints, and can be written in the Fourier representation as

$$\delta(\nabla \cdot \boldsymbol{\Pi}) = \int D\varphi \exp\left(-\frac{i}{\hbar} \int d\mathbf{r} \varphi(\mathbf{r}) \nabla \cdot \boldsymbol{\Pi}(\mathbf{r})\right). \quad (2.22)$$

Since the fields and momenta obey canonical commutation relations, the overlap between field and momentum states is

$$\langle \phi, \mathbf{A} | \Pi_0, \boldsymbol{\Pi} \rangle = \exp\left(-\frac{i}{\hbar} \int d\mathbf{r} \mathbf{A} \cdot \boldsymbol{\Pi}\right), \quad (2.23)$$

where the term in $\phi\Pi_0$ has been dropped due to the $\Pi_0 = 0$ constraint.

2.4. Electromagnetic Partition Function

In order to calculate the energy in the field at zero and nonzero temperature, we will evaluate the partition function for the fields, and take the appropriate derivatives. The EM partition function is defined as

$$Z_{\text{EM}} = \text{Tr}\left(e^{-\beta\hat{H}_{\text{EM}}}\right) = \int d\phi_0 d\mathbf{A}_0 \langle \phi_0, \mathbf{A}_0 | e^{-\beta\hat{H}_{\text{EM}}} | \phi_0, \mathbf{A}_0 \rangle. \quad (2.24)$$

In analogy with the scalar field path integrals described in Section 1.4, this is can be converted into a field path integral. (From here on, the subscript on the Hamiltonian will be suppressed.) The path integral is given by

$$Z_{\text{EM}} = \int d\phi_0 d\mathbf{A}_0 \langle \phi_0, \mathbf{A}_0 | \prod_{i=1}^N e^{-\Delta\beta\hat{H}} | \phi_0, \mathbf{A}_0 \rangle, \quad (2.25)$$

where $\Delta\beta = \beta/N$. A factor of the gauge volume (2.20) can be inserted between each factor of $e^{-\Delta\beta\hat{H}}$. Then, a complementary identity for the momentum fields (2.21) can be inserted between each matrix element. Each field will be labeled by a subscript with its “temperature” $A_\beta(\mathbf{r})$. All fields are functions of position \mathbf{r} , so this label will be suppressed for the moment. Since Π_0 (the momentum conjugate to ϕ) is constrained to vanish, the Π_0 integrals can be carried out for every matrix element. In addition, the ϕ integrals are independent of the other fields and lead to a (divergent) constant. However, since the constant is the same for all configurations of bodies, it will cancel out after renormalization.

Using the Fourier representation of the delta function (2.22), the matrix elements can be written as

$$\langle \phi_{\beta+\Delta\beta}, \mathbf{A}_{\beta+\Delta\beta} | e^{-\Delta\beta\hat{H}} | \phi_{\beta}, \mathbf{A}_{\beta} \rangle = \int d\mathbf{\Pi}_{\beta} \int D\varphi_{\beta} e^{-\Delta\beta \int d\mathbf{r} [\mathcal{H}_{\beta} - i\mathbf{\Pi}_{\beta} \cdot (\partial_{\beta}\mathbf{A}_{\beta} + \nabla\varphi_{\beta})/\hbar]}, \quad (2.26)$$

where the Hamiltonian density for a particular value of β is

$$\mathcal{H}_{\beta} = \frac{\mathbf{\Pi}_{\beta}^2}{2\epsilon_0\epsilon_{\mathbf{r}}(\mathbf{r})} + \frac{\epsilon_0 c^2}{2\mu_{\mathbf{r}}(\mathbf{r})} (\nabla \times \mathbf{A}_{\beta})^2. \quad (2.27)$$

We have also integrated by parts on the term coming from the Fourier representation of the delta function, and identified $\partial_{\beta}\mathbf{A}_{\beta} := (\mathbf{A}_{\beta+\Delta\beta} - \mathbf{A}_{\beta})/\Delta\beta$. After the Gaussian momentum integrals have been carried out, the matrix element is

$$\begin{aligned} & \langle \phi_{\beta+\Delta\beta}, \mathbf{A}_{\beta+\Delta\beta} | e^{-\Delta\beta\hat{H}} | \phi_{\beta}, \mathbf{A}_{\beta} \rangle \\ & \propto \det[\epsilon_{\mathbf{r}}]^{3/2} \exp \left[-\frac{\epsilon_0\Delta\beta}{2} \int d\mathbf{r} \left(\frac{\epsilon_{\mathbf{r}}(\mathbf{r})}{\hbar^2} (\partial_{\beta}\mathbf{A}_{\beta} + \nabla\varphi_{\beta})^2 + \frac{c^2}{\mu_{\mathbf{r}}(\mathbf{r})} (\nabla \times \mathbf{A}_{\beta})^2 \right) \right]. \end{aligned} \quad (2.28)$$

When we consider the integrals over the products of all of these matrix elements it is convenient to introduce a notation

$$\int D\mathbf{A}D\varphi \det[\epsilon_{\mathbf{r}}]^{3/2} := \prod_{i=1}^N \prod_{\mathbf{r}_k} \int d\mathbf{A}(\mathbf{r}_k, \beta_i) \int d\varphi(\mathbf{r}_k, \beta_i) \epsilon^{3/2}(\mathbf{r}_k), \quad (2.29)$$

where the product \mathbf{r}_k runs over all positions $\mathbf{r} \in \mathbb{R}^3$ and inverse temperatures of $\beta_j = j\Delta\beta$. We can change variables to $\tau := \beta\hbar c$, $A_4(\mathbf{x}, \beta) := \varphi_{\beta}(\mathbf{x})/\hbar c$, and $\mathbf{A}(\mathbf{x}, \beta) = \mathbf{A}_{\beta}(\mathbf{x})$, and rescale all of the fields to eliminate the leading constants in the exponential. The new parameter τ is proportional to the thermal de Broglie

wavelength $\lambda_{\text{dB}} = 2\pi\hbar c/(k_{\text{B}}T)$. The resulting partition function is

$$Z_{\text{EM}} = \int D\mathbf{A}DA_4 \det[\epsilon_{\text{r}}]^{3/2} e^{-S_{\text{E}}[\mathbf{A}, A_4]}, \quad (2.30)$$

where the Euclidean action is

$$S_{\text{E}}[\mathbf{A}, A_4] = \frac{\epsilon_0}{2} \int d\mathbf{r} \int_0^{\beta\hbar c} d\tau \left(\epsilon_{\text{r}}(\mathbf{r}) (\partial_{\tau}\mathbf{A} + \nabla A_4)^2 + \frac{1}{\mu_{\text{r}}(\mathbf{r})} (\nabla \times \mathbf{A})^2 \right). \quad (2.31)$$

The action is the imaginary-time action corresponding to the EM Lagrangian (2.7). We will compare this partition function to the case when the bodies are infinitely far apart, which we will denote as Z_0 . In that case, the bodies are still present, but they will be too far apart to interact significantly. If the bodies are rigidly translated, then $\det[\epsilon_{\text{r}}(\mathbf{r})]^{3/2} = \prod_{\mathbf{r}_k} \epsilon_{\text{r}}(\mathbf{r}_k)^{3/2}$ is constant, since the amount of matter in $\epsilon_{\text{r}}(\mathbf{r})$ is fixed. Since the determinants are the same in both cases, they will cancel out under this renormalization, and we will ignore them.

2.4.1. Faddeev–Popov Gauge Fixing

The path integral (2.30) includes infinitely many physically equivalent fields that are related by a gauge transformation (2.6). If that redundancy is not removed, the path integral will yield nonsensical infinite results. The redundancy is lifted by introducing a gauge-fixing condition so that only one gauge field corresponding to a each physical field configuration is included in the path integral. This gauge fixing is carried out by introducing a gauge fixing function $G[\mathbf{A}, A_4]$ inside a functional delta function. A further Jacobian determinant must be included to ensure each physically distinct state also receives the same weight.

In order to fix the gauge, and assign each state equal weight, the following combination should be inserted into the path integral

$$\delta[G(\mathbf{A}, A_4,)] \det \left(\frac{\delta G}{\delta g} \right), \quad (2.32)$$

where the determinant is known as the Faddeev–Popov determinant (Faddeev and Popov, 1967; Faddeev and Slavnov, 1991). The determinant ensures that after integrating over g , each physical state receives the same weight.² This can be understood in analogy with the change of variable for a double integral with a redundant degree of freedom

$$I = \int_{-\infty}^{\infty} dx \int_{-\infty}^{\infty} dy h(x). \quad (2.33)$$

This integral diverges due to the integral over the redundant variables y . A “gauge-fixed” integral can be constructed if we insert a combination $\delta[G(x, y)]|\partial_y G|$. If we change integration variable to G , and integrate over G , the resulting integral is

$$I' = \int_{-\infty}^{\infty} dx \int_{-\infty}^{\infty} dy h(x) \delta[G(x, y)] |\partial_y G| = \int_{-\infty}^{\infty} dx \int_{-\infty}^{\infty} \frac{dG}{|\partial_y G|} h(x) \delta(G) |\partial_y G| = \int dx h(x), \quad (2.34)$$

where the same physical result emerges, regardless of the choice of gauge fixing function. In higher dimensional integrals, the derivative becomes the Jacobian determinant, and in a path integral the Jacobian matrix of derivatives becomes the functional derivative.

One further trick is often used in gauge-fixing the path integral. Instead of fixing a gauge with $G[\mathbf{A}, A_4] = 0$, an alternative gauge $G[\mathbf{A}, A_4] = \gamma$ can be used. Since γ

² For example see Peskin and Schroeder (1995, Section 9.4), or Srednicki (2008, Chapter 71)

is an arbitrary function, it can be integrated out, using a Gaussian with width ξ_{FP} ,

$$\text{const} = \int D\gamma \exp\left(-\int d\mathbf{r}d\tau \frac{\gamma^2(\mathbf{r}, \tau)}{2\xi_{\text{FP}}}\right). \quad (2.35)$$

Such factors are constant in the path integral sense that they will cancel out when considering physical energies, which require renormalization. Finally, the gauge-fixed partition function is

$$\begin{aligned} Z &= \int D\mathbf{A}DA_4D\gamma \delta[G[A] - \gamma] \det\left(\frac{\delta G}{\delta g}\right) \exp\left(-S_{\text{E}} - \int d\mathbf{r}d\tau \frac{\gamma^2}{2\xi_{\text{FP}}}\right) \\ &= \int D\mathbf{A}DA_4 \det\left(\frac{\delta G}{\delta g}\right) \exp\left(-S_{\text{E}} - \int d\mathbf{r}d\tau \frac{G^2}{2\xi_{\text{FP}}}\right), \end{aligned} \quad (2.36)$$

where the Gaussian integral over γ was evaluated in the second equality and S_{E} is given by Eq. (2.31). For EM, since the gauge transformation is independent of the potentials A^μ , the gauge-fixing functional determinant is also independent of the potentials. Nonetheless, this determinant is necessary to correctly count the degrees of freedom, and it cannot be ignored since it depends on the material properties of the interacting bodies. As the bodies are removed arbitrarily far apart, the value of the gauge fixing determinant will vary, so it must be retained, unlike $\det[\epsilon_{\text{r}}]^{3/2}$, which canceled out since it was constant.

2.4.2. Gauge Choices

There are a number of gauges available, only some of which are naturally suited to the path integral. Overall, physical results should be independent of our choice of gauge. Gauge invariance of the final results could be verified by carrying out the calculation within two different gauges, and ensuring the results agree. In the path

integral this can also be done by showing that the final results are independent of the choice of ξ_{FP} , the width the Gaussian. Let us now review a number of the usual gauge choices.

Coulomb gauge ($\nabla \cdot \mathbf{A} = 0$) is the familiar choice in non-relativistic quantum optics, since in free space it decouples the scalar potential A_4 from the vector potential \mathbf{A} , which then only has two transverse degrees of freedom. However, in the presence of a space-dependent dielectric $\epsilon_r(\mathbf{r})$, this is no longer true and there is still some residual coupling between \mathbf{A} and A_4 . Generalized Coulomb gauge ($\nabla \cdot \epsilon \mathbf{A} = 0$) does remove that coupling, and is in fact the choice used in other attempts to quantize the EM field inside a dielectric (Glauber and Lewenstein, 1991; Knöll *et al.*, 1987). However, generalized Coulomb gauge not essential, since Philbin (2010) fixes Coulomb gauge in his work on quantization within media. Unfortunately, this is not well suited to the above gauge-fixing techniques within the path integral. Generalized Lorenz gauge solves that issue, and is how we will proceed.

Another common choice of gauge is Weyl or temporal gauge where the scalar potential vanishes, $A_4 = 0$. This gauge simply removes the scalar field, and the longitudinal part of \mathbf{A} would be responsible for the electrostatic potential if any charges were present. This condition does not completely fix the gauge, since there are still gauge transformations from fields independent of τ : $g(\mathbf{r}, \tau) = g(\mathbf{r})$. Surprisingly, this does seem to be a common gauge for work involving path integrals in dielectrics (Bechler, 1999; Rahi *et al.*, 2009). But given those flaws, we will not pursue Weyl gauge any further.

Finally, there is a generalized Lorenz gauge $\epsilon_r^{-1} \nabla \cdot \epsilon_r \mathbf{A} - \epsilon_r \partial_\tau A_4 = 0$, introduced by Bordag *et al.* (1998). This gauge allows path integral quantization to proceed

in close parallel to the free space case.³ This gauge removes any coupling between the scalar (A_4) and vector (\mathbf{A}) degrees of freedom. In addition, this choice makes the worldline calculations simpler. After expanding out G^2 and integrating by parts, the quadratic term in the vector potential is $\sum_{ij} A_i(-\partial_i\partial_j + V_{ij})A_j$, where V_{ij} is a function of the derivative of $\log \epsilon_r$. If we had adopted $\nabla \cdot \epsilon_r \mathbf{A} + \partial_\tau A_4 = 0$, then the equivalent term would be $\sum_{ij} A_i(-\partial_i\epsilon_r\partial_j)A_j$. In this case ϵ_r acts as a metric in the worldline path integral, which is more complicated. Despite these appealing features, Bordag *et al.* (1998) found the disquieting feature that the longitudinal and scalar degrees of freedom do not cancel out the Faddeev–Popov determinant or “ghost” degrees of freedom. In a later calculation adapted to spherical geometries, Bordag *et al.* (1999) found that using the dual potentials (2.5) led to more physical results where the ghost degrees of freedom canceled. However any attempt to move away from spherical geometry spoiled that cancellation, and some degree of mixing is expected in general (Bordag *et al.*, 1999). Ultimately, the results will have essentially the same form in terms of both the usual potentials and the dual potentials, so we proceed with the regular potentials for now.

2.5. Gauge-Fixing: Generalized Lorenz Gauge

Of the gauges discussed in Section 2.4.2, the generalized Lorenz gauge is best suited to the vector path integral (2.30). In this case the gauge function is

$$G[\mathbf{A}, A_4] = \frac{1}{\epsilon_r(\mathbf{r})\sqrt{\mu_r(\mathbf{r})}} \nabla \cdot \epsilon_r(\mathbf{r})\mathbf{A}(\mathbf{r}, \tau) - \epsilon_r(\mathbf{r})\sqrt{\mu_r(\mathbf{r})}\partial_\tau A_4(\mathbf{r}, \tau), \quad (2.37)$$

³A similar gauge condition was used by Reid *et al.* (2013) in their development of the numerical scattering method. However, that work explicitly relied on fixing EM boundary conditions at surfaces. The resulting computations proceeded using homogeneous formulae for all quantities and ignoring any singularities arising at interfaces, or terms like $\mathbf{A} \cdot \nabla \log \epsilon_r$. In work on the worldline, it is more natural to keep these terms, anticipating that they will enforce boundary conditions.

which has also been scaled to include a permittivity. This gauge function eliminates the cross coupling between the A_4 and the vector potential \mathbf{A} . It also eliminates the longitudinal part of $(\nabla \times \mathbf{A})^2/\mu_r$, but does lead to some extra terms involving derivatives of the permittivity.

To carry out the Faddeev–Popov gauge fixing, we need the functional derivative of the gauge-fixing function with respect to the gauge parameter g . The functional derivative appears as the linear term in g after making a gauge transformation on the gauge-fixing condition,

$$\begin{aligned} G[\mathbf{A} + \nabla g, A_4 + \partial_\tau g] &= \frac{1}{\epsilon_r \sqrt{\mu_r}} \nabla \cdot [\epsilon_r (\mathbf{A} + \nabla g)] - \epsilon_r \sqrt{\mu_r} \partial_\tau (A_4 + \partial_\tau g) \\ &= G[\mathbf{A}, A_4] + \left(\frac{1}{\epsilon_r \sqrt{\mu_r}} \nabla \cdot \epsilon_r \nabla + \epsilon_r \sqrt{\mu_r} \partial_\tau^2 \right) g. \end{aligned} \quad (2.38)$$

The Euclidean action (2.31) after gauge-fixing, canceling terms, and integrating by parts, becomes

$$S_E = \frac{1}{2} \int d\mathbf{r} d\tau \left(A_4 L^{(4)} A_4 + A_i L_{ij} A_j \right), \quad (2.39)$$

where we have started using the Einstein summation convention (where repeated Latin and Greek indices are summed over). The operators $L^{(4)}$ and L_{ij} are given by

$$L^{(4)} = -\epsilon_r^2 \mu_r \partial_\tau^2 - \nabla \cdot \epsilon_r \nabla \quad (2.40)$$

$$L_{ij} = -\left(\epsilon_r \partial_\tau^2 + \nabla \cdot \frac{1}{\mu_r} \nabla \right) \delta_{ij} + \partial_j \frac{1}{\mu_r} \partial_i - \epsilon_r \partial_i \frac{1}{\mu_r \epsilon_r^2} \partial_j \epsilon_r. \quad (2.41)$$

At this point, it is useful to rescale the fields,

$$A_4 := \frac{1}{\sqrt{\epsilon_r}} \tilde{A}_4 \quad \mathbf{A} := \sqrt{\mu_r} \tilde{\mathbf{A}}. \quad (2.42)$$

These field scalings are chosen to simplify the worldline path integrals, and for the same reason as the gauge choice. This rescaling eliminates any combinations like $\partial_x \epsilon \partial_x$, which in path integral terms should be interpreted as a metric. In this case, $\epsilon(x)$ would also mean the diffusion constant of the paths vary throughout space, which complicates path construction. The field rescaling also leads to functional determinants $\det(\mu_r)$ and $\det(\epsilon_r)$, but these can be ignored since they disappear after renormalization. After the rescaling (2.42), the differential operators in Eqs. (2.40) and (2.44) become

$$\tilde{L}^{(4)} = -\epsilon_r \mu_r \partial_\tau^2 - \frac{1}{\sqrt{\epsilon_r}} \nabla \cdot \epsilon_r \nabla \frac{1}{\sqrt{\epsilon_r}}. \quad (2.43)$$

$$\tilde{L}_{ij} = - \left(\epsilon_r \mu_r \partial_\tau^2 + \sqrt{\mu_r} \nabla \cdot \frac{1}{\mu_r} \nabla \sqrt{\mu_r} \right) \delta_{ij} + \sqrt{\mu_r} \partial_j \frac{1}{\mu_r} \partial_i \sqrt{\mu_r} - \epsilon_r \sqrt{\mu_r} \partial_i \frac{1}{\mu_r \epsilon_r^2} \partial_j \epsilon_r \sqrt{\mu_r}. \quad (2.44)$$

The combination of derivatives and functions of the form $f^{-1/2}(x) \partial_i f(x) \partial_j f^{-1/2}(x)$ will recur multiple times in handling worldline path integrals. This can be written out as a second derivative with an additional potential in terms of derivatives of $F_i := \partial_i \log \sqrt{f}$. This derivative operator can be rewritten as

$$\begin{aligned} [f^{-1/2} \partial_i f \partial_j f^{-1/2}] \psi &= (f^{-1/2} \partial_i f^{1/2}) (f^{1/2} \partial_j f^{-1/2}) \psi \\ &= (F_i + \partial_i)(-F_j + \partial_j) \psi \\ &= [-F_i F_j - (\partial_i F_j) - F_j \partial_i + F_i \partial_j + \partial_i \partial_j] \psi, \end{aligned} \quad (2.45)$$

for an unspecified function ψ . The $\partial_i F_j$ term is understood as a function rather than a differential operator, while the other derivatives are still operators acting to the right. This result is needed in both the scalar and matrix differential operators.

The Gaussian integrals can be formally carried out, with the result that

$$\begin{aligned}
Z_{\text{EM}} &\propto \det \left(-\frac{1}{2}(\epsilon_r \mu_r \partial_4^2 + \nabla^2) + V_4 \right)^{-1/2} \\
&\quad \times \det \left(-\frac{1}{2}(\epsilon_r \mu_r \partial_4^2 + \nabla^2) \delta_{ij} - u_{ij} + V_{ij} \right)^{-1/2} \\
&\quad \times \det \left(-\frac{1}{2}(\epsilon_r \mu_r \partial_4^2 + \nabla^2) - u_g + V_g \right)
\end{aligned} \tag{2.46}$$

where the first determinant comes from the scalar potential path integral, the second comes from the vector potential, and the final determinant comes is the Faddeev–Popov gauge-fixing determinant. The Faddeev–Popov gauge-fixing determinant has also been scaled symmetrically by $\mu^{1/4}$. The potentials V_4 , $V_{ij}^{(A)}$, V_g and the operators u_{ij} , u_g , are defined as

$$V_4 = \frac{1}{2}(\nabla \log \sqrt{\epsilon_r})^2 + \frac{1}{2}\nabla^2 \log \sqrt{\epsilon_r} \tag{2.47a}$$

$$\begin{aligned}
V_{ij} &= \frac{1}{2} [(\nabla \log \sqrt{\mu_r})^2 - \nabla^2 \log \sqrt{\mu_r}] \delta_{ij} \\
&\quad - \frac{1}{2} [\partial_i \log \sqrt{\mu_r} \partial_j \log \sqrt{\mu_r} - \partial_i \partial_j \log \sqrt{\mu_r}] \\
&\quad + \frac{1}{2} [\partial_i \log(\epsilon_r \sqrt{\mu_r}) \partial_j \log(\epsilon_r \sqrt{\mu_r}) - \partial_i \partial_j \log(\epsilon_r \sqrt{\mu_r})]
\end{aligned} \tag{2.47b}$$

$$V_g = -\nabla \log \epsilon_r \cdot \nabla \log \mu_r^{1/4} - \nabla^2 \log \mu_r^{1/4} - (\nabla \log \mu_r^{1/4})^2 \tag{2.47c}$$

$$u_{ij} = \frac{1}{2}(\partial_i \log \epsilon_r \mu_r) \partial_j - \frac{1}{2}(\partial_j \log \epsilon_r \mu_r) \partial_i \tag{2.47d}$$

$$u_g = -\frac{1}{2}[\nabla \log(\epsilon_r \mu_r^{1/2})] \cdot \nabla \tag{2.47e}$$

These potentials are highly singular for discontinuous media. If the permittivity or permeability have a jump discontinuity represented by a step function $\Theta(x)$, then

potentials have the form

$$[\partial_x \Theta(x)]^2 - \partial_x^2 \Theta(x) \sim \delta^2(x) - \delta'(x), \quad (2.48)$$

which is extremely singular. These expressions must be regularized by smoothing out the step, and taking the limit of a sharp step at the end of the calculation. This regularization allows finite results to be recovered from such singular potentials. This will be discussed further in Chapter III.

We also assume that the functional determinant of a matrix operator does not pose any problems. While $\det(AB) = \det(A)\det(B)$ for finite matrices, for infinite matrices this is not strictly true. Instead, a regularization-dependent factor can arise, known as the “multiplicative anomaly” (Elizalde *et al.*, 1998). As discussed by McKenzie-Smith and Toms (1998), the multiplicative anomaly is essential to ensure agreement between formal path integral calculations and more straightforward canonical methods. This is important for ζ -function regularization of functional determinants, which is closely related to the worldline method (Elizalde, 2008).

The vector worldline path integral for the EM field can be computed straightforwardly from the partition function (2.46). The relations from Eqs. (1.54) and (1.55) can be used to convert the functional determinants into worldline path integrals, where each functional determinant in Eq. (2.46) leads to an independent

path integral. The renormalized free energy is given by

$$\mathcal{F} - \mathcal{F}^{(0)} = -k_{\text{B}}T(\log Z_{\text{TE}} - \log Z_{\text{TE}}^{(0)}) \quad (2.49)$$

$$\begin{aligned} &= -\frac{k_{\text{B}}T}{2} \int_0^\infty \frac{d\mathcal{T}}{\mathcal{T}} \text{tr} \left(\left[\exp(-M_{ij}\mathcal{T}) - \delta_{ij} \exp(-M^{(0)}\mathcal{T}) \right] \right. \\ &\quad \left. + \left[\exp(-M_4\mathcal{T}) - \exp(-M^{(0)}\mathcal{T}) \right] - 2 \left[\exp(-M_{\text{g}}\mathcal{T}) - \exp(-M^{(0)}\mathcal{T}) \right] \right) \end{aligned} \quad (2.50)$$

where now the trace runs over \mathbf{x} and τ as well as any vector indices i, j . The operators for the vector potential, scalar potential, gauge fixing, and vacuum terms are respectively given by

$$\begin{aligned} M_{ij} &= \frac{1}{2} [\epsilon_{\text{r}}(\hat{\mathbf{x}}) \mu_{\text{r}}(\hat{\mathbf{x}}) \hat{p}_\tau^2 + \hat{\mathbf{p}}^2] \delta_{ij} + V_{ij}(\hat{x}) \\ &\quad + \frac{i}{2} \partial_i \log[\epsilon_{\text{r}}(\hat{\mathbf{x}}) \mu_{\text{r}}(\hat{\mathbf{x}})] \hat{p}_j - \frac{i}{2} \partial_j \log[\epsilon_{\text{r}}(\hat{\mathbf{x}}) \mu_{\text{r}}(\hat{\mathbf{x}})] \hat{p}_i \end{aligned} \quad (2.51\text{a})$$

$$M_4 = \frac{1}{2} [\epsilon_{\text{r}}(\hat{\mathbf{x}}) \mu_{\text{r}}(\hat{\mathbf{x}}) \hat{p}_\tau^2 + \hat{\mathbf{p}}^2] + V_4(\hat{x}) \quad (2.51\text{b})$$

$$M_{\text{g}} = \frac{1}{2} [\epsilon_{\text{r}}(\hat{\mathbf{x}}) \mu_{\text{r}}(\hat{\mathbf{x}}) \hat{p}_\tau^2 + \hat{\mathbf{p}}^2] - \frac{i}{2} \nabla \log[\epsilon_{\text{r}}(\hat{\mathbf{x}}) \sqrt{\mu_{\text{r}}(\hat{\mathbf{x}})}] \cdot \hat{\mathbf{p}} + V_{\text{g}}(\hat{\mathbf{x}}) \quad (2.51\text{c})$$

$$M^{(0)} = \frac{1}{2} (\hat{p}_\tau^2 + \hat{\mathbf{p}}^2), \quad (2.51\text{d})$$

where the potentials $V_{ij}^{(A)}$ and V_4 were specified in Eq. (2.47). This expression for the free energy is quite hard to evaluate, and it is not clear that the two physical degrees of freedom emerge from that path integral in a general medium. This path integral involves contributions from three interacting vector degrees of freedom, a scalar, and a subtraction from gauge-fixing. Somehow all of these path integrals with different potentials must conspire to give the energy of two physical polarizations.

It may be possible that we have not made an error, and this complicated set of path integrals does yield the correct answer. Ultimately, a correct calculation should

reproduce known answers, which in certain geometries only involve two physical degrees of freedom. However, it may be that there were errors in the calculation presented here. Potential areas for errors include incorrect gauge-fixing of an effective theory, insufficient care in handling rescaling the fields and functional determinants, and errors involving the multiplicative anomaly in a matrix path integral. Instead of pursuing the matrix path integral further, we have developed an alternative method explicitly focusing on the two physical degrees of freedom in a simple geometry. The two scalar degrees of freedom that we introduce coincide with the scalars used by Schwinger (1992), and Bordag *et al.* (1999). In fact, they also agree with the Hertz potentials for a plane discussed by Nisbet (1955, 1957).

2.6. Scalar Decomposition for Planar Geometries

The EM field can be split into two non-interacting polarizations for media where the material properties $\epsilon_r(z)$ and $\mu_r(z)$ only vary in one Cartesian direction. These are the transverse-electric (TE) and transverse-magnetic (TM) polarizations. The situation for plane waves scattering off a planar surface is illustrated in Figure 2.1. In the TE polarization, the electric field is perpendicular to the plane of incidence, while in the TM polarization the magnetic field is perpendicular to the plane of incidence. In each case a scalar field theory can be developed. For the TE polarization the electric field behaves as a scalar throughout the problem: while its magnitude may vary, its direction does not. The same is true for the magnetic field in the TM polarization. In this case, the two fields will turn out to mirror each other under the duality transformation (2.4) exchanging electric and magnetic properties of both fields and matter. [The following work is expanded from the presentation in Mackrory *et al.* (2016).]

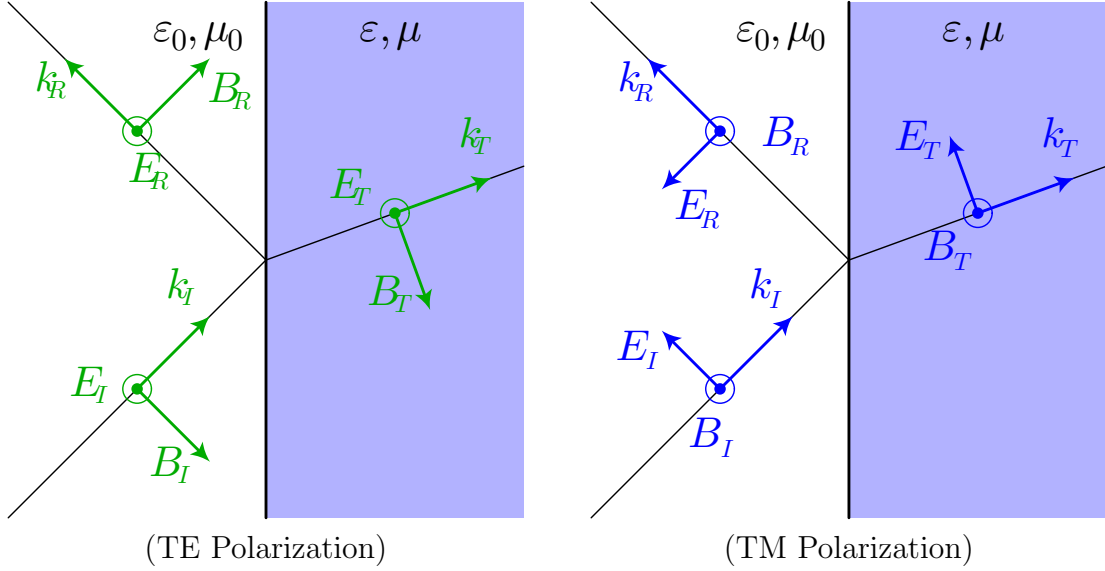


FIGURE 2.1. Scalar polarizations for EM field at a planar dielectric interface.

2.6.1. Scalar-Polarization Partition Functions

In the TE polarization the electric field is described by a single scalar field, $\mathbf{E} = \partial_t \phi \hat{y}$, where $\phi := \phi(\mathbf{r}, t)$. In this case ϕ corresponds to the y-component of the vector potential. The magnetic field can also be written in terms of this scalar. In Coulomb gauge $\nabla \cdot \mathbf{A} = 0$, and using Maxwell's equations, the square of the magnetic field is $|\mathbf{B}|^2 = |\nabla \phi|^2$. The action for the TE scalar ϕ is then given by

$$S_{\text{TE}} = \frac{\epsilon_0}{2} \int_0^T dt \left(\epsilon_r(\mathbf{r}) (\partial_t \phi)^2 - \frac{c^2}{\mu_r(\mathbf{r})} |\nabla \phi|^2 \right). \quad (2.52)$$

The partition function can be found via the same procedure that was used for the Dirichlet scalar, and full vector path integral. The resulting partition function is

$$Z_{\text{TE}} = \int D\phi \exp \left[-\frac{1}{2} \int d\mathbf{r} \int_0^{\beta \hbar c} d\tau \left(\epsilon_r(\mathbf{r}) (\partial_\tau \phi)^2 + \frac{1}{\mu_r(\mathbf{r})} |\nabla \phi|^2 \right) \right]. \quad (2.53)$$

The field ϕ can be rescaled by redefining $\phi := \sqrt{\mu_r} \tilde{\phi}$ for the same reasons as in the matrix path integral: The scaled field yields a Gaussian probability density in the worldline formulation, and sidesteps any possible issues related to quantizing a field on a curved manifold. The path integral can be rewritten in terms of these new variables, and after an integration by parts is given by

$$Z_{\text{TE}} = \int D\tilde{\phi} \exp \left[-\frac{1}{2} \int d\mathbf{r} \int_0^{\beta\hbar c} d\tau \tilde{\phi} \left(-\epsilon_r \mu_r \partial_\tau^2 - \sqrt{\mu_r} \nabla \cdot \frac{1}{\mu_r} \nabla \sqrt{\mu_r} \right) \tilde{\phi} \right]. \quad (2.54)$$

The gradients can be expanded out in the same fashion as Eq. (2.45), which yields the additional potential,

$$V_{\text{TE}}(z) := \frac{1}{2} [(\partial_z \log \sqrt{\mu_r})^2 - \partial_z^2 \log \sqrt{\mu_r}]. \quad (2.55)$$

The Gaussian integral over ϕ can be carried out, with the result

$$Z_{\text{TE}} = \det \left(-\frac{1}{2} [\epsilon_r(z) \mu_r(z) \partial_\tau^2 + \nabla^2] + V_{\text{TE}}(z) \right)^{-1/2}. \quad (2.56)$$

A similar derivation is possible for fields where $\mathbf{H} := \partial_t \psi \hat{y}$. In that case electromagnetic duality (2.4) can be exploited to rewrite the results. As one might expect, this field theory can be naturally formulated in terms of the dual potentials (2.5), subject to “dual Coulomb gauge,” $\nabla \cdot \mathbf{C} = 0$. Exactly the same manipulations as in the TE case lead to the TM partition function:

$$Z_{\text{TM}} = \det \left(-\frac{1}{2} [\epsilon_r(z) \mu_r(z) \partial_\tau^2 + \nabla^2] + V_{\text{TM}}(z) \right)^{-1/2}, \quad (2.57)$$

where the potential is

$$V_{\text{TM}}(z) := \frac{1}{2} [(\partial_z \log \sqrt{\epsilon_r})^2 - \partial_z^2 \log \sqrt{\epsilon_r}]. \quad (2.58)$$

Note that the TM potential depends on the dielectric function, and will play a much larger role than the TE potential for typical media. The simplicity of this derivation is one reason for working with both magnetic and dielectric media in this geometry. However, we will often set $\mu_r = 1$, since magnetic media are rare in typical quantum optical situations. Since we have been working under the assumption of electromagnetism in planar media, the functions are restricted to varying in z -direction. We can also work with more general expressions for similar scalar fields where the material functions vary in multiple dimensions: $\epsilon_r(\mathbf{x}), \mu_r(\mathbf{x})$. Throughout the rest of this thesis we will work with these more general scalar field theories, but remain cognizant of the fact that they only correspond to electromagnetism in a planar geometry.

2.6.2. TE Polarization Worldline

It is a straightforward matter to develop the TE worldline path integral. In the same fashion as the Dirichlet scalar method in Section 1.5, two formal identities can be used to rewrite the free energy in exponential form. The renormalized TE free energy is

$$\mathcal{F}_{\text{TE}} - \mathcal{F}_{\text{TE}}^{(0)} = \frac{k_B T}{2} (\log \det \hat{D}_{\text{TE}} - \log \det \hat{D}^{(0)}), \quad (2.59)$$

where the partition functions Z_{TE} has been written as the functional determinant of a differential operator. The differential operators are

$$\hat{D}_{\text{TE}} := -\frac{1}{2}[\epsilon_{\text{r}}(\mathbf{x})\mu_{\text{r}}(\mathbf{x})\partial_{\tau}^2 + \nabla^2] + V_{\text{TE}}(\mathbf{x}) \quad (2.60)$$

$$\hat{D}^{(0)} := -\frac{1}{2}(\partial_{\tau}^2 + \nabla^2). \quad (2.61)$$

The vacuum operator $\hat{D}^{(0)}$ is the same for both polarizations and is determined by moving the dielectric bodies arbitrarily far apart (operationally, this can be done by setting the $\epsilon_{\text{r}} = \mu_{\text{r}} = 1$ everywhere). The free energy can be rewritten using the identities in Eqs. (1.54) and (1.55), with the result

$$\mathcal{F}_{\text{TE}} - \mathcal{F}_{\text{TE}}^{(0)} = \frac{k_{\text{B}}T}{2} \text{tr}(\log \hat{D}_{\text{TE}} - \log \hat{D}) \quad (2.62)$$

$$= -\frac{k_{\text{B}}T}{2} \int_0^{\infty} \frac{d\mathcal{T}}{\mathcal{T}} \text{tr}[\exp(-\hat{D}_{\text{TE}}\mathcal{T}) - \exp(-\hat{D}^{(0)}\mathcal{T})]. \quad (2.63)$$

For simplicity, we will suppress the renormalization term while developing the path integral.

The worldline path integrals can be developed in the usual fashion, where differential operators become momentum operators in the auxiliary Hilbert space. There are no problems with operator ordering since $\epsilon_{\text{r}}(\mathbf{x})\mu_{\text{r}}(\mathbf{x})\partial_{\tau}^2$ is the only term involving joint position and momentum operators, and these operators commute. After converting the operators, the TE partition function is

$$\mathcal{F}_{\text{TE}} = \frac{k_{\text{B}}T}{2} \int_0^{\infty} \frac{d\mathcal{T}}{\mathcal{T}} \int d\mathbf{x}_0 d\tau_0 \langle \mathbf{x}_0, \tau_0 | e^{-[\epsilon_{\text{r}}(\hat{\mathbf{x}})\mu_{\text{r}}(\hat{\mathbf{x}})\hat{p}_{\tau}^2 + \hat{\mathbf{p}}^2]\mathcal{T}/2 - V_{\text{TE}}(\hat{\mathbf{x}})\mathcal{T}} | \mathbf{x}_0, \tau_0 \rangle. \quad (2.64)$$

Note that although the potential only varies in one dimension, it is still necessary to evaluate the trace and path integrals over all of the dimensions. There is one

change from the normal path integral derivation. Since the exponential operator is independent of τ , it is not necessary to develop the path integral in the τ -direction. As a result, only single integrals over τ and p_τ will be required. However, it is still essential to develop the spatial path integral since $\epsilon_r(\mathbf{x})\mu_r(\mathbf{x})$ and $\hat{\mathbf{p}}^2$ do not commute. After splitting the operator into a product of many terms and inserting the momentum identities, the free energy is

$$\begin{aligned} \mathcal{F}_{\text{TE}} = & -\frac{k_{\text{B}}T}{2} \int_0^\infty \frac{d\mathcal{T}}{\mathcal{T}} \int d\mathbf{x}_N \frac{d\tau_0 dp_\tau}{2\pi} \int \prod_{k=0}^{N-1} \frac{d\mathbf{x}_k d\mathbf{p}_k}{(2\pi)^{D-1}} \delta(\mathbf{x}_N - \mathbf{x}_0) \\ & \times \left(\prod_{j=0}^{N-1} e^{-\epsilon_r(\mathbf{x}_j)\mu_r(\mathbf{x}_j)p_\tau^2\Delta\mathcal{T}/2 - \mathbf{p}_j^2\Delta\mathcal{T}/2 + i\mathbf{p}_j \cdot (\mathbf{x}_{j+1} - \mathbf{x}_j) - V_{\text{TE}}(\mathbf{x}_j)\Delta\mathcal{T}} \right), \end{aligned} \quad (2.65)$$

where $\Delta\mathcal{T} := \mathcal{T}/N$, and the delta functions ensure path closure. The \mathbf{p}_k integrals can be evaluated since they are Gaussian, and the τ integrals can be evaluated at zero temperature using

$$\int_0^{\beta\hbar c} d\tau \int_{-\infty}^\infty \frac{dp_\tau}{2\pi} \exp\left(-\sum_{j=0}^N \epsilon_r(\mathbf{x}_j)\mu_r(\mathbf{x}_j)p_\tau^2 \frac{\Delta\mathcal{T}}{2}\right) = \frac{\beta\hbar c}{\sqrt{2\pi\mathcal{T}\langle\epsilon_r(\mathbf{x})\mu_r(\mathbf{x})\rangle}}, \quad (2.66)$$

where the path average is defined as

$$\langle\epsilon_r(\mathbf{x})\mu_r(\mathbf{x})\rangle = \frac{1}{N} \sum_{j=0}^{N-1} \epsilon_r(\mathbf{x}_j)\mu_r(\mathbf{x}_j) = \frac{1}{\mathcal{T}} \int_0^\mathcal{T} dt \epsilon_r[\mathbf{x}(t)]\mu_r[\mathbf{x}(t)]. \quad (2.67)$$

The resulting free energy is

$$\begin{aligned} \mathcal{F}_{\text{TE}} = & -\frac{k_{\text{B}}T}{2} \int_0^\infty \frac{d\mathcal{T}}{\mathcal{T}} \int d\mathbf{x}_N \int d\tau_0 \int \prod_{k=0}^{N-1} d\mathbf{x}_k \delta(\mathbf{x}_N - \mathbf{x}_0) \frac{1}{\sqrt{2\pi\langle\epsilon_r(\mathbf{x})\mu_r(\mathbf{x})\rangle\mathcal{T}}} \\ & \times \left[\prod_{j=0}^{N-1} \frac{1}{(2\pi\Delta\mathcal{T})^{(D-1)/2}} \exp\left(-\frac{(\mathbf{x}_{j+1} - \mathbf{x}_j)^2}{2\Delta\mathcal{T}} - V_{\text{TE}}(\mathbf{x}_j)\Delta\mathcal{T}\right) \right]. \end{aligned} \quad (2.68)$$

The coupled Gaussians will be used as the probability distribution for paths, where \mathbf{x}_0 is the starting (and finishing) point. The normalized Gaussian probability density for a random walk of N steps between \mathbf{x}_0 and \mathbf{x}_N is

$$P(\mathbf{x}_0, \mathbf{x}_1, \dots, \mathbf{x}_{N-1}) := \mathcal{N} \int \prod_{k=1}^{N-1} d\mathbf{x}_k \prod_{j=0}^{N-1} \left[\frac{1}{(2\pi\Delta\mathcal{T})^{(D-1)/2}} \exp\left(-\frac{(\mathbf{x}_{j+1} - \mathbf{x}_j)^2}{2\Delta\mathcal{T}}\right) \right]. \quad (2.69)$$

The normalization constant \mathcal{N} is determined by requiring that the probability density is normalized,

$$1 = \int \prod_{k=1}^{N-1} d\mathbf{x}_k P \implies \mathcal{N} = \left[\frac{1}{\sqrt{2\pi\mathcal{T}}} \exp\left(-\frac{(\mathbf{x}_N - \mathbf{x}_0)^2}{2\mathcal{T}}\right) \right]^{-1}. \quad (2.70)$$

Like the Dirichlet scalar worldline path integral (1.59), the TE path integral can be written as an ensemble average over closed Brownian bridges

$$\mathcal{F}_{\text{TE}} - \mathcal{F}^{(0)} = -\frac{\hbar c}{2} \int_0^\infty \frac{d\mathcal{T}}{(2\pi\mathcal{T})^{D/2}\mathcal{T}} \int d\mathbf{x}_0 \left\langle\left\langle \frac{e^{-\langle V_{\text{TE}}(\mathbf{x}) \rangle \mathcal{T}}}{\sqrt{\langle \epsilon_r(\mathbf{x}) \mu_r(\mathbf{x}) \rangle}} - 1 \right\rangle\right\rangle_{\mathbf{x}(t)}. \quad (2.71)$$

For completeness we note that the corresponding TM worldline method is derived in exactly the same way, with V_{TM} replacing V_{TE} . The main difference between the two path integrals is that V_{TE} depends on the magnetic response, while V_{TM} depends on the dielectric response.

Let us contrast the TE worldline (2.71) with the Dirichlet worldline path integral (1.59). First, there is a factor $\langle \epsilon_r \mu_r \rangle^{1/2}$ (corresponding to the square of the refractive index) which arose from modifying the thermal direction, and an additional potential V_{TE} arising from the derivatives of the media. Both of these emerge from the underlying material constants, rather than arising from imposed boundary conditions.

Second, the TE path integral is related to one polarization of the EM field in a planar geometry. While the TE path integral can be evaluated in arbitrary geometries of bodies, its relation to the complete EM field in those cases is unclear. In contrast, the Dirichlet path integral (1.59) is geometry independent, and is usually only used to impose Dirichlet boundary conditions. But the Dirichlet worldline only recovers half of the perfect conductor Casimir energy in planar geometries. In this sense the TE path integral surpasses the Dirichlet worldline. We will test the TE path integral in a planar geometry to verify that known electromagnetic results can be recovered from this worldline formalism. In addition, we will develop techniques that may be useful in a general geometry, and evaluate the path integrals in a manner that should straightforwardly generalize. We will see that the TE path integral can recover the Dirichlet results in the strong-coupling ($\chi \rightarrow \infty$) limit. So despite being adapted to a particular geometry the TE path integral may suggest ways to develop a better uncontrolled approximation to the full EM path integral.

2.7. Nonzero Temperature Worldline Path Integrals

The preceding derivation can be extended to finite temperature and dispersion by making the substitution $\epsilon_r(\mathbf{r}) \rightarrow \epsilon_r(\mathbf{r}, i\omega)$. This substitution was carefully examined and justified in the context of the Lifshitz theory by Barash and Ginzburg (1975), and more recently Rosa *et al.* (2010). As noted earlier, Rahi *et al.* (2009) derived their effective Lagrangian at finite temperature via linear-response theory. Presumably the same arguments apply here, for the frequency-dependent, non-zero temperature path integral.

The fields $\phi(\mathbf{r}, \tau)$ in the partition function path integral are periodic, since $Z = \text{tr}[e^{-\beta\hat{H}}] = \int d\phi \langle \phi | e^{-\beta\hat{H}} | \phi \rangle$, so that the starting and ending states are identical.

The fields can then be expanded in a Fourier series,

$$\phi(\tau, \mathbf{r}) = \sum_{n=-\infty}^{\infty} e^{is_n\tau/c} \phi_n(\mathbf{r}), \quad (2.72)$$

where the Matsubara frequencies are defined as $s_n := 2\pi n/(\beta\hbar)$, and the ϕ_n are complex fields. We will also need to use the orthogonality relation between different Matsubara frequencies,

$$\int_0^{\beta\hbar c} d\tau e^{i(s_n+s_m)\tau/c} \phi_n \phi_m = \beta\hbar c \delta_{n,-m} \phi_n \phi_m = \beta\hbar c \delta_{nm} |\phi_n|^2, \quad (2.73)$$

where $\phi_n^* = \phi_{-n}$ since the fields are real. The partition function can then be written as

$$Z_{\text{TE}} = \prod_{n=-\infty}^{\infty} \int D\phi_n \exp \left[-\frac{\beta\epsilon_0 c^2}{2} \int d\mathbf{r} \phi_n^*(\mathbf{r}) \left(\epsilon_{\mathbf{r}}(\mathbf{r}, is_n) \frac{s_n^2}{c^2} - \nabla \cdot \frac{1}{\mu_{\mathbf{r}}(\mathbf{r}, is_n)} \nabla \right) \phi_n(\mathbf{r}) \right]. \quad (2.74)$$

The same field rescaling $\phi_n \rightarrow \sqrt{\mu_{\mathbf{r}}}\phi_n$, can be carried out as for the frequency independent case. At nonzero temperature, assuming that the system is in thermal equilibrium, then the free energy \mathcal{F} is of interest, rather than the mean energy E .⁴ The Gaussian integrals for each ϕ_n can be carried out, so that the free energy can be written as

$$\mathcal{F} = -k_{\text{B}}T \log Z_{\text{TE}} = -\sum_{n=0}^{\infty}{}' \log \det \left(\epsilon_{\mathbf{r}}(\mathbf{r}, is_n) \mu_{\mathbf{r}}(\mathbf{r}, is_n) \frac{s_n^2}{2c^2} - \frac{1}{2} \nabla^2 + V_{\text{TE}}(\mathbf{r}, is_n) \right), \quad (2.75)$$

⁴ The free energy is defined as $\mathcal{F} = E - TS$, where E is the mean energy, S is the entropy and T is the temperature. From the fundamental thermodynamic relation, $dE = TdS + \delta W$, where δW is the work done on the system, the differential for the free energy is $d\mathcal{F} = SdT + \delta W$. Thus at constant temperature, the work done on the system (such as by moving plates) changes the free energy.

where the prime on the sum indicates that the $n = 0$ term is multiplied by a $1/2$ and

$$V_{\text{TE}}(\mathbf{r}, is_n) := \frac{1}{2} \left\{ [\nabla \log \sqrt{\mu_r(\mathbf{r}, is_n)}]^2 - \nabla^2 \log \sqrt{\mu_r(\mathbf{r}, is_n)} \right\}. \quad (2.76)$$

The free energy is renormalized by subtracting off the vacuum energy where $\epsilon_r = \mu_r = 1$ and $V_{\text{TE}}^{(n)}$ is zero. Note that the zero frequency contribution vanishes if $\lim_{\omega \rightarrow 0} \omega^2 \epsilon_r(\omega) = 0$, and $\mu_r = 1$. This is related to the dispute over the role of the zero frequency pole in the dielectric response of a metal.⁵

The nonzero-temperature TE worldline path integral can be developed as before. The Hilbert space is only $(D-1)$ -dimensional, since the thermal dimension has already been treated with the Matsubara frequencies. The resulting worldline path integral is

$$\begin{aligned} \mathcal{F}_{\text{TE}} - \mathcal{F}_0 = & -k_B T \sum_{n=0}^{\infty}{}' \int_0^{\infty} \frac{d\mathcal{T}}{\mathcal{T} (2\pi\mathcal{T})^{(D-1)/2}} \int d\mathbf{x}_0 \\ & \times \left\langle \left\langle e^{-s_n^2 \mathcal{T} / (2c^2)} - e^{-s_n^2 \langle \epsilon_r(\mathbf{x}, is_n) \mu_r(\mathbf{x}, is_n) \rangle \mathcal{T} / (2c^2)} e^{-\mathcal{T} \langle V_{\text{TE}}(\mathbf{x}, is_n) \rangle} \right\rangle \right\rangle_{\mathbf{x}(t)}, \quad (2.77) \end{aligned}$$

where the paths are $D-1$ dimensional spatial paths. This \mathcal{T} -dependence also reflects the different d -dependent scaling behaviors in the near-field, thermal and far-field regions, as these will each have different approximations to the Matsubara sum. This will be discussed further in Section 4.7.

The zero-temperature, dispersion-free Casimir energy (2.71) can be recovered from the free energy (2.77). In the limit $T \rightarrow 0$, the spacing between frequencies $\Delta s = (2\pi)/\beta\hbar \rightarrow 0$, so s_n can be approximated as a continuous variable, $s = n\Delta s$,

⁵One perspective on this dispute is given in Bordag *et al.* (2009, Chapter 14).

and the sum can be approximated using

$$\lim_{n \rightarrow \infty} \sum_n f(n\Delta s) \approx (\Delta s)^{-1} \int ds f(s). \quad (2.78)$$

In this limit the free energy is

$$\begin{aligned} \mathcal{F}_{\text{TE}} - \mathcal{F}_0 \approx & -k_B T \frac{\hbar\beta}{2\pi} \int_0^\infty ds \int_0^\infty \frac{d\mathcal{T}}{\mathcal{T}(2\pi\mathcal{T})^{(D-1)/2}} \int d\mathbf{x}_0 \\ & \times \left\langle \left\langle e^{-s^2\mathcal{T}/(2c^2)} - e^{-s^2\langle\epsilon_r(\mathbf{x},is)\mu_r(\mathbf{x},is)\rangle\mathcal{T}/(2c^2)} e^{-\mathcal{T}\langle V_{\text{TE}}(\mathbf{x},is)\rangle} \right\rangle \right\rangle_{\mathbf{x}(t)}, \end{aligned} \quad (2.79)$$

If we further approximate the material responses by their zero frequency values, then the s integral is Gaussian and can be evaluated, with the result that

$$\mathcal{F}_{\text{TE}} - \mathcal{F}_0 \approx -\frac{\hbar c}{2} \int_0^\infty \frac{d\mathcal{T}}{\mathcal{T}(2\pi\mathcal{T})^{D/2}} \int d\mathbf{x}_0 \left\langle \left\langle 1 - \frac{e^{-\mathcal{T}\langle V_{\text{TE}}(\mathbf{x},0)\rangle}}{\sqrt{\langle\epsilon_r(\mathbf{x},0)\mu_r(\mathbf{x},0)\rangle}} \right\rangle \right\rangle_{\mathbf{x}(t)}, \quad (2.80)$$

which is the anticipated zero-temperature, dispersion-free TE worldline energy (2.71).

The next chapter develops analytical methods for evaluating the scalar worldline path integrals that we have derived.

CHAPTER III

PATH INTEGRALS AND FEYNMAN–KAC FORMULAE

The imaginary-time path integral is closely connected with other ways of describing stochastic processes, such as stochastic differential equations and Fokker-Planck equations. If stochastic paths are sampled from the path integral, then the path's evolution is governed by stochastic differential equations or Langevin equations, where the noise is associated with the random sampling. The path integral is also the solution to the diffusion or Fokker-Planck equation (Durrett, 1996; Karatzas and Shreve, 1991). While stochastic differential equations describe single trajectories, the Fokker-Planck equation gives the equation of motion for the ensemble-averaged probability distribution for the paths (Gardiner, 2009). The path integral solution to the diffusion equations is known as the Feynman–Kac formula, after the work by Feynman (1948) describing the evolution of a quantum particle, and Kac (1949) where analogous methods were applied to the diffusion equation.

Section 3.1 presents the path integral solution (3.13) to the diffusion equation (3.1). Sections 3.2 and 3.3 then develop the analytical expressions relevant for the TE worldline path integral in planar geometries. The sharp dielectric interfaces are modeled by step functions, and the analytical solutions are given by Eqs. (3.25) and (3.31), respectively. The worldline path integral also involves a highly singular potential (2.58). In Section 3.4 this potential is regularized, and found to lead to an effective boundary condition (3.45). The path integral solution corresponding to the TM potential for open paths is given in Eq. (3.52). This result is essential for the numerical methods involving the TM polarization. Sections 3.5 and 3.6, present the analytical expressions for path integrals that include the TM potential, as well as a

step potential. These results are given in Eqs. (3.56) and (3.60). These analytical formulae will be used in Chapter IV to demonstrate agreement with known results for both Casimir and Casimir–Polder energies.

3.1. Derivation of the Feynman–Kac formula

In this section, we will derive the path integral as the solution to a diffusion equation, using techniques from quantum mechanics. The derivation will stay close in spirit to the one presented by Sakurai (1994) and Section 1.4, but it will be extended to include a source term. More formal derivations are available from mathematical (Cartier and deWitte Morette, 2006), and probabilistic perspectives (Durrett, 1996; Karatzas and Shreve, 1991). A detailed discussion of the more formal probabilistic derivation is given by Steck (2015, Section 17.9).

The goal of this section is to find a solution $f(\mathbf{x}, t)$ to the driven diffusion equation

$$\partial_t f = \frac{1}{2} \nabla^2 f - [V(\mathbf{x}) + \lambda] f + g, \quad (3.1)$$

where the potential is given by $V = V(\mathbf{x})$, λ is a constant, and the source term is $g = g(\mathbf{x}, t)$. In this form f corresponds to the probability distribution for a diffusing particle with a source of particles g , and the solution decays at a spatially dependent rate V . The Schrödinger equation is recovered under the $t \rightarrow -it$ substitution. The differential equation can be written in operator form using the same Hilbert space (1.32)–(1.33) that was used for the worldline path integrals (with $\hbar = 1$):

$$\partial_t \langle \mathbf{x} | f(t) \rangle = -\langle \mathbf{x} | \left(\frac{1}{2} \hat{\mathbf{p}}^2 + V(\hat{\mathbf{x}}) + \lambda \right) | f(t) \rangle + \langle \mathbf{x} | g(t) \rangle. \quad (3.2)$$

This equation can be solved in analogy with solving the Schrödinger equation by introducing the evolution operator:

$$U(t) := \exp \left[- \left(\frac{1}{2} \hat{\mathbf{p}}^2 + V(\hat{\mathbf{x}}) + \lambda \right) t \right]. \quad (3.3)$$

Eq. (3.2) is written in the Schrödinger picture, where the operators are time independent, and the states $|f(t)\rangle$ carry all of the time dependence. After transforming to the Heisenberg picture where $|f(t)\rangle \rightarrow |\tilde{f}\rangle := U^{-1}(t)|f(t)\rangle$, the transformed vectors evolve in time according to

$$\partial_t |\tilde{f}\rangle = U^{-1}(t)|g\rangle. \quad (3.4)$$

This equation can be formally integrated with respect to time, and after transforming back to the Schrödinger picture, the result is

$$|f(t)\rangle = U(t)|f(0)\rangle + U(t) \int_0^t ds U(-s)|g(s)\rangle, \quad (3.5)$$

where we used $U^{-1}(s) = U(-s)$. After combining the evolution operators, and projecting onto a final position \mathbf{x}_N the solution is

$$f(\mathbf{x}_N, t) = \langle \mathbf{x}_N | U(t) | f(0) \rangle + \int_0^t ds \langle \mathbf{x}_N | U(t-s) | g(s) \rangle. \quad (3.6)$$

The matrix elements in both terms have the same form $M = \langle \mathbf{x}_N | U(t) | f \rangle$, so we will develop the path integral for just one such matrix element. For time-independent Hamiltonians, the evolution operator can be split into a product of N identical evolution operators $U(\Delta t)$ where $\Delta t := t/N$. Position and momentum identities

can be inserted between each term, with the result that

$$M = \int \prod_{k=0}^{N-1} \frac{d\mathbf{x}_k d\mathbf{p}_k}{(2\pi)^{D/2}} \prod_{j=1}^N \left(\langle \mathbf{x}_{j+1} | e^{-\hat{H}\Delta t} | \mathbf{p}_j \rangle \langle \mathbf{p}_j | \mathbf{x}_j \rangle \right) \langle \mathbf{x}_0 | f(0) \rangle. \quad (3.7)$$

The exponential operator is split into position and momentum pieces using the Baker-Campbell-Hausdorff theorem, $e^{-\Delta t[\hat{p}^2 + V(\hat{x})]} = e^{-\Delta t V(\hat{x})} e^{-\Delta t \hat{p}^2} + \mathcal{O}(\Delta t^2)$. The position and momentum operators then acquire the eigenvalues from operating to the left and right respectively,

$$M = \int \prod_{k=0}^{N-1} \frac{d\mathbf{x}_k d\mathbf{p}_k}{(2\pi)^{D/2}} \prod_{j=1}^N \left(e^{-\mathbf{p}_j^2 \Delta t / 2 - [V(\mathbf{x}_{j+1}) + \lambda] \Delta t + i \mathbf{p}_j \cdot (\mathbf{x}_{j+1} - \mathbf{x}_j)} \right) f(\mathbf{x}_0, 0). \quad (3.8)$$

After carrying out the Gaussian momentum integrals, the matrix element is

$$M = \int \prod_{k=0}^{N-1} d\mathbf{x}_k \prod_{j=1}^N \frac{e^{-(\mathbf{x}_{j+1} - \mathbf{x}_j)^2 / (2\Delta t)}}{(2\pi \Delta t)^{D/2}} e^{-[V(\mathbf{x}_j) + \lambda] \Delta t} f(\mathbf{x}_0, 0). \quad (3.9)$$

This is the traditional discrete form of the imaginary-time path integral. The connection to Brownian motion can be made even clearer by changing integration variables. The arguments of the Gaussians $\mathbf{x}_{j+1} - \mathbf{x}_j$, are zero mean random variables, with variance Δt . The Gaussians can be interpreted as the probability distributions for the vector Wiener increments discussed in Section 1.5.1. In this particular case, the vector Wiener increments are defined as $\Delta \mathbf{W}_j := \mathbf{x}_{N-j-1} - \mathbf{x}_{N-j}$. Note that this labeling is backwards in time from the usual convention, but it ensures that the solutions are defined in reference to the final coordinate \mathbf{x}_N . A general point along the path is given by

$$\mathbf{x}_j = \mathbf{x}_N + \sum_{k=0}^{N-j-1} \Delta \mathbf{W}_k = \mathbf{x}_N + \mathbf{W}_{N-j}, \quad (3.10)$$

where the Wiener process is defined as $\mathbf{W}_j := \sum_{k=0}^{j-1} \Delta \mathbf{W}_k$. In terms of the Wiener paths, the path integral is

$$M = e^{-\lambda t} \int \prod_{k=0}^{N-1} d(\Delta \mathbf{W}_k) \prod_{j=1}^N \frac{e^{-(\Delta \mathbf{W}_j)^2/(2\Delta t)}}{(2\pi\Delta t)^{D/2}} e^{-\Delta t V(\mathbf{x}_N + \mathbf{W}_{N-j})} f[\mathbf{x}_N + \mathbf{W}_N, 0]. \quad (3.11)$$

After taking the continuum limit $N \rightarrow \infty$, the Wiener path $\mathbf{W}_k = \mathbf{W}(t_k)$ becomes a continuously varying stochastic process, and the sum over potentials $\sum_j V(\mathbf{x}_j)\Delta t$ can be written as an integral. The path integral can then be written as

$$M = \left\langle\left\langle \exp\left(-\lambda t - \int_0^t du V[\mathbf{x} + \mathbf{W}(t-u)]\right) f[\mathbf{x} + \mathbf{W}(t), 0] \right\rangle\right\rangle. \quad (3.12)$$

The same style of reasoning can be used for both terms in Eq. (3.6). After substituting this result in to Eq. (3.6), the solution to the diffusion equation is

$$\begin{aligned} f(\mathbf{x}, t) = & \left\langle\left\langle f[\mathbf{x} + \mathbf{W}(t), 0] \exp\left(-\lambda t - \int_0^t du V[\mathbf{x} + \mathbf{W}(t-u)]\right) \right\rangle\right\rangle \\ & + \int_0^t ds \left\langle\left\langle g[\mathbf{x} + \mathbf{W}(s), s] \exp\left(-\lambda s - \int_0^s du V[\mathbf{x} + \mathbf{W}(s-u)]\right) \right\rangle\right\rangle. \end{aligned} \quad (3.13)$$

This agrees with the results of the more formal methods presented in Durrett (1996), and Steck (2015). In this case the ensemble average is over free Brownian motions. This result was derived under the assumption that the potential is independent of time, since that is all that is required for this dissertation. This derivation can be extended to a time-dependent potential $V(\mathbf{x}, t)$ by using the time-ordered evolution operator, as used in the Dyson series (Sakurai, 1994, Section 6.6).

3.1.1. Steady-State Brownian Bridge Path Integral

In worldline path integrals such as Eq. (2.71), the Brownian motions are closed, with the same beginning and ending point. The solution to the diffusion equation (3.13) can be converted into an ensemble average over pinned Brownian bridges with some manipulation. We will follow a solution method used by Hooghiemstra (2002) to compute the sojourn time. This solution method is explained in detail by Steck (2015, Sections 17.9–17.11).

The path integral (3.13) can be converted into the same form as the TE worldline path integrals (2.71) using two transformations. First, the path integral is written in the steady-state limit where $t \rightarrow \infty$. In this limit the initial condition $f(\mathbf{x}, t = 0)$ is irrelevant so it can be set to zero. Second, the source function g can be used to construct the path pinning by setting $g(\mathbf{x}) = \delta(\mathbf{x} - \mathbf{c})$. After those manipulations, the general solution is

$$f(\mathbf{x}) = \int_0^\infty ds \left\langle\left\langle \delta[\mathbf{x} + \mathbf{W}(s) - \mathbf{c}] \exp\left(-\lambda s - \int_0^s du V[\mathbf{x} + \mathbf{W}(s-u)]\right) \right\rangle\right\rangle, \quad (3.14)$$

which has the form of a Laplace transform in λ . The Laplace transform is defined as

$$\mathcal{L}[f(t)](\lambda) := \int_0^\infty dt e^{-\lambda t} f(t). \quad (3.15)$$

The delta function in Eq. (3.14) selects paths that satisfy $\mathbf{W}(s) = \mathbf{c} - \mathbf{x}$. Since the Brownian motion $\mathbf{W}(t)$ starts at the origin, and we want to select Brownian paths starting from $\mathbf{W} = 0$ and propagating to $\mathbf{W} = \mathbf{c}$, we should only consider the solution at the origin $f(\mathbf{x} = 0)$. In that case, the path integral (3.14) satisfies the steady-state

diffusion equation

$$\frac{1}{2}\nabla^2 f - [V(\mathbf{x}) + \lambda]f + \delta(\mathbf{x} - \mathbf{c}) = 0, \quad (3.16)$$

which can be solved analytically for simple potentials $V(\mathbf{x})$. The closed form for the path integral is then found by inverting the Laplace transform on the analytical solution to Eq. (3.16). These path integral expressions will also be used to develop analytical expressions for both open paths where $\mathbf{c} \neq 0$, and closed paths $\mathbf{c} = 0$.

The path integral results for open paths can be used to find the ensemble averaged solution between two points $\mathbf{x} = 0$ and \mathbf{c} . The results can be applied to paths between any pair of positions \mathbf{x}_k and \mathbf{x}_{k+1} , by translating all positions in the path integral by \mathbf{x}_k so that the starting point of the path coincides with the origin. This is particularly useful in applying these results to accelerating numerical computations, as will be discussed further in Chapter V.

It might seem circular having passed from wave equations that are too hard to solve, to path integrals, and back to diffusion equations that can only be solved in particular geometries. However, the path integral provides a way to join together results from a simpler geometry to calculate results in a more complicated geometry. For example, at each step of the path, planar results could be used to estimate a potential, by treating the bodies in terms of their nearest tangent planes. This is not the same approximation as the proximity force approximation discussed in Section 1.3.1, which approximates the bodies *globally* by the tangent planes. This is a local approximation based on a particular point in space. As the path steps through space, the nearest tangent plane will vary, but assuming that each step is small relative to the scale over which the potential changes, the contribution from each step should be well approximated by the interaction with a single plane. These

contributions could be accumulated along the path to develop the full path integral solution, even in potentials that might not be directly solvable in a global sense.

The remainder of this chapter is devoted to solving the diffusion equation (3.16) for some simple planar geometries. These geometries are important for analytically calculating Casimir and Casimir–Polder energies from the worldline path integrals.

3.2. Single Step Potential

As a first example, consider a step potential $V = \chi\Theta(x - d)$. [As noted earlier, this is closely related to the sojourn time for a Brownian bridge (Hooghiemstra, 2002).] The step potential will be used to compute the Casimir–Polder energy for an atom above a dielectric half-space. Throughout what follows, we will work in one spatial dimension. In this case, f solves

$$\frac{1}{2}\partial_x^2 f - [\chi\Theta(x - d) + \lambda]f + \delta(x) = 0 \quad (3.17)$$

In general the solutions are of the form,

$$f(x) = Ae^{\kappa x} + Be^{-\kappa x}, \quad (3.18)$$

where κ will be determined by solving the differential equation in each region of constant dielectric, and A and B will be determined by the boundary conditions at the discontinuities. The boundary conditions follow from integrating the diffusion equation across the relevant discontinuity. At finite step discontinuities (such as at $x = d$), the solution and its derivative must be continuous across the surface,

$$\partial_x f(d + 0_+) - \partial_x f(d - 0_+) = 0 \quad f(d + 0_+) - f(d - 0_+) = 0, \quad (3.19)$$

where 0_+ indicates the limit of approaching zero from above. At a delta function singularity the derivative of the solution is discontinuous, but the function itself is continuous,

$$\partial_x f(0_+) - \partial_x f(-0_+) = -2 \quad f(d + 0_+) - f(d - 0_+) = 0. \quad (3.20)$$

Then assuming $d > 0$ and taking the bounded solution in each region, the solution is

$$f(x) = \begin{cases} Ae^{\sqrt{2\lambda}x} & x < 0 \\ Be^{\sqrt{2\lambda}x} + Ce^{-\sqrt{2\lambda}x} & 0 < x < d \\ De^{-\sqrt{2(\lambda+\chi)}x} & x > d. \end{cases} \quad (3.21)$$

The coefficients are determined by applying the boundary conditions at the interfaces at $x = 0$ and $x = d$. This was done using Mathematica to speed up the tedious algebraic work. The worldline path integral solution only requires $f(x = 0)$, so only A needs to be found. The A coefficient is given by

$$A = \frac{1}{\sqrt{2\lambda}} + r^{(\text{TE})} e^{-2\sqrt{2\lambda}d}, \quad (3.22)$$

where

$$r^{(\text{TE})} = \frac{\sqrt{\lambda} - \sqrt{\lambda + \chi}}{\sqrt{\lambda} + \sqrt{\lambda + \chi}}. \quad (3.23)$$

The reflection coefficient $r^{(\text{TE})}$ plays the same role as the TE-reflection coefficients in the Lifshitz formula. A similar computation can be carried out for $d < 0$, which

corresponds to finding the solution inside the medium. The solution for both cases is

$$f_{\text{TE},1}(x) = \begin{cases} \frac{1}{\sqrt{2\lambda}} \left[1 + r^{(\text{TE})} e^{-2\sqrt{2\lambda}d} \right] & d > 0 \\ \frac{1}{\sqrt{2(\lambda + \chi)}} \left[1 - r^{(\text{TE})} e^{-2\sqrt{2(\lambda + \chi)}d} \right] & d < 0. \end{cases} \quad (3.24)$$

The subscript denotes the relevance of this solution to a single body in the TE polarization. This solution is explicitly related to the path integral via

$$f_{\text{TE},1} = \int_0^\infty d\mathcal{T} e^{-\lambda\mathcal{T}} \left\langle\left\langle \delta(x) e^{-\chi\Theta[x(\mathcal{T})-d]} \right\rangle\right\rangle = \int_0^\infty d\mathcal{T} e^{-\lambda\mathcal{T}} \left\langle\left\langle \frac{e^{-\chi\int_0^\mathcal{T} dt \Theta[x(\mathcal{T})-d]}}{\sqrt{2\pi\mathcal{T}}} \right\rangle\right\rangle_{x(\mathcal{T})}, \quad (3.25)$$

where the first ensemble average is over free, unconstrained Wiener paths, while the second is over Brownian bridges that satisfy $x(0) = x(\mathcal{T}) = 0$. The factor of $\sqrt{2\pi\mathcal{T}}$ is the normalization for using closed Brownian bridges. In this case, we will not invert the Laplace transform, since in Chapter IV we will convert the relevant Casimir energies to exploit these analytical expression.

It is possible to generalize this calculation to compute the equivalent formulae for open Brownian bridges from $0 \rightarrow c$, as discussed in Appendix B of Mackrory *et al.* (2016). These formulae may be useful in accelerating numerical techniques, with relatively coarse bridges.

3.2.1. Planar Dirichlet Conditions

It is possible to take the strong-coupling limit where $\chi \rightarrow \infty$. In that Dirichlet limit, $r^{(\text{TE})} \rightarrow -1$, and the solution vanishes on the surface. The path integral solution is

$$f_{\text{D},1}(x) = \begin{cases} \frac{1}{\sqrt{2\lambda}} \left[1 - e^{-2\sqrt{2\lambda}d} \right] & d > 0 \\ 0 & d < 0 \end{cases} \quad (3.26)$$

The path integral can be converted back to the time domain by inverting the Laplace transform using

$$\mathcal{L}^{-1}\left(\frac{1}{\sqrt{2\lambda}}e^{-2\sqrt{2\lambda}d}\right) = \frac{1}{\sqrt{2\pi t}}e^{-d^2/(2t)}, \quad (3.27)$$

with the result

$$f_{D,1}(x) = \begin{cases} \frac{1}{\sqrt{2\pi t}}(1 - e^{-d^2/2t}) & x < d \\ 0 & x > d. \end{cases} \quad (3.28)$$

As paths get closer to the surface, or as the time increases, the probability of touching the surface increases, so the solution approaches zero. The solution also vanishes for points starting inside the surface.

Given the prevalence of the Dirichlet worldline path integral discussed in Section 1.5, it would be useful to develop an analytical expression for open paths from $x = 0$ to $x = c$, interacting with $V(x) = \kappa\delta(x - d)$. In this case, the solution is non-zero for $x > d$, but only vanishes for paths that touch the surface at $x = d$. This result can straightforwardly be generalized to open Brownian bridges for paths between x and y , and a surface at d , by taking $c \rightarrow x - y$, $d \rightarrow d - x$. The solution can be derived, and after taking $\kappa \rightarrow \infty$, the solution is

$$f_{D,1}(x, y) = \begin{cases} \frac{e^{-(x-y)^2/2t}}{\sqrt{2\pi t}}(1 - e^{-2(d-x)(d-y)/t}) & (d-x)(d-y) > 0 \\ 0 & (d-x)(d-y) < 0. \end{cases} \quad (3.29)$$

The lower solution applies when x and y are on different sides of the surface and the path must cross through. The upper solution applies when the points are both on the same side. As the points x and y get closer to the surface, the probability of touching the surface increases, and the amplitude of the solution decreases.

3.3. Two Step Potentials

The next case of importance is for two step potentials with interfaces at $x = d_1$ and $x = d_2$, where the distance between them is $d = d_1 - d_2$. The combined potential is $V = \chi_1\Theta[d_1 - x] + \chi_2\Theta[x - d_2]$. This potential is useful for analytically calculating the Casimir energy between two dielectric half-spaces, or the Casimir–Polder energy for an atom between two half-spaces. The same procedure as a single half-space can be used, albeit with another set of boundary conditions to manage. The solution and its derivative must be continuous at both surfaces.

Skipping what is some tedious algebra, the solution for closed Brownian paths can be written in each of three regions: Region I is inside the left hand body with $x_0 < d_1$, Region II is between the bodies with $d_1 < x_0 < d_2$, and Region III is inside the right hand body with $d_2 < x_0$. The reflection coefficients for each body are given by

$$r_i^{(\text{TE})} = \frac{\sqrt{\lambda} - \sqrt{\lambda + \chi_i}}{\sqrt{\lambda} + \sqrt{\lambda + \chi_i}}. \quad (3.30)$$

The solutions for each region are

$$f_{\text{TE},12}^{(I)}(x_0) = \frac{1}{\sqrt{2(\lambda + \chi_1)}} + e^{-2\sqrt{2(\lambda + \chi_1)}(d_1 - x_0)} \frac{r_2^{(\text{TE})}e^{-2\sqrt{2\lambda}d} - r_1^{(\text{TE})}}{\sqrt{2(\lambda + \chi_1)}(1 - r_1^{(\text{TE})}r_2^{(\text{TE})}e^{-2\sqrt{2\lambda}d})} \quad (3.31a)$$

$$f_{\text{TE},12}^{(II)}(x_0) = \frac{1}{\sqrt{2\lambda}} + \frac{2r_1^{(\text{TE})}r_2^{(\text{TE})}e^{-2\sqrt{2\lambda}d} + r_1^{(\text{TE})}e^{2\sqrt{2\lambda}(d_1 - x_0)} + r_2^{(\text{TE})}e^{-2\sqrt{2\lambda}(d_2 - x_0)}}{\sqrt{2\lambda}(1 - r_1^{(\text{TE})}r_2^{(\text{TE})}e^{-2\sqrt{2\lambda}d})} \quad (3.31b)$$

$$f_{\text{TE},12}^{(III)}(x_0) = \frac{1}{\sqrt{2(\lambda + \chi_2)}} + e^{2\sqrt{2(\lambda + \chi_2)}(d_2 - x_0)} \frac{(r_1^{(\text{TE})}e^{-2\sqrt{2\lambda}d} - r_2^{(\text{TE})})}{\sqrt{2(\lambda + \chi_2)}(1 - r_1^{(\text{TE})}r_2^{(\text{TE})}e^{-2\sqrt{2\lambda}d})}. \quad (3.31c)$$

The “12” subscript indicates that both the first and second bodies are present. The equivalent single body expressions can be derived from these. For example, the solution for body 1 can be found by keeping d_1 fixed, but taking the limit where d and d_2 approach positive infinity.

The solutions all involve $1 - r_1^{(\text{TE})} r_2^{(\text{TE})} e^{-2\sqrt{2\lambda}d}$ in the denominators. This factor was previously encountered in deriving the Lifshitz formula in Section 1.1.2.1, so its presence is perhaps not surprising. However, in this case there is no need to make any conditions on which modes contribute. In addition, this derivation assumes there is vacuum between the dielectrics, although it could be easily generalized.

We will not attempt to invert the Laplace transform to find the solution in the time domain. Later we will transform the worldline energy into a suitable form to use these results as written. However, in the strong coupling ($r_i^{(\text{TE})} \rightarrow -1$) limit, the Laplace transform can be inverted. In that case the denominator can be expanded by using $(1 - e^{-2\sqrt{2\lambda}d})^{-1} = \sum_{n=0}^{\infty} (-1)^n e^{-2n\sqrt{2\lambda}d}$ since $e^{-2\sqrt{2\lambda}d} < 1$. The n^{th} order term corresponds to the n^{th} reflection from the far surface. After inverting the Laplace transforms, each Gaussian in the sum would be of the form $\exp[-2(n+1)^2 d^2/t]$, corresponding to the probability for a Brownian path to bounce $n+1$ times between two surfaces a distance d apart. This naturally goes over to the reflection picture for the Dirichlet scalar discussed by Steck (2015, Section 21.1.5.3).

3.4. Feynman–Kac Formula for Singular Potentials

The same methods can be used to yield sensible, finite results for worldline path integrals involving singular potentials, such as V_{TE} and V_{TM} where

$$V_{\text{TM}}(x-d) = \frac{1}{2} [(\partial_x \log \sqrt{\epsilon})^2 - \partial_x^2 \log \sqrt{\epsilon}]. \quad (3.32)$$

(We will focus on V_{TM} , since $\mu_{\text{r}} = 1$ for almost all materials, so $V_{\text{TE}} = 0$.)

For a dielectric-vacuum interface described by $\epsilon_{\text{r}} = 1 + \chi\Theta(x - d)$, the resulting potential is highly singular. The first derivative of a step function is a delta function, and the second derivative is δ' , or the derivative of a delta function. We define a parameter $\Xi := \log\sqrt{1 + \chi}$, which implies $\log\sqrt{\epsilon_{\text{r}}}(x) = \Xi\Theta(x - d)$. If the derivatives are taken directly then the potential is given by

$$V_{\text{TM}}(x - d, \Xi) \sim \frac{1}{2}[\Xi^2\delta^2(x - d) - \Xi\delta'(x - d)], \quad (3.33)$$

which involves the square of the delta function! The only way to make sense of this is to regularize the singularity in the step function, and take the limit of vanishing regularization at the end of the computation.

We will consider an exponential interpolation of the dielectric between the two values 1 and $1 + \chi$, over a distance a , so that the logarithm of the dielectric can then be written

$$\log\sqrt{\epsilon_{\text{r}}^{(a)}}(x) = \begin{cases} 0 & x < d \\ \frac{\Xi}{a}(x - d) & d < x < d + a \\ \Xi & x > d + a \end{cases}. \quad (3.34)$$

The regularized TM potential is now given by

$$V_{\text{TM}}^{(a)}(x - d, \Xi) = \frac{\Xi^2}{2a^2}\Theta(x - d)\Theta(d + a - x) - \frac{\Xi}{2a}[\delta(x - d) - \delta(x - d - a)], \quad (3.35)$$

as sketched in Figure 3.1. The only singularities present are the delta functions from the second derivative. The potential is still singular, and it is difficult reliably simulate for a single path as $a \rightarrow 0$. However, the ensemble averaged expression over many such paths is well behaved.

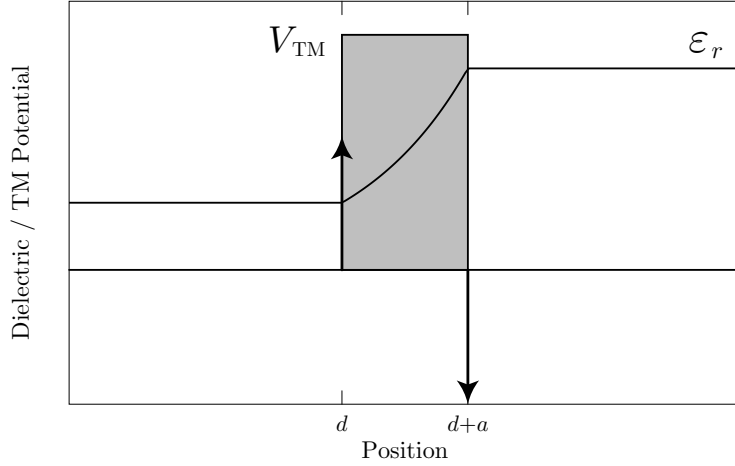


FIGURE 3.1. Schematic drawing of a regularized TM potential (3.35) at a regularized dielectric surface. Vertical arrows denote delta functions with heights Ξ/a , and solid rectangle marks the step function of height $(\Xi/a)^2$.

3.4.1. Transfer Layer Boundary Conditions for the TM Potential

We will now show that the regularized TM potential (3.35) imposes an effective boundary condition at the interface. The diffusion equation can be solved inside the boundary layer $x \in (d, d+a)$, and all references to the interior can be eliminated. The result of this will be conditions relating the solution and its derivatives on either side of the surface. Points starting inside the surface will not be considered, since the surface is infinitesimally thin.

The analytical solutions for the path integral obey

$$\frac{1}{2}\partial_x^2 f = \left(\lambda + \frac{\Xi^2}{2a^2}\Theta(x-d)\Theta(d+a-x) - \frac{\Xi}{2a}[\delta(x-d) - \delta(x-d-a)] \right) f. \quad (3.36)$$

Since a is small, Ξ/a is large relative to λ , so λ can be ignored in the thin-surface limit. At $x = d$, and $x = d+a$, the delta function boundary conditions (3.20) will be enforced.

Let f_{mid} be the solution in the middle region for $x \in (d, d + a)$,

$$f_{\text{mid}} = B e^{\Xi x/a} + C e^{-\Xi x/a}, \quad (3.37)$$

where B and C are constants to be determined. Let the solution from the left be $f_1 := f(d - 0_+)$, and the gradient $\partial_x f_1 := \partial_x f(d - 0_+)$, with corresponding solution on the right $f_2 := f(d + a + 0_+)$, $\partial_x f_2 := \partial_x f(d + a + 0_+)$. The external solutions are assumed to be independent of a . The continuity conditions at $x = d$ and $x = d + a$ require that

$$f_{\text{mid}}(d) - f_1 = 0 \quad (3.38a)$$

$$f_2 - f_{\text{mid}}(d + a) = 0 \quad (3.38b)$$

$$\partial_x f_{\text{mid}}(d) - \partial_x f_1 = -\frac{\Xi}{a} f_1 \quad (3.38c)$$

$$\partial_x f_2 - \partial_x f_{\text{mid}}(d + a) = +\frac{\Xi}{a} f_2. \quad (3.38d)$$

These equations can be solved for the internal parameters B and C , as well as two of the external parameters, f_2 and $\partial_x f_2$ in terms of f_1 and $\partial_x f_1$.

The continuity conditions in Eqs. (3.38a) and (3.38b) require that

$$f_1 = B e^{\Xi d/a} + C e^{-\Xi d/a} \quad (3.39)$$

$$f_2 = B e^{\Xi(d+a)/a} + C e^{-\Xi(d+a)/a}. \quad (3.40)$$

The derivative conditions in Eqs. (3.38c) and (3.38d) then require that

$$\partial_x f_1 = 2 \frac{\Xi}{a} B e^{\Xi d/a} \quad (3.41)$$

$$\partial_x f_2 = 2 \frac{\Xi}{a} B e^{\Xi d/a} e^{\Xi}, \quad (3.42)$$

where the continuity conditions have been exploited. From the derivative conditions (3.41) and (3.42), $\partial_x f_1$ and $\partial_x f_2$ can be related to one another:

$$\partial_x f_2 = e^{\Xi} \partial_x f_1. \quad (3.43)$$

In addition, under the assumption that the external gradients $\partial_x f_1$ and $\partial_x f_2$ are independent of a and of order one, then Eq. (3.41) implies that $B \sim \mathcal{O}(a)$, since B/a is proportional to $\partial_x f_1$. That implies that in the continuity conditions (3.39) and (3.40), B is much smaller than C which must also be order one. On setting $B = 0$, it is clear from Eqs. (3.39)-(3.40) that

$$f_2 = e^{-\Xi} f_1. \quad (3.44)$$

At this point, the $a \rightarrow 0$ limit can be taken, since the conditions between the solutions outside the boundary layer have been derived. The regularized dielectric step produces the following effective boundary boundary conditions at an interface:

$$\boxed{f(d + 0_+) = e^{-\Xi} f(d - 0_+) \quad \partial_x f(d + 0_+) = e^{\Xi} \partial_x f(d - 0_+).} \quad (3.45)$$

These boundary conditions can then be used to find the ensemble averaged solution for the regularized TM potential.

3.4.2. Finding the Path Integral Solution for the TM Potential

We aim to find a closed form solution for the path integral over paths starting at $x = 0$ and terminating at $x = c$ after time t , and interacting with potential V_{TM} :

$$f_{\text{TM-BC}} = \int_0^\infty dt e^{-\lambda t} \frac{e^{-c^2/(2t)}}{\sqrt{2\pi t}} \left\langle\left\langle e^{-\int_0^T dt V_{\text{TM}}(x-d,\Xi)} \right\rangle\right\rangle. \quad (3.46)$$

The Gaussian factor is the probability density for a 1D Brownian bridge between $x = 0$ and c in time t . This path integral is found by solving

$$0 = \frac{1}{2} \partial_x^2 f_{\text{TM-BC}} - [V_{\text{TM}}(x-d, \Xi) + \lambda] f_{\text{TM-BC}} + \delta(x-c), \quad (3.47)$$

where TM boundary conditions (3.45) are imposed at $x = d$, and delta function boundary conditions (3.20) are imposed at $x = c$. The solutions naturally decompose into two cases: one where the end points of the path are on the same side of the surface, and another where the points are on different sides. When both points are on the same side, or $d(d-c) > 0$, the solution at $x = 0$ is

$$f_{\text{TM-BC}} = \frac{e^{-\sqrt{2\lambda}|c|}}{\sqrt{2\lambda}} + \text{sgn}(d) \frac{e^{-\sqrt{2\lambda}|2d-c|}}{\sqrt{2\lambda}} \frac{e^{2\Xi} - 1}{e^{2\Xi} + 1}, \quad (3.48)$$

where $\text{sgn}(x)$ is the signum function: $\text{sgn}(0) = 0$, $\text{sgn}(x > 0) = 1$, $\text{sgn}(x < 0) = -1$. When the paths cross through the surface since $x = 0$ and $x = c$ are on different sides of the surface, the solution at $x = 0$ is

$$f_{\text{TM-BC}} = \frac{e^{-\sqrt{2\lambda}|c|}}{\sqrt{2\lambda}} \frac{2e^\Xi}{1 + e^{2\Xi}}. \quad (3.49)$$

The material constants can be rewritten in terms of χ , by using $\Xi = \log \sqrt{1 + \chi}$, with the result

$$\tanh \Xi = \frac{e^{2\Xi} - 1}{e^{2\Xi} + 1} = \frac{\chi}{2 + \chi} = \frac{\epsilon_r - 1}{\epsilon_r + 1} \quad (3.50)$$

$$\operatorname{sech} \Xi = \frac{2e^\Xi}{1 + e^{2\Xi}} = \frac{2\sqrt{1 + \chi}}{2 + \chi}. \quad (3.51)$$

In both cases the Laplace transforms in λ can be inverted yielding Gaussians [following from Eq. (3.27)]. After canceling out the Gaussian factor $e^{-c^2/(2t)}/\sqrt{2\pi t}$, the analytical expression for the path integral is

$$\left\langle\left\langle e^{-\int_0^t dt' V_{\text{TM}}(x-d,\Xi)} \right\rangle\right\rangle = \begin{cases} 1 + \operatorname{sgn}(d) \tanh \Xi e^{-2d(d-c)/t} & d(d-c) > 0 \\ \operatorname{sech} \Xi & d(d-c) < 0. \end{cases} \quad (3.52)$$

This result is absolutely crucial for developing numerical methods for the TM polarization. Even the regularized potential is too unruly to handle on a single path wise basis. The analytical solution smooths the result out by averaging over all possible sub-paths. The result can be extended to include any starting point x_i by shifting $d \rightarrow d - x_i$, and identifying $c = x_f - x_i$, where x_f is the final point.

The potential has been plotted in Figure 3.2 as a function of ending point for paths starting inside and outside the dielectric step. Note that the potential leads to larger values on the vacuum side of the interface, and suppresses values for starting points inside the surface or paths that must cross the surface.

In the strong-coupling limit $\tanh \Xi \rightarrow 1$, $\operatorname{sech} \Xi \rightarrow 0$, and the solution for paths starting at the origin is

$$f_N = \Theta[d(d-c)] \frac{e^{-c^2/2t}}{\sqrt{2\pi t}} \left(1 + \operatorname{sgn}(d) e^{-2d(d-c)/t} \right). \quad (3.53)$$

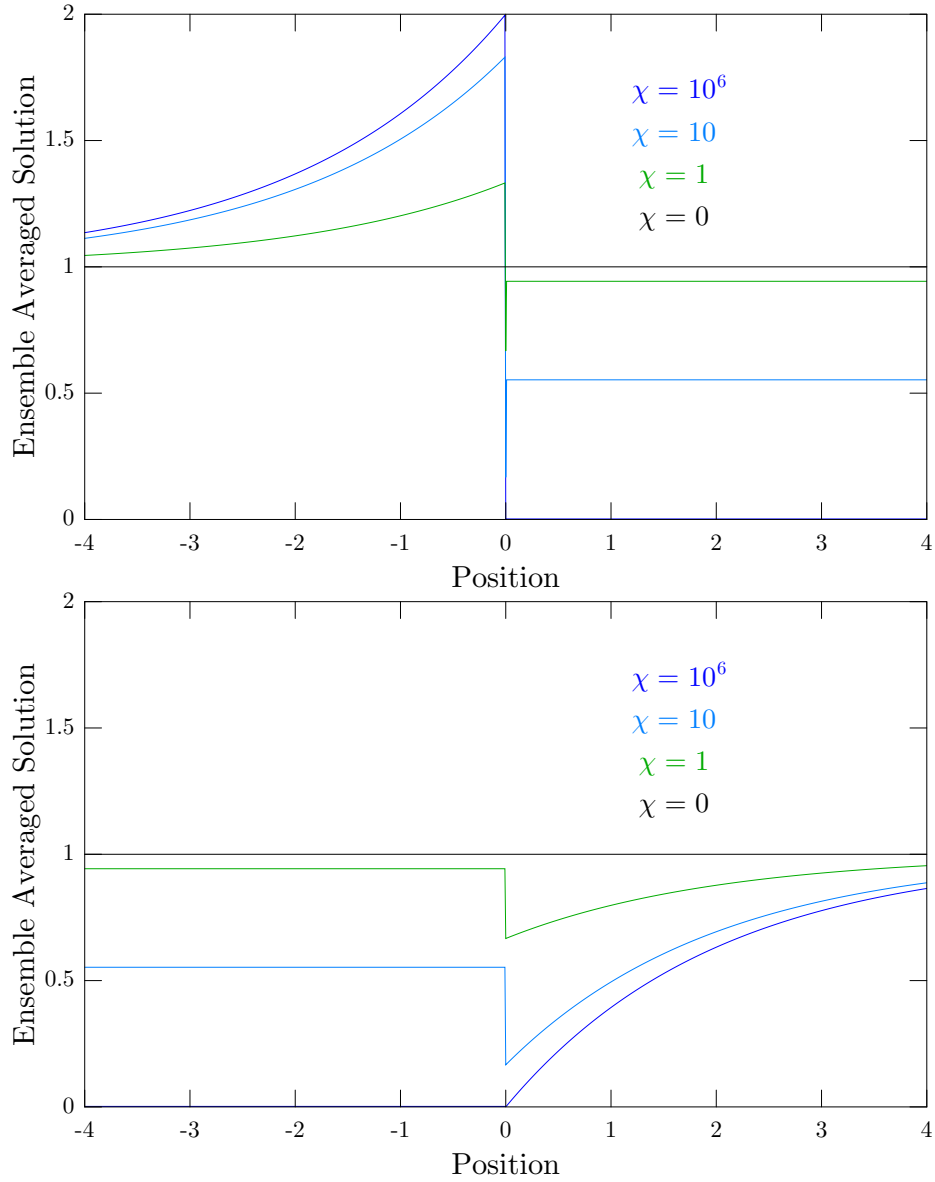


FIGURE 3.2. Plot of ensemble-averaged TM solution (3.52) outside dielectric step at the origin $\epsilon_r = 1 + \chi\Theta(x)$ for various χ , as function of final position x . The top plot considers paths starting outside medium at $x_0 = -1$, while the lower plot considers paths starting inside the medium at $x_0 = 1$.

This is in some sense dual to the solution for open paths in the Dirichlet limit (3.29). In that case paths reflect off with the opposite phase, leading to a value of zero on the boundary. Here, the paths reflecting off the surface add in phase, suggesting a correspondence to Neumann boundary conditions. However, this does not hold for paths starting inside the body, where the solution is the same as for Dirichlet boundary conditions (3.29).

3.5. Single TM potential and Step

Next, we consider a dielectric step combined with a TM boundary condition. This is required to analytically compute the TM component of the Casimir–Polder energy for an atom near a dielectric half-space. We will only develop the solution for closed paths. The path integral

$$f_{\text{TM},1} = \int_0^\infty dt e^{-\lambda t} \frac{1}{\sqrt{2\pi t}} \langle\langle e^{-\int_0^t dt' [V_{\text{TM}}(x-d, \Xi) + \chi\Theta(x-d)]} \rangle\rangle, \quad (3.54)$$

is the steady-state solution to

$$\partial_t f_{\text{TM},1} = \frac{1}{2} \partial_x^2 f_{\text{TM},1} - [V_{\text{TM}}(x-d, \Xi) + \chi\Theta(x-d) + \lambda] f_{\text{TM},1} + \delta(x). \quad (3.55)$$

The analytical expression is found by solving the diffusion equation directly, with TM boundary conditions (3.45) at $x = d$ and delta function boundary conditions (3.20) at $x = 0$. The solution for a single TM body is

$$f_{\text{TM},1}(x) = \begin{cases} \frac{1}{\sqrt{2\lambda}} \left(1 + r^{(\text{TM})} e^{-2\sqrt{2\lambda}d} \right) & d < 0 \\ \frac{1}{\sqrt{2(\lambda + \chi)}} \left(1 - r^{(\text{TM})} e^{-2\sqrt{2(\lambda + \chi)}d} \right) & d > 0, \end{cases} \quad (3.56)$$

where

$$r^{(\text{TM})} = \frac{\sqrt{\lambda}e^{2\Xi} - \sqrt{\lambda + \chi}}{\sqrt{\lambda}e^{2\Xi} + \sqrt{\lambda + \chi}}. \quad (3.57)$$

The reflection coefficient $r^{(\text{TM})}$ corresponds to the TM reflection coefficient used in Section 1.1.2.1, since $e^{2\Xi} = 1 + \chi$. This calculation can also be naturally extended to include a magnetic response. The parameter Ξ is defined in relation to the potential V_{TM} , while χ relates to the step discontinuity. To include a magnetic response, one could take $\chi \rightarrow (\epsilon_r \mu_r - 1)$ and leave Ξ unchanged. Similar reasoning could apply these results to the TE potential, after the $\epsilon_r \leftrightarrow \mu_r$ duality transformation is carried out.

3.6. Two TM Step Potentials

The preceding calculations can be extended to handle two planar dielectric half-spaces subject to TM boundary conditions. This time, the solution is the path integral for a potential

$$V = \chi_1 \Theta(d_1 - x) + \chi_2 \Theta(x - d_2) + V_{\text{TM}}(d_1 - x, \Xi_1) + V_{\text{TM}}(x - d_2, \Xi_2). \quad (3.58)$$

In this case a little care is needed in defining the boundary conditions at the left hand surface. Since the left body has the opposite orientation (the permittivity decreases as x increases at $x = d_1$), the correct TM potential for the left body has $\Xi_1 \rightarrow -\Xi_1$ replaced everywhere. This change reverses the nature of the effective boundary conditions at the surface: if passing through the surface decreases the function, and increases the gradient, then traversing the surface in the opposite direction should

have the opposite effect. So at the left hand surface, the boundary conditions are

$$f(d_1 + 0_+) = e^{\Xi_1} f(d_1 - 0_+) \quad \partial_x f(d_1 + 0_+) = e^{-\Xi_1} \partial_x f(d_1 - 0_+). \quad (3.59)$$

The resulting solutions have the same form and structure as the TE solutions, but with the TE reflection coefficients replaced by their TM counterparts. The two-body TM solution can be written in the same three regions as two-body TE solution:

$$f_{\text{TM},12}^{(\text{I})}(x) = \frac{1}{\sqrt{2(\lambda + \chi_1)}} + e^{-2\sqrt{2(\lambda + \chi_1)}(d_1 - x_0)} \frac{r_2^{(\text{TM})} e^{-2\sqrt{2\lambda}d} - r_1^{(\text{TM})}}{\sqrt{2(\lambda + \chi_1)}(1 - r_1^{(\text{TM})} r_2^{(\text{TM})} e^{-2\sqrt{2\lambda}d})} \quad (3.60a)$$

$$f_{\text{TM},12}^{(\text{II})}(x) = \frac{1}{\sqrt{2\lambda}} + \frac{2r_1^{(\text{TM})} r_2^{(\text{TM})} e^{-2\sqrt{2\lambda}d} + r_1^{(\text{TM})} e^{2\sqrt{2\lambda}(d_1 - x_0)} + r_2^{(\text{TM})} e^{-2\sqrt{2\lambda}(d_2 - x_0)}}{\sqrt{2\lambda}(1 - r_1^{(\text{TM})} r_2^{(\text{TM})} e^{-2\sqrt{2\lambda}d})} \quad (3.60b)$$

$$f_{\text{TM},12}^{(\text{III})}(x) = \frac{1}{\sqrt{2(\lambda + \chi_2)}} + e^{2\sqrt{2(\lambda + \chi_2)}(d_2 - x_0)} \frac{(r_1^{(\text{TM})} e^{-2\sqrt{2\lambda}d} - r_2^{(\text{TM})})}{\sqrt{2(\lambda + \chi_2)}(1 - r_1^{(\text{TM})} r_2^{(\text{TM})} e^{-2\sqrt{2\lambda}d})}, \quad (3.60c)$$

where the TM reflection coefficients for each body are given by

$$r_i^{(\text{TM})} = \frac{e^{2\Xi_i} \sqrt{\lambda} - \sqrt{\lambda + \chi_i}}{e^{2\Xi_i} \sqrt{\lambda} + \sqrt{\lambda + \chi_i}}. \quad (3.61)$$

This result contains all of the previous results for closed paths. The TE results are recovered by taking $\Xi \rightarrow 0$. In taking $\chi \rightarrow 0$ while leaving Ξ fixed, only the TM boundary conditions are present, and this is the solution for two TM boundary conditions with opposite orientations. The equivalent single body results can be found by moving the other body arbitrarily far away.

These formulae are most useful for showing the analytical agreement with existing Casimir energy results. The next chapter uses the results from this chapter to derive known analytical results for Casimir and Casimir–Polder energies for both polarizations from the worldline formalism.

CHAPTER IV

ELECTROMAGNETIC WORLDLINES: ANALYTICAL RESULTS

This chapter shows that in planar media the worldline path integrals yield the same results as the more direct calculations outlined in Chapter I. Section 4.1 extracts the Casimir–Polder energy from the worldline expressions by treating the atom as a localized perturbation. The resulting Casimir–Polder worldline path integrals given for non-magnetic media by Eqs. (4.14) and (4.15). Section 4.2 then uses the Laplace–Mellin transform (4.18) and the inverse moment theorem (4.22) to rewrite the worldline expressions so that the analytical solutions from Chapter III can be substituted into the worldline path integral. Sections 4.3–4.6 show that the worldline expressions yield the correct Casimir and Casimir–Polder energies for the TE and TM polarizations in planar geometries. Finally, Section 4.7 examines the behavior of the worldline path integrals in the case of nonzero temperature, and shows that known results for the near-field and high temperature results emerge from this formalism.

[The work presented on the TE polarization was published as Mackrory *et al.* (2016), and the work on the TM polarization is being prepared for publication.]

4.1. Extracting Casimir–Polder Energies

The Casimir–Polder energy for an atom interacting with macroscopic bodies can be derived by treating the atom as a perturbation to the permittivity and permeability. The atom is located at \mathbf{r}_A , and has static polarizability α_0 and magnetizability β_0 . The atom perturbs the background permittivity $\epsilon_r(\mathbf{r}) \rightarrow \epsilon_r(\mathbf{r}) +$

$\delta\epsilon_r(\mathbf{r})$, and permeability $\mu_r(\mathbf{r}) \rightarrow \mu_r(\mathbf{r}) + \delta\mu_r(\mathbf{r})$, where

$$\delta\epsilon_r(\mathbf{r}) = \frac{\alpha_0}{\epsilon_0}\delta(\mathbf{r} - \mathbf{r}_A), \quad \delta\mu_r(\mathbf{r}) = \mu_0\beta_0\delta(\mathbf{r} - \mathbf{r}_A). \quad (4.1)$$

Note that the delta functions physically represent a sharply localized atom. All expansions involving these delta functions can be carried out with a finite regularization of the delta function, and the limit of an arbitrarily small particle can be taken at the end of the computations. We will initially carry out calculations for dispersion-free media, at zero temperature. The generalization to nonzero temperature will be considered in Section 4.7.

The Casimir energy for TE and TM polarizations was derived in Chapter II. In the zero-temperature limit, the energy in the EM field in the TE polarization is

$$E_{\text{TE}} - E^{(0)} = -\frac{\hbar c}{2} \int_0^\infty \frac{d\mathcal{T}}{(2\pi\mathcal{T})^{D/2}\mathcal{T}} \int d\mathbf{x}_0 \left\langle \left\langle \frac{e^{-\langle V_{\text{TE}}(\mathbf{x})\rangle\mathcal{T}}}{\sqrt{\langle \epsilon_r(\mathbf{x})\mu_r(\mathbf{x})\rangle}} - 1 \right\rangle \right\rangle_{\mathbf{x}(t)}. \quad (4.2)$$

The Casimir–Polder energy comes from expanding the energy to linear order in the α_0/ϵ_0 and $\mu_0\beta_0$. The expansions must be carried out in both $\langle \epsilon_r\mu_r \rangle$, and the potential V_{TE} . Considering the similarities between the polarizations, we will carry these expansions out for only the TE polarization, since the TM results follow by duality (2.4).

The energy (4.2) can be written as a functional of the permittivity and permeability, $E[\epsilon_r, \mu_r]$. The change in energy for adding an atom is then

$$\delta E[\epsilon_r, \mu_r] = E[\epsilon_r + \delta\epsilon_r, \mu_r + \delta\mu_r] - E[\epsilon_r, \mu_r]. \quad (4.3)$$

The Casimir–Polder energy can be found by expanding the change in energy to linear order in α_0/ϵ_0 and $\mu_0\beta_0$, which corresponds to taking the following functional derivatives:

$$V_{\text{CP}}(\mathbf{r}_A) = \frac{\alpha_0}{\epsilon_0} \frac{\delta}{\delta\epsilon_r(\mathbf{r}_A)} E + \mu_0\beta_0 \frac{\delta}{\delta\mu_r(\mathbf{r}_A)} E, \quad (4.4)$$

where \mathbf{r}_A is the atom’s location. The Casimir–Polder energy must then be renormalized by considering the change in the energy as the atom is removed arbitrarily from the dielectric objects.

The expansion for the path-averaged permittivity and permeability is

$$\begin{aligned} \langle(\epsilon_r + \delta\epsilon_r)(\mu_r + \delta\mu_r)\rangle^{-1/2} &= \langle\epsilon_r\mu_r\rangle^{-1/2} - \frac{1}{2}\langle\mu_r\delta\epsilon_r + \epsilon_r\delta\mu_r\rangle\langle\epsilon_r\mu_r\rangle^{-3/2} \\ &= \langle\epsilon_r\mu_r\rangle^{-1/2} - \frac{1}{2}\frac{\alpha_0}{\epsilon_0}\langle\mu_r(\mathbf{x})\delta(\mathbf{x} - \mathbf{r}_A)\rangle\langle\epsilon_r\mu_r\rangle^{-3/2} \\ &\quad - \frac{1}{2}\mu_0\beta_0\langle\epsilon_r(\mathbf{x})\delta(\mathbf{x} - \mathbf{r}_A)\rangle\langle\epsilon_r\mu_r\rangle^{-3/2}. \end{aligned} \quad (4.5)$$

The singular potentials $V_{\text{TE}}, V_{\text{TM}}$ can be expanded in the same fashion,

$$\begin{aligned} \langle V_{\text{TE}}[\mu_r + \delta\mu_r] \rangle &= \frac{1}{2} \left\langle (\nabla \log \sqrt{\mu_r + \delta\mu_r})^2 - \nabla^2 \log \sqrt{\mu_r + \delta\mu_r} \right\rangle \\ &= \langle V_{\text{TE}}[\mu_r] \rangle + \left\langle \frac{1}{4} \nabla \log \mu_r \cdot \nabla \frac{\delta\mu_r}{\mu_r} - \frac{1}{4} \nabla^2 \frac{\delta\mu_r}{\mu_r} \right\rangle. \end{aligned} \quad (4.6)$$

It is straightforward to then expand the exponential using

$$e^{-\mathcal{T}\langle V_{\text{TE}}[\mu_r + \delta\mu_r] \rangle} = e^{-\mathcal{T}\langle V_{\text{TE}}[\mu_r] \rangle} (1 - \mathcal{T}\langle \delta V_{\text{TE}}[\mu_r] \rangle), \quad (4.7)$$

where δV_{TE} is the second term in Eq. (4.6). The terms involving $\nabla\delta\mu_r$ will yield derivatives (such as ∇^2) acting on the path integral after an integration by parts. In all of these expansions, the path-averaged delta functions restrict the path

integrals to paths starting at the atom's position \mathbf{r}_A . The path integral can be written schematically as some path-averaged function $\Phi(\mathbf{x})$, and a path-averaged delta function,

$$I = \int d\mathbf{x}_0 \left\langle\left\langle \langle \Phi(\mathbf{x}) \rangle \langle g(\mathbf{x}) \delta(\mathbf{x} - \mathbf{r}_A) \rangle \right\rangle\right\rangle_{\mathbf{x}(t)}. \quad (4.8)$$

In discrete notation this is

$$I = \int \prod_{n=0}^{N-1} d\mathbf{x}_n P(\mathbf{x}_0, \dots, \mathbf{x}_{N-1}) \frac{1}{N} \sum_{k=0}^{N-1} \Phi(\mathbf{x}_k) \frac{1}{N} \sum_{j=0}^{N-1} \delta(\mathbf{x}_j - \mathbf{r}_A) g(\mathbf{x}_j) \quad (4.9)$$

where the delta function enforces path closure. All of the functions are invariant under cyclic permutations of the path labels. This is true of the path-averaged functions such as $\langle \epsilon_r \mu_r \rangle$ and $\langle V_{\text{TM}} \rangle$, and the Gaussian probability for closed Brownian bridges. Then for each term $\delta(\mathbf{x}_j - \mathbf{r}_A)$, the labels can be permuted j times so that in the shifted coordinates $\mathbf{x}_j \rightarrow \mathbf{x}_0$. Since there is now a sum of N identical terms, the path integral can be written as

$$I = \int \prod_{n=0}^{N-1} d\mathbf{x}_n P(\mathbf{x}_0, \dots, \mathbf{x}_{N-1}) \sum_{k=0}^{N-1} \Phi(\mathbf{x}_k) \delta(\mathbf{x}_0 - \mathbf{r}_A) g(\mathbf{x}_0) = \left\langle\left\langle \langle \Phi \rangle g(\mathbf{r}_A) \right\rangle\right\rangle_{\mathbf{x}(t), \mathbf{x}(0)=\mathbf{r}_A}. \quad (4.10)$$

Since only paths that satisfy the delta function constraint will contribute to the path integral, we are free to call the point at \mathbf{r}_A the path origin.

Using the results in Eqs. (4.5) and (4.6), the Casimir–Polder energy for the TE polarization can be written

$$V_{\text{CP}}^{(\text{TE})}(\mathbf{r}_A) = \frac{\hbar c}{4} \int_0^\infty \frac{d\mathcal{T}}{(2\pi\mathcal{T})^{D/2}\mathcal{T}} \int d\mathbf{x}_0 \left\langle\left\langle \left(\frac{\langle \mu_r \delta \epsilon_r + \epsilon_r \delta \mu_r \rangle}{\langle \epsilon_r \mu_r \rangle^{3/2}} \right) e^{-\langle V_{\text{TE}} \rangle \mathcal{T}} + e^{-\langle V_{\text{TE}} \rangle \mathcal{T}} \frac{\mathcal{T}}{2\langle \epsilon_r \mu_r \rangle^{1/2}} \left\langle \left(\nabla \log \mu_r \right) \cdot \nabla \frac{\delta \mu_r}{\mu_r} - \nabla^2 \frac{\delta \mu_r}{\mu_r} \right\rangle \right\rangle\right\rangle_{\mathbf{x}(t)}. \quad (4.11)$$

Then after manipulating the path-averaged delta functions using Eq. (4.10), and integrating by parts, the Casimir–Polder energy is

$$\begin{aligned}
V_{\text{CP}}^{(\text{TE})}(\mathbf{r}_A) = & \frac{\hbar c}{4} \int_0^\infty \frac{d\mathcal{T}}{(2\pi\mathcal{T})^{D/2}\mathcal{T}} \left\langle\left\langle \left(\frac{\alpha_0\mu_r(\mathbf{r}_A)}{\epsilon_0\langle\epsilon_r\mu_r\rangle^{3/2}} + \frac{\beta_0\mu_0\epsilon_r(\mathbf{r}_A)}{\langle\epsilon_r\mu_r\rangle^{3/2}} \right) e^{-\langle V_{\text{TE}}\rangle\mathcal{T}} \right. \right. \\
& \left. \left. - \frac{\mathcal{T}}{2} \frac{\beta_0\mu_0}{\mu_r(\mathbf{r}_A)} [\nabla^2 + (\nabla^2 \log \mu_r) + (\nabla \log \mu_r) \cdot \nabla] \frac{e^{-\langle V_{\text{TE}}\rangle\mathcal{T}}}{\langle\epsilon_r\mu_r\rangle^{1/2}} \right\rangle\right\rangle_{\mathbf{x}(t),\mathbf{x}(0)=\mathbf{r}_A}.
\end{aligned} \tag{4.12}$$

Note that the gradients in parentheses such as $(\nabla \log \mu_r)$ should be interpreted as functions, while the other gradient operators act on everything to their right. The remaining gradients act with respect to the path origin $\mathbf{x}_0 = \mathbf{r}_A$. The corresponding TM Casimir–Polder energy is given by

$$\begin{aligned}
V_{\text{CP}}^{(\text{TM})}(\mathbf{r}_A) = & \frac{\hbar c}{4} \int_0^\infty \frac{d\mathcal{T}}{(2\pi\mathcal{T})^{D/2}\mathcal{T}} \left\langle\left\langle \left(\frac{\alpha_0\mu_r(\mathbf{r}_A)}{\epsilon_0\langle\epsilon_r\mu_r\rangle^{3/2}} + \frac{\beta_0\mu_0\epsilon_r(\mathbf{r}_A)}{\langle\epsilon_r\mu_r\rangle^{3/2}} \right) e^{-\langle V_{\text{TM}}\rangle\mathcal{T}} \right. \right. \\
& \left. \left. - \frac{\mathcal{T}}{2} \frac{\alpha_0}{\epsilon_0\epsilon_r(\mathbf{r}_A)} [\nabla^2 + \nabla^2(\log \epsilon_r) + \nabla(\log \epsilon_r) \cdot \nabla] \frac{e^{-\langle V_{\text{TM}}\rangle\mathcal{T}}}{\langle\epsilon_r\mu_r\rangle^{1/2}} \right\rangle\right\rangle_{\mathbf{x}(t),\mathbf{x}(0)=\mathbf{r}_A}.
\end{aligned} \tag{4.13}$$

These expressions can be further simplified if the atom is in a region where the dielectric is not varying spatially [which implies that $\nabla \log \sqrt{\epsilon_r}(\mathbf{r}_A) = 0$], and we consider non-magnetic atoms and media, so that $\beta_0 = 0$ and $\mu_r = 1$. In this case, the TE and TM Casimir–Polder energies are given by

$$V_{\text{CP}}^{(\text{TE})}(\mathbf{r}_A) = \frac{\hbar c\alpha_0}{4\epsilon_0(2\pi)^{D/2}} \int_0^\infty \frac{d\mathcal{T}}{\mathcal{T}^{1+D/2}} \left\langle\left\langle \frac{1}{\langle\epsilon_r\rangle^{3/2}} - \frac{1}{[\epsilon_r(\mathbf{r}_A)]^{3/2}} \right\rangle\right\rangle_{\mathbf{x}(t),\mathbf{x}(0)=\mathbf{r}_A} \tag{4.14}$$

$$\begin{aligned}
V_{\text{CP}}^{(\text{TM})}(\mathbf{r}_A) = & \frac{\hbar c\alpha_0}{4\epsilon_0(2\pi)^{D/2}} \int_0^\infty \frac{d\mathcal{T}}{\mathcal{T}^{1+D/2}} \left\langle\left\langle \frac{e^{-\langle V_{\text{TM}}\rangle\mathcal{T}}}{\langle\epsilon_r\rangle^{3/2}} - \frac{1}{[\epsilon_r(\mathbf{r}_A)]^{3/2}} \right. \right. \\
& \left. \left. - \frac{\mathcal{T}}{2\epsilon_r(\mathbf{r}_A)} \nabla^2 \frac{e^{-\langle V_{\text{TM}}\rangle\mathcal{T}}}{\langle\epsilon_r\rangle^{1/2}} \right\rangle\right\rangle_{\mathbf{x}(t),\mathbf{x}(0)=\mathbf{r}_A}.
\end{aligned} \tag{4.15}$$

These expressions were renormalized by subtracting off the equivalent expressions with a constant dielectric of permittivity $\epsilon_T(\mathbf{r}_A)$. This corresponds to finding the change in energy for the atom when it is brought to a finite distance from the dielectric interface, after starting arbitrarily far away. In non magnetic media, the TE Casimir–Polder energy is the simpler case to evaluate since it only depends on $\langle\epsilon_T\rangle$, which is well behaved. By contrast, the TM Casimir–Polder energy involves the singular TM potential, which implies the need for spatial derivatives. Both of those factors will require some care in numerical methods involving stochastic paths interacting with discontinuous or singular potentials.

4.2. Rearranging Worldline Casimir Energies

The TE and TM worldline energies can be some rewritten in a form better suited to use the analytical results that were derived in Chapter III. This can be done with two integral identities. The first identity converts the worldline path integral into a form involving the Laplace transform of the path integral. The second identity puts the prefactor $\langle\epsilon_T\rangle$ in exponential form by means of the Gamma function.

4.2.1. Laplace–Mellin Transforms

The worldline path integral has the form of a Mellin transform. The Mellin transform of a function f is defined as

$$\mathcal{M}[f](z) = \int_0^\infty dt t^{z-1} f(t). \quad (4.16)$$

The Mellin transform also appears in the context of ζ -function renormalization for functional determinants (Elizalde, 2008), which is closely related to the worldline path

integral. In the application to the worldline path integral, f will be the ensemble-averaged path integral and z will be $1 + D/2$.

There is a useful relationship between Laplace transforms and Mellin transforms (Lew, 1975). The Laplace transform was defined in Eq. (3.15), and the Γ function is defined as

$$\Gamma(z) = \int_0^\infty ds s^{z-1} e^{-s} = \mathcal{M}[e^{-s}](z). \quad (4.17)$$

The Laplace–Mellin theorem (Lew, 1975) states that

$$\Gamma(1-z)\mathcal{M}[f](z) = \mathcal{M}[\mathcal{L}[f]](1-z). \quad (4.18)$$

This relation is most easily motivated by starting with the right hand side:

$$\mathcal{M}[\mathcal{L}[f]](1-z) = \int_0^\infty ds s^{-z} \int_0^\infty dt e^{-st} f(t). \quad (4.19)$$

The order of s and t integration can be swapped, and $s \rightarrow t/u$, with the result

$$\mathcal{M}[\mathcal{L}[f]](1-z) = \int_0^\infty dt \int_0^\infty du u^{-z} e^{-u} t^{z-1} f(t) \quad (4.20)$$

$$= \Gamma(1-z)\mathcal{M}[f](z). \quad (4.21)$$

This result can be used to rewrite worldline path integrals in terms of their Laplace transforms. This is useful since the solution method in Chapter III naturally yields the Laplace transform of the path integral.

4.2.2. Inverse Moment Theorem

One further step is required to put all of the material functions in the path integral into exponential form. This is necessary since the solutions from the previous chapter were for path integrals with exponential potentials. If positive powers were required, then the usual moment generating tricks could be used such as $\langle x \rangle^n = \frac{d^n}{ds^n} e^{-s\langle x \rangle} \Big|_{s=0}$. However, for the inverse moments required in the worldline method, the following integral transformation involving the Gamma function can be used

$$\frac{1}{\Gamma[a]} \int_0^\infty ds s^{a-1} \langle\langle e^{-s(x+\beta)} \rangle\rangle = \left\langle\left\langle \frac{1}{(x+\beta)^a} \right\rangle\right\rangle. \quad (4.22)$$

This is restricted to $x + \beta > 0$ and $a > 0$. In the worldline calculations $x + \beta$ will be $\langle\epsilon_r(\mathbf{x})\rangle$, where the dielectric function is real and positive. In addition, a will be 1/2 for Casimir energies, and 3/2 for Casimir–Polder energies, respectively.

4.2.3. Rewriting the Worldline in Analytical Form

As an example, consider the TE path integral, with dielectric function $\epsilon_r(\mathbf{x}) = 1 + \chi(\mathbf{x})$, where $\chi(\mathbf{x})$ is the space-dependent dielectric susceptibility. In both the Casimir and Casimir–Polder cases, the energy involves the factor $\langle\epsilon_r\rangle^{-a}$, with $a = 1/2$ and $a = 3/2$ respectively. The energy density can be rewritten using the inverse moment theorem (4.22):

$$\int_0^\infty \frac{d\mathcal{T}}{\mathcal{T}^{1+D/2}} \left\langle\left\langle \frac{1}{\langle 1 + \chi(\mathbf{x}) \rangle^a} \right\rangle\right\rangle_{\mathbf{x}(t)} = \int_0^\infty ds \frac{s^{a-1}}{\Gamma(a)} \int_0^\infty \frac{d\mathcal{T}}{\mathcal{T}^{1+D/2-a}} \left\langle\left\langle e^{-s\mathcal{T} - \int_0^\mathcal{T} dt \chi[\mathbf{x}(t)]} \right\rangle\right\rangle_{\mathbf{x}(t)}. \quad (4.23)$$

In the second equality the integration variable was rescaled to $s \rightarrow s\mathcal{T}$, and the definition of the path average, $\langle f \rangle = \mathcal{T}^{-1} \int_0^{\mathcal{T}} dt f(t)$ was used. The energy density can be further transformed with the Laplace–Mellin theorem (4.18),

$$\int_0^\infty \frac{d\mathcal{T}}{\mathcal{T}^{1+D/2}} \left\langle \left\langle \frac{1}{\langle 1 + \chi(\mathbf{x}) \rangle^a} \right\rangle \right\rangle_{\mathbf{x}(t)} = \int_0^\infty ds \frac{s^{a-1}}{\Gamma(a)} \int_0^\infty d\lambda \frac{\lambda^{(D-n)/2-a}}{\Gamma[(D-n)/2-a+1]} \times \int_0^\infty d\mathcal{T} e^{-(\lambda+s)\mathcal{T}} \left\langle \left\langle \frac{e^{-s \int_0^{\mathcal{T}} dt \chi(\mathbf{x})}}{\mathcal{T}^{n/2}} \right\rangle \right\rangle_{\mathbf{x}(t)}. \quad (4.24)$$

In the last line $\mathcal{T}^{n/2}$ was factored out to act as the normalization for a n -dimensional Brownian bridge, which assumes that the path integral solution was computed in n -dimensions. We will typically work with planar media where $n = 1$. (Despite knowing the specific values for a, D and n , it is useful to track them as algebraic variables in calculations.) The Laplace transformed path integral can be computed as the solution (3.14) to the relevant diffusion equation (3.16), as discussed in Chapter III.

4.3. Analytical TE Casimir–Polder Energy for an Atom and a Dielectric Plane

The TE contribution to the Casimir–Polder energy for an atom interacting with a dielectric body is given by combining these formal manipulations with the relevant path integral solution. For an atom at the origin, interacting with a planar dielectric interface $\epsilon_r(z) = 1 + \chi\Theta(x - d)$, the path integral solution is given by Eq. (3.25). After rescalings the path integral (3.25) with $s \rightarrow s\chi, \lambda \rightarrow \lambda + s$, the renormalized

TE Casimir–Polder potential can be written as

$$V_{\text{CP}}^{(\text{TE})} - V_{\text{CP}}^{(0)} = - \frac{\hbar c \alpha_0}{4\epsilon_0 (2\pi)^{D/2}} \frac{\sqrt{\pi}}{\Gamma[a]\Gamma[(D+1)/2-a]} \int_0^\infty ds s^{a-1} \int_0^\infty d\lambda \lambda^{(D-1)/2-a} \times \frac{e^{-2\sqrt{2(\lambda+s)}|d|}}{\sqrt{\lambda+s}} \frac{\sqrt{\lambda+s(1+\chi)} - \sqrt{\lambda+s}}{\sqrt{\lambda+s(1+\chi)} + \sqrt{\lambda+s}}. \quad (4.25)$$

This can be put into the same form as the known results by changing integration variables. The integral over s and λ have the form:

$$J = \int_0^\infty ds s^{a-1} \int_0^\infty d\lambda \lambda^{(D-1)/2-a} \frac{e^{-2\sqrt{2(\lambda+s)}|d|}}{\sqrt{\lambda+s}} \frac{\sqrt{\lambda+s(1+\chi)} - \sqrt{\lambda+s}}{\sqrt{\lambda+s(1+\chi)} + \sqrt{\lambda+s}}. \quad (4.26)$$

The integral can be transformed by changing variable from λ to $p := \sqrt{\lambda/s+1}$,

$$J = 2 \int_0^\infty ds s^{D/2-1} \int_1^\infty dp (p^2-1)^{(D-1)/2-a} e^{-\sqrt{8d^2}sp} \frac{\sqrt{p^2+\chi}-p}{\sqrt{p^2+\chi+p}}. \quad (4.27)$$

After changing variables from s to $t := \sqrt{8d^2}sp$, and swapping the t and p integrals, the result is

$$J = \frac{1}{2^{3D/2-2}d^D} \int_1^\infty dp p^{-D} (p^2-1)^{(D-1)/2-a} \frac{\sqrt{p^2+\chi}-p}{\sqrt{p^2+\chi+p}} \int_0^\infty dt t^{D-1} e^{-t}. \quad (4.28)$$

The t integral has the value $\Gamma[D]$. Substituting the transformed integral (4.28) back into the Casimir–Polder energy (4.25), while setting $D = 4$ and $a = 3/2$ yields

$$V_{\text{CP}}^{(\text{TE})} - V_{\text{CP}}^{(0)} = - \frac{3\hbar c \alpha_0}{32\epsilon_0 \pi^2 d^4} \int_1^\infty dp \frac{1}{2p^4} \frac{\sqrt{p^2+\chi}-p}{\sqrt{p^2+\chi+p}}. \quad (4.29)$$

The prefactor is the Casimir–Polder energy for an atom above a perfect conductor (1.16). This result agrees with the known result for the TE contribution

to the Casimir–Polder energy [see Eq. (14.210) in Section 14.3 of Steck (2015)]. An “efficiency” η_{TE} can be defined by the ratio of the Casimir–Polder energy for an atom and a dielectric to the Casimir–Polder energy between an atom and a perfect conductor. The integral over p is the TE contribution to the efficiency, η_{TE} , and can be evaluated in closed form:

$$\begin{aligned}\eta_{\text{TE}}(\chi) &= \frac{1}{2} \int_1^\infty dp p^{-4} \frac{p - \sqrt{p^2 + \chi}}{p + \sqrt{p^2 + \chi}} \\ &= \frac{1}{3} + \frac{2}{\chi} - \frac{\sqrt{\chi(\chi + 1)}}{\chi^{3/2}} - \frac{1}{4\chi^{3/2}} \log \left[2\chi + 2\sqrt{\chi(\chi + 1)} + 1 \right] - \frac{\text{arcsinh}(\sqrt{\chi})}{2\chi^{3/2}}.\end{aligned}\tag{4.30}$$

The efficiency η_{TE} smoothly interpolates between 0 and 1/6 as χ varies from 0 to ∞ . In the strong-coupling limit, the TE polarization provides 1/6 of the Casimir–Polder energy, and the remaining 5/6 is provided by the TM polarization.

4.4. Analytical TM Casimir–Polder Energy for an Atom and a Dielectric Plane

The calculation for the TM Casimir–Polder energy proceeds in a similar fashion to the TE case. The renormalized TM Casimir–Polder energy can be split into two pieces

$$V_{\text{CP}}^{(\text{TM})}(\mathbf{r}_A) - V_{\text{CP}}^{(0)} = \frac{\hbar c \alpha_0}{4\epsilon_0 (2\pi)^{D/2}} \left(\mathcal{V}_{D,3/2} - \frac{1}{2} \nabla^2 \mathcal{V}_{(D-2),1/2} \right),\tag{4.31}$$

where

$$\mathcal{V}_{\nu,a} := \int_0^\infty \frac{d\mathcal{T}}{\mathcal{T}^{1+\nu/2}} \left\langle \left\langle \frac{e^{-\langle V_{\text{TM}} \rangle \mathcal{T}}}{\langle \epsilon_r \rangle^a} - 1 \right\rangle \right\rangle_{\mathbf{x}(t), \mathbf{x}(0) = \mathbf{r}_A}.\tag{4.32}$$

Each term $\mathcal{V}_{\nu,a}$ can in turn be transformed using the combination of the Laplace–Mellin theorem and the inverse moment theorem:

$$\begin{aligned} \mathcal{V}_{\nu,a} := & \frac{\sqrt{\pi}}{\Gamma[a]\Gamma[(\nu+1)/2-a]} \int_0^\infty d\lambda \lambda^{(\nu-1)/2-a} \int_0^\infty ds s^{a-1} \\ & \times \int_0^\infty d\mathcal{T} \frac{e^{-(\lambda+s)\mathcal{T}}}{\sqrt{\mathcal{T}}} \left\langle\left\langle e^{-\int_0^\mathcal{T} dt [V_{\text{TM}}(\mathbf{x})+s\chi(\mathbf{x})]} - 1 \right\rangle\right\rangle_{\mathbf{x}(t),\mathbf{x}(0)=\mathbf{r}_A}. \end{aligned} \quad (4.33)$$

Note that the TM potential is already in the exponential, so the TM potential and Ξ does not need to be rescaled by s . The analytical result (3.56) can be substituted into Eq. (4.33), and the integral can be transformed in the same manner as in Section 4.3, with the result

$$\mathcal{V}_{\nu,a} = - \frac{\sqrt{\pi}\Gamma[\nu]}{2^{3\nu/2-2}d^\nu\Gamma[a]\Gamma[(\nu+1)/2-a]} \int_1^\infty dp \frac{1}{p^\nu} (p^2-1)^{(\nu-1)/2-a} \frac{pe^{2\Xi} - \sqrt{p^2+\chi}}{pe^{2\Xi} + \sqrt{p^2+\chi}}. \quad (4.34)$$

The two cases of interest are for $\nu=4, a=3/2$ and $\nu=2, a=1/2$:

$$\mathcal{V}_{4,3/2} = - \frac{3}{4d^4} \int_1^\infty dp \frac{1}{p^4} \frac{pe^{2\Xi} - \sqrt{p^2+\chi}}{pe^{2\Xi} + \sqrt{p^2+\chi}} \quad (4.35)$$

$$\mathcal{V}_{2,1/2} = - \frac{1}{2d^2} \int_1^\infty dp \frac{1}{p^2} \frac{pe^{2\Xi} - \sqrt{p^2+\chi}}{pe^{2\Xi} + \sqrt{p^2+\chi}}. \quad (4.36)$$

In Eq. (4.31), the derivatives with respect to the starting position \mathbf{r}_A are equivalent to derivatives with respect to the distance d . After substituting these expressions back into the atom-surface energy (4.31), the TM Casimir–Polder energy is given by

$$V_{\text{CP}}^{(\text{TM})}(\mathbf{r}_A) - V_{\text{CP}}^{(0)} = - \frac{3\hbar c\alpha_0}{32\pi^2\epsilon_0 d^4} \int_1^\infty dp \frac{1}{2p^4} (1-2p^2) \frac{p(1+\chi) - \sqrt{p^2+\chi}}{p(1+\chi) + \sqrt{p^2+\chi}}, \quad (4.37)$$

where we used $e^{2\Xi} = 1 + \chi$. This agrees with the Lifshitz results for the TM Casimir–Polder energy for an atom near a dielectric half-space [Eq. (14.205) in Steck (2015)].

The TM efficiency η_{TM} also has a closed-form expression,

$$\begin{aligned} \eta_{\text{TM}}(\chi) &:= \frac{1}{2} \int_1^\infty dp p^{-4} (1 - 2p^2) \frac{p(1 + \chi) - \sqrt{p^2 + \chi}}{p(1 + \chi) + \sqrt{p^2 + \chi}} \\ &= \frac{7}{6} + \chi + \frac{2 - (1 + \chi)^{3/2}}{2\chi} - \frac{\operatorname{arcsinh}\sqrt{\chi}}{2\chi^{3/2}} [1 + \chi + 2\chi^2(1 + \chi)] \\ &\quad + \frac{(1 + \chi)^2}{\sqrt{2 + \chi}} \left[\operatorname{arcsinh}\sqrt{1 + \chi} - \operatorname{arcsinh}\left(\frac{1}{\sqrt{1 + \chi}}\right) \right], \end{aligned} \quad (4.38)$$

which smoothly interpolates between 0 and $5/6$ as χ increases from 0 to ∞ . The TM polarization provides the majority of the Casimir–Polder energy for between an atom and a dielectric plane. From the worldline point of view, most of the TM energy comes from the term involving $-\partial_d^2 \mathcal{V}_{2,1/2}/2$, which suggest it is essential to correctly estimate the derivatives in a numerical procedure.

4.5. Analytical TE Casimir Energy between Two Dielectric Planes

The Casimir energy for two dielectric planes can also be calculated within this formalism. The dielectric function is given by

$$\epsilon_{r,12}(x) = 1 + \chi_1 \Theta(d_1 - x) + \chi_2 \Theta(x - d_2). \quad (4.39)$$

The calculation proceeds in the same way, except for two changes. First, the Casimir energy requires a further integral over the starting points of the paths. Second, the two-body interaction energy is found by subtracting the one-body energies involving $\epsilon_{r,1}$ and $\epsilon_{r,2}$ from the two-body expressions with $\epsilon_{r,12}$. This subtraction renormalizes the energy by considering the change in energy as the two dielectrics are moved from

arbitrarily far apart to a finite distance from one another. The fully renormalized Casimir energy between two planes is

$$E_{\text{TE}} - E^{(0)} = -\frac{\hbar c}{2(2\pi)^{D/2}} \int_0^\infty \frac{d\mathcal{T}}{\mathcal{T}^{1+D/2}} \int d\mathbf{x}_0 \left\langle\left\langle \left(\frac{1}{\sqrt{\langle\epsilon_{r,12}\rangle}} - \frac{1}{\sqrt{\epsilon_{r,12}(\mathbf{x}_0)}} \right) - \left(\frac{1}{\sqrt{\langle\epsilon_{r,1}\rangle}} - \frac{1}{\sqrt{\epsilon_{r,1}(\mathbf{x}_0)}} \right) - \left(\frac{1}{\sqrt{\langle\epsilon_{r,2}\rangle}} - \frac{1}{\sqrt{\epsilon_{r,2}(\mathbf{x}_0)}} \right) \right\rangle\right\rangle_{\mathbf{x}(t)}. \quad (4.40)$$

Each term is renormalized by subtracting off the constant value of the dielectric evaluated at the start of the paths. This is chosen to eliminate the $\mathcal{T} = 0$ divergence from each term individually. (In this case it is also possible to renormalize the energy by instead subtracting off the value of the surrounding medium, which is vacuum in this case.) Subtracting off the one-body energies then removes the divergences that occur at the interfaces at $x_0 = d_1$ and $x_0 = d_2$, where at small \mathcal{T} paths can enter a region of different dielectric constant, leading to a non-zero integrand.

The Casimir energy can be recast using the inverse moment Laplace–Mellin theorems as

$$E_{\text{TE}} - E^{(0)} = -\frac{\hbar c}{2(2\pi)^{D/2}} \int_0^\infty ds \frac{s^{a-1}}{\Gamma(a)} \int d\lambda \frac{\lambda^{(D-1)/2-a}}{\Gamma[(D+1)/2-a]} \times \int d\mathbf{x}_0 \left[(f_{12}^{(\text{TE})}(\mathbf{x}_0) - f_{12}^{(0)}) - (f_1^{(\text{TE})}(\mathbf{x}_0) - f_1^{(0)}) - (f_2^{(\text{TE})}(\mathbf{x}_0) - f_2^{(0)}) \right]. \quad (4.41)$$

The values for $a = 1/2$ and $D = 4$ will be used at the end of the computation. The solutions $f_i^{(\text{TE})}$ are the path integral solutions derived in Eqs. (3.25) and (3.31) for one and two dielectric steps respectively. These are renormalized by subtracting $f_i^{(0)}$, the solution for a constant dielectric filling space. The spatial integral can be carried out for each of the three regions: Region I where $x_0 < d_1$, Region II

where $d_1 < x_0 < d_2$, and Region III where $d_2 < x_0$. Fortunately, the solutions are simple exponentials in x_0 , making these integrals straightforward. This calculation is deferred to Appendix A, since simplifying the expressions is straightforward, but messy. The integrated, renormalized solution can be written as

$$\begin{aligned} & \int_{-\infty}^{\infty} dx_0 \left([f_{12}^{(\text{TE})}(x_0) - f_{12}^{(0)}] - [f_1^{(\text{TE})}(x_0) - f_1^{(0)}] - [f_2^{(\text{TE})}(x_0) - f_2^{(0)}] \right) \\ &= \frac{A\sqrt{\pi}r_1^{(\text{TE})}r_2^{(\text{TE})}e^{-2\sqrt{2(\lambda+s)d}}}{\sqrt{(\lambda+s)(1-r_1^{(\text{TE})}r_2^{(\text{TE})}e^{-2\sqrt{2(\lambda+s)d})}} \left(2d + \frac{\sqrt{2}}{\sqrt{\lambda+s(1+\chi_1)}} + \frac{\sqrt{2}}{\sqrt{\lambda+s(1+\chi_2)}} \right), \end{aligned} \quad (4.42)$$

where A is the (infinite) transverse area of the dielectric planes, and the reflection coefficients for each surface are

$$r_i^{(\text{TE})} = \frac{\sqrt{\lambda+s} - \sqrt{\lambda+s(1+\chi_i)}}{\sqrt{\lambda+s} + \sqrt{\lambda+s(1+\chi_i)}}. \quad (4.43)$$

In order to recover a finite quantity it is necessary to calculate the energy per unit area. The integrals can be transformed into Lifshitz form via similar transformations to those used previously. The integration variable λ is transformed to $p := \sqrt{\lambda/s + 1}$, with the result

$$\begin{aligned} \frac{E_{\text{TE}} - E^{(0)}}{A} &= -\frac{\hbar c}{(2\pi)^{D/2}} \sqrt{\pi} \int_0^\infty ds \frac{s^{(D-2)/2}}{\Gamma(a)} \int_1^\infty dp \frac{(p^2-1)^{(D-1)/2-a}}{\Gamma[(D+1)/2-a]} \\ &\quad \times \frac{r_1^{(\text{TE})}r_2^{(\text{TE})}e^{-2\sqrt{2}spd}}{(1-r_1^{(\text{TE})}r_2^{(\text{TE})}e^{-2\sqrt{2}spd})} \left(2d + \frac{\sqrt{2}}{\sqrt{s(p^2+\chi_1)}} + \frac{\sqrt{2}}{\sqrt{s(p^2+\chi_2)}} \right), \end{aligned} \quad (4.44)$$

where the reflection coefficients are now given by

$$r_i^{(\text{TE})} = \frac{p - \sqrt{p^2 + \chi_i}}{p + \sqrt{p^2 + \chi_i}}. \quad (4.45)$$

Next, the s integral is transformed s to $t = \sqrt{2s}$, then the t and p integrals are swapped, and finally the values of $a = 1/2$ and $D = 4$ are used. The result of those manipulations is

$$\begin{aligned} \frac{E_{\text{TE}} - E^{(0)}}{A} &= -\frac{\hbar c}{8\pi^2} \int_0^\infty dt t^3 \int_1^\infty dp (p^2 - 1) \\ &\times \frac{r_1^{(\text{TE})} r_2^{(\text{TE})} e^{-2tpd}}{(1 - r_1^{(\text{TE})} r_2^{(\text{TE})} e^{-2tpd})} \left(2d + \frac{2}{t\sqrt{p^2 + \chi_1}} + \frac{2}{t\sqrt{p^2 + \chi_2}} \right). \end{aligned} \quad (4.46)$$

Finally, the integral can be simplified by integrating by parts with respect to p . The following derivatives will be of use:

$$\frac{dr_i^{(\text{TE})}}{dp} = \frac{d p - \sqrt{p^2 + \chi_i}}{dp p + \sqrt{p^2 + \chi_i}} = \frac{-2r_i^{(\text{TE})}}{\sqrt{p^2 + \chi_i}} \quad (4.47)$$

$$\frac{d}{dp} \log[1 - r_1^{(\text{TE})} r_2^{(\text{TE})} e^{-2tpd}] = \frac{r_1^{(\text{TE})} r_2^{(\text{TE})} e^{-2tpd}}{1 - r_1^{(\text{TE})} r_2^{(\text{TE})} e^{-2tpd}} \left(2td + \frac{2}{\sqrt{p^2 + \chi_1}} + \frac{2}{\sqrt{p^2 + \chi_2}} \right). \quad (4.48)$$

The TE Casimir energy between two half-spaces is then

$$\begin{aligned} \frac{E_{\text{TE}} - E^{(0)}}{A} &= -\frac{\hbar c}{8\pi^2} \int_0^\infty dt t^3 \int_1^\infty dp (p^2 - 1) \frac{d}{dp} \left[\frac{1}{t} \log(1 - r_1^{(\text{TE})} r_2^{(\text{TE})} e^{-2tpd}) \right] \\ &= \frac{\hbar c}{4\pi^2} \int_0^\infty dt t^2 \int_1^\infty dp p \log(1 - r_1^{(\text{TE})} r_2^{(\text{TE})} e^{-2tpd}), \end{aligned} \quad (4.49)$$

since the boundary term from the integration by parts vanishes. This is exactly the TE component of the Lifshitz energy that was derived by more straightforward means in Section 1.1.2.1. In this derivation, the gap between the spaces was filled with vacuum ($\epsilon_3 = 1$). The TE Casimir energy per unit area can be written as

$$\frac{E_{\text{TE}} - E^{(0)}}{A} = -\frac{\hbar c \pi^2}{720d^3} \gamma_{\text{TE}}(\chi_1, \chi_2), \quad (4.50)$$

where the prefactor is the perfect conductor Casimir energy, and the efficiency γ_{TE} is

$$\gamma_{\text{TE}}(\chi_1, \chi_2) := -\frac{180}{\pi^4 d^3} \int_0^\infty dt t^2 \int_1^\infty dp \log[1 - r_1^{(\text{TE})} r_2^{(\text{TE})} e^{-2tpd}]. \quad (4.51)$$

The efficiency is the ratio of the TE Casimir energy between the dielectrics to the total Casimir energy between perfectly-conducting plates at the same distance. In this case, γ_{TE} increases monotonically between 0 and 1/2 as both χ_1 and χ_2 increase from 0 to ∞ . Note that both the TE and TM polarizations contribute equally to the Casimir energy in the strong-coupling limit.

4.6. Analytical TM Casimir Energy between Two Dielectric Planes

The TM Casimir energy calculation is carried out in a similar manner to the TE case. Despite the similarities between the two solutions, it is still necessary to check that this calculation also works, since the differences in the reflection coefficients may upset the cancellations that occurred. The renormalized two-body TM Casimir interaction energy is

$$\begin{aligned} E_{\text{TM}} - E^{(0)} = & -\frac{\hbar c}{2(2\pi)^{D/2}} \int_0^\infty \frac{d\mathcal{T}}{\mathcal{T}^{1+D/2}} \int d\mathbf{x}_0 \left\langle \left\langle \left(\frac{e^{-\mathcal{T}\langle V_{\text{TM}}^{(1)} + V_{\text{TM}}^{(2)} \rangle}}{\sqrt{\langle \epsilon_{\text{r},12} \rangle}} - \frac{1}{\sqrt{\epsilon_{\text{r},12}(\mathbf{x}_0)}} \right) \right. \right. \\ & \left. \left. - \left(\frac{e^{-\mathcal{T}\langle V_{\text{TM}}^{(1)} \rangle}}{\sqrt{\langle \epsilon_{\text{r},1} \rangle}} - \frac{1}{\sqrt{\epsilon_{\text{r},1}(\mathbf{x}_0)}} \right) - \left(\frac{e^{-\mathcal{T}\langle V_{\text{TM}}^{(2)} \rangle}}{\sqrt{\langle \epsilon_{\text{r},2} \rangle}} - \frac{1}{\sqrt{\epsilon_{\text{r},2}(\mathbf{x}_0)}} \right) \right\rangle \right\rangle_{\mathbf{x}(t)}. \end{aligned} \quad (4.52)$$

In addition to the two-body dielectric function $\epsilon_{\text{r},12}$, the path integral is augmented by the TM potentials at both surfaces $V_{\text{TM}}^{(1)}$ and $V_{\text{TM}}^{(2)}$. The TM potentials all vanish in the renormalization terms, which are evaluated for the case of a constant dielectric.

After the Laplace–Mellin and inverse moment transforms, the TM Casimir energy is

$$\begin{aligned}
E_{\text{TM}} - E^{(0)} &= -\frac{\hbar c}{2(2\pi)^{D/2}} \int_0^\infty ds \frac{s^{a-1}}{\Gamma(a)} \int_0^\infty d\lambda \frac{\lambda^{(D-1)/2-a}}{\Gamma[(D+1)/2-a]} \\
&\quad \times \int d\mathbf{x}_0 \left[(f_{12}^{(\text{TM})}(\mathbf{x}_0) - f_{12}^{(0)}) - (f_1^{(\text{TM})}(\mathbf{x}_0) - f_1^{(0)}) - (f_2^{(\text{TM})}(\mathbf{x}_0) - f_1^{(0)}) \right],
\end{aligned} \tag{4.53}$$

where the solutions f_i are the path integrals in Eqs. (3.56) and (3.60). The solutions must be rescaled using $\Xi_i \rightarrow \Xi_i$, $\lambda \rightarrow \lambda + s$, and $\chi_i \rightarrow s\chi_i$. Evaluating the energy requires integrating the solutions of \mathbf{x}_0 and combining the results. This algebra is again deferred to Appendix A. In this case, the integrated solution is

$$\begin{aligned}
&\int d\mathbf{x}_0 \left[(f_{12}^{(\text{TM})}(\mathbf{x}_0) - f_{12}^{(0)}) - (f_1^{(\text{TM})}(\mathbf{x}_0) - f_1^{(0)}) - (f_2^{(\text{TM})}(\mathbf{x}_0) - f_1^{(0)}) \right] \\
&= \frac{\sqrt{\pi} A r_1^{(\text{TM})} r_2^{(\text{TM})} e^{-2\sqrt{2(\lambda+s)}d}}{\sqrt{\lambda+s}(1 - r_1^{(\text{TM})} r_2^{(\text{TM})} e^{-2\sqrt{2(\lambda+s)}d})} \\
&\quad \times \left(2d - \sum_{i=1}^2 \frac{\sqrt{2} e^{2\Xi_i} s \chi_i}{\sqrt{\lambda+s}(1 + \chi_i)[(\lambda+s) e^{4\Xi_i} - \lambda - s(1 + \chi_i)]} \right),
\end{aligned} \tag{4.54}$$

where the integral over the transverse coordinates introduced the area A , and the reflection coefficients are given by,

$$r_i^{(\text{TM})} = \frac{e^{2\Xi_i} \sqrt{\lambda+s} - \sqrt{\lambda+s(1 + \chi_i)}}{e^{2\Xi_i} \sqrt{\lambda+s} + \sqrt{\lambda+s(1 + \chi_i)}}. \tag{4.55}$$

The same transformations as in Section 4.2 can be employed to find the TM Casimir energy. After changing integration variables from λ to $p := \sqrt{\lambda/s + 1}$, the result is

$$E_{\text{TM}} - E^{(0)} = -\frac{\hbar c A}{(2\pi)^{D/2}} \int_0^\infty ds \frac{s^{(D-2)/2}}{\Gamma(a)} \int_1^\infty dp \frac{(p^2 - 1)^{(D-1)/2-a}}{\Gamma[(D+1)/2-a]} \\ \times \frac{\sqrt{\pi} r_1^{(\text{TM})} r_2^{(\text{TM})} e^{-2\sqrt{2}spd}}{(1 - r_1^{(\text{TM})} r_2^{(\text{TM})} e^{-2\sqrt{2}spd})} \left(2d - \sum_{i=1}^2 \frac{\sqrt{2}e^{2\Xi_i} \chi_i}{\sqrt{s} \sqrt{p^2 + \chi_i} [p^2 e^{4\Xi_i} - p^2 - \chi_i]} \right), \quad (4.56)$$

where the reflection coefficients are now given by

$$r_i^{(\text{TM})} = \frac{e^{2\Xi_i} p - \sqrt{p^2 + \chi_i}}{e^{2\Xi_i} p + \sqrt{p^2 + \chi_i}}. \quad (4.57)$$

The s integral can be transformed using $t = \sqrt{2s}$, and the values for $a = 1/2$ and $D = 4$ can be used, with the result

$$E_{\text{TM}} - E^{(0)} = -\frac{\hbar c A}{4\pi^2} \int_0^\infty dt t^3 \int_1^\infty dp (p^2 - 1) \\ \times \frac{r_1^{(\text{TM})} r_2^{(\text{TM})} e^{-2tpd}}{(1 - r_1^{(\text{TM})} r_2^{(\text{TM})} e^{-2tpd})} \left[2d - \sum_{i=1}^2 \frac{2e^{2\Xi_i} \chi_i}{t \sqrt{p^2 + \chi_i} [p^2 e^{4\Xi_i} - p^2 - \chi_i]} \right]. \quad (4.58)$$

Once again, an integration by parts with respect to p will put the energy in standard form. The following derivatives will be required:

$$\frac{d}{dp} \log[1 - r_1^{(\text{TM})} r_2^{(\text{TM})} e^{-2ptd}] = \frac{r_1^{(\text{TM})} r_2^{(\text{TM})} e^{-2ptd}}{1 - r_1^{(\text{TM})} r_2^{(\text{TM})} e^{-2ptd}} \left(2td - \sum_{i=1}^2 \frac{d \log r_i^{(\text{TM})}}{dp} \right) \quad (4.59)$$

$$\frac{d}{dp} \log[r_i^{(\text{TM})}] = \frac{2\chi e^{2\Xi_i}}{\sqrt{p^2 + \chi_i} [e^{4\Xi_i} p^2 - (p^2 + \chi_i)]}. \quad (4.60)$$

After integrating by parts, the TM Casimir energy is

$$E_{\text{TM}} - E^{(0)} = \frac{\hbar c A}{4\pi^2} \int_0^\infty dt t^2 \int_1^\infty dp \log[1 - r_1^{(\text{TM})} r_2^{(\text{TM})} e^{-2tpd}]. \quad (4.61)$$

The TM Casimir energy per unit area can be written as

$$\frac{E_{\text{TM}} - E^{(0)}}{A} = -\frac{\pi^2 \hbar c}{720d^3} \gamma_{\text{TM}}(\chi_1, \chi_2), \quad (4.62)$$

where the prefactor is the perfect-conductor Casimir energy, and the efficiency γ_{TM} is

$$\gamma_{\text{TM}}(\chi_1, \chi_2) := -\frac{180d^3}{\pi^4} \int_0^\infty dt t^2 \int_1^\infty dp \log[1 - r_1^{(\text{TM})} r_2^{(\text{TM})} e^{-2tpd}]. \quad (4.63)$$

This result has the same form as the corresponding TE result (4.51), but with the TE reflection coefficients replaced by their TM counterparts. At the end of the computation the relation $e^{2\Xi_i} = (1 + \chi_i)$ can be used in the reflection coefficients. Similarly to the TE case, γ_{TM} increases monotonically between 0 and 1/2 as both χ_1 and χ_2 increase from 0 to ∞ . Despite the TE and TM polarizations having equal contributions to the Casimir energy in the strong-coupling limit, the TM is typically the larger of the two.

4.7. Nonzero Temperature and Dispersion

The preceding results were all derived for dispersion free media at zero temperature. These calculations can be extended to nonzero temperature and to account for dispersion, which is needed to describe the near-field and high temperature limiting cases. For systems in thermal equilibrium at nonzero temperature, the free energy \mathcal{F} is used instead of the mean energy E . The free energy for the TE and TM

polarizations (for non-magnetic media) is

$$\mathcal{F}^{(\text{TE})} = k_B T \sum_{n=0}^{\infty'} \int_0^{\infty} \frac{d\mathcal{T}}{\mathcal{T}(2\pi\mathcal{T})^{(D-1)/2}} \int d\mathbf{x}_0 \left\langle \left\langle e^{-s_n^2 \langle \epsilon_r(\mathbf{x}, is_n) \rangle \mathcal{T} / (2c^2)} \right\rangle \right\rangle_{\mathbf{x}(t)} \quad (4.64)$$

$$\mathcal{F}^{(\text{TM})} = k_B T \sum_{n=0}^{\infty'} \int_0^{\infty} \frac{d\mathcal{T}}{\mathcal{T}(2\pi\mathcal{T})^{(D-1)/2}} \int d\mathbf{x}_0 \left\langle \left\langle e^{-s_n^2 \langle \epsilon_r(\mathbf{x}, is_n) \rangle \mathcal{T} / (2c^2)} e^{-\mathcal{T} \langle V_{\text{TM}}(\mathbf{x}, is_n) \rangle} \right\rangle \right\rangle_{\mathbf{x}(t)}, \quad (4.65)$$

where we have suppressed renormalization terms. The Casimir–Polder energies can be derived by the same reasoning used in Section 4.1, extending the energies (4.14) and (4.15) to nonzero temperature. In this case, the results are

$$V_{\text{CP}}^{(\text{TE})} = k_B T \sum_{n=0}^{\infty'} \frac{\alpha(is_n)}{\epsilon_0} \int_0^{\infty} \frac{d\mathcal{T}}{(2\pi\mathcal{T})^{(D-1)/2}} \int d\mathbf{x}_0 \times \left\langle \left\langle \frac{s_n^2}{2c^2} e^{-s_n^2 \langle \epsilon_r(\mathbf{x}, is_n) \rangle \mathcal{T} / (2c^2)} \right\rangle \right\rangle_{\mathbf{x}(t), \mathbf{x}(0)=\mathbf{r}_A} \quad (4.66)$$

$$V_{\text{CP}}^{(\text{TM})} = k_B T \sum_{n=0}^{\infty'} \frac{\alpha(is_n)}{\epsilon_0} \int_0^{\infty} \frac{d\mathcal{T}}{(2\pi\mathcal{T})^{(D-1)/2}} \int d\mathbf{x}_0 \times \left\langle \left\langle \left(\frac{s_n^2}{2c^2} - \frac{1}{4} \nabla^2 \right) e^{-s_n^2 \langle \epsilon_r(\mathbf{x}, is_n) \rangle \mathcal{T} / (2c^2)} e^{-\mathcal{T} \langle V_{\text{TM}}(\mathbf{x}, is_n) \rangle} \right\rangle \right\rangle_{\mathbf{x}(t), \mathbf{x}(0)=\mathbf{r}_A}. \quad (4.67)$$

There are some noteworthy features of the finite-temperature worldline expression. First, all material functions are already in the exponent, so there is no need for the inverse moment theorem when using results from Chapter III to analytically evaluate the finite-temperature Casimir energy. In fact, at zero temperature the Matsubara sum is replaced by an integral, which corresponds to the Gamma function used in the inverse moment theorem.

Second, for the TE polarization the dielectric path average is proportional to s_n^2 . In contrast, the TM polarization also has the TM potential. The TM potential might depend on the frequency via $\epsilon_r(\mathbf{x}, is_n)$, but it is not multiplied by s_n . This

has important ramifications for the near-field and high temperature limits. In those limits, the Casimir effect is dominated by the TM polarization.

The high temperature limit touches on one of the arguments in the literature. There has been a dispute in the literature over the correct model for the frequency dependence of a realistic metal, and the correct contribution from the TE mode at zero frequency [a summary is given by Bordag *et al.* (2009, Chapter 14)]. This is particularly relevant for describing metals with effective dielectric functions. The Drude and plasma models of the dielectric function of a metal are given respectively by

$$\epsilon_r^{(\text{Drude})}(is) = 1 + \frac{\omega_p^2}{s(s + i\gamma)} \quad \epsilon_r^{(\text{plasma})}(is) = 1 + \frac{\omega_p^2}{s^2}, \quad (4.68)$$

where ω_p is the plasma frequency and γ is the dissipation rate of the metal. The Drude model diverges as s^{-1} at zero frequency, whereas the plasma model diverges as s^{-2} . The faster divergence of the plasma model would lead to a nonzero contribution from the TE polarization at zero frequency or high temperature. Early experiments were unable to distinguish between the two models, although recent measurements have claimed to eliminate the plasma model from consideration (Sushkov *et al.*, 2011b). We will assume that $\lim_{s \rightarrow 0} s^2 \epsilon_r(is) = 0$ in the remainder of this section.

At high temperature, $\beta \rightarrow 0$, so the spacing between the Matsubara frequencies $s_n = 2\pi n/(\hbar\beta)$ diverges. As a result, only the first term significantly contributes. In fact, the first mode is exponentially suppressed relative to the zero frequency mode. Since the TE energy contribution vanishes at zero frequency, the leading order term comes from the TM energy, with the result that

$$\lim_{\beta \rightarrow 0} (\mathcal{F}^{(\text{TM})} - \mathcal{F}^{(0)}) = \frac{k_B T}{4} \int_0^\infty \frac{d\mathcal{T}}{\mathcal{T}(2\pi\mathcal{T})^{(D-1)/2}} \int d\mathbf{x}_0 \langle\langle 1 - e^{-\mathcal{T}\langle V_{\text{TM}}(\mathbf{x}, 0) \rangle} \rangle\rangle. \quad (4.69)$$

Similar considerations apply to both the Casimir and Casimir–Polder energy. The TM polarization is similarly dominant at small distances at zero temperature. As noted at the end of Section 2.7, the zero-temperature, far-field limit can be recovered by replacing the Matsubara sum with a frequency integral. In a similar fashion, Eqs. (4.14) and (4.15) can be recovered from Eqs. (4.66) and (4.66).

In general, the dominant frequencies can be estimated from the worldline expression for the Casimir energy. Since the worldline path integral is an ensemble average is over Gaussian random walks, the relevant range of \mathcal{T} can estimated from the distances of the problem. The paths will typically intersect all the surfaces when $\mathcal{T} \sim d^2$, where d is the distance from the source point x_0 to the farthest surface. Secondly, the frequency sum is dominated by the exponential factors with the form $e^{-s_n^2 \mathcal{T}/2c^2}$, which contribute most when $\mathcal{T} s_n^2/c^2 \sim 1$. This suggests that frequencies $s_n \sim c/d$ will contribute most to the Casimir energy in general. However, this estimate may be superseded by the frequency responses of the atom or medium, as indicated by the polarizability $\alpha(is_n)$ and the susceptibility $\chi(is_n)$, which will dominate in certain limits.

4.7.1. Thermal TE Casimir–Polder Energy

We will limit our discussion for checking the high temperature and near-field limits to the Casimir–Polder case of an atom near a dielectric plane. The preceding calculations are straightforwardly extended to dispersion and finite temperature. The analytical solutions for the TE and TM path integrals for a single dielectric plane in Eqs. (3.25) and (3.56) can be substituted into the appropriate path integrals. After using the Laplace–Mellin theorem (4.18), the renormalized TE worldline path integral

is

$$\begin{aligned} & \int_0^\infty d\mathcal{T} \frac{1}{(2\pi\mathcal{T})^{(D-1)/2}} \langle\langle e^{-v\mathcal{T}} - e^{-v\mathcal{T}(\epsilon_r(is_n))} \rangle\rangle \\ &= \frac{1}{2\pi} \int_0^\infty d\lambda \frac{e^{-2\sqrt{2(\lambda+v)}|d|}}{\sqrt{2(\lambda+v)}} \frac{\sqrt{\lambda+v[1+\chi(is_n)]} - \sqrt{\lambda+v}}{\sqrt{\lambda+v[1+\chi(is_n)]} + \sqrt{\lambda+v}}. \end{aligned} \quad (4.70)$$

There are no extra λ terms from the Laplace–Mellin theorem since $\lambda^{(D-3)/2-1/2} = 1$ when $D = 4$. This result can be used in the TE Casimir free energy if v is transformed according to $v \rightarrow s_n^2/(2c^2)$. After changing integration variable to $p = \sqrt{1 + 2c^2\lambda/s_n^2}$, the free energy is

$$V_{\text{CP}}^{(\text{TE})} - V_0 = -k_{\text{B}}T \sum_n' \frac{s_n^3 \alpha(is_n)}{4\pi\epsilon_0 c^3} \int_1^\infty dp e^{-2s_n p|d|/c} \frac{\sqrt{p^2 + \chi(is_n)} - p}{\sqrt{p^2 + \chi(is_n)} + p}, \quad (4.71)$$

This is the general result accounting for finite temperature and dispersion for the TE polarization for an atom near a planar dielectric.

We will now show that the TE contribution is negligible in the near-field regime at zero temperature. In the near field regime, the separation between the atom and the wall is much smaller than the atom's dominant wavelength, $d \ll 2\pi c/\omega_{j_0}$. In the zero temperature limit, the free energy (4.71) becomes

$$V_{\text{CP}}^{(\text{TE})} - V_0 = -\frac{\hbar}{8\pi^2\epsilon_0 c^3} \int_0^\infty d\omega \omega^3 \alpha(i\omega) \int_1^\infty dp e^{-2\omega p|d|/c} \frac{\sqrt{p^2 + \chi(i\omega)} - p}{\sqrt{p^2 + \chi(i\omega)} + p}. \quad (4.72)$$

The presence of the atom's polarizability $\alpha(i\omega)$ means that frequencies around the atom's dominant transition frequency ω_{j_0} will dominate the frequency integral. In that case, since $p \sim c/(d\omega_{j_0})$, the dominant values of p are much greater than one.

The reflection coefficient can be approximated in this limit,

$$\frac{\sqrt{p^2 + \chi(i\omega)} - p}{\sqrt{p^2 + \chi(i\omega)} + p} \approx \frac{\chi(i\omega)}{4p^2}. \quad (4.73)$$

The p integral can be approximately evaluated as

$$\int_1^\infty dp \frac{1}{4p^2} e^{-2\omega p|d|/c} \approx \frac{1}{4}. \quad (4.74)$$

Substituting this into the energy (4.72), the result is

$$V_{\text{CP}}^{(\text{TE})} - V_0 = -\frac{\hbar}{32\pi^2\epsilon_0 c^3} \int_0^\infty d\omega \omega^3 \alpha(i\omega) \chi(i\omega) \quad (4.75)$$

$$= -\frac{\hbar}{32\pi^2\epsilon_0 d^3} \int_0^\infty d\omega \frac{\omega^3 d^3}{c^3} \alpha(i\omega) \chi(i\omega) \approx 0. \quad (4.76)$$

This is suppressed by $\mathcal{O}[(\omega d/c)^3]$ relative to the TM contributions and can be ignored.

4.7.2. Thermal TM Casimir-Polder Energy

The TM contribution to the Casimir–Polder free energy for an atom near a dielectric plane proceeds in the same manner as in the TE case. This time, the nonzero contribution comes from the presence of the TM potential, which is reflected in the presence of Ξ in the TM reflection coefficients. The relevant analytical expression (3.56) for the path integral can be substituted in, and the Laplace–Mellin transform can be used to write

$$V_{\text{CP}}^{(\text{TM})} - V_0 = -k_B T \sum_n' \frac{s_n \alpha(is_n)}{4\pi\epsilon_0 c} \left(\frac{s_n^2}{c^2} - \frac{1}{2} \partial_d^2 \right) \int_1^\infty dp e^{-2ps_n d/c} \frac{\sqrt{p^2 + \chi} - pe^{2\Xi}}{\sqrt{p^2 + \chi} + pe^{2\Xi}}. \quad (4.77)$$

In this geometry the derivatives with respect to the atom's starting position can be evaluated as derivatives with respect to the surface's distance. After taking the derivatives with respect to distance, the free energy is

$$V_{\text{CP}}^{(\text{TM})} - V_0 = -k_B T \sum_n' \frac{s_n^3 \alpha(is_n)}{4\pi\epsilon_0 c^3} \int_1^\infty dp (1 - 2p^2) e^{-2ps_n d/c} \frac{\sqrt{p^2 + \chi(is_n)} - pe^{2\Xi(is_n)}}{\sqrt{p^2 + \chi(is_n)} + pe^{2\Xi(is_n)}}. \quad (4.78)$$

This expression can then be evaluated approximately in the near-field and high-temperature limits.

4.7.2.1. The Zero Temperature, Near-Field Limit

Let us consider the zero-temperature, near-field limit, in which case the TM Casimir–Polder energy is

$$V_{\text{CP}}^{(\text{TM})} - V_0 = -\frac{\hbar}{8\pi^2\epsilon_0 c^3} \int_0^\infty d\omega \omega^3 \alpha(i\omega) \int_1^\infty dp (1 - 2p^2) e^{-2p\omega d/c} \frac{\sqrt{p^2 + \chi} - pe^{2\Xi}}{\sqrt{p^2 + \chi} + pe^{2\Xi}}. \quad (4.79)$$

Once again, the atom's polarizability dominates the frequency integral, so the dominant frequencies occur for $\omega < \omega_{j0}$. In the near-field limit, the distances are much smaller than these wavelengths, so $\omega d/c \ll 1$. Since the p integral is dominated by the exponential, the relevant p are large. In this limit, the reflection coefficient becomes

$$\frac{\sqrt{p^2 + \chi} - pe^{2\Xi}}{\sqrt{p^2 + \chi} + pe^{2\Xi}} \approx -\frac{\epsilon_r(i\omega) - 1}{\epsilon_r(i\omega) + 1}, \quad (4.80)$$

where we used $\Xi = \log \sqrt{\epsilon_r}$. After substituting this in, and evaluating the p integral, the energy becomes

$$V_{\text{CP}}^{(\text{TM})} - V_0 \approx \frac{\hbar}{8\pi^2\epsilon_0 c^3} \int_0^\infty d\omega \omega^3 \alpha(i\omega) \frac{\epsilon_r(i\omega) - 1}{\epsilon_r(i\omega) + 1} \int_1^\infty dp (1 - 2p^2) e^{-2p\omega d/c} \quad (4.81)$$

$$= \frac{\hbar}{8\pi^2\epsilon_0 c^3} \int_0^\infty d\omega \omega^3 \alpha(i\omega) \frac{\epsilon_r(i\omega) - 1}{\epsilon_r(i\omega) + 1} \left(-\frac{c^3 e^{-2\omega d/c} (1 + \omega d/c)^2}{2d^3 \omega^3} \right) \quad (4.82)$$

$$\approx -\frac{\hbar}{16\pi^2\epsilon_0 d^3} \int_0^\infty d\omega \alpha(i\omega) \frac{\epsilon_r(i\omega) - 1}{\epsilon_r(i\omega) + 1}, \quad (4.83)$$

which is the well known result for the van der Waals energy for an atom near a dielectric wall [see Eq. (14.199) of Steck (2015)].

4.7.2.2. The High Temperature, Far Field Limit

In the high-temperature limit, only the zero-frequency term contributes, so the TM Casimir–Polder energy is

$$V_{\text{CP}}^{(\text{TM})} - V_0 = -\frac{1}{2} k_B T \frac{\alpha(0)}{\epsilon_0} \int_0^\infty d\mathcal{T} \frac{1}{(2\pi\mathcal{T})^{3/2}} \left\langle \left\langle \frac{1}{2} \partial_x^2 e^{-\mathcal{T}\langle V_{\text{TM}} \rangle} \right\rangle \right\rangle_{\mathbf{x}(t)}. \quad (4.84)$$

In this case the solution can be directly integrated, without the need for Laplace transforms. After substituting in the analytical solution (3.52), and differentiating, the TM Casimir–Polder energy becomes

$$V_{\text{CP}}^{(\text{TM})} - V_0 = -\frac{k_B T \alpha_0}{16\pi\epsilon_0} \frac{\epsilon_r(0) - 1}{\epsilon_r(0) + 1} \int_0^\infty d\mathcal{T} \partial_d^2 \frac{1}{\sqrt{2\pi\mathcal{T}^{3/2}}} e^{-2d^2/\mathcal{T}} \quad (4.85)$$

$$= -\frac{k_B T \alpha_0}{16\pi\epsilon_0 d^3} \frac{\epsilon_r(0) - 1}{\epsilon_r(0) + 1}. \quad (4.86)$$

This is the expected high temperature result for an atom and a dielectric wall [see Eq. (14.324) of Steck (2015)]. Although we have not examined the equivalent Casimir

expressions, they could be readily evaluated. As noted in Eq. (4.69), it is expected that the dominant contribution comes from the TM polarization, due to the TM potential. Since the TM potential also provides the majority of the Casimir energy in these limiting cases and the majority of the Casimir–Polder energy, it is essential to correctly account for it in a numerical method. Having shown that the worldline expressions reproduce previously known analytical results, we now turn to developing numerical methods for the worldline path integrals.

CHAPTER V
ELECTROMAGNETIC WORLDLINES: NUMERICAL METHODS AND
RESULTS

The goal of this project is to build a general numerical method for computing Casimir energies. As a first step, it is necessary to test the proposed methods in well understood cases, such as planar media. We have developed numerical methods that should allow efficient computations in the general case, despite emphasizing planar media in these calculations. In a general geometry, these methods could still be applied to describe scalar fields coupled to a dielectric, and could be used in an uncontrolled approximation to the full EM field.

Even in a planar geometry a number of tools are required to make the electromagnetic worldline methods tractable. The TM polarization is particularly challenging, and has prompted most of these developments. The same developments have been used to enhance the TE polarization methods, and could be applied to improve existing Dirichlet worldline methods.

The basic approach of the worldline method relies on Monte Carlo calculation of the worldline path integral. The numerical methods for the TE polarization are presented in Section 5.1. Section 5.1.1.1 discusses the “v-loop” method for constructing paths, and Sections 5.1.2.1 and 5.1.2.2 introduce the methods for Monte Carlo sampling for the path time \mathcal{T} , and the path starting points \mathbf{x}_0 , respectively. Then Section 5.1.2.3 discusses some approaches to computing the path-averaged dielectric constant $\langle\epsilon_r\rangle$, which is needed in the TE worldline integrand. Section 5.1.3 then presents the numerical results for the TE path integral, and briefly studies the systematic error in the method.

The numerics for the TM polarization are more complicated than in the TE case, since there is an additional potential V_{TM} , given by Eq. (3.32). Section 5.2 presents our strategy for computing the accumulated potential $\exp\{-\int_0^{\mathcal{T}} dt V_{\text{TM}}[\mathbf{x}(t)]\}$ along the entire path. The total contribution from the TM potential by using Eq. (3.52) to calculate the potential for a single step from x_k to x_{k+1} , and multiplying all of those contributions along the entire path. Unfortunately, as shown in Section 5.2.1, the simplest numerical estimates of the TM Casimir energy have a large variance which grows as the path resolution N is increased. The growth of the variance is reduced by introducing two different methods for constructing the paths. The first is the “TM-Gaussian” approach is covered in Section 5.2.1.1 which includes the TM potential in constructing the path increments. However, while this method has better convergence, it still shows the problem of growing statistical errors. Section 5.2.1.2 develops the “birth-death” method, where paths branch, or are truncated based on the accumulated potential along the path thus far. This effectively changes the path creation to sample more from important regions of the integral. The birth-death method reduces the statistical errors to manageable levels for both Gaussian and TM-Gaussian methods for constructing the paths. In addition, the TM Casimir–Polder energy involves spatial derivatives of the worldline path integral. Section 5.2.3.3, introduces a “partial averaging” method for evaluating the derivatives that bypasses some of the errors in even simpler approaches. Altogether, these methods reproduce the TM Casimir–Polder energy, and partially reproduce the TM Casimir energy, as shown by the numerical results presented in Section 5.2.4.

The numerical tests rely on comparing the numerically computed efficiency to the known analytical value. The worldline method tends to straightforwardly reproduce the expected distance dependence due to the integration over \mathcal{T} , as was briefly

discussed in Section 1.5.2. That is still true within the context of electromagnetic worldlines. All of the calculations are carried out for non-dispersive media at zero temperature. In Section 5.3, we will suggest how to generalize the calculations to include dispersion and nonzero temperature.

[The numerical results on the TE Casimir energies were published as Mackrory *et al.* (2016). A manuscript discussing the derivative estimation methods presented here and in the next chapter is in preparation, and the TM results and methods will also be published.]

5.1. TE Casimir Numerics

In this section we will discuss numerically calculating the TE Casimir and Casimir–Polder energies from the worldline expressions in Eqs. (4.40) and (4.14). We will first discuss generating the paths, sampling starting positions \mathbf{x}_0 and path times \mathcal{T} , and evaluating the dielectric path average $\langle \epsilon_{\mathcal{T}} \rangle$.

5.1.1. Path Generation

The principal element of the worldline method is evaluating a potential along an ensemble of Gaussian paths. This allows the N -dimensional integral over positions to be efficiently evaluated in a Monte Carlo fashion by generating an ensemble of Brownian bridges. It is of primary importance to be able to efficiently generate these Gaussian sample paths.

5.1.1.1. Open Brownian Bridges: v-loop Construction

Since the numerical methods will require open and closed Brownian bridges of fixed length N , we will derive the “v-loop” algorithm for generating open paths (Gies

et al., 2003). For open paths the starting and end points x_0 and x_N differ, while for closed paths $x_N = x_0$. The Gaussian density of N steps in one dimension, where the end points x_0 and x_N are fixed is:

$$P(x_1, \dots, x_{N-1}) = (2\pi\Delta\mathcal{T})^{-N/2} \exp \left[- \sum_{j=0}^{N-1} \frac{(x_{j+1} - x_j)^2}{2\Delta\mathcal{T}} \right]. \quad (5.1)$$

It is convenient to define shifted, normalized variables $y_k = (x_k - x_0)/\sqrt{\Delta\mathcal{T}}$. The exponent for the product of coupled Gaussians then involves the sum

$$\frac{y_1^2}{2} + \frac{(y_2 - y_1)^2}{2} + \dots + \frac{(y_{N-1} - y_{N-2})^2}{2} + \frac{(\Delta y - y_{N-1})^2}{2}, \quad (5.2)$$

where $\Delta y := (x_N - x_0)/\sqrt{\Delta\mathcal{T}}$. The exponent (5.2) can be decoupled by completing the square repeatedly, starting at y_{N-1} . The two terms of the sum involving y_{N-1} can be rewritten as

$$\begin{aligned} & \frac{(y_{N-1} - \Delta y)^2}{2\sigma_{N-1}^2} + \frac{(y_{N-1} - y_{N-2})^2}{2} \\ &= \frac{\sigma_{N-1}^2 + 1}{2\sigma_{N-1}^2} \left(y_{N-1} - \frac{\sigma_{N-1}^2 y_{N-2} + \Delta y}{\sigma_{N-1}^2 + 1} \right)^2 + \frac{(y_{N-2} - \Delta y)^2}{2(\sigma_{N-1}^2 + 1)}, \end{aligned} \quad (5.3)$$

where $\sigma_{N-1}^2 := 1$, $\sigma_{N-2}^2 := \sigma_{N-1}^2 + 1$. After each completion of the square, the variance changes according to $\sigma_{N-j}^2 \rightarrow \sigma_{N-j-1}^2 + 1 = j + 1$. With each completion of the square, the algebra takes on the same form as Eq. (5.3), with the label indices decreased by one. Once the process has been repeated $N - 1$ times the exponent becomes

$$\frac{\Delta x^2}{2N} + \sum_{j=1}^{N-1} \frac{z_j^2}{2}, \quad (5.4)$$

where

$$z_j := \frac{1}{c_j} \left(y_j - c_j y_{j-1} - \frac{\Delta x}{N-j+1} \right)^2, \quad (5.5)$$

and

$$c_j = \frac{N-j}{N-j+1}. \quad (5.6)$$

The probability distribution (5.1) is then

$$P(z_1, \dots, z_{N-1}) = \frac{1}{\sqrt{2\pi\mathcal{T}}} e^{-(x_0-x_N)^2/(2\mathcal{T})} \prod_{k=1}^{N-1} \frac{e^{-z_k^2/2}}{\sqrt{2\pi}}, \quad (5.7)$$

which accounts for the Jacobian determinant $\prod_j \sqrt{c_j} = N^{-1/2}$ from changing variables. The z_j are independent, standard normal variables. Once the z_j have been sampled, Eq. (5.5) can be inverted to find the coordinates:

$$x_k = x_0 + \frac{x_N - x_0}{N - k + 1} + c_k x_{k-1} + \sqrt{c_k \Delta \mathcal{T}} z_k. \quad (5.8)$$

This recursion formula shows how to construct a discrete representation for a Brownian bridge from $x_0 \rightarrow x_N$ in time \mathcal{T} . An integral involving the probability density (5.1), and another function of the path Φ , could be rewritten as

$$I = \int \prod_{j=1}^{N-1} dx_j P(x_1, \dots, x_{N-1}) \Phi(x_1, \dots, x_N) = \frac{e^{-(x_0-x_N)^2/2\mathcal{T}}}{\sqrt{2\pi\mathcal{T}}} \langle\langle \Phi \rangle\rangle_{x(t)}, \quad (5.9)$$

where the ensemble average is taken over open Brownian bridges between x_0 and x_N . The limit of closed paths can be taken by setting $x_N - x_0 = 0$. The v-loop construction is also straightforwardly generalized to multi-dimensional Brownian bridges. This recursion procedure (5.8) also allows the generation of a unit loop for $\mathcal{T} = 1$, which can then be integrated over multiple starting points x_0 and total path times \mathcal{T} . A

closed unit Brownian bridge can be constructed via

$$B_k = c_k B_{k-1} + \sqrt{\frac{c_k}{N}} z_k, \quad k = 1, \dots, N-1, \quad (5.10)$$

where $B_0 = 0$. A shifted, scaled Brownian bridge can then be constructed as

$$x_k = x_0 + \sqrt{\mathcal{T}} B_k, \quad (5.11)$$

where x_0 is the shifted starting position of the path, and \mathcal{T} is the path time.

The v-loop constructed here has an advantage over other methods of generating Brownian bridges, since it only needs to keep track of the current position x_k and index k to develop a Brownian bridge. Other methods such as pro-rated Brownian motion (1.63) or “d-loops” [which starts with a coarse path, and then refines the path by doubling the number of points (Gies *et al.*, 2005)] require knowledge of the whole Brownian motion.

The original v-loop algorithm used centered paths, where the average position $\langle x \rangle$ is subtracted from the path (Gies *et al.*, 2003). This requires first constructing the Brownian bridge, and then subtracting off the mean position. This is inconvenient if the path is being generated on the fly without storage, or if there are stochastic elements to path construction. In Casimir–Polder applications [or when computing the stress-energy tensor Schäfer *et al.* (2016)], it is preferable to consider paths emanating from a single point \mathbf{x}_0 . The starting point corresponds to the atom’s location, or the point where the stress-energy tensor is being computed.

5.1.2. Monte Carlo Sampling

To evaluate the Casimir energy it is necessary to take an ensemble average over many path realizations, at all starting positions \mathbf{x}_0 and path times \mathcal{T} . The original computations by Gies *et al.* (2003) emphasized computing the \mathcal{T} and \mathbf{x}_0 integrals for each path. For Dirichlet worldlines, the path integrand is either zero or one based on whether the path intersects all of the bodies. This makes evaluating these integrals a tractable problem, since it only requires finding the set of times $\{\mathcal{T}_k\}$ when paths enter the body, and evaluating $\int d\mathcal{T} \mathcal{T}^{-(1+D/2)}$ during those times the integral is nonzero. For example, in their paper computing forces in a sphere-plane geometry, Weber and Gies (2010b) found analytical expressions in terms of \mathbf{x}_0 and \mathcal{T} for when each random path will intersect both bodies. The remaining integrals over \mathbf{x}_0 and \mathcal{T} were then evaluated on a path-wise basis.

However, for the dielectric integrands of the TE and TM path integrals, the integrand varies based on the number of points that are inside the surface. For a path of length N , this direct method would become impractical for large N , as a large computational effort must be expended on even a single path.

Since the N -fold integral over positions is being handled in a Monte Carlo fashion, it makes sense to treat the remaining integrals over the starting position \mathbf{x}_0 and path times \mathcal{T} in the same manner. Each path can be evaluated for a single pair of $\mathbf{x}_0, \mathcal{T}$ picked from suitable distributions. This is a form of importance sampling, which is a powerful tool for accelerating Monte Carlo numerical computations (Asmussen and Glynn, 2007; Glasserman, 2004). This style of importance sampling goes beyond just using the Gaussian probability density to evaluate the spatial integrals over the intermediate positions \mathbf{x}_k . In this case, the importance sampling relies on estimating which positions and times are likely to contribute the most to the integral. This

Monte Carlo sampling of x_0 and \mathcal{T} extends the number of independent paths that can be averaged in a given time, since effort is not wasted on multiple computations on a single path.

5.1.2.1. Sampling Path-Times from a Power Law

The simplest method of sampling path times is to exploit the $\mathcal{T}^{-(1+D/2)}$ factor in the integral. For a particular path, the renormalized TE integrand is only non-zero after the path touches all of the bodies, which occurs at some path time \mathcal{T}_0 .¹ For $\mathcal{T} > \mathcal{T}_0$, the extent of the path grows as $\sqrt{\mathcal{T}}$, so the magnitude of the integrand ($\langle \epsilon_r \rangle^{-a} - 1$) increases as more points enter the bodies. However, the $\mathcal{T}^{-(1+D/2)}$ factor reduces the contributions from large \mathcal{T} . These facts suggest sampling \mathcal{T} from a probability distribution

$$P(\mathcal{T}; \mathcal{T}_0, m) = \frac{(m-1)\mathcal{T}_0^{m-1}}{\mathcal{T}^m} \Theta(\mathcal{T} - \mathcal{T}_0), \quad (5.12)$$

where $m > 1$ and $\mathcal{T}_0 > 0$. Sampling from this distribution requires being able to estimate the value of \mathcal{T}_0 for each path. The path time \mathcal{T}_0 is the minimum value of \mathcal{T} such that the path will touch the relevant bodies, as required to contribute to the renormalized energy. In computing Casimir interaction energies, the path must touch *all* of the bodies, while in Casimir–Polder calculations, the path must touch *any* of the bodies (other than the atom) to contribute. For the example of paths starting

¹For a Brownian motion $\mathbf{x}(t)$, the term “first-touching time” is reserved for the first time t_0 along a path that a Brownian bridge intersects a surface: $\mathbf{x}(t_0) = d$. This is distinct from the first path time \mathcal{T} when the scaled path intersects a surface.

between parallel planes,

$$\mathcal{T}_0 = \min \left[\left(\frac{d_1 - x_0}{B_-} \right)^2, \left(\frac{d_2 - x_0}{B_+} \right)^2 \right] \quad (5.13)$$

where $d_1 < x_0 < d_2$, and B_{\pm} are the maximum and minimum points of the unit Brownian path.

Samples from the distribution (5.12) can be generated by inverting the cumulative probability distribution. [Inversion is a general purpose method of generating random deviates from a given distribution (Press *et al.*, 1990, Section 7.2).] In this case, the inversion requires solving

$$u = (m - 1) \mathcal{T}_0^{m-1} \int_{\mathcal{T}_0}^{\mathcal{T}} dt t^{-m}, \quad (5.14)$$

where $u \in [0, 1)$ is a uniform random number and \mathcal{T} is the desired deviate. Eq. (5.14) can be easily solved, with the result that

$$\mathcal{T} = \frac{\mathcal{T}_0}{(1 - u)^{1/(m-1)}}. \quad (5.15)$$

The lower-bound \mathcal{T}_0 can be easily found in simple geometries on a path-wise basis. Random deviates \mathcal{T} can then be generated for each path, and each path is then guaranteed to contribute.

5.1.2.2. Sampling Starting Positions

The integral over the starting point x_0 can also be evaluated in Monte Carlo fashion by exploiting some knowledge about the form of the integrand. For points far from all bodies, which are clustered around the origin, the expected minimum path

time when the integrand is nonzero is $\mathcal{T}_0 \sim x_0^2$. In that case, and approximating the integrand $(\langle \epsilon_r \rangle^{-a} - 1)$ by its strong-coupling limit, the path time integral is bounded by

$$\int_{\mathcal{T}_0}^{\infty} \frac{d\mathcal{T}}{\mathcal{T}^{1+D/2}} \sim \frac{1}{x_0^D} \quad (5.16)$$

This suggests that the contribution from points far from the bodies scales as x_0^{-D} . Between the bodies, the contribution from each starting position is roughly equal, since each path must have sufficient extent to touch all bodies. This occurs for times $\mathcal{T} \sim d_0^2$, where d_0 is the separation between bodies. In a one-dimensional geometry, embedded in a four-dimensional space-time, these considerations suggest sampling from

$$P_x(x; d_0) := \frac{3}{8d_0} \begin{cases} 1 & |x| < d_0 \\ \frac{d_0^4}{|x|^4} & |x| > d_0. \end{cases} \quad (5.17)$$

This reasoning can be easily extended to higher-dimensional problems, where a sphere of radius d_0 should bound all of the interfaces between the bodies. Outside of that sphere, the sampling would again fall off as $|x_0|^{-D}$. While it may be possible to develop sampling procedures better suited to a particular geometry, this method provides a general purpose way of sampling x_0 .

5.1.2.3. Evaluating the Dielectric Path Average

Once a path is constructed, the rest of the path integrand can be computed along that path. For example, the path average of the dielectric can be evaluated as

$$\langle \epsilon_r \rangle = \frac{1}{N} \sum_{k=1}^N \epsilon_r(x_k). \quad (5.18)$$

This corresponds to the trapezoidal rule for evaluating the path average,

$$\langle \epsilon_r \rangle = \frac{1}{\mathcal{T}} \sum_{k=0}^{N-1} \int_{k\Delta\mathcal{T}}^{(k+1)\Delta\mathcal{T}} dt' \epsilon_r[x(t')] \approx \frac{\Delta\mathcal{T}}{N} \sum_{k=0}^{N-1} \frac{\epsilon_r(x_k) + \epsilon_r(x_{k+1})}{2} = \frac{1}{N} \sum_{k=1}^N \epsilon_r(x_k), \quad (5.19)$$

where the trapezoidal rule $\int_a^b dx f(x) = (b-a)[f(a) + f(b)]/2$ was used for each time integral. As discussed in Mackrory *et al.* (2016, Section 5.C.3), the trapezoidal rule outperforms some “improved” methods. One alternative is to approximate the contribution from each path increment for a dielectric step as

$$\frac{1}{\mathcal{T}} \int_{k\Delta\mathcal{T}}^{(k+1)\Delta\mathcal{T}} dt \Theta[x(t) - d] \approx \frac{1}{N(x_{k+1} - x_k)} \int_{x_k}^{x_{k+1}} dx \Theta[x - d]. \quad (5.20)$$

Then in cases where the path straddles a surface with points $x_k < d$ and $x_{k+1} > d$, the contribution from that step would be $(x_{k+1} - d)/(x_{k+1} - x_k)$. This reduces the contribution from path increments where one point just enters the surface. Unfortunately, this does not correct an opposing error from paths that come close to the surface but do not enter the surface, where $x_k, x_{k+1} < d$ but $|d - x_k| \ll \sqrt{\Delta\mathcal{T}}$. There is some finite probability that a sub-path between x_k and x_{k+1} would have entered the body, and given a greater contribution to the integrand. Since the reduction of the contribution to the path average is not offset, this method fares worse than the straightforward trapezoidal method.

5.1.3. Results: TE Casimir and Casimir–Polder Energies for Planar Geometries

Figure 5.1 shows the numerical results for evaluating the TE Casimir–Polder path integral (4.14) at over a wide range of χ . The atom is located at the origin in the

vacuum, with a dielectric half-space a distance d away with a constant susceptibility χ . The TE Casimir–Polder energy is calculated numerically by evaluating

$$V_{\text{CP}}^{(\text{TE})} - V_0 = \frac{\hbar c \alpha_0}{8\pi^2} \left\langle\left\langle \frac{1}{2\mathcal{T}_0^2} \left(\frac{1}{\langle \epsilon_r(x) \rangle^{1/2}} - 1 \right) \right\rangle\right\rangle_{x_k, \mathcal{T}}, \quad (5.21)$$

where $\langle\langle \dots \rangle\rangle_{x_k, \mathcal{T}}$ denotes an ensemble average over path times \mathcal{T} , and one-dimensional discrete Brownian bridges. The Brownian bridges are constructed using the v-loop algorithm (5.10). The minimum path time \mathcal{T}_0 is determined on a path-wise basis by the condition $\sqrt{\mathcal{T}_0} \max(B_k) = d$. The path time is sampled for each path from Eq. (5.12), with $m = 1 + D/2 = 3$. The unit path is then scaled, $x_k = \sqrt{\mathcal{T}} B_k$, and the trapezoidal method is used to evaluate $\langle \epsilon_r \rangle$ around each path. The sojourn time $\langle \Theta(x - d) \rangle$ can be estimated once per path, and then the integrand can be computed using $\langle \epsilon_r \rangle = 1 + \chi \langle \Theta(x - d) \rangle$. The same path and sojourn times can be reused to compute the contribution for multiple values of χ at once. The results are then accumulated over many paths and path times. The numerically calculated efficiency $\eta(\chi)$ is found by dividing the numerical results by the perfect-conductor result (1.1), which cancels out the leading constants and the d^{-4} distance dependence.

Figure 5.2 shows the numerically computed Casimir energy between two planar dielectric interfaces a distance d apart, separated by vacuum, with dielectric function $\epsilon_r(x) = 1 + \chi \Theta(-x + d/2) + \chi \Theta(x - d/2)$. This is computed numerically by evaluating

$$E^{(\text{TE})} - E_0 = -\frac{\hbar c \alpha_0}{8\pi^2} \left\langle\left\langle \frac{1}{2\mathcal{T}_0^2 P_x(x_0)} \left(1 + \frac{1}{\langle \epsilon_{r,12}(x) \rangle^{1/2}} - \frac{1}{\langle \epsilon_{r,1}(x) \rangle^{1/2}} - \frac{1}{\langle \epsilon_{r,2}(x) \rangle^{1/2}} \right) \right\rangle\right\rangle_{x_k, \mathcal{T}, x_0}, \quad (5.22)$$

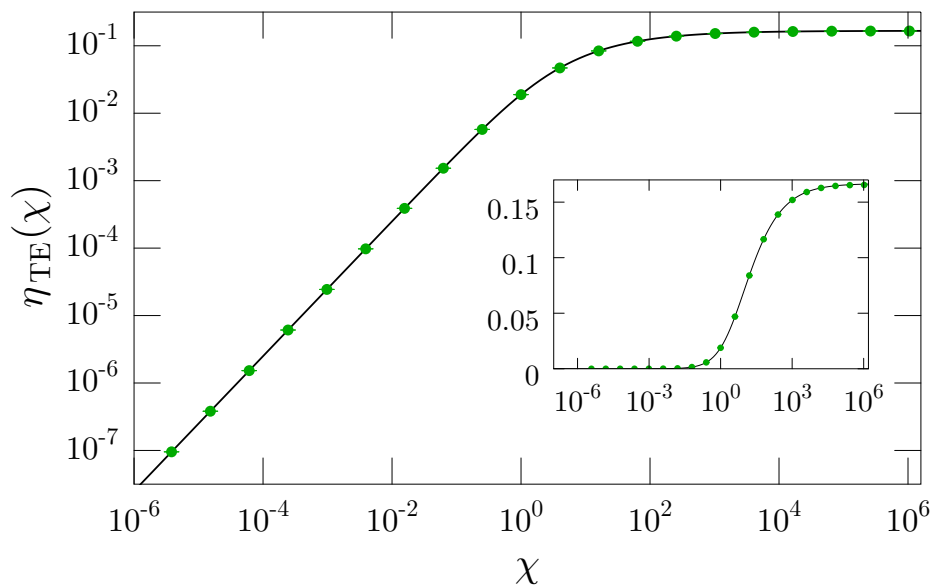


FIGURE 5.1. Planar Casimir–Polder TE energy normalized to atom-conductor Casimir–Polder energy, plotted as a function of susceptibility χ . The calculations used 10^8 paths, with 10^4 points per path. The results for each χ were computed using the same ensemble of paths. The solid black line is the analytical result (4.30), and the points are the numerical values computed using Eq. (5.21). (The inset shows same data on a linear vertical scale.)

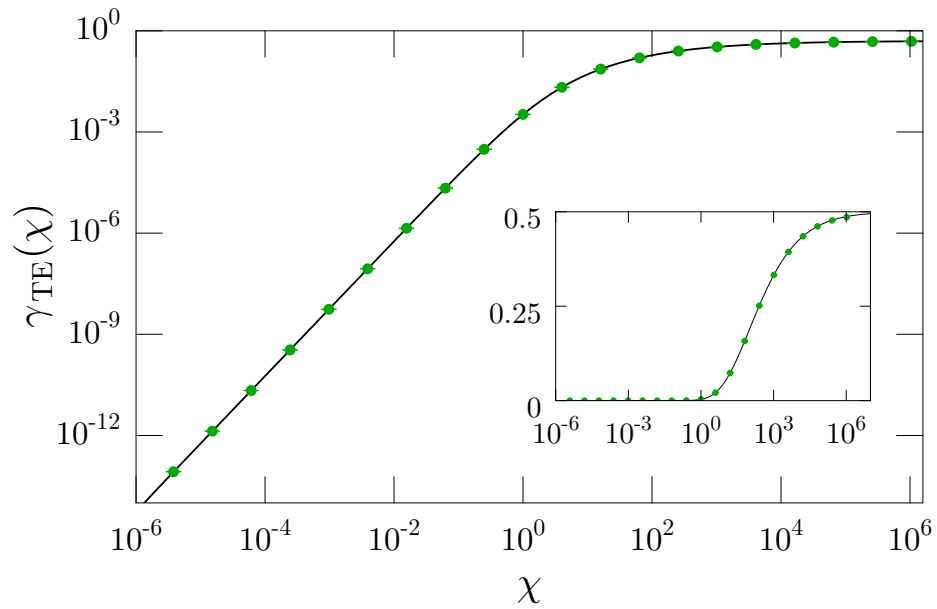


FIGURE 5.2. Numerically calculated TE Casimir energy for two planes, normalized to Casimir energy between perfect-conducting plates, plotted as function of χ . The black line shows the integral solution (4.51), and the points show the numerical estimates computed using Eq. (5.22). The calculations used 10^8 paths, with 10^4 points per path. All values of χ were computed using the same ensemble of paths. (Inset shows same data on a linear vertical scale.)

where the ensemble average now also includes the sampled starting positions x_0 . The starting positions are sampled from Eq. (5.17), with $d_0 = d$, which is twice the size of the region between the interfaces. The results are robust as this threshold is varied. In this case, it is necessary to compute both $\langle \Theta(x - d_2) \rangle$ and $\langle \Theta(d_1 - x) \rangle$. One upshot of Monte Carlo sampling of x_0 and \mathcal{T} is that this is *much* faster than directly evaluating the position and path time integrals on a path-wise basis. In fact, evaluating the Casimir energy takes roughly the same amount of time as the Casimir–Polder energy. However, it does give a larger sample variance.

5.1.3.1. Error Scaling with Path Length N

Some interesting scaling behavior was found by examining the relative error of the numerical estimates. In this case the systematic error is due to the discretization of the path. The path integral was derived under the assumption that $N \rightarrow \infty$, while the numerical calculations use a discrete path with a finite N . There is an additional statistical error associated with the finite number of paths. However, for N_{path} paths, this error scales as $N_{\text{path}}^{-1/2}$, as is typical for Monte Carlo sampling error. This is what determines the noise floor in Figures 5.3 and 5.4.

As the path length N increases for fixed χ , the systematic error shows two different scaling behaviors. In the weak-coupling limit $\chi/N \ll 1$, the error scales as $N^{-3/2}$, while in the strong-coupling limit $\chi/N \gg 1$, the error scales $N^{-1/2}$. These behaviors are analyzed in Mackrory *et al.* (2016), but the basic reasoning will be summarized here. The numerical computations use discrete paths, while the path integral is only exact in the limit that N is arbitrarily large. The continuous paths considered by the path integral have arbitrarily fine structure, and always have a

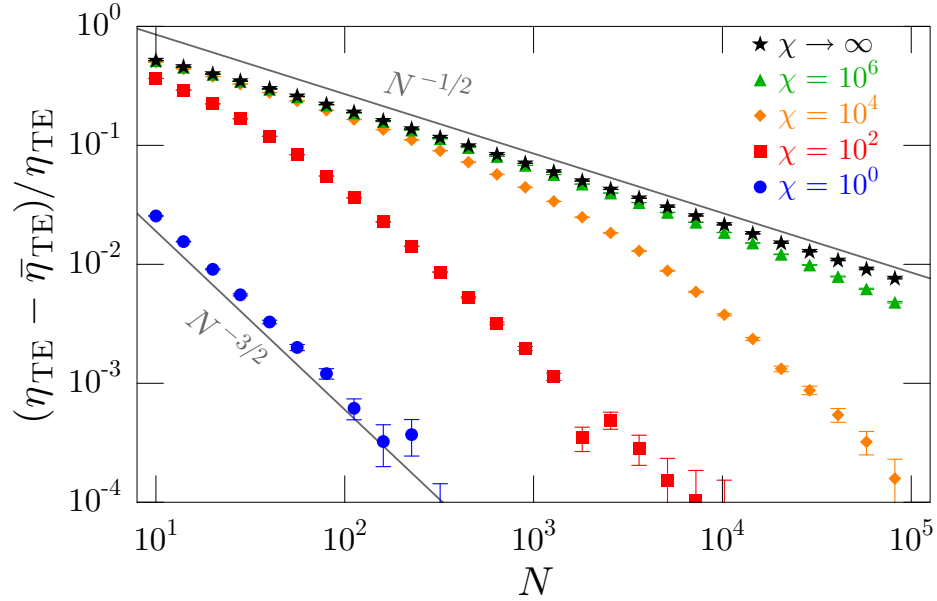


FIGURE 5.3. Convergence of planar TE Casimir–Polder energy as a function of N . Results plot the absolute relative error between the numerical estimates from Eq. (5.21) and the analytical result (4.30). Different values of χ use the same ensemble of paths. Calculations used 10^8 paths.

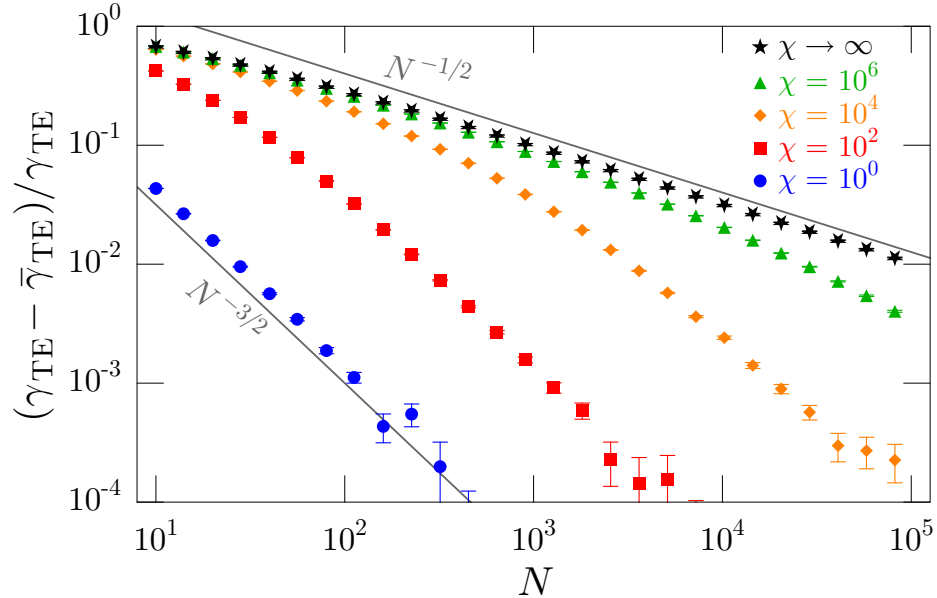


FIGURE 5.4. Convergence of planar TE Casimir energy as function of N . Results plot the absolute relative error between the numerical estimates from Eq. (5.22) and the analytical result (4.51). Different values of χ use the same ensemble of paths. Calculations used 10^8 paths.

non-zero probability to touch the dielectric body. The discrete paths used in the numerical method miss those contributions, leading to a systematic error.

In the weak-coupling limit $\chi/N \ll 1$, the numerical estimate is dominated by accurately estimating the sojourn time $\langle \Theta \rangle$ for a given path. Further increasing N increases the accuracy of this estimate and the renormalized integrand. The $N^{-3/2}$ scaling can be deduced by integrating the probability for a nonzero sojourn time from each increment.

In the strong-coupling limit $\chi/N \gg 1$, as soon as a path touches the surface the integrand immediately saturates to its extreme value of negative one. Thus the dominant error comes from underestimating the path time that this occurs. The error is estimated by integrating the probability that a continuous path touched the surface prior to the estimated first contact time. This leads to a $N^{-1/2}$ scaling.

For a fixed χ , the transition between both behaviors is observed at $N \sim \chi$. In the strict $\chi \rightarrow \infty$ Dirichlet limit, the numerical results and scaling arguments indicate that there will always be a $N^{-1/2}$ systematic error scaling.

5.2. TM Casimir Numerics

Numerically calculating Casimir energies due to the TM polarization is much harder than the TE case. This is due to the singular nature of the TM potential. Even after regularization, and analytical path averaging, is still challenging to handle numerically. We will develop a number of techniques to temper these difficulties. As a side effect, they should have applications for more general Casimir worldlines.

The most daunting feature of the TM Casimir worldline (4.52) is the singular TM potential (3.32). A closed-form solution for the TM potential V_{TM} at a single planar boundary was found in Chapter III. The ensemble-averaged solution for all

Brownian paths between points x_k and x_{k+1} in time $\Delta\mathcal{T}$ is

$$v_{k,k+1} := \left\langle\left\langle e^{-\int_0^{\Delta\mathcal{T}} dt' V_{\text{TM}}(x-d)} \right\rangle\right\rangle_{x_k \rightarrow x_{k+1}} \quad (5.23)$$

$$= \begin{cases} 1 + \text{sgn}(d-x_k) \tanh \Xi e^{-2(d-x_k)(d-x_{k+1})/\Delta\mathcal{T}} & (d-x_k)(d-x_{k+1}) > 0 \\ \text{sech } \Xi & (d-x_k)(d-x_{k+1}) < 0. \end{cases} \quad (5.24)$$

This ensemble-averaged solution was plotted in Figure 3.1, for x_k and x_{k+1} on either side of the interface at various values of Ξ . The solution varies between zero and one for paths that start inside a dielectric body, or path that cross a vacuum-dielectric interface. For paths starting in vacuum outside a dielectric body, the solution varies between one and two. The extreme values of zero and two only appear in the strong-coupling limit close to the surface.

This solution can be used in the path integral by identifying averages of sub-paths between discrete points with the analytical solutions. The path averaged exponential potential can be refined into arbitrarily many steps between \mathbf{x}_k and \mathbf{x}_{k+1} at times \mathcal{T}_k and \mathcal{T}_{k+1} . Each exponential potential can be averaged over all possible continuous sub-paths between x_k and x_{k+1} , with the result,

$$\left\langle\left\langle \frac{e^{-\mathcal{T}(V_{\text{TM}})}}{\langle \epsilon_{\text{r}} \rangle^{1/2}} \right\rangle\right\rangle \approx \left\langle\left\langle \frac{1}{\langle \epsilon_{\text{r}} \rangle^{1/2}} \prod_{k=1}^N \left\langle\left\langle \exp \left(- \int_{\mathcal{T}_k}^{\mathcal{T}_{k+1}} dt V_{\text{TM}}[x(t)] \right) \right\rangle\right\rangle_{x_k \rightarrow x_{k+1}} \right\rangle\right\rangle \quad (5.25)$$

$$= \left\langle\left\langle \frac{1}{\langle \epsilon_{\text{r}} \rangle^{1/2}} \prod_{k=1}^N v_{k,k+1} \right\rangle\right\rangle, \quad (5.26)$$

where $\langle\langle \dots \rangle\rangle$ denotes an average over continuous sub-paths between x_k and x_{k+1} .

5.2.1. Scaling of the Averaged TM Potential with Path Length N

The numerical properties of the solution can be examined by considering a simplified path integral that only includes a single TM potential a distance d away,

$$I = \left\langle\left\langle e^{-\int_0^{\mathcal{T}} dt V_{\text{TM}}[x(t)]} \right\rangle\right\rangle_{\mathbf{x}(t)} = \left\langle\left\langle \prod_{k=0}^{N-1} \left\langle\left\langle e^{-\int_0^{\Delta\mathcal{T}} dt V_{\text{TM}}[x(t)]} \right\rangle\right\rangle_{x_k \rightarrow x_{k+1}} \right\rangle\right\rangle_{\mathbf{x}_k} \quad (5.27)$$

$$= \left\langle\left\langle \prod_{k=0}^{N-1} v_{k,k+1} \right\rangle\right\rangle_{\mathbf{x}_k} . \quad (5.28)$$

The left-hand ensemble average is over continuous Brownian bridges, whereas the right-hand ensemble averages run over discrete Brownian bridges (and the solutions have been analytically averaged over continuous sub-paths between points on the discrete path, as indicated by $\langle\langle \dots \rangle\rangle$). In this case, the exact value of the integral is just the TM potential solution Eq. (5.24), for $x_k, x_{k+1} \rightarrow x_0$. The right hand side can be computed numerically to examine its scaling with N .

Figure 5.5 shows a histogram of numerically estimated values for closed Brownian paths interacting with the TM potential. Each Brownian path is generated via the v-loop algorithm (5.10), and scaled by $\sqrt{\mathcal{T}}$. The total contribution from each path is the product of the TM solutions (5.24) for every step along the path. The direct estimate of the TM potential shows a wide spread of values over different paths. Most paths return values close to zero, while a few rare paths return very large values. This suggests that the plain Gaussian paths are poorly suited to this problem, and that the path generation scheme should be modified. Given a large enough ensemble, this method eventually converges to the right answer, but it displays unacceptably large statistical errors.

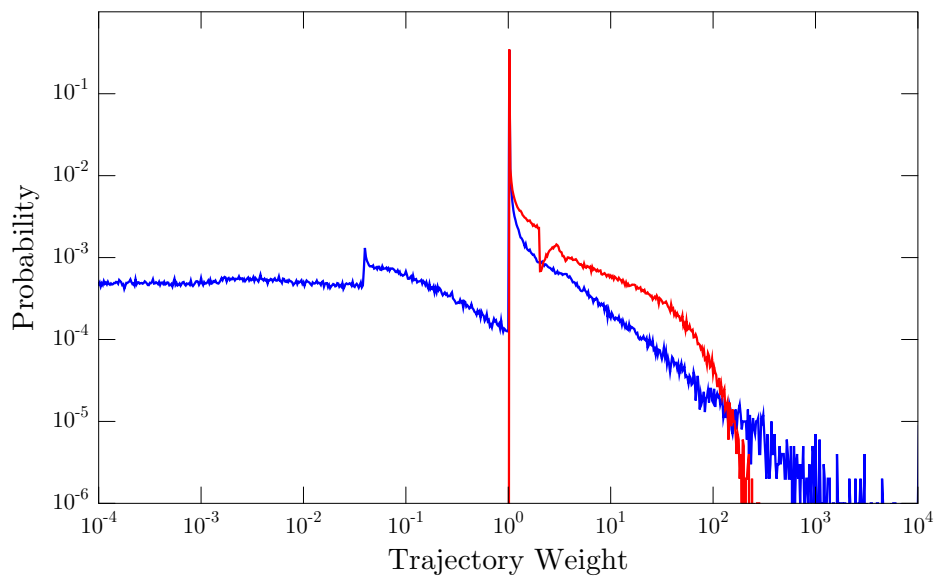


FIGURE 5.5. Histogram of accumulated numerical TM estimates, for Gaussian paths (blue) and birth-death Gaussian paths (red). Calculations used 10^6 paths, with $N = 200$ points per path, $\chi = 100$, $d = 1$, and $\mathcal{T} = 1$. The correct value for the integral at these parameters is ($I = 1.595$). The Gaussian estimate is (1.40 ± 0.14). The birth-death estimate is (1.602 ± 0.006). (The birth-death method is discussed in Section 5.2.1.2.) The Gaussian distribution extends off to zero, while the birth-death distribution has truncated peak at zero.

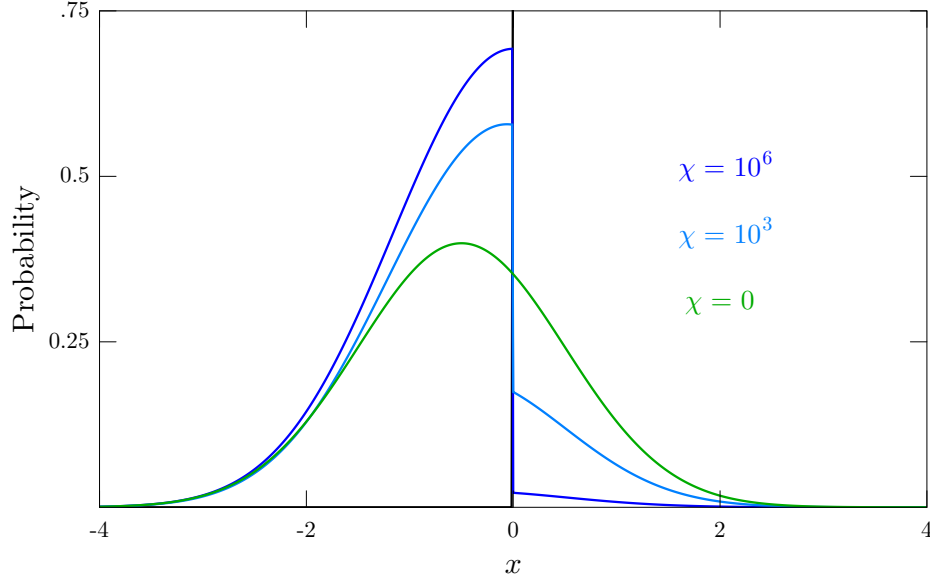


FIGURE 5.6. Combined TM-Gaussian probability distribution plotted for various χ . Corresponds to a single term in the product in Eq. (5.29). Increment starting position is $x = -1$, and $\mathcal{T} = 1$. The boundary is at the origin.

5.2.1.1. TM-Gaussian Paths

One possible solution to the fluctuations is to sample from a combination of a Gaussian and the path-averaged exponential (5.24) for the path increment. We will refer to these paths as “TM-Gaussian” paths. Since the path-averaged exponential is taken into account in the sampling, more representative values should be chosen, which should reduce the number of extreme values of the estimates. In this case, the total probability distribution for the paths is

$$P(x_1, \dots, x_{N-1}) = \prod_{k=0}^{N-1} \frac{e^{-(x_{k+1}-x_k)^2/(2\Delta\mathcal{T})}}{\sqrt{2\pi\Delta\mathcal{T}}} \left\langle\left\langle e^{-\int_0^{\Delta\mathcal{T}} dt V_{\text{TM}}} \right\rangle\right\rangle_{x_k \rightarrow x_{k+1}}. \quad (5.29)$$

In the same manner as the v-loops, the Gaussian probability distribution can be decoupled into a set of independent Gaussians. As seen from Eq. (5.8), the argument of each of those Gaussians involves $z_k = (x_k - c_k x_{k-1})/\sqrt{c_k \Delta\mathcal{T}}$, where c_k is defined

in Eq. (5.6). After implementing the v-loop change of variables, the probability distribution (5.29) can be written as

$$P(x_1, \dots, x_{N-1}) = v_{N,N-1} \prod_{k=0}^{N-1} \mathcal{N}_{k+1} P_{k+1}^{(\text{TM})}(x_{k+1}), \quad (5.30)$$

where the new probability distribution for x_{k+1} is

$$P_{k+1}^{(\text{TM})}(x_{k+1}) := \mathcal{N}_{k+1}^{-1} \frac{e^{-(x_{k+1}-c_k x_k)^2/(2c_k \Delta \mathcal{T})}}{\sqrt{2\pi c_k \Delta \mathcal{T}}} v_{k,k+1}(x_k, x_{k+1}), \quad (5.31)$$

with normalization constant

$$\mathcal{N}_k = \int dy \frac{e^{-(y-c_k x_k)^2/(2c_k \Delta \mathcal{T})}}{\sqrt{2\pi c_k \Delta \mathcal{T}}} v_{k,k+1}(x_k, y). \quad (5.32)$$

The crucial point is that the $P_{k+1}^{(\text{TM})}$ can act as the probability distribution for x_{k+1} , accounting only for the present position x_k . Although the next position x_{k+1} is still coupled to future positions via $v_{k+1,k+2}$, the sampling procedure ignores that and samples x_{k+1} based solely on $P_{k+1}^{(\text{TM})}$. The probability distribution can be put into a convenient numerical form by completing the square to account for $v_{k,k+1}$. The resulting piecewise Gaussian probability distributions can be split into “no-crossing” and “crossing” terms, where

$$P_{k+1}^{(\text{TM})}(x_{k+1}) = \mathcal{N}_{k+1}^{-1} [P_{\text{NC},k+1}^{(\text{TM})}(x_{k+1}) + P_{\text{C},k+1}^{(\text{TM})}(x_{k+1})] \quad (5.33)$$

and

$$P_{\text{NC},k+1}^{(\text{TM})}(x_{k+1}) = \Theta[(d-x_k)(d-x_{k+1})] \left(\frac{e^{-(x_{k+1}-c_k x_k)^2/(2c_k \Delta \mathcal{T})}}{\sqrt{2\pi c_k \Delta \mathcal{T}}} + \frac{\text{sgn}(d-x_k) \tanh \Xi}{\sqrt{2\pi c_k \Delta \mathcal{T}}} e^{-2(1-c_k)d(d-x_k)/\Delta \mathcal{T}} e^{-[x_{k+1}-c_k(2d-x_k)]^2/(2c_k \Delta \mathcal{T})} \right) \quad (5.34)$$

$$P_{\text{C},k+1}^{(\text{TM})}(x_{k+1}) = \Theta[-(d-x_k)(d-x_{k+1})] \frac{\text{sech} \Xi}{\sqrt{2\pi c_k \Delta \mathcal{T}}} e^{-(x_{k+1}-c_k x_k)^2/(2c_k \Delta \mathcal{T})}. \quad (5.35)$$

The normalization constant can be evaluated in two parts, $\mathcal{N}_{k+1} = \mathcal{N}_{k+1}^{\text{C}} + \mathcal{N}_{k+1}^{\text{NC}}$, where the parts are:

$$\begin{aligned} \mathcal{N}_{k+1}^{\text{C}} = & \frac{1}{2} \left[1 + \text{sgn}(d-x_k) \text{erf} \left(\frac{d-c_k x_k}{\sqrt{2c_k \Delta \mathcal{T}}} \right) \right] \\ & + \text{sgn}(d-x_k) \frac{\tanh \Xi}{2} \left[1 + \text{sgn}(d-x_k) \text{erf} \left(\frac{d(1-2c_k) + c_k x_k}{\sqrt{2c_k \Delta \mathcal{T}}} \right) \right] \\ & \times e^{-2(1-c_k)d(d-x_k)/\Delta \mathcal{T}} \end{aligned} \quad (5.36)$$

$$\mathcal{N}_{k+1}^{\text{NC}} = \frac{\text{sech} \Xi}{2} \left[1 - \text{sgn}(d-x_k) \text{erf} \left(\frac{d-c_k x_k}{\sqrt{2c_k \Delta \mathcal{T}}} \right) \right]. \quad (5.37)$$

The probability distribution (5.33) can be sampled via the following procedure. First, note that the probability distributions involve truncated Gaussians in x_{k+1} . The truncation occurs at the surface $x_{k+1} = d$, since the probability distribution was split based on whether path increments cross through the surface or not. At each step the computation picks the crossing or no-crossing branch of the probability distribution. The branch is randomly chosen based on the relative probabilities for the crossing and no-crossing branches which are given by $(\mathcal{N}_{k+1}^{\text{C}}/\mathcal{N}_{k+1})$, and $(\mathcal{N}_{k+1}^{\text{NC}}/\mathcal{N}_{k+1})$, respectively. If the crossing branch is chosen [Eq. (5.35)], then a deviate is sampled from the truncated Gaussian distribution. Otherwise, if the no-crossing branch is

chosen [Eq. (5.34)], then depending on the sign of $\text{sgn}(d - x_{k+1})$, there are another two options. If $\text{sgn}(d - x_{k+1}) = 1$, then one of the Gaussians is picked based on their relative probability of occurring, and a deviate is sampled from that Gaussian. In these cases, the truncated Gaussian distributions can be sampled relatively quickly via the inverse error function. If however, $\text{sgn}(d - x_{k+1}) = -1$, then the rejection method is used to generate a deviate. In the rejection method, a deviate is sampled from a “proposal” distribution $P_1(x)$ (such as the sum of the Gaussians), and accepted with a probability $P_2(x)/P_1(x)$, where P_2 is the “target” distribution (Press *et al.*, 1990, Section 7.3).

While this method does improve performance, it still involves taking a product of $N - 1$ normalization factors \mathcal{N}_{k+1} , where $0 < \mathcal{N}_{k+1} < 2$. This leads to the same problems with large statistical errors as the plain Gaussians as the path length N is increased. It is also much more involved to implement than the plain Gaussian approach.

5.2.1.2. Birth-Death Path Swarm

Both the plain Gaussian and TM-Gaussian paths can be improved by further adjusting the sampling procedure. In both cases, the path can accumulate a large weight. After k steps, the weight is $w_k = \prod_{j=1}^k \nu_j$, where ν_j represents either $v_{j,j+1}$ for Gaussian paths or \mathcal{N}_j for TM-Gaussian paths. Most paths propagating close to the surface will acquire a number of large weights with $\nu_j > 1$ when they are on the vacuum side of the interface, and small weights $0 < \nu_j < 1$ when they are on the dielectric side of the interface. The logarithm of the accumulated weight is $\log w_k = \sum_{j=1}^k \log \nu_j$. Since the ν_j are random variables (both $v_{k,k+1}$ and \mathcal{N}_k are functions of an underlying random path), then from the central limit theorem, we

would expect $\log w_k$ to be normally distributed, with some standard deviation σ^2 . (The central limit theorem applies to the sum of a large number of independent random variables—it maybe that the independence assumption is violated in this case, as the path position acts as a memory.) Nevertheless, this predicts that the accumulated weight is expected to behave as a log-normal deviate, with variance $e^{\sigma^2}(e^{\sigma^2} - 1)$. Since σ^2 grows linearly with N , the variance of the product w_k would grow exponentially with N . Note that the mean would still have the correct value, but the variance, and the sampling error would grow unacceptably as N increases.

The path generation both Gaussian and TM-Gaussian methods can be modified by introducing a “birth-death path swarm”. The weight w_k is effectively treated as the fitness function for the path. Paths with large weights will spawn further paths (“birth”), while paths with small weights will be terminated and return zero (“death”). At each step of the path, the accumulated weight must be checked. If the weight is becoming small, $w_k < 0.5$ then the weight should be compared with a uniform random number u . If $w_k < u$, then the path dies; alternatively, if $w_k > u$, then the path survives and the weight is reset $w_k = 1$. This is the death process. In an ensemble average, an average fraction of the paths u survive the death process, which gives the correct average value. If the weight becomes large, $w_k > 2$, then the weight is split in two, and each half is assigned to one of two independent paths. Altogether, this is called a “birth-death” process, and should be applied at every step of the random path. If a path survives for N steps, then its contribution is added to a running total for this swarm. Once all of the paths have either died, or reached the end, the accumulated total for this swarm is then renormalized (by subtracting 1), and added to the running totals used to estimate the mean and variance. Implementing the deaths ensures that the number of computations does not grow exponentially as

a function of path length, while the birth process ensures that successful trajectories with a large weight have contribute more to the path integral. The death process also speeds up the computation by not computing negligible corrections to the swarm value.

The birth-death process is effectively a very simple Markov Chain Monte Carlo method. The birth-death process modifies the preferred motions based on the accumulated weight. Paths are likely to be born on the vacuum side of interfaces, and they are likely to die on the dielectric side of the interface. Far away from the interface on either side, the paths are unlikely to branch or terminate.

Similar terms are discussed throughout stochastic processes literature. As a matter of nomenclature, it is worth distinguishing the birth-death process we are using from the more popular birth-death process used in queuing theory. In queuing theory, the number of objects in a queue randomly increases and decreases at a fixed average rate. In our case, that rate depends on the past behavior of the system, and where the path has gone. The process used here is closer to the genealogical methods for evaluating path integrals (Del Moral, 2004). A similar genealogical idea has been used in quantum trajectory simulations (Jacobs, 2010), which is a technique for simulating open quantum systems. In that variant, each quantum state in an ensemble carries a probability weight. If that weight becomes too small, then that random trajectory is discarded, and another more successful trajectory is split in two, and given half the weight. A similar method has been used to discuss simulating rare events, such as the extreme tails of a Gaussian. In that case, one splits trajectories based on whether they exceed a certain threshold criterion (Garvels, 2000; Glasserman *et al.*, 1999). These methods essentially reward the trajectories or paths of the system that enter regions with a large contribution to the integral (or other figure of merit).

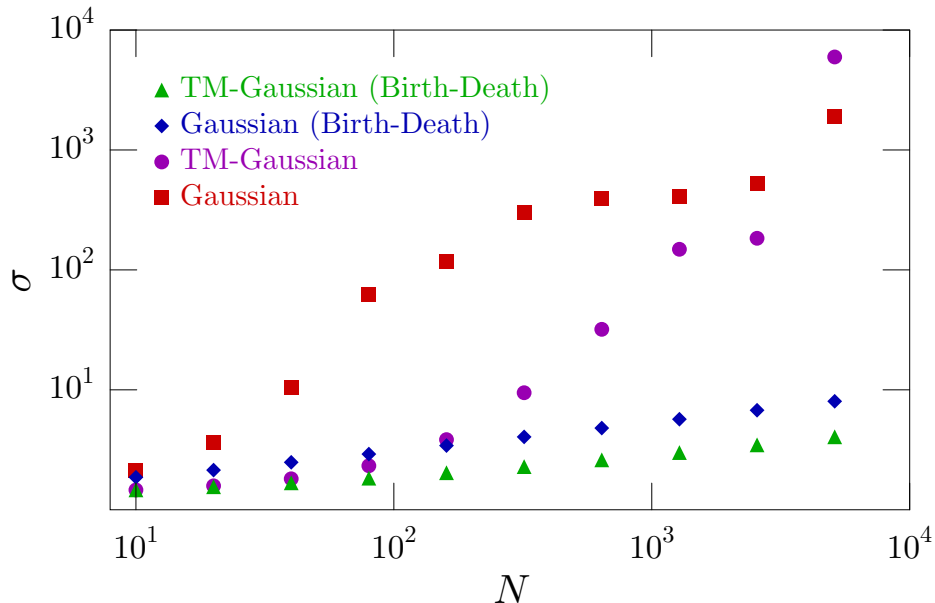


FIGURE 5.7. (Preliminary data) Scaling of standard deviation for the accumulated TM potential as function of N for four methods. Eq. (5.28) is evaluated for both plain Gaussian steps, TM-Gaussian steps, and then for birth-death variants of both methods. Calculations used 10^9 trials, with $\chi = 12$, $d = 1$, and $\mathcal{T} = 2$.

Thus more computational effort is spent in regions with significant contributions to the final result.

Figure 5.7 shows how the plain Gaussian and TM-Gaussian estimates of the simple path integral scale with the path resolution. This figure contains preliminary data, since there are still very large statistical fluctuations on the Gaussian estimates, and a very large number of samples is required to ensure decent convergence. The birth-death process has been applied to both ways of generating paths. The birth-death process reduces the variance, and makes both methods much more tractable. The difference between Gaussian and TM-Gaussians is small under the birth-death process. In addition, generating Gaussian paths is faster than generating TM-Gaussians. Given that small difference, and the simplicity of the plain Gaussian paths,

we have opted to use the birth-death process in conjunction with plain Gaussian paths throughout the remainder.

5.2.2. Monte Carlo Sampling for the Path Time

When using the birth-death method for generating paths, the TM polarization requires a slightly different sampling method for generating path times \mathcal{T} . In some limited cases it may be possible to estimate a minimum \mathcal{T}_0 where the integrand is small for a given path, and a path is unlikely to have branched or birthed new paths. For paths starting on the vacuum side near a dielectric, the accumulated potential at small path times is approximately $\prod_k (1 + \tanh \Xi e^{-2(d-x_k)(d-x_{k+1})/\Delta\mathcal{T}})$, which increases smoothly with \mathcal{T} . In that case, \mathcal{T}_0 can be estimated from the time an initial, fiducial path would contact a surface and the integrand would be nonzero. The path time can be sampled from the power law distribution (5.12). The birth-death process then proceeds starting with a version of the initial path that is scaled by $\sqrt{\mathcal{T}}$.

However, in a two-body geometry that estimate fails. The renormalized integrand is only nonzero for paths that come close to both surfaces. Since the birth-death method may split the trajectory, it is not always possible to reliably find a minimum time \mathcal{T}_0 when the renormalized integrand turns on. (In principle, a small value of \mathcal{T}_0 could be picked, where the path has no chance of touching the surface, but most computations would return zero, since the most sampled values of \mathcal{T} are close to \mathcal{T}_0 .)

Once paths are large enough to contribute to the energy, they are guaranteed to have intersected both bodies. As a result, the intersection path time of the fiducial path with the surface has little bearing on when the resulting path swarm would contribute. For example, the fiducial path might have started next to one surface, and branched immediately. The fiducial path might extend further in one direction, and

only intersect the second body at much later times than the branched path. Sampling the path time based on when the fiducial path intersects the body would miss that contribution. This suggests that the path time for the birth-death path swarm is best sampled from the ensemble average estimate of when a path will contact the surface.

Since the birth-death method essentially enlarges the ensemble of paths selected, the behavior of the integrand as a function of \mathcal{T} mimics the probability for a Brownian bridge to touch a surface. The probability for a Brownian bridge to touch a surface a distance d away in path time \mathcal{T} is

$$P_{\text{touch}}(\mathcal{T}) = e^{-2d^2/\mathcal{T}}. \quad (5.38)$$

The combined potential term $\prod_k v_{k,k+1}$, also has a similar dependence on the path time. This could be combined with the $\mathcal{T}^{-(1+D/2)}$ power law for a new probability distribution.

$$P(\mathcal{T}; \mathcal{T}_0, s) = \frac{\mathcal{T}_0^{s-1}}{\Gamma[s-1]\mathcal{T}^s} e^{-\mathcal{T}_0/\mathcal{T}}, \quad (5.39)$$

where $s > 1$ and $\mathcal{T}_0 > 0$. The probability distribution (5.39) can be transformed by setting $u = \mathcal{T}_0/\mathcal{T}$, for which the probability distribution is

$$P(u; s) = \frac{u^{s-2}}{\Gamma[s-1]} e^{-u}. \quad (5.40)$$

This distribution has the form of a Gamma distribution, which has probability density

$$f(x) = \frac{x^{a-1} e^{-x/b}}{\Gamma(a)b^a}, \quad (5.41)$$

where $a > 0$ and $b > 0$ are the shape and scale parameters respectively (Devroye, 2003). The shape parameter a changes the mean value of the distribution by changing

the shape of the function close to $x = 0$, while the scale parameter b scales the deviates. For small integer or half-integer powers a , there are some simple methods for generating Gamma deviates g_i . A sum of Gamma deviates $g_{\text{tot}} = \sum_{i=1} g_i$ with shape parameters a_i , is also a Gamma deviate with shape parameter $\sum_i a_i$ (Devroye, 2003, pg. 402). A Gamma deviate with shape parameter $a = 1$ is an exponential deviate, which can be computed using $e_i = -\log(u)$ where u is a uniform random number. In particular, this means the sum of n exponential deviates yields a Gamma deviate with shape parameter $a = n$. In addition, if z is a standard normal variable, then $z^2/2$ is Gamma distributed with $a = 1/2$. For small integer powers of s , \mathcal{T} can be efficiently generated using

$$\mathcal{T} = \frac{\mathcal{T}_0}{-\sum_{i=1}^s \log u_i}, \quad (5.42)$$

while for half-integer powers,

$$\mathcal{T} = \frac{\mathcal{T}_0}{-\sum_{i=1}^{\text{floor}(s)} \log u_i + z^2/2}. \quad (5.43)$$

The integer powers are useful for estimating zero temperature Casimir energies. The half-integer powers naturally emerge when considering the thermal Casimir energy, or derivatives of the Casimir energy such as the force. This distribution can also be used to sample times \mathcal{T} even for TE integrands. In that case however, it is possible the generated path will not touch all of the relevant bodies and merely return zero, which will increase the variance of the numerical estimated energy.

5.2.3. Gradient Estimation

Computing the TM Casimir–Polder energy (4.15) also requires taking two spatial derivatives of the worldline path integral. Furthermore, in some experiments on the Casimir–Polder effect such as BEC experiments (Harber *et al.*, 2005), the Casimir–Polder potential is estimated from how it shifts the frequency of the atom’s oscillations in a harmonic potential. This frequency shift is calculated by taking two derivatives of the Casimir–Polder potential, which corresponds to finding the potential curvature. For the TM polarization within the worldline method, this would require a fourth spatial derivative, so it is essential to be able to efficiently compute these derivatives for worldline path integrals.

Let us consider a generic worldline path integral involving pinned Brownian motions in path time \mathcal{T} with starting point \mathbf{x}_0 :

$$I(\mathbf{x}_0) = \langle\langle \Phi(\mathbf{x}_0, \mathbf{x}_1, \dots, \mathbf{x}_{N-1}) \rangle\rangle_{\mathbf{x}(t), \mathbf{x}(0)=\mathbf{x}_0}. \quad (5.44)$$

The function Φ depends on the whole path, and serves as a placeholder for the path averaged dielectric or TM potentials. We will discuss how to evaluate these derivatives with both the standard finite difference method and a new partial-averaging approach.

5.2.3.1. Finite Differences

The finite-difference method is straightforward method for numerically evaluating derivatives. It has the great virtue of simplicity, since it only requires that we evaluate the function multiple times. For smooth functions, the finite-difference method works well, but it behaves poorly when applied to stochastic, discontinuous functions such as the worldline path integral.

For example, consider the first derivative of the TE Casimir–Polder worldline integrand, at a dielectric step $\epsilon_r = 1 + \chi\Theta(x - d)$. The finite difference integrand is

$$\frac{\partial}{\partial x_0} \left\langle\left\langle \langle \epsilon_r[x(t)] \rangle^{-3/2} - 1 \right\rangle\right\rangle_{B_k} = \frac{1}{\Delta s} \left\langle\left\langle \langle \epsilon_r(x_0 + \Delta s + \sqrt{\mathcal{T}} B_k) \rangle^{-3/2} - \langle \epsilon_r(x_0 + \sqrt{\mathcal{T}} B_k) \rangle^{-3/2} \right\rangle\right\rangle_{B_k}, \quad (5.45)$$

where Δs is the finite difference step size, B_k is a closed unit Brownian bridge. This estimate can be evaluated on a pathwise basis, in keeping with the suggestion that using common random numbers yields the best results for finite differences [as discussed in Asmussen and Glynn (2007, Section 7.2A)]. In order to be accurate, the step size Δs must be small, since the error in this approximation to the derivative is $\mathcal{O}(\Delta s)$. Unfortunately, that limit leads to large statistical uncertainty. If the finite difference is much smaller than a typical path increment, $\Delta s \ll \sqrt{\Delta \mathcal{T}}$, the estimates for path averaged dielectric $\langle \epsilon_r(\mathbf{x}_0) \rangle$ for the two starting positions are likely to be the same, so the estimate is zero. In rare circumstances, a point is within Δs of the surface, and the finite difference returns the large value of $(\Delta s)^{-1}$. However, this arguments neglects that as $\Delta s \rightarrow 0$, the probability for a point to be within Δs of the surface, also approaches zero. For the first order finite difference, the error is constant as $\Delta s \rightarrow 0$. However, at higher derivatives this is no longer true and the variance grows as $\Delta s \rightarrow 0$.

The finite difference method is also problematic for the birth-death method for TM potentials. In that case, as the starting position of the paths varies, a different family of birth-death paths may be generated, which further compounds the fluctuation problem.

5.2.3.2. Malliavin Calculus

Similar derivatives are required in quantitative finance, where the sensitivity of a financial product to variations its underlying parameters must be estimated (Glasserman, 2004). Since financial simulations also typically involved averages over stochastic processes, similar problems emerge when trying to estimate derivatives with finite differences. One approach with a number of appealing properties is based on the Malliavin calculus.² In this approach, the derivative can be estimated by multiplying the integrand by a suitably chosen weight function, which depends on the nature of the derivative and the random path. The Malliavin calculus is essentially functional differentiation with respect to the Brownian motion, and an associated integration by parts formula. The weights can be derived by rewriting derivatives with respect to a parameter as derivatives with respect to the Brownian motion, and integrating by parts (Kohatsu-Higa and Montero, 2004). In effect, differentiation is replaced by multiplication with a weighting function, where the form of the function depends on the required derivatives. The advantage is the same sample paths can be used for both the estimate and its derivative. In addition the derivative estimates are well behaved, since the weight functions are typically simple, smooth functions of the stochastic path. While the Malliavin approach to derivative estimation did not yield better results for the worldline method, it did inspire the partial-averaging approach, which has similar virtues.

² The Malliavin calculus is formally discussed in Nualart (2006), Malliavin and Thalmaier (2006), and DiNunno *et al.* (2009). Less formal (and far more understandable) discussions of the Malliavin approach are presented in Chen and Glasserman (2007), and Kohatsu-Higa and Montero (2003, 2004).

5.2.3.3. Partial Averaging Gaussian Paths

Let us consider directly evaluating the derivatives in one Cartesian direction on a generic path integral (5.44), which can be written in discrete form as

$$\partial_0^n I(\mathbf{x}_0) = \frac{\partial^n}{\partial x_0^n} \int \prod_{j=1}^N d\mathbf{x}_j \delta(\mathbf{x}_N - \mathbf{x}_0) \prod_{k=1}^N \frac{e^{-(\mathbf{x}_{k+1} - \mathbf{x}_k)^2 / (2\Delta\mathcal{T})}}{(2\pi\Delta\mathcal{T})^{(D-1)/2}} \Phi(\mathbf{x}_0, \mathbf{x}_1, \dots, \mathbf{x}_{N-1}). \quad (5.46)$$

Note there is some freedom in how the derivative is evaluated, which leads to slightly different approaches. If the integration variables are shifted to $\mathbf{y}_k = \mathbf{x}_k - \mathbf{x}_0$, then the derivatives only act on Φ . This is close to the approach used in the finite difference approach where the whole path was translated by Δs . If however, the original \mathbf{x}_k variables are used and the derivatives are evaluated, the derivatives act on the coupled Gaussian.

$$\partial_0^n I(\mathbf{x}_0) = \int \prod_{j=1}^{N-1} d\mathbf{x}_j \frac{\partial^n}{\partial x_0^n} \prod_{k=0}^{N-1} \frac{e^{-(\mathbf{x}_{k+1} - \mathbf{x}_k)^2 / (2\Delta\mathcal{T})}}{(2\pi\Delta\mathcal{T})^{(D-1)/2}} \Phi(\mathbf{x}_0, \mathbf{x}_1, \dots, \mathbf{x}_{N-1}). \quad (5.47)$$

The derivatives acting on Φ have been neglected, which effectively assumes that Φ does not vary significantly at the path origin. The derivatives of the Gaussian distributions yield Hermite Polynomials, which are defined via

$$\frac{d^n}{dx^n} e^{-(x-\mu)^2/a^2} = (-a)^{-n} H_n\left(\frac{x-\mu}{a}\right) e^{-(x-\mu)^2/a^2}. \quad (5.48)$$

The Gaussian distributions for the first and last steps can be differentiated n times with respect to x_0 , with the result

$$\begin{aligned} & \frac{\partial_0^n}{\partial x_0^n} \frac{e^{-(\mathbf{x}_0 - \mathbf{x}_1)^2/(2\Delta\mathcal{T}) - (\mathbf{x}_0 - \mathbf{x}_2)^2/(2\Delta\mathcal{T})}}{(2\pi\Delta\mathcal{T})^{(D-1)}} \\ &= \left(\frac{-1}{\sqrt{\Delta\mathcal{T}}} \right)^n H_n \left(\frac{x_0 - \bar{x}_1}{\sqrt{\Delta\mathcal{T}}} \right) \frac{e^{-(x_0 - \bar{x}_1)^2/\Delta\mathcal{T} - (\Delta\mathbf{x}_1)^2/(4\Delta\mathcal{T})}}{[(\pi\Delta\mathcal{T})(4\pi\Delta\mathcal{T})]^{(D-1)/2}}. \end{aligned} \quad (5.49)$$

The following variables were defined,

$$\Delta\mathbf{x}_k := \mathbf{x}_{N-k} - \mathbf{x}_k \quad \bar{\mathbf{x}}_k := (\mathbf{x}_k + \mathbf{x}_{N-k})/2, \quad (5.50)$$

and used with $k = 1$. The differentiated path integral is then

$$\partial_0^n I(\mathbf{x}_0) = \left\langle\left\langle \left(\frac{-1}{\sqrt{\Delta\mathcal{T}}} \right)^n H_n \left(\frac{x_0 - \bar{x}_1}{\sqrt{\Delta\mathcal{T}}} \right) \Phi(\mathbf{x}_0, \mathbf{x}_1, \dots, \mathbf{x}_{N-1}) \right\rangle\right\rangle_{\mathbf{x}_k}, \quad (5.51)$$

where the Gaussians have been restored to their usual form and the path integral has been rewritten in ensemble average form. In principle this method would also work for estimating the derivatives. However as written, this will have a large statistical error. In particular, the estimates will be distributed around zero, with some reweighting due to Φ , which preferentially weights certain values. However, the overall standard deviation scales as $(\Delta\mathcal{T})^{-n/2}$. As N increases, the fluctuations will scale as $N^{n/2}$ which is unacceptable.

This method can be improved by partial averaging over the path. In particular, we assume that $\Phi = \prod_{k=1}^N \phi(\mathbf{x}_k)$, and each $\phi(\mathbf{x}_k)$ only varies significantly for $\mathbf{x}_k \sim d$, and when $\mathbf{x}_k \ll d$, $\phi(\mathbf{x}_k)$ can be approximated as a constant. An example of this geometry is illustrated in Figure 5.8, for an atom near a dielectric surface. For the first and last m points along the path, the integrals can be carried out assuming

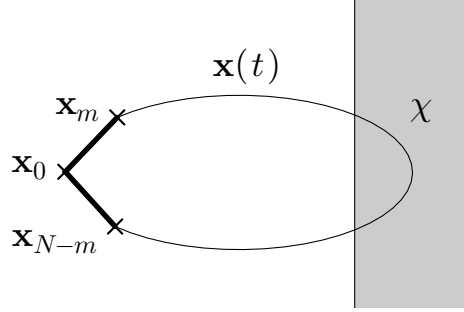


FIGURE 5.8. Partial averaging along a path close to a surface. The extent of the averaging m is chosen to be as large as possible, while ensuring that the likely paths between x_m and x_{N-m} are unlikely to enter the dielectric.

that Φ is approximately independent of these coordinates. The resulting combined steps from \mathbf{x}_0 to \mathbf{x}_m involve a path time $\mathcal{T}_m := m\Delta\mathcal{T}$. The result for integrating out $\mathbf{x}_1, \dots, \mathbf{x}_{m-1}$ and $\mathbf{x}_{N-m+1}, \dots, \mathbf{x}_{N-1}$ in Eq. (5.49) is

$$\begin{aligned} \partial_0^n I(\mathbf{x}_0) &\approx \int \prod_{k=m}^{N-m} d\mathbf{x}_k \left(\frac{-1}{\sqrt{\mathcal{T}_m}} \right)^n H_n \left(\frac{x_0 - \bar{x}_m}{\sqrt{\mathcal{T}_m}} \right) e^{-(x_0 - \bar{x}_m)^2 / \mathcal{T}_m - \Delta \mathbf{x}_m^2 / (4\mathcal{T}_m)} \\ &\quad \times \prod_{k=m}^{N-m+1} \frac{e^{-(\mathbf{x}_{k+1} - \mathbf{x}_k)^2 / (2\Delta\mathcal{T})}}{(2\pi\Delta\mathcal{T})^{(D-1)/2}} \Phi(\mathbf{x}_m, \dots, \mathbf{x}_{N-m}) \end{aligned} \quad (5.52)$$

$$= \left\langle\left\langle \left(\frac{-1}{\sqrt{\mathcal{T}_m}} \right)^n H_n \left(\frac{x_0 - \bar{x}_m}{\sqrt{\mathcal{T}_m}} \right) \Phi(\mathbf{x}_m, \dots, \mathbf{x}_{N-m}) \right\rangle\right\rangle. \quad (5.53)$$

The combination of the Hermite polynomial and $(\mathcal{T}_m)^{n/2}$ is effectively the desired Malliavin weighting function in this case. The partial-averaging approach has replaced differentiation with multiplication by a function whose variance does not increase as the path length increases. The threshold m can be chosen based on how likely the path of a given time step is to touch the surface. That threshold will depend on the distances in the problem and the path-time, which determines a fraction of the path that can be averaged over. The fraction becomes a constant as N increases, so $\mathcal{T}_m = m\mathcal{T}/N$ also becomes a constant for a particular \mathcal{T} , and the variance no longer grows as N increases.

Each integration over an intermediate coordinate makes some small error in approximating Φ as independent of that coordinate. The partial averaging should only be carried out to the point where that error can no longer be ignored. If the function Φ starts to vary when any of its arguments approach d , such as for the TE Casimir worldline integrand, then the error can be estimated from the probability that x_m would enter the region $x_m > d$. Although the paths are actually Brownian bridges, for small times ($\mathcal{T}_m \ll \mathcal{T}$) the paths can be approximated as Brownian walks in order to estimate the touching probability. The probability that a Brownian walk will touch a surface at $x = d$ after starting at the origin, in time \mathcal{T}_m is

$$P_{\text{touch}} = \operatorname{erfc} \left(\frac{d}{\sqrt{2\mathcal{T}_m}} \right). \quad (5.54)$$

For small \mathcal{T}_m , the error function is bounded by $e^{-d^2/(2\mathcal{T}_m)}$. If the maximum acceptable error is denoted ε , then this equation can be solved to estimate the maximum amount of averaging allowed. Using $\mathcal{T}_m = m\mathcal{T}/N$, the maximum amount of averaging should be

$$\frac{m}{N} = \frac{d^2}{2\mathcal{T} \log \varepsilon}. \quad (5.55)$$

The most important feature of this estimate, is that it suggests m/N is a constant fraction as N increases. As a consequence, the fluctuations in Eq. (5.53) scale as $[N/(m\mathcal{T})]^{n/2}$, but since m/N is a constant, the scale of the fluctuations is also constant as N increases. However, the size of that fraction will vary as a function of $d/\sqrt{\mathcal{T}}$ and the desired tolerance ε . As a practical matter, m/N should not exceed 1/2, so that there are at least two points in the path.

The partial averaging effectively constructs a path with a variable step size. At points close to the path origin, the path steps can be large since these increments are

unlikely to intersect the surfaces. Since the length of the first and last increments set the scale of the fluctuations by their presence in $(N/m\mathcal{T})^{n/2}$, the steps should be chosen to be as large as possible. However, once the path gets close to the interface, it is necessary to accurately estimate quantities such as the touching time or sojourn time. The accuracy of these estimates depends sensitively on the size of the steps, and thus the path should have a finer resolution when it is close to the interface.

The path can be generated using the v-loop algorithm (5.10), and the larger steps can be constructed by identifying them with the m th step on the initial path. Those steps are used to evaluate the Hermite-Gaussian terms. The rest of the path between x_m and x_{N-m} can then be used to evaluate any potentials or spatial functions in the path integral. In the context of the birth-death algorithm, these gradients are only evaluated on paths that survive to the end to contribute to the path swarm. This method naturally generalizes to include multiple Cartesian derivatives.

5.2.3.4. General Method Near Surfaces

In some cases, it might be necessary to take derivatives of a two body energy for paths that start much closer to one body than another. This could be necessary when trying to calculate the two body energy shift for an atom, or when computing the stress-tensor close to one surface (Schäfer *et al.*, 2016). For a renormalized energy, only paths that touch both surfaces will contribute. The preceding approach was based on integrating out intermediate coordinates by approximating the integrals as Gaussians [as used in Eq. (5.53)]. In this case however, that approach can only be used to average out a very small number of steps.

This problem is illustrated in Figure 5.9, for the example of an atom near two dielectric surfaces, in the case when the atom is much closer to one surface than the

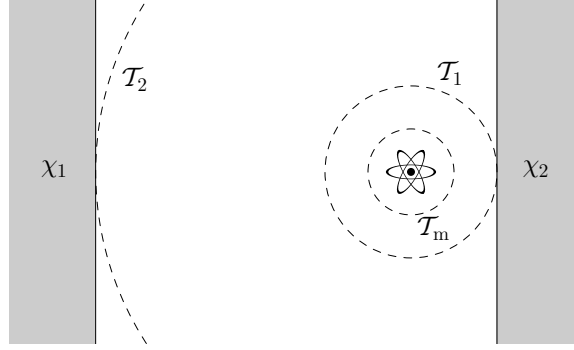


FIGURE 5.9. Thresholds for partial averaging for the case of an atom between two dielectric bodies. The dashed circles show the typical scales of paths at some important path times. The extent of the averaging is given by \mathcal{T}_m . The first path time when paths touch one body is \mathcal{T}_1 . This is much smaller than \mathcal{T}_2 , the path time to touch *both* bodies. These considerations also apply to the calculating stress-energy tensor close to one body.

other. The path time when a typical path will touch one body is denoted \mathcal{T}_1 , and \mathcal{T}_2 is the typical path time to touch both bodies. If the two-body contribution to the Casimir–Polder force is sought, then only paths that touch *both* bodies will contribute. The partial averaging advocated in Section 5.2.3.3 is only valid so long as Φ is approximately independent of the coordinates, and the probability of touching either surface is small. In that case, the integrals are approximately Gaussian, provided that $\mathcal{T}_m \ll \mathcal{T}_1$, so that the first and last m path increments are not likely to intersect or interact with either surface.

However, if there is an analytical expression for the path integral near one surface, then further partial averaging is possible. In such a two-body geometry, the renormalized interaction energy would lead to a function Φ of the form,

$$\Phi[\mathbf{x}(t)] = \left(e^{-\int_0^T dt \{V_1[\mathbf{x}(t)] + V_2[\mathbf{x}(t)]\}} - e^{-\int_0^T dt \{V_1(\mathbf{x}_0) + V_2(\mathbf{x}_0)\}} \right) - \left(e^{-\int_0^T dt V_1[\mathbf{x}(t)]} - e^{-\int_0^T dt V_1(\mathbf{x}_0)} \right) - \left(e^{-\int_0^T dt V_2[\mathbf{x}(t)]} - e^{-\int_0^T dt V_2(\mathbf{x}_0)} \right), \quad (5.56)$$

where V_1 and V_2 describe the two surfaces. For points much closer to one body, and for short times $\Delta\mathcal{T}$, then the dominant contribution to the potential can be approximated based on the nearest body

$$\left\langle\left\langle e^{-\int_0^{\Delta\mathcal{T}} dt \{V_1[\mathbf{x}(t)]+V_2[\mathbf{x}(t)]\}} \right\rangle\right\rangle \approx \left\langle\left\langle e^{-\int_0^{\Delta\mathcal{T}} dt V_2[\mathbf{x}(t)]} \right\rangle\right\rangle, \quad (5.57)$$

where the presence of the far body can be ignored for $\Delta\mathcal{T} \ll d^2$. The partial averaging can be carried out by using the fact that the path integral is a propagator for the diffusion equation. The path integral between two points \mathbf{x}_j and \mathbf{x}_{j+1} , interacting with a potential $V(\mathbf{x})$, is

$$U(\mathbf{x}_j, \mathbf{x}_{j+1}, t) := \frac{e^{-(\mathbf{x}_j - \mathbf{x}_{j+1})^2 / (2t)}}{\sqrt{2\pi t}} \left\langle\left\langle e^{-\int_0^t dt' V[\mathbf{x}(t')]} \right\rangle\right\rangle_{\mathbf{x}_j \rightarrow \mathbf{x}_{j+1}}. \quad (5.58)$$

The path integral expression for the propagator (5.58) obeys the composition law,

$$\int d\mathbf{x}_j U(\mathbf{x}_{j-1}, \mathbf{x}_j, t_1) U(\mathbf{x}_j, \mathbf{x}_{j+1}, t_2) = U(\mathbf{x}_{j-1}, \mathbf{x}_{j+1}, t_1 + t_2). \quad (5.59)$$

If the geometry can be described by some potential V , and if an analytical expression for the path integral can be found, then the partial averaging can be carried out to a threshold \mathcal{T}_m where the analytical solution for the path integral is no longer an acceptable approximation to the true solution for multiple bodies. This could happen either due to the presence of multiple bodies, or the path exploring a region where the geometry differs from the geometry assumed in the analytical expression. For example, if a curved surface is approximated by its nearest tangent plane, then the partial averaging is limited to regions smaller than the typical radius of curvature.

After the partial averaging, the derivatives can be carried out, with the result

$$\partial_0^n I(\mathbf{x}_0) = \left\langle\left\langle \partial_0^n [U(\mathbf{x}_0, \mathbf{x}_m, \mathcal{T}_m)U(\mathbf{x}_0, \mathbf{x}_{N-m}, \mathcal{T}_m)] \prod_{j=m}^{N-m-1} U(\mathbf{x}_{j+1}, \mathbf{x}_j, \Delta\mathcal{T}) \right\rangle\right\rangle. \quad (5.60)$$

In this case, the derivatives act on the whole propagator (5.58), rather than just the Gaussian parts. This could be applied using the Dirichlet solution to the path integral (3.29) to evaluate the stress-energy tensor [as was studied by Schäfer *et al.* (2016)]. The method suggested here applies to any potential V (assuming the solution can be found), so it could also be applied to TE and TM potentials under similar circumstances.

5.2.4. Results: TM Casimir and Casimir–Polder Energies for Planar Geometries

Figure 5.10 shows the numerical results for the efficiency η_{TM} (4.38) and compares it to the analytical expression (4.38). The numerical results were generated using the preceding methods for birth-death path swarms. The path times were sampled from Eq. (5.39), and the derivatives in Eq. (4.15) were evaluated using the Gaussian partial averaging discussed in Section 5.2.3.3.

The statistical errors are obviously much larger than their TE counterparts. The resolution of the path, N is also more coarse. Finer paths take more computation time, since there is more opportunity for branching. Attempts to test these methods at larger N have run into very large numerical fluctuations due to the increased variance. In the TE case, the convergence was found to improve as N was increased, since the systematic error decreased. In the TM case, the decreased systematic error from larger N conflicts with the growing statistical fluctuations. Of course, the numerical

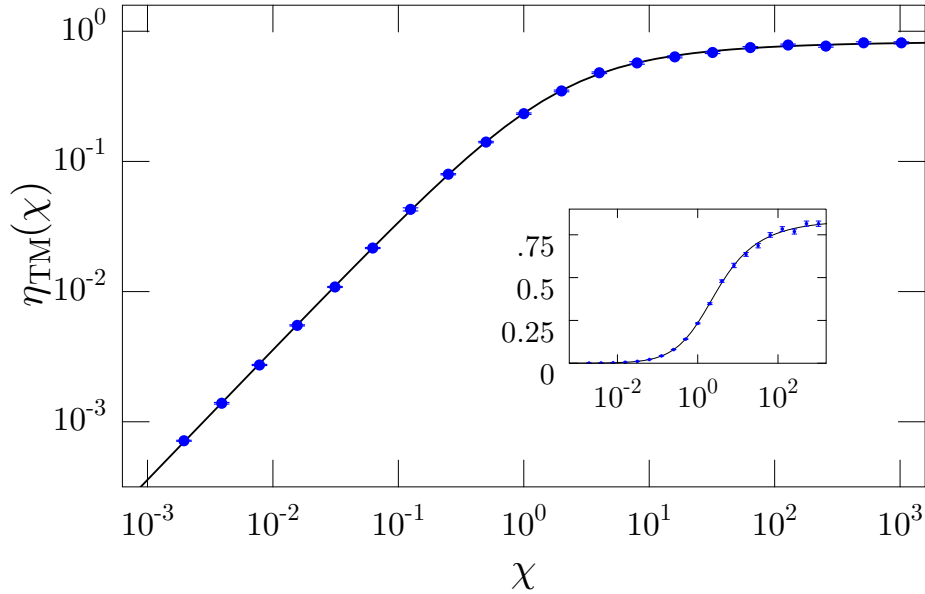


FIGURE 5.10. Numerically computed TM Casimir–Polder efficiency between an atom and a dielectric plane. Efficiency η_{TM} (4.38) is found by normalizing the numerical energy to the energy between an atom and a perfect conductor (1.1). Calculations used 10^9 initial paths, with $N = 10^3$ points per path. The birth-death method was used for path generation, and partial averaging was used for derivatives.

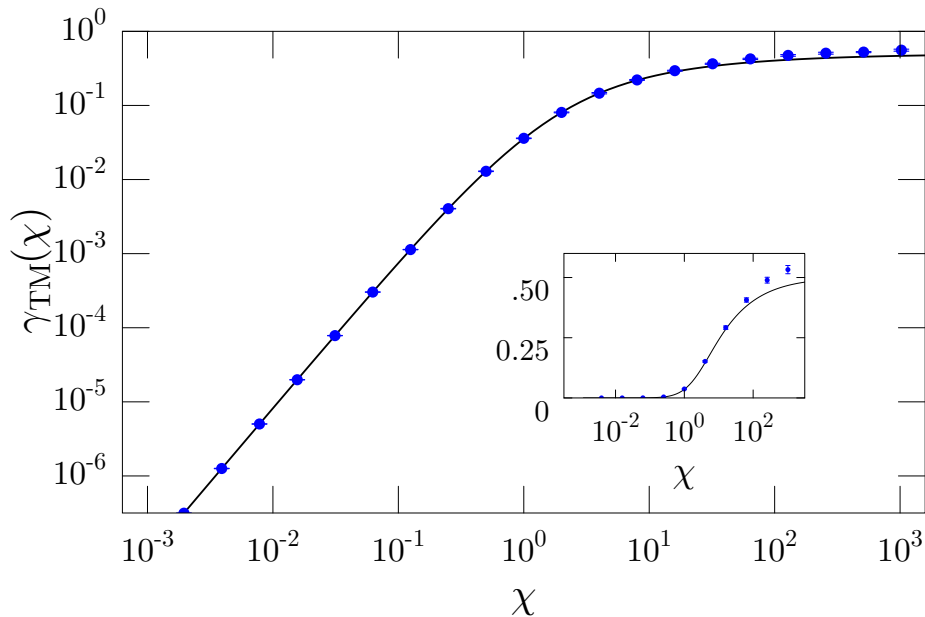


FIGURE 5.11. Numerically computed TM Casimir efficiency for two planar dielectrics. Efficiency γ_{TM} (4.63) is numerically calculated by finding the energy and normalizing to the perfect conductor limit (1.19). for $N = 200$, with 4.8×10^8 trajectories.

fluctuations can be mitigated by more averaging. In addition, each susceptibility χ is calculated individually, since the branching in the birth-death depends on the value of χ . Alternatively, this effort could be partially reduced by keeping track of the weights associated with multiple susceptibilities on a single path. In that case, the births take place when any of the weights for a given χ exceeds two. If a birth or branching occurs, then the weights for all χ are split between the two new paths. However, the death process occurs on an individual level for each χ . Only once the path reaches the end, or all of the weights have died does the path stop. It seems this approach roughly halves the computation time required to calculate the Casimir energy for multiple susceptibilities, rather than providing an $\mathcal{O}(N_\chi)$ speedup. This perhaps reflects that different classes of paths contribute at different χ , and yoking the calculations together does not offer a great speedup.

Figure 5.11 shows the numerically computed TM Casimir energy for two planar dielectrics. The numerical efficiency is found by normalizing the calculated energy to the perfect conductor result. This numerical calculated efficiency is compared with the integral solution γ_{TM} (4.63).

The TM potential in the two body case is handled by splitting the two-body potential into a product of single-body potentials:

$$\left\langle\left\langle e^{-\int_0^{\Delta\mathcal{T}} dt (V_{\text{TM}}^{(1)} + V_{\text{TM}}^{(2)})} \right\rangle\right\rangle_{x_k \rightarrow x_{k+1}} \approx \left\langle\left\langle e^{-\int_0^{\Delta\mathcal{T}} dt V_{\text{TM}}^{(1)}} \right\rangle\right\rangle_{x_k \rightarrow x_{k+1}} \left\langle\left\langle e^{-\int_0^{\Delta\mathcal{T}} dt V_{\text{TM}}^{(2)}} \right\rangle\right\rangle_{x_k \rightarrow x_{k+1}}. \quad (5.61)$$

This is only valid for $\sqrt{\Delta\mathcal{T}} \ll d$, which given that $\mathcal{T} \sim d^2$, implicitly requires that $\sqrt{N} \gg 1$. For typical calculations used in the TM case, $N \sim 100$, so the calculations do not strongly satisfy that criterion. Although we are employing analytical solutions, they are the analytical solutions for single bodies, rather than two bodies. The good

agreement suggests that the approach of using the solution for the nearest body actually does manage to recover the correct two-body energy when the potential employed varies across a path.

The birth-death method in the two body case is handled in a similar manner to the method discussed for multiple χ . The accumulated two-body and respective one-body potentials are tracked around a given path. If any of those exceeds two, the path splits and all of the weights are shared evenly across the two new paths. However the death-process occurs individually for the two-body and one-body potentials. Only at the end of the path, or when all of the paths have died are the results accumulated, or the dielectric path average used. Given that the dielectric average $\langle \epsilon_r \rangle^{-1/2}$ acts to bring the answer closer to zero, this does not miss any contributions.

The agreement is not great in this case. At large χ , the error bars do not overlap with the analytical solution. This is likely due to the very small N used in this calculation ($N = 200$), which would lead to a large systematic error. In comparison the TE calculations used $N = 10^4$. The TM Casimir results seem to be biased above the expected result. The performance is still reasonably good. This might be due to the fact that the TM energy uses an analytical solution to handle the TM potential. In the strong-coupling limit, that potential provides most of the Casimir energy. The analytical solutions capture more of the first-touching dependence than the simple estimates used for $\langle \epsilon_r \rangle$ discussed in Section 5.1.2.3. So the TM integrand performs relatively well even for a small N . However, this is probably outweighed by the increased statistical errors.

Sampling from the exponential path time distribution (5.39) is essential for the renormalized two-body TM Casimir energy. As noted earlier, the paths must touch both bodies to contribute. Given that branching is likely to occur near one surface,

those new paths may start to contribute to the Casimir energy before the initial path would.

The renormalized TM Casimir energy path integral has an additional problem. As currently implemented, the starting position for paths is randomly sampled from Eq. (5.17). The paths can start close to one surface, and spawn a number of child paths immediately. However, these paths are not guaranteed to intersect both bodies, and thus a large number of them contribute nothing to the path integral. This wastes a lot of computational effort on unimportant paths. One possible improvement to this method is to explicitly condition the path to touch both bodies. This would be another form of importance sampling, since only paths that touch both bodies will actually contribute to the path integral.

5.3. Frequency Sampling

Currently these numerical calculations ignore dispersion and nonzero temperatures, such as occur in Eq. (2.77). Given that each frequency contributes independently to the Casimir energy, the integral over frequencies could be handled in a similar fashion to handling multiple constant χ . In the TE case, the sojourn time for each body $\langle\Theta_i\rangle$ must be estimated on a pathwise basis, and then the results could be used to evaluate multiple frequencies at once using $\langle\epsilon_r(i\omega)\rangle = 1 + \sum_j \chi_j(i\omega)\langle\Theta_j\rangle$. The \mathcal{T} sampling can be carried out using the procedure discussed in Section 5.2.2. Alternatively, further Monte Carlo sampling could be used to randomly select a single frequency for each path. We anticipate these methods would also work when applied to $\epsilon_r(i\omega)$ due to the relative success of the worldline method at recovering the distance dependence (which is mostly bound up in the \mathcal{T} integral), and in capturing the efficiency at a wide range of χ . Since ϵ_r is positive along the imaginary frequency axis, capturing

the correct answer at all positive χ should translate to capturing the correct answers once ϵ_r is allowed to be a function of frequency.

CHAPTER VI

ELECTROMAGNETIC WORLDLINES: NUMERICAL FORCES AND CURVATURES FOR THE TE POLARIZATION

The preceding work has focused on computing the Casimir energy between dielectric bodies. However, a number of experiments directly measure the force, or even the second spatial derivative of the energy. For example, Chan *et al.* (2001) detected the Casimir force by measuring the shift in frequency of a nanoelectromechanical oscillator, and that frequency shift is sensitive to the second derivative (or curvature) of the Casimir energy.

As already noted in Section 5.2.3.1, the finite-difference method has some drawbacks when applied to worldline path integrals. Derivatives of discontinuous functions such as those required in worldline path integrals lead to large statistical errors. Section 5.2.3.3 develops specialized techniques for handling derivatives of Casimir–Polder energies. The current chapter develops a parallel discussion for computing the force on macroscopic bodies.

Prior investigations by Weber and Gies (2009, 2010b) computed the Casimir force in the worldline method for the Dirichlet boundary conditions. They computed the force between a planar surface and a cylindrical or spherical body, and the torque between inclined plates. Their methods typically rely on finding analytical expressions for the path times \mathcal{T} when a particular Brownian path will intersect the surfaces, and analytically integrate over the path time \mathcal{T} and path starting position \mathbf{x}_0 .

In contrast, our approach to the worldline method has also emphasized Monte Carlo integration over the path time and starting position. Section 6.1 derives the “pinning” approach, where the forces emerge from paths that are pinned to

start on the surfaces of the relevant bodies. This approach is used to derive worldline expressions for the force (6.8), potential curvature (6.14) and torque (6.19). Unfortunately, when $\chi/N \gg 1$ the pinning expressions give too small an answer, which prompts developing the “occupation” method in Section 6.2. The occupation method leads to alternative expressions for the force (6.29), potential curvature (6.33) and torque (6.32). These expressions also make contact with the approach used by Weber and Gies (2009, 2010b). These occupation expressions still work at large χ/N , but some care is needed to sample from all of the relevant classes of paths at both weak ($\chi/N \ll 1$) and strong ($\chi/N \gg 1$) coupling. Section 6.3 discusses the numerical simulations for planar media where the correspondence to the TE polarization can be used to check the numerical results. We find that even the occupation methods of Section 6.2 can fail at strong coupling. However, this is due to the strong-coupling limit requiring a rare set of paths which just “graze” the bodies. This can be confronted by either using a large ensemble of paths, or adjusting the sampling procedure to explicitly capture the strong-coupling limit. In Section 6.3.1, a “general- χ ” approach is used for small χ , and in Section 6.3.2 one possible approach to capturing the strong-coupling limit is presented.

The results in this chapter are explicitly derived for the TE worldline path integral, although presumably these results can be generalized to the TM worldline path integral. That could be done by exploiting the partial averaging methods discussed in Section 5.2.3.3. The partial averaging is necessary since directly evaluating the derivatives on the path-averaged TM potential (5.24) leads to terms like $(d - x_k)/\Delta\mathcal{T}$. Those terms have large statistical fluctuations as $\Delta\mathcal{T} \rightarrow 0$, but partial averaging could mitigate those fluctuations. [The results presented here, along with the material on partial averaging in Section 5.2.3.3 are in preparation for publication.]

6.1. Surface Pinned Paths

The renormalized TE Casimir energy was given in Eq. (4.40). Although the energy was derived under the assumptions of describing electromagnetism in planar media, it can be studied in its own right as a scalar field theory in arbitrary geometries of bodies. We will consider the following worldline path integral

$$E = \frac{\hbar c}{2(2\pi)^{D/2}} \int_0^\infty \frac{d\mathcal{T}}{\mathcal{T}^{1+D/2}} W, \quad (6.1)$$

where the integrals over the spatial coordinates in the worldline path integral are given by

$$W := \int d\mathbf{x}_0 \left\langle \left\langle \frac{1}{\langle \epsilon_r \rangle^a} - \frac{1}{[\epsilon_r(\mathbf{x}_0)]^a} \right\rangle \right\rangle_{\mathbf{x}(t)}, \quad (6.2)$$

where $a = 1/2$ when applied to TE Casimir energies in planar geometries.

In the following treatment we will consider a general geometry for computing Casimir forces between material bodies (Figure 6.1). For simplicity, we will assume uniform dielectric bodies separated by vacuum. In this case, the relative dielectric permittivity $\epsilon_r(\mathbf{r})$ is given by

$$\epsilon_r(\mathbf{r}) = 1 + \sum_j \chi_j \Theta[\sigma_j(\mathbf{r} - \mathbf{R}_j)], \quad (6.3)$$

where χ_j is the dielectric susceptibility of body j ; $\sigma_j(\mathbf{r}) = 0$ defines the surface of the j th body, with $\sigma_j > 0$ and $\sigma_j < 0$ on the interior and exterior of the body, respectively; and \mathbf{R}_j is the center of the j th body.

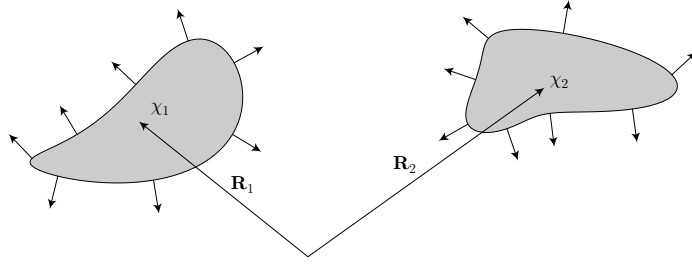


FIGURE 6.1. Sketch of the geometry for interacting dielectric bodies of susceptibility χ_j , centered at \mathbf{R}_j relative to the origin. The surface of the j th body is defined by the condition $\sigma_j = 0$. The unit normal vectors \hat{n}_j to the surface of the j th body are also shown.

6.1.1. Force

The force on a body follows from a gradient of the Casimir energy, where the derivatives are taken with respect to the body's position. For example, the components of the force on body 2, expressed with Cartesian basis vectors \hat{r}_i , are given by directional derivatives of the path integral in Eqs. (6.1) and (6.2) with respect to the components of the body position \mathbf{R}_2 . The resulting force is

$$\begin{aligned}
 F_{2,i} &:= -\frac{\hbar c}{2(2\pi)^{D/2}} \int_0^\infty \frac{d\mathcal{T}}{\mathcal{T}^{1+D/2}} \hat{r}_i \cdot \nabla_{\mathbf{R}_2} W \\
 &= -\frac{a\chi_2 \hbar c}{2(2\pi)^{D/2}} \int_0^\infty \frac{d\mathcal{T}}{\mathcal{T}^{1+D/2}} \int d\mathbf{x}_0 \left\langle \left\langle \frac{\hat{r}_i \cdot \langle \delta(\sigma_2) \nabla \sigma_2 \rangle}{\langle \epsilon_r \rangle^{a+1}} \right\rangle \right\rangle_{\mathbf{x}(t)}, \quad (6.4)
 \end{aligned}$$

where $\sigma_2 = \sigma_2[\mathbf{x}(t) - \mathbf{R}_2]$ in this expression, and $\nabla_{\mathbf{R}_i}$ denotes the gradient with respect \mathbf{R}_i . The path-averaged delta function acts to pin the paths to the surface where $\sigma_2 = 0$. Writing out the relevant part of the path integral (6.4), the delta function reduces the $D - 1$ -dimensional integration over \mathbf{x}_0 to a $(D - 2)$ -dimensional

integration over the surface of the second body, with the result

$$\begin{aligned}
& \int d\mathbf{x}_0 \left\langle \left\langle \frac{\langle \delta(\sigma_2[\mathbf{x}(t) - \mathbf{R}_2]) \nabla \sigma_2[\mathbf{x}(t) - \mathbf{R}_2] \rangle}{\langle \epsilon_r \rangle^{a+1}} \right\rangle \right\rangle_{\mathbf{x}(t)} \\
&= \oint_{\sigma_2(\mathbf{x}_0 - \mathbf{R}_2)=0} dS \left\langle \left\langle \frac{\nabla \sigma_2(\mathbf{x}_0 - \mathbf{R}_2)}{\langle \epsilon_r \rangle^{a+1} |\nabla \sigma_2(\mathbf{x}_0 - \mathbf{R}_2)|} \right\rangle \right\rangle_{\mathbf{x}(t)}. \tag{6.5}
\end{aligned}$$

This relation follows from simplifying the path-averaged delta function using Eq. (4.10), and the result (Hörmander, 1983)

$$\int d\mathbf{x} \delta[h(\mathbf{x})] f(\mathbf{x}) = \int_{h^{-1}(0)} dS \frac{1}{|\nabla h(\mathbf{x})|} f(\mathbf{x}), \tag{6.6}$$

where S is the surface defined by $h(\mathbf{x}) = 0$, and

$$|\nabla h(\mathbf{x})| = \left[\sum_k \left(\frac{\partial h}{\partial x_k} \right)^2 \right]^{1/2}. \tag{6.7}$$

The renormalized force vector can be found by summing over all force components, and subtracting the corresponding single-body force,

$$\mathbf{F}_2 = -\frac{a\chi_2\hbar c}{2(2\pi)^{D/2}} \int_0^\infty \frac{d\mathcal{T}}{\mathcal{T}^{1+D/2}} \oint_{\sigma_2(\mathbf{x}_0 - \mathbf{R}_2)=0} dS \hat{n}_2(\mathbf{x}_0) \left\langle \left\langle \frac{1}{\langle \epsilon_{r,12} \rangle^{a+1}} - \frac{1}{\langle \epsilon_{r,2} \rangle^{a+1}} \right\rangle \right\rangle_{\mathbf{x}(t)}, \tag{6.8}$$

where the unit-normal vector for the surface of the second body is defined as

$$\hat{n}_2(\mathbf{x}_0) := -\frac{\nabla \sigma_2(\mathbf{x}_0 - \mathbf{R}_2)}{|\nabla \sigma_2(\mathbf{x}_0 - \mathbf{R}_2)|}. \tag{6.9}$$

Qualitatively, the Casimir force on a body arises from paths that start on a body's surface. The direction of the force from a small patch of the surface is determined

by the local surface normal. Since each patch is at different distances from the other bodies, the paths from each patch contribute at different path times. Once the integral over the surface is carried out, this results in a net force on the body.

6.1.2. Potential Curvature

This method can be easily extended to the second derivative of the worldline energy (6.1), which computes the potential curvature,

$$C_{ij} := (\hat{r}_i \cdot \nabla_{\mathbf{R}_2})(\hat{r}_j \cdot \nabla_{\mathbf{R}_2})E. \quad (6.10)$$

For a dielectric describing two bodies, the gradients with respect to \mathbf{R}_2 can be rewritten in terms of gradients with respect to the first body's center \mathbf{R}_1 , and the path coordinates \mathbf{x}_k ,

$$\nabla_{\mathbf{R}_2} \langle \epsilon_r \rangle = \left(\sum_{k=1}^N \nabla_{\mathbf{x}_k} - \nabla_{\mathbf{R}_1} \right) [\langle \epsilon_1(\mathbf{x} - \mathbf{R}_1) \rangle + \langle \epsilon_2(\mathbf{x} - \mathbf{R}_2) \rangle], \quad (6.11)$$

where $\nabla_{\mathbf{x}_k}$ is the gradient of the path position \mathbf{x}_k . The first derivative can be carried out as before:

$$C_{ij} = \frac{a\chi_1\hbar c}{2(2\pi)^{D/2}} \int_0^\infty \frac{d\mathcal{T}}{\mathcal{T}^{1+D/2}} \int d\mathbf{x}_0 \left\langle \left\langle \hat{r}_i \cdot \left(\sum_k \nabla_{\mathbf{x}_k} - \nabla_{\mathbf{R}_1} \right) \frac{[\hat{r}_j \cdot \langle \nabla \sigma_2 \delta(\sigma_2) \rangle]}{\langle \epsilon_r \rangle^{a+1}} \right\rangle \right\rangle_{\mathbf{x}(t)}. \quad (6.12)$$

It is possible to integrate by parts with respect to \mathbf{x}_k , so that the gradient $\nabla_{\mathbf{x}_k}$ then acts on the Gaussian probability density, which yields a term proportional to $\sum_k (\mathbf{x}_k - \mathbf{x}_{k+1})$. This sum of path increments vanishes for closed paths, and thus this term can be dropped. The remaining gradient $\nabla_{\mathbf{R}_1}$ can be straightforwardly

evaluated, which yields a second independent path-averaged delta function:

$$C_{ij} = \frac{a(a+1)\chi_1\chi_2\hbar c}{2(2\pi)^{D/2}} \int_0^\infty \frac{d\mathcal{T}}{\mathcal{T}^{1+D/2}} \int d\mathbf{x}_0 \left\langle\left\langle \frac{[\hat{r}_i \cdot \langle \delta(\sigma_1) \nabla \sigma_1 \rangle] [\langle \delta(\sigma_2) \nabla \sigma_2 \rangle \cdot \hat{r}_j]}{\langle \epsilon_r \rangle^{a+2}} \right\rangle\right\rangle_{\mathbf{x}(t)}. \quad (6.13)$$

One delta function can be manipulated as in Eq. (6.5) to pin the paths to start on the first body, while the second path-averaged delta function pins another point of the path to the second body. There is then a further average over which point is pinned to the second surface. The resulting expression for the potential curvature is

$$C_{ij} = \frac{a(a+1)\chi_1\chi_2\hbar c}{2(2\pi)^{D/2}} \int_0^\infty \frac{d\mathcal{T}}{\mathcal{T}^{1+D/2}} \oint_{\sigma_1(\mathbf{x}_0 - \mathbf{R}_1) = 0} dS_0 \frac{1}{N} \sum_{k=1}^{N-1} \oint_{\sigma_2(\mathbf{x}_k - \mathbf{R}_2) = 0} dS_k \times \left\langle\left\langle \mathcal{G}(\mathbf{x}_0 - \mathbf{x}_k, k(N-k)\mathcal{T}/N^2) \frac{[\hat{r}_i \cdot \hat{n}_1(\mathbf{x}_0)][\hat{r}_j \cdot \hat{n}_2(\mathbf{x}_k)]}{\langle \epsilon_{r,12} \rangle^{a+2}} \right\rangle\right\rangle_{\sigma_2(\mathbf{x}_k - \mathbf{R}_2) = 0}, \quad (6.14)$$

where $\langle\langle \dots \rangle\rangle_{\sigma_2(\mathbf{x}_k - \mathbf{R}_2) = 0}$ is the ensemble average over discrete paths $\mathbf{x}(t)$ subject to the constraint that $\sigma_2(\mathbf{x}_k - \mathbf{R}_2) = 0$. The $D - 1$ -dimensional Gaussian probability density

$$\mathcal{G}(\mathbf{x}, \sigma^2) = \frac{e^{-(\mathbf{x})^2/2\sigma^2}}{[2\pi\sigma^2]^{(D-1)/2}}, \quad (6.15)$$

has been used to write the combined normalization factor for Brownian bridges propagating from \mathbf{x}_0 to \mathbf{x}_k in k steps, and returning to \mathbf{x}_0 in $N - k$ steps. There is no need for any further renormalization, since this expression is only non-zero in the presence of both bodies, and \mathcal{G} exponentially cuts off the integral at small \mathcal{T} .

6.1.3. Torque

The torque on a body can be found from the first-order variation in the energy as that body is rotated about some axis. For concreteness, consider perturbing the dielectric function by rotating the second body about its center by angle ϕ about axis \hat{m} :

$$\epsilon_r(\mathbf{x}) = 1 + \chi_1 \Theta[\sigma_1(\mathbf{x} - \mathbf{R}_1)] + \chi_2 \Theta\{\sigma_2[\mathcal{R}(\phi)(\mathbf{x} - \mathbf{R}_2)]\}. \quad (6.16)$$

The infinitesimal rotation matrix is

$$\mathcal{R}_{ij}(\phi) = \delta_{ij} - m_k \epsilon_{ijk} \phi + \mathcal{O}(\phi^2), \quad (6.17)$$

where δ_{ij} is the Kronecker delta, and ϵ_{ijk} is the antisymmetric Levi-Civita tensor. Throughout this section there are implicit sums over repeated indices. The torque for a rotation about axis \hat{m} can be written as $K_m = -\partial_\phi E$. The ϕ derivative only acts on the path-averaged dielectric part of the energy integrand,

$$\begin{aligned} \partial_\phi \langle \epsilon \rangle &= \chi_2 \langle \partial_\phi \mathcal{R}_{ij}(\phi)(\mathbf{x} - \mathbf{R}_2)_j [\hat{r}_i \cdot \nabla \Theta(\sigma_2)] \rangle \\ &= \chi_2 \hat{m} \cdot \langle (\mathbf{x} - \mathbf{R}_2) \wedge \nabla \Theta(\sigma_2) \rangle, \end{aligned} \quad (6.18)$$

where we used Eq. (6.17) to write the result as a cross product¹ via $(\mathbf{a} \wedge \mathbf{b})_i = \epsilon_{ijk} a_j b_k$. This derivative can be directly substituted into the torque path integral, and similar manipulations to those in Eq. (6.5) can be carried out to pin the paths to the surface of the second body. The total torque on the body can be found by adding up the torques for infinitesimal rotations about each of the Cartesian axes (*i.e.* taking \hat{m} to

¹ The wedge operator \wedge denotes the vector cross product to avoid confusion with the traditional multiplication sign \times , which denotes multi-line multiplication throughout this thesis.

be each Cartesian axis in turn, and summing the results). The renormalized torque worldline path integral is

$$\mathbf{K} = \frac{a\hbar c\chi_2}{2(2\pi)^{D/2}} \int_0^\infty \frac{d\mathcal{T}}{\mathcal{T}^{1+D/2}} \oint_{\sigma_2(\mathbf{x}_0 - \mathbf{R}_2)=0} dS_0 [(\mathbf{x}_0 - \mathbf{R}_2) \wedge \hat{n}_2(\mathbf{x}_0)] \left\langle\left\langle \frac{1}{\langle \epsilon_{r,12} \rangle^{a+1}} - \frac{1}{\langle \epsilon_{r,2} \rangle^{a+1}} \right\rangle\right\rangle_{\mathbf{x}(t)}. \quad (6.19)$$

This has a similar form to the force path integral (6.8). Here the integrand is weighted by the cross product of the vector from the body's center the surface, and the surface normal. If the spatial integrand in Eq. (6.8) is loosely interpreted as a force density, then the torque integrand for each patch of the surface can interpreted as the local torque density. This is in direct analogy with the expression for the torque $\mathbf{K} = \mathbf{r} \wedge \mathbf{F}$ from classical mechanics.

6.1.4. Casimir–Polder Force

An alternative expression for the Casimir–Polder force on an atom near a surface can be found in analogy to the potential curvature in Eq. (6.14). The force on the atom due to the TE Casimir effect is $F_{\text{CP},i}^{(\text{TE})} = -\hat{r}_i \cdot \nabla_{\mathbf{r}_A} V_{\text{CP}}^{(\text{TE})}$. In Section 5.2.3.3 the derivatives of the path integral were taken directly, and the only contribution to the derivative came from the Gaussian probability distribution. Alternatively, one can change the coordinates to $\mathbf{x}(t) = \mathbf{r}_A + \mathbf{y}(t)$, where $\mathbf{y}(t)$ is a Brownian bridge starting and returning to the origin, $\mathbf{y}(0) = \mathbf{y}(\mathcal{T}) = 0$. Then after taking the desired derivatives with respect to the components of \mathbf{r}_A , the force is

$$F_i^{(\text{TE})} = -\frac{\hbar c\alpha_0}{4(2\pi)^{D/2}} \int_0^\infty \frac{d\mathcal{T}}{\mathcal{T}^{1+D/2}} \left\langle\left\langle \hat{r}_i \cdot \nabla_{\mathbf{r}_A} \langle \epsilon_r \rangle^{-3/2} \right\rangle\right\rangle_{\mathbf{y}(t)}, \quad (6.20)$$

where \hat{r}_i is a Cartesian unit vector. This path integral considers the change in energy as the whole path is rigidly translated, while the results in Section 5.2.3.3 correspond to shifting only the origin of the path, while keeping the rest of the path fixed. The derivatives create delta functions for piece-wise constant media. In analogy with the potential curvature, since the starting point is fixed, it is necessary to average over pinning other path points to the dielectric surface for each of the bodies. The Casimir–Polder force, after summing over all force components, is

$$\mathbf{F}_{\text{CP}}^{(\text{TE})} = -\frac{3\hbar c\alpha_0}{8(2\pi)^{D/2}} \sum_{i=1}^{N_b} \sum_{k=1}^{N-1} \frac{\chi_i}{N} \int_0^\infty \frac{d\mathcal{T}}{\mathcal{T}^{1+D/2}} \oint_{\sigma_i(\mathbf{x}_k - \mathbf{R}_i)=0} dS_k \\ \times \left\langle\left\langle \mathcal{G}[\mathbf{r}_A - \mathbf{x}_k, k(N-k)\mathcal{T}/N^2] \frac{\hat{v}_i(\mathbf{x}_k)}{\langle\epsilon_r\rangle^{5/2}} \right\rangle\right\rangle_{\sigma_i(\mathbf{x}_k - \mathbf{R}_i)=0}, \quad (6.21)$$

where we have reverted to using $\mathbf{x}(t)$, and \mathcal{G} is given by Eq. (6.15). In this method the paths are constrained to touch the bodies. This must be taken into account numerically by averaging over which index along the paths is constrained. By contrast, the Hermite-Gaussian method discussed in Section 5.2.3.3 can use the same ensemble of paths regardless of the dielectric background. While the path-pinning method requires more complicated methods for path generation, it does not suffer from diverging fluctuations as the path resolution is increased. The Gaussian factor \mathcal{G} exponentially suppresses contributions from pinning small indices k , which would be the problematic terms as $\Delta\mathcal{T} \rightarrow 0$, and thus this method does not require careful handling as N increases. This is in contrast to the Hermite-Gaussian method which required partial averaging to avoid growing statistical errors as N increased. However, any further derivatives would require the techniques used in Section 5.2.3.3.

6.2. Occupation Number

The preceding methods offer an intuitive picture of the Casimir force, however they are poorly behaved in the strong-coupling limit. For a typical discrete path of N steps pinned to the surface, a substantial fraction of the path will lie inside the body. For $\chi \gg N$, the denominator $\langle \epsilon_r \rangle^{-(a+1)}$ dominates the integrand, so the estimated derivatives decay as χ^{-a} for almost all paths, where $a = 1/2$ for Casimir energies. Only rare paths that start on the surface, but do not enter the bulk of the body will contribute substantially. As a result, the numerically estimated force will likewise decay in the strong-coupling limit. In this section we develop alternative expressions that behave better in the strong-coupling limit. This method also makes contact with the work by Weber and Gies (2009, 2010b) on forces and torques for Dirichlet worldlines.

The spatial path integral (6.2) can be written in exponential form via the inverse-moment theorem (4.22),

$$W = \frac{1}{\Gamma[a]} \int d\mathbf{x}_0 \int ds s^{a-1} e^{-s} \left\langle\left\langle e^{-\langle \sum_i \chi_i \Theta_i(\mathbf{x}) \rangle} - e^{-\sum_i \chi_i \Theta_i(\mathbf{x}_0)} \right\rangle\right\rangle_{\mathbf{x}(t)}, \quad (6.22)$$

where we have introduced the shorthand notation $\Theta_i(\mathbf{x}) = \Theta[\sigma_i(\mathbf{x} - \mathbf{R}_i)]$. After the single body energies $e^{-\langle \chi_i \Theta_i(\mathbf{x}) \rangle}$ have been subtracted, the renormalized two body energy can be factorized as

$$W = \frac{1}{\Gamma[a]} \int d\mathbf{x}_0 \int ds s^{a-1} e^{-s} \left\langle\left\langle (e^{-\langle \chi_1 \Theta_1(\mathbf{x}) \rangle} - 1)(e^{-\langle \chi_2 \Theta_2(\mathbf{x}) \rangle} - 1) - (e^{-\chi_1 \Theta_1(\mathbf{x}_0)} - 1)(e^{-\chi_2 \Theta_2(\mathbf{x}_0)} - 1) \right\rangle\right\rangle_{\mathbf{x}(t)}. \quad (6.23)$$

The exponentials can be simplified as

$$e^{-s\langle\chi_i\Theta_i(\mathbf{x})\rangle} = \prod_{k=1}^{N-1} e^{-s\chi_i\Theta_i(\mathbf{x}_k)/N} = \prod_{k=0}^{N-1} [1 + \Theta_i(\mathbf{x}_k)(e^{-s\chi_i/N} - 1)]. \quad (6.24)$$

(The results in Section 6.1 can be recovered when $\chi/N \ll 1$.)

The force on the second body can be computed by differentiating the energy with respect to the body position \mathbf{R}_2 . The spatial part of the force integral can be written

$$\begin{aligned} \mathbf{F}_2 &:= -\nabla_{\mathbf{R}_2} W \\ &= -\frac{1}{\Gamma[a]} \int d\mathbf{x}_0 \int ds s^{a-1} e^{-s} \left\langle \left(1 - \prod_{k=0}^{N-1} [1 + \Theta_1(\mathbf{x}_k)(e^{-s\chi_1/N} - 1)] \right) \right. \\ &\quad \left. \times \sum_{j=0}^{N-1} \left\{ (e^{-s\chi_2/N} - 1) \mathbf{n}_2(\mathbf{x}_j) \delta[\sigma_2(\mathbf{x}_j - \mathbf{R}_2)] \prod_{k \neq j} [1 + \Theta_2(\mathbf{x}_k)(e^{-s\chi_2/N} - 1)] \right\} \right\rangle_{\mathbf{x}(t)}, \end{aligned} \quad (6.25)$$

where the constant term from renormalization has zero derivative. The integral over s can be carried out more easily if the integrand is rearranged into terms with a definite number of points n inside each body i . We define the indicator functions as

$$\mathbb{1}_0^{(i)} := \prod_{j=0}^{N-1} [1 - \Theta_i(\mathbf{x}_j)] \quad (6.26)$$

$$\mathbb{1}_n^{(i)} := \sum_{j_1=1}^{N-1} \sum_{j_2>j_1} \cdots \sum_{j_n>j_{n-1}} \Theta_i(\mathbf{x}_{j_1}) \Theta_i(\mathbf{x}_{j_2}) \cdots \Theta_i(\mathbf{x}_{j_n}) \quad (n \geq 1), \quad (6.27)$$

where $\mathbb{1}_n^{(i)} = 1$ when there are exactly n points inside body i , and zero otherwise; there are n sums over indices j_n , each of which terminates at $j_n = N$. There are further restrictions on which of these terms contribute to the integrand. Due to the

presence of the delta functions, only $N - 1$ points are free to enter the bodies. This further implies that the number of points inside both bodies must be less than $N - 1$. Finally, due to the renormalization, only paths with at least one point inside the first body contribute. Using the indicator functions, the rearranged spatial path integral for the force is

$$\mathbf{F}_2 = - \int d\mathbf{x}_0 \int ds s^{a-1} e^{-s} \left\langle\left\langle \sum_{j=0}^{N-1} \hat{n}_2(\mathbf{x}_j) \delta[\sigma_2(\mathbf{x}_j - \mathbf{R}_2)] \right. \right. \\ \left. \left. \times \sum_{n=0}^{N-1} (e^{-s(n+1)\chi_2/N} - e^{-sn\chi_2/N}) \mathbb{1}_n^{(2)} \sum_{m=1}^{N-n-1} (1 - e^{-sm\chi_1/N}) \mathbb{1}_m^{(1)} \right\rangle\right\rangle_{\mathbf{x}(t)}. \quad (6.28)$$

The s integral can be carried out term by term, and the delta function can be used to pin paths onto the surface. The cyclic-permutation invariance of the integrand can be used to remove the path-average over pinning, as in Eq. (6.5). The force path integral becomes

$$\mathbf{F}_2 = - \frac{\hbar c N}{2(2\pi)^{D/2}} \int_0^\infty \frac{d\mathcal{T}}{\mathcal{T}^{1+D/2}} \oint_{\sigma_2(\mathbf{x}_0 - \mathbf{R}_2) = 0} dS_0 \hat{n}_2(\mathbf{x}_0) \sum_{m=0}^{N-1} \sum_{n=1}^{N-m-1} \left\langle\left\langle \mathbb{1}_m^{(1)} \mathbb{1}_n^{(2)} f_{m,n} \right\rangle\right\rangle_{\mathbf{x}(t)}. \quad (6.29)$$

where the material dependence is carried by the factors

$$f_{m,n} := c_{m,n} - c_{m,n+1} - c_{0,n} + c_{0,n+1}, \quad (6.30)$$

$$c_{m,n} := \left(1 + \frac{m\chi_1 + n\chi_2}{N} \right)^{-a}, \quad (6.31)$$

which come from computing the change in the renormalized energy integrand as another point enters the second body. When $\chi_2/N \ll 1$, an expansion of $f_{m,n}$ to leading order in χ_2/N , recovers the earlier result, Eq. (6.8) for the force.

In this result, the indicator functions carry the geometry dependence of whether a given number of points are within each body, while $f_{n,m}$ carries the dependence of the material properties based on the number of points inside each body. This expression is well-behaved in the strong-coupling $\chi \rightarrow \infty$ limit, where only the terms where $n = 0$ and $m > 0$ contribute. In the strong-coupling limit, the main contribution to the force comes from paths that “graze” the second surface, while also overlapping the first body.

For completeness we note the analogous expressions for the torque and potential curvature. The manipulations and reasoning used in Section 6.1 for the torque and potential curvature apply here—the only difference is the form chosen for the derivative, and the use of the indicator functions in the integrand. The torque path integral is

$$\mathbf{K}_2 = -\frac{\hbar c N}{2(2\pi)^{D/2}} \int_0^\infty \frac{d\mathcal{T}}{\mathcal{T}^{1+D/2}} \oint_{\sigma_2(\mathbf{x}_0 - \mathbf{R}_2)=0} dS_0 \sum_{m=0}^{N-1} \sum_{n=1}^{N-m-1} \times \left\langle\left\langle [(\mathbf{x}_0 - \mathbf{R}_2) \wedge \hat{n}_2(\mathbf{x}_0)] \mathbb{1}_m^{(1)} \mathbb{1}_n^{(2)} f_{m,n} \right\rangle\right\rangle_{\mathbf{x}(t)}. \quad (6.32)$$

The potential curvature is given by

$$C_{ij} = \frac{\hbar c N}{2(2\pi)^{D/2}} \sum_{k=1}^{N-1} \int_0^\infty \frac{d\mathcal{T}}{\mathcal{T}^{1+D/2}} \oint_{\sigma_1(\mathbf{x}_0 - \mathbf{R}_1)=0} dS_0 \hat{r}_i \cdot \hat{n}_1(\mathbf{x}_0) \oint_{\sigma_2(\mathbf{x}_k - \mathbf{R}_2)=0} dS_k \hat{r}_j \cdot \hat{n}_2(\mathbf{x}_k) \times \sum_{m=0}^{N-2} \sum_{n=0}^{N-m-2} \left\langle\left\langle \mathcal{G}(\mathbf{x}_0 - \mathbf{x}_k, k(N-k)\mathcal{T}/N^2) \mathbb{1}_m^{(1)} \mathbb{1}_n^{(2)} g_{m,n} \right\rangle\right\rangle_{\sigma_2(\mathbf{x}_k - \mathbf{R}_2)=0}, \quad (6.33)$$

where

$$g_{m,n} = c_{m+1,n+1} + c_{m,n} - c_{m+1,n} - c_{m,n+1}, \quad (6.34)$$

accounts for the change in the energy integrand as the number of points in the first and second bodies increase. In the strong-coupling limit, the potential curvature is dominated by terms with $n = m = 0$, which correspond to paths that graze both bodies.

The formulation for the Casimir force in Eq. (6.29) is analogous to the construction of paths employed by Weber and Gies (2010b) for computing forces in the sphere-plane and cylinder-plane geometries in the Dirichlet limit. In that work, the paths are shifted so that they start on the plane, but do not pass through the plane. The force on the planar surface is computed by integrating over the values of \mathcal{T} when the path intersects the other surface. The expressions presented here extend their expressions by accounting for finite χ , and accounting for arbitrary geometries.

In general, different classes of paths are important in the finite- χ and strong-coupling cases. At small χ , the most important path statistic is the sojourn time, while in the strong-coupling regime, the first path time when the path intersects the bodies is the most important statistic. This correspondence was used to discuss the numerical convergence properties of the method as the path length was varied. [There is a brief discussion on this point in Section 5.1.3.1, and an extended discussion in Mackrory *et al.* (2016).] More practically, these different requirements make it difficult to use a single class of path to efficiently evaluate the potential at all χ . In weak coupling, the paths should enter all of the bodies, while in strong coupling the most important paths are those that just touch the surfaces.

It is important to distinguish between two facets of the different methods. The first is the choice of starting points for the paths, and the second is the form of the integrand. In the path-pinning or occupation methods, we are free to consider a single path $\{B_j\}$ starting at x_0 : $x_j = x_0 + \sqrt{T}B_j$. There is also an associated family of

paths starting at x_0 that translate the original Brownian path by $-\sqrt{T}B_k$, such that $x_j^{(k)} = x_0 + \sqrt{T}(B_j - B_k)$. This transformation effectively shifts the bridge so that B_k is at the origin. This sampling is essential for strong-coupling limits where only paths that graze the bodies contribute to the force or potential curvature. However, the choice of how to shift that paths is distinct from the choice of the integrand. In the strong-coupling limit, all of the path-pinning estimates are zero, regardless of the ensemble of paths used. In the occupation methods that is not true, but some care is required to ensure that both types of paths are used in the strong-coupling limit.

6.3. Force and Curvature Numerics

The numerical computations were carried out in planar media with the dielectric function,

$$\epsilon_r(x) = 1 + \chi\Theta(-x + d_1) + \chi\Theta(x - d_2). \quad (6.35)$$

This allows us to compare the numerical results to the TE Casimir force. For a non-dispersive material the Casimir force is proportional to the energy, and thus the same efficiency factor (4.51) is the appropriate normalized result. Figure 6.2 shows the numerically calculated force on two dielectric planes of equal dielectric constant, normalized to the total EM force between perfect-conducting plates. This computation was carried out for the pinning, occupation and finite-difference methods. In all cases, the paths were generated using the v-loop algorithm (5.10), and the dielectric path averages were calculated using the trapezoidal method (5.19). Note that in computing path averages for the occupation method, only points *inside* the body contribute—any points pinned to the surface do not contribute to the dielectric path-average.

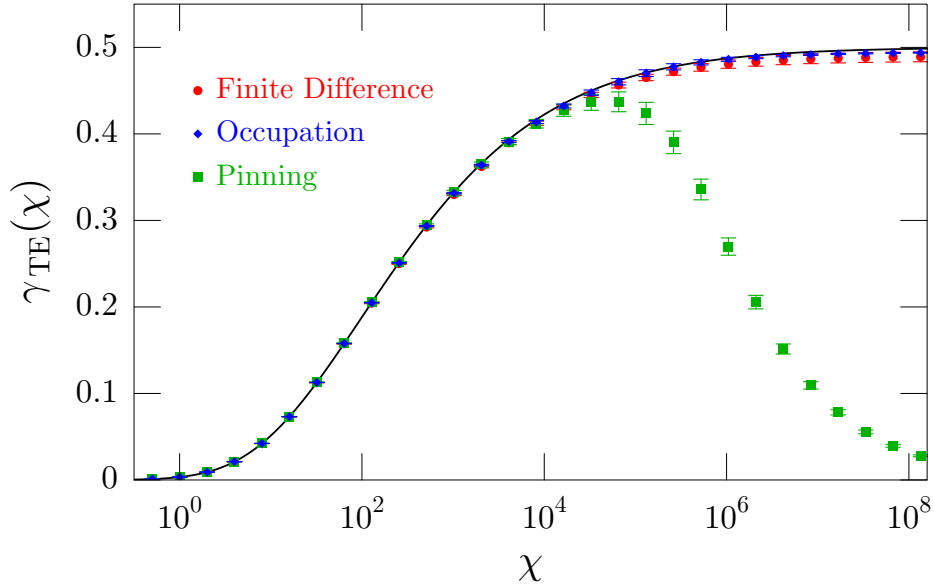


FIGURE 6.2. (Preliminary data) Numerically computed TE force for pinning (squares), occupation (diamonds), and finite difference (circles) methods. The finite difference used a step-size $\delta = d/\sqrt{N}$. The calculations used $N = 10^4$ points per path, and 10^8 trajectories.

The pinning methods discussed in Section 6.1 start to fail for $\chi \gtrsim N$, as expected. For $\chi \gg N$, the estimate of the force shows the expected $\chi^{-1/2}$ decay. For a finite susceptibility, it should be possible to carry out the calculation for large enough N , but if one is interested in the strong-coupling regime of this theory, then the pinning method is unsuitable.

By contrast, the occupation method is better behaved in the strong-coupling limit. The occupation-method estimate for the force is computed by generating an initial path $\{\mathbf{y}_k\}$, and translating it via $\mathbf{x}_k = \mathbf{y}_k - \mathbf{y}_j + \mathbf{d}$, so that that each point \mathbf{x}_j lies on the surface. The results are then averaged over all such pinnings. However, naively implementing this method leads to N evaluations of the path integral, which could be inefficient. It may be possible to capture both strong-coupling and general-coupling regimes with only two samples. First, in order to capture the strong-coupling limit the path integral can be computed for a path where only one point is on the first

surface, and no points are inside the first body. Second, to capture the remaining χ -dependence, the integrand should be calculated again for a path where a randomly selected point is pinned to the first surface, without any constraints on the other occupation numbers. The strong coupling estimate for the force f_s , and the general- χ estimate f_g , are combined with weights N^{-1} and $(N - 1)/N$ respectively, which account for enforcing the restrictions.

In the absence of that step to explicitly capture the strong-coupling limit, only very rare paths will contribute, since most random paths starting on the surface are equally like to explore both positive and negative regions. Most paths will intersect both bodies, and contribute zero to the force. For small ensembles ($N_{\text{path}} \leq 10^7$) this causes similar convergence problems to the pinning methods at large χ . However, this would be a statistical error due to insufficient sampling, as opposed to the intrinsic problems in the pinning method. Similar methods will be discussed in more detail regarding the potential curvature.

In fact, the general- χ samples were gathered using stratified sampling, where the path index k was broken into uniform strata. This basically splits the sum into multiple pieces and samples from each of those sub-pieces. For example,

$$\sum_{k=1}^N a_k = \sum_{j=1}^{N_{\text{strata}}} \sum_{n=1}^{N_{\text{sub}}} a_{n+j N_{\text{sub}}}, \quad (6.36)$$

where $N_{\text{sub}} N_{\text{strata}} = N$. Each stratum was then sampled from uniformly. In the calculations in Figure 6.2, ten strata were used.

Given the deficiencies of the pinning method for finite paths, we will compute the potential curvature using the occupation method. Since the potential curvature requires paths pinned on two different surfaces, and will exhibit similar convergence

issues at strong coupling, we will develop two different approaches to generating paths and sampling times.

6.3.1. Direct Path Construction for General- χ Coupling Method for Potential Curvature

In a method suitable for general coupling, all of the paths start on the surface of the first body, and are explicitly constructed to intersect the second body after k steps, where the index k is also sampled randomly. The paths can be explicitly constructed as Brownian bridges from $x = 0$ to $x_k = d$, using Eq. (5.8). The Gaussian factor $\mathcal{G}[d, k(N - k)\mathcal{T}/N^2]$ in Eq. (6.33) is used to sample path times by treating it and $\mathcal{T}^{-(1+D/2)}$ as the gamma distribution in \mathcal{T} . Path times can be sampled from Eq. (5.39), with $\mathcal{T}_0 = N^2 d^2 / [2k(N - k)]$ and $a = 1 + (D + 1)/2$. The pinned point k can be sampled from the combination of \mathcal{T}_0^{1-a} for normalization $P(\mathcal{T})$ and the normalization constant from $\mathcal{G}[d, k(N - k)\mathcal{T}/N^2]$, with distribution

$$P_{\text{pin}}(k; N) = \mathcal{N}_{\text{pin}} \left(\frac{k(N - k)}{N^2} \right)^{D/2}, \quad (6.37)$$

where $\mathcal{N}_{\text{pin}} = \sum_{k=1}^N P(k; N) \approx N/30$ for large N . In addition for planar surfaces, the integral over the transverse dimensions amounts to an area factor.

The expression for the potential curvature for general- χ coupling is

$$C_{ij} = \frac{\hbar c N}{2(2\pi)^{D/2}} \sum_{k=1}^{N-1} \oint_{\sigma_1(\mathbf{x}_0 - \mathbf{R}_1)=0} dS_0 \left\langle \left\langle \oint_{\sigma_2(\mathbf{x}_k - \mathbf{R}_2)=0} dS_k \frac{3\mathcal{N}_{\text{pin}}[\hat{r}_i \cdot \hat{n}_1(\mathbf{x}_0)][\hat{r}_j \cdot \hat{n}_2(\mathbf{x}_k)]}{|\mathbf{x}_0 - \mathbf{x}_k|^5} \right. \right. \\ \left. \left. \sum_{n=0}^{N-2} \sum_{m=0}^{N-n-2} \mathbb{1}_n^{(1)} \mathbb{1}_m^{(2)} g_{m,n} \right\rangle \right\rangle_{k, \mathcal{T}, \mathbf{x}_0 \leftrightarrow \mathbf{x}_k}, \quad (6.38)$$

where the ensemble average is over path times, pinning separations k , and Brownian bridges from \mathbf{x}_0 to \mathbf{x}_k , where \mathbf{x}_0 is on the first surface, and \mathbf{x}_k is on the second surface.

In Figure 6.3, we have used this general- χ coupling method to compute the potential curvature without special treatment for strong coupling, with two different ensemble sizes to show the effect of additional averaging. The general- χ coupling integrand does eventually lead to the correct answer in the strong-coupling limit once enough averaging has taken place. However, achieving that convergence requires a large ensemble to capture the relatively rare, but important, paths that just graze both surfaces. Performance can be improved by introducing separate estimates adapted for the strong-coupling limit.

This suggests a two-fold approach: First, paths should be generated under the constraint that they touch both surfaces without regard for their occupation time (which will capture general χ). Second, another set of paths should be generated which just touch the bodies (which will capture large χ).

6.3.2. Softened Delta Function Pinning for Strong-Coupling Limit for Potential Curvature

An alternative method to the one presented in Section (6.3.1), one more suited to the strong-coupling limit, arises from a different treatment of the second delta function $\delta[\sigma_2(\mathbf{x}_k - \mathbf{R}_2)]$. In this case, the first delta function $\delta[\sigma_1(\mathbf{x}_0 - \mathbf{R}_1)]$, is still used to pin the paths to start on the first body. Although the paths are assumed to start on the surface of the first body, they do not enter the bulk of that body. In order to contribute to the curvature path integral in the strong-coupling limit, the paths should move towards the second body, and just graze its surface.

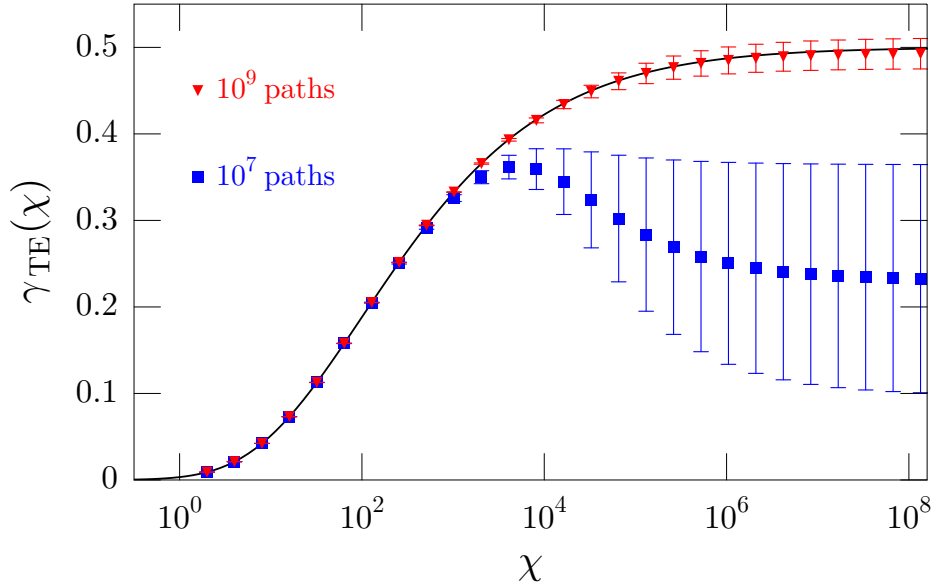


FIGURE 6.3. Numerically computed second derivative of potential for two planar surfaces as function of dielectric, for $N = 10^5$, each with 10^7 and 10^9 trajectories. All results are computed using the “occupation” method with general- χ coupling method presented in Eq. (6.33).

The goal of this method is to develop a way of handling delta function constraints within a path integral without having to drastically change the way the paths are generated. This would be particularly useful for handling pinning in an application involving paths that are hard to construct, such as the TM-Gaussian paths discussed in Section 5.2.1.1. In the resulting method, any path can in principle contribute, even if only a few of them will give an important contribution.

6.3.2.1. Softened Delta Function Pinning

Let us consider the term involving $\delta[\sigma_2(\mathbf{x}_k - \mathbf{R}_2)]$ from the curvature path integral (6.33). After suppressing the integrals over S_0 and \mathcal{T} , as well as the leading

constants, the remaining spatial path integral can be written in a schematic form as

$$I = \frac{1}{(2\pi\mathcal{T})^{(D-1)/2}} \left\langle\left\langle \delta[f(\mathbf{x}_k)]\Phi(\mathbf{x}_1, \dots, \mathbf{x}_{N-1}) \right\rangle\right\rangle_{\mathbf{x}(t)} \quad (6.39)$$

$$= \int \prod_{n=1}^{N-1} d\mathbf{x}_n \prod_{k=0}^{N-1} \left(\frac{e^{-(\mathbf{x}_{k+1}-\mathbf{x}_k)^2/(2\Delta\mathcal{T})}}{(2\pi\Delta\mathcal{T})^{(D-1)/2}} \right) \delta[f(\mathbf{x}_k)]\Phi(\mathbf{x}_1, \dots, \mathbf{x}_{N-1}), \quad (6.40)$$

where $f(\mathbf{x}_k)$ and Φ are placeholders for the constraint $\sigma_2(\mathbf{x}_k - \mathbf{R}_2)$, and integrand $\sum_n \sum_m \mathbb{1}_m^{(1)} \mathbb{1}_n^{(2)} g_{m,n}$, respectively. There is no Gaussian term, since that only arises after pinning the paths, and normalizing for pinned Brownian bridges.

Instead of just evaluating the integral over \mathbf{x}_k (which pins the paths), the integral can be multiplied by a factor of unity of the form:

$$1 = \frac{(2\pi\Delta\mathcal{T})^{-(D-1)} \int d\mathbf{y}_k e^{-(\mathbf{x}_{k+1}-\mathbf{y}_k)^2/(2\Delta\mathcal{T})-(\mathbf{y}_k-\mathbf{x}_{k-1})^2/(2\Delta\mathcal{T})}}{(4\pi\Delta\mathcal{T})^{-(D-1)/2} e^{-(\mathbf{x}_{k+1}-\mathbf{x}_{k-1})^2/(4\Delta\mathcal{T})}}. \quad (6.41)$$

This involves multiplying and dividing by an unconstrained integral connecting \mathbf{x}_{k-1} and \mathbf{x}_{k+1} via a new coordinate \mathbf{y}_k . The integral has been evaluated in the denominator. Then the constrained integral (6.40) can now be written

$$I = \int d\mathbf{y}_k \int \prod_{n=1}^{N-1} d\mathbf{x}_n \prod_{k=0}^{N-1} \left(\frac{e^{-(\mathbf{x}_{k+1}-\mathbf{x}_k)^2/(2\Delta\mathcal{T})}}{(2\pi\Delta\mathcal{T})^{(D-1)/2}} \right) \frac{e^{-(\mathbf{x}_{k+1}-\mathbf{y}_k)^2/(2\Delta\mathcal{T})-(\mathbf{y}_k-\mathbf{x}_{k-1})^2/(2\Delta\mathcal{T})}}{(2\pi\Delta\mathcal{T})^{D-1}} \\ \times (4\pi\Delta\mathcal{T})^{(D-1)/2} e^{(\mathbf{x}_{k+1}-\mathbf{x}_{k-1})^2/(4\Delta\mathcal{T})} \delta[f(\mathbf{x}_k)]\Phi(\mathbf{x}_1, \dots, \mathbf{x}_k, \dots, \mathbf{x}_{N-1}). \quad (6.42)$$

The label for the constrained coordinate \mathbf{x}_k and the unconstrained coordinate \mathbf{y}_k can be swapped using $\mathbf{x}_k \leftrightarrow \mathbf{y}_k$. The unconstrained coordinates \mathbf{x}_k will then be used with all of the other coordinates to create free Brownian bridges, and $\delta[f(\mathbf{y}_k)]$ is now isolated in an auxiliary integral. The path integral can be written in ensemble-

averaged form,

$$I = \frac{1}{(2\pi\mathcal{T})^{(D-1)/2}} \left\langle\left\langle \int d\mathbf{y}_k \frac{e^{-(\mathbf{y}_k - \bar{\mathbf{x}}_k)^2/\Delta\mathcal{T}}}{(\pi\Delta\mathcal{T})^{(D-1)/2}} \delta[f(\mathbf{y}_k)] \Phi(\mathbf{x}_1, \dots, \mathbf{y}_k, \dots, \mathbf{x}_{N-1}) \right\rangle\right\rangle, \quad (6.43)$$

where $\bar{\mathbf{x}}_k := (\mathbf{x}_{k-1} + \mathbf{x}_{k+1})^2$, and the exponential terms were combined using

$$(\mathbf{x}_{k+1} - \mathbf{y}_k)^2 + (\mathbf{y}_k - \mathbf{x}_{k-1})^2 - \frac{(\mathbf{x}_{k+1} - \mathbf{x}_{k-1})^2}{2} = 2(\mathbf{y} - \bar{\mathbf{x}}_k)^2. \quad (6.44)$$

Now the delta function can be integrated over using Eq. (6.6), with the result

$$I = \frac{1}{(2\pi\mathcal{T})^{(D-1)/2}} \left\langle\left\langle \oint_{f(\mathbf{y})=0} dS(\mathbf{y}) \frac{1}{|\nabla_{\mathbf{y}} f(\mathbf{y})|} \frac{e^{-(\mathbf{y} - \bar{\mathbf{x}}_k)^2/\Delta\mathcal{T}}}{(\pi\Delta\mathcal{T})^{(D-1)/2}} \Phi(\mathbf{x}_1, \dots, \mathbf{y}, \dots, \mathbf{x}_{N-1}) \right\rangle\right\rangle_{\mathbf{x}(t)}. \quad (6.45)$$

There is an integral over the surface of constraint $f(\mathbf{y})$, and the functional Φ is constrained such that its k th coordinate is on the surface. The paths can be constructed without any concern for the constraints, but they will be suppressed by the Gaussian if they strongly violate the constraint that $\mathbf{y} \approx \bar{\mathbf{x}}_k$. In effect, this manipulation has “softened” the constraints. Previously, \mathbf{x}_k had to lie exactly on the surface, whereas now $\bar{\mathbf{x}}_k$ should be within $\sqrt{\Delta\mathcal{T}}$ of the surface to contribute to the path integral. Since a broader class of paths can be considered, it maybe easier to find sample paths where that almost obey the constraint $\mathbf{y} \approx \bar{\mathbf{x}}_k$. Those paths can then contribute to the path integral in regions where Φ is nonzero.

6.3.2.2. Splitting the Potential Curvature

Since the strong-coupling limit in the curvature (6.33) comes from the terms proportional to $\mathbb{1}_0^{(1)}\mathbb{1}_0^{(2)}$, those terms can be separated out, and treated using the

softened delta function approach. The remaining terms will be treated using the generic coupling discussed in Section 6.3.1. The curvature can be split into a strong-coupling and general- χ coupling term

$$C_{ij} = C_{ij}^{(S)} + C_{ij}^{(g)}, \quad (6.46)$$

where the strong-coupling term is

$$\begin{aligned} C_{ij}^{(S)} &= \frac{\hbar c N}{2(2\pi)^{D/2}} \int_0^\infty \frac{d\mathcal{T}}{\mathcal{T}^{1+D/2}} \oint_{\sigma_1(\mathbf{x}_0 - \mathbf{R}_1)=0} dS_0 \hat{r}_i \cdot \hat{n}_1(\mathbf{x}_0) \oint_{\sigma_2(\mathbf{y} - \mathbf{R}_2)=0} dS(\mathbf{y}) \hat{r}_j \cdot \hat{n}_2(\mathbf{y}) \\ &\times \left\langle \left\langle \sum_{k=1}^{N-1} \frac{e^{-(\mathbf{y} - \bar{\mathbf{x}}_k)^2 / \Delta \mathcal{T}}}{(\pi \Delta \mathcal{T})^{D/2}} \mathbb{1}_0^{(1)} \mathbb{1}_0^{(2)} g_{0,0} \right\rangle \right\rangle_{\mathbf{x}(t)}, \end{aligned} \quad (6.47)$$

and the general- χ coupling term $C_{ij}^{(g)}$ is

$$\begin{aligned} C_{ij}^{(g)} &= \frac{\hbar c N}{2(2\pi)^{D/2}} \sum_{k=1}^{N-1} \int_0^\infty \frac{d\mathcal{T}}{\mathcal{T}^{1+D/2}} \oint_{\sigma_1(\mathbf{x}_0 - \mathbf{R}_1)=0} dS_0 \hat{r}_i \cdot \hat{n}_1(\mathbf{x}_0) \oint_{\sigma_2(\mathbf{x}_k - \mathbf{R}_2)=0} dS_k \hat{r}_j \cdot \hat{n}_2(\mathbf{x}_k) \\ &\times \sum_{m,n \neq 0} \left\langle \left\langle \mathcal{G}(\mathbf{x}_0 - \mathbf{x}_k, k(N-k)\mathcal{T}/N^2) \mathbb{1}_m^{(1)} \mathbb{1}_n^{(2)} g_{m,n} \right\rangle \right\rangle_{\sigma_2(\mathbf{x}_k - \mathbf{R}_2)=0}. \end{aligned} \quad (6.48)$$

The integral (6.47) is only substantially nonzero under two conditions. First, the path must pass within a distance $\sqrt{\Delta \mathcal{T}}$ of the surface, and second the paths must not enter either body. Note that due to the pinning, the indicator functions $\mathbb{1}_0^{(1)} \mathbb{1}_0^{(2)}$ are currently defined with \mathbf{y} in the k th spot. This means that if \mathbf{x}_k lies inside either body, that does not influence the integrand. The indicators only go to zero when one of the *other* points on the path crosses into the bodies.

In a planar geometry, the $(D-2)$ -dimensional surface integrals can be evaluated. The integral over $S(\mathbf{y})$ eliminates the transverse Gaussian integrals, and integral over

the starting surface gives a factor of the transverse area. In $D = 4$ dimensions, Eq. (6.47) then simplifies to

$$C_{ij}^{(S)} = \frac{\hbar c N A}{2(2\pi)^2} \int_0^\infty \frac{d\mathcal{T}}{\mathcal{T}^3} \left\langle \left\langle \sum_{k=1}^{N-1} \frac{e^{-(d_2 - \bar{x}_k)^2 / \Delta \mathcal{T}}}{(\pi \Delta \mathcal{T})^{1/2}} \mathbb{1}_0^{(1)} \mathbb{1}_0^{(2)} g_{0,0} \right\rangle \right\rangle_{x(t), x_0=d_1}, \quad (6.49)$$

In order to capture the strong-coupling dependence it is necessary to sample from the set of paths that do not enter either body. For two dielectric planes with dielectric function (4.39) the paths can be constructed by shifting the paths so they start on the first surface at $x = d_1$. For paths constructed by scaling unit Brownian bridges, $x_k = d_1 + \sqrt{\mathcal{T}} B_k$, this can be done by translating the unit Brownian bridge $B(t) \rightarrow B(t) - B_{\min}$, where B_{\min} is the minimum value of the path. This ensures that the paths start at $x = d_1$, but since $\sqrt{\mathcal{T}} B(t) > 0$ for all points of the path, the paths will not enter the first body. Then suppose that the maximum point of the bridge is B_{\max} , and the maximum point of the path is $x_{\max} = d_1 + \sqrt{\mathcal{T}} B_{\max}$. Only this point will have an opportunity to contribute. Once it passes through the surface, $\mathbb{1}_0^{(1)} \mathbb{1}_0^{(2)}$ is zero, and so the integrand is also zero. Then the Gaussian $e^{-(d_2 - \bar{x}_{\max})^2 / \Delta \mathcal{T}}$ can be used to sample a path-time, while ensuring that the path does not actually enter the surface. That crossing time \mathcal{T}_{\max} definitely happens when $\sqrt{\mathcal{T}_{\max}} B_{\max} = d$, where $d = d_2 - d_1$. The exponential factor in Eq. (6.49) can be written using the definition of x_{\max} as

$$\exp\left(-\frac{1}{\Delta \mathcal{T}} [d - \sqrt{\mathcal{T}} \bar{B}_{\max}]^2\right) = \exp\left[-N d^2 \left(\frac{1}{\sqrt{\mathcal{T}}} - \frac{\bar{B}_{\max}}{d}\right)^2\right], \quad (6.50)$$

where $\bar{B}_{\max} := (B_{m^*+1} - B_{m^*-1})/2$, and m^* is the index of the maximum value. This can be regarded as the probability distribution for \mathcal{T} . The normalized probability

distribution for $1/\sqrt{\mathcal{T}}$ is

$$P_S(\mathcal{T}; \bar{B}_{\max}, d, N) = \sqrt{\frac{Nd^2}{\pi\mathcal{T}^3}} \exp \left[-Nd^2 \left(\frac{1}{\sqrt{\mathcal{T}}} - \frac{\bar{B}_{\max}}{d} \right)^2 \right] \Theta \left(\frac{d^2}{\bar{B}_{\max}^2} - \mathcal{T} \right). \quad (6.51)$$

The probability distribution can be simplified by defining

$$s = \sqrt{2Nd^2} \left(\frac{1}{\sqrt{\mathcal{T}}} - \frac{\bar{B}_{\max}}{d} \right), \quad (6.52)$$

where

$$P_S(s) = \left| \frac{d\mathcal{T}}{ds} \right| P_S(\mathcal{T}) = \sqrt{\frac{2}{\pi}} e^{-s^2/2} \Theta(s), \quad (6.53)$$

is a one-sided normal distribution. In this case, s is the absolute value of a standard normal deviate, and the path times can be written in terms of standard normal deviates as

$$\mathcal{T} = \left(\frac{|z|}{\sqrt{2Nd^2}} + \frac{\bar{B}_{\max}}{d} \right)^{-2}. \quad (6.54)$$

The \mathcal{T} integral will be computed in Monte Carlo fashion after factoring out the probability density (6.51), and using Eq. (6.54). The sum over k is assumed to be dominated by the contribution at the maximum point,

$$C_{ij}^{(S)} = \frac{\hbar c N A}{2(2\pi)^2} \left\langle \left\langle \frac{1}{\mathcal{T}^2 d} \left(\sqrt{\frac{Nd^2}{\pi\mathcal{T}^3}} e^{-(d_2 - \bar{x}_{\max})^2 / \Delta\mathcal{T}} \right) \mathbb{1}_0^{(1)} \mathbb{1}_0^{(2)} g_{0,0} \right\rangle \right\rangle_{\mathbf{x}(\mathcal{T}), x_0=d_1}. \quad (6.55)$$

Note that there is no explicit pinning on the paths, but this integrand is only non-zero if the paths do not enter the bodies.

Figure 6.4 shows the effects of including the strong coupling term (6.55). The strong-coupling term only becomes important for $\chi/N \gg 1$, and there is a transition between the generic coupling and strong-coupling regimes. The variance of the

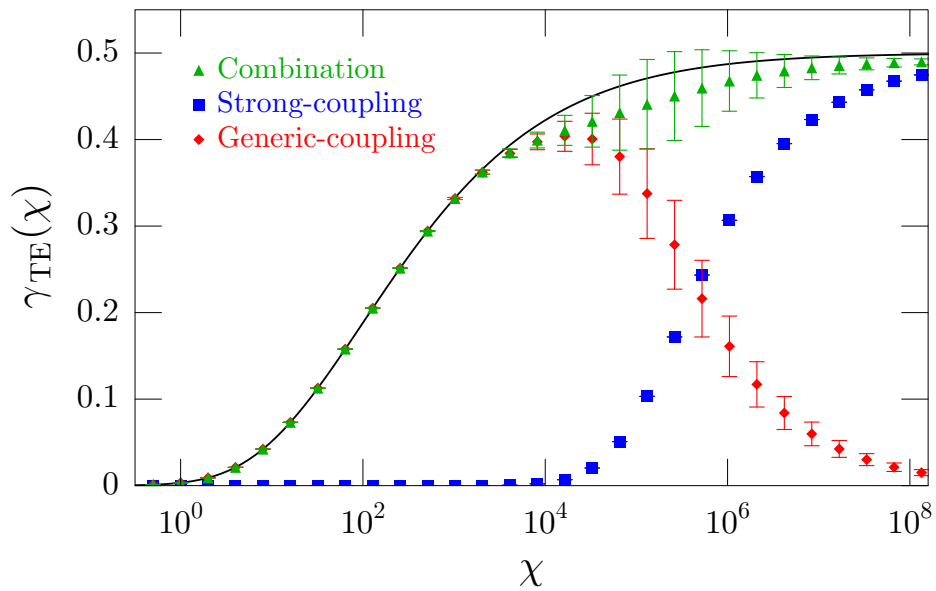


FIGURE 6.4. (Preliminary data) Numerically computed second derivative of TE potential for two planar surfaces as function of dielectric, for $N = 10^5$, with 10^8 trajectories. Strong coupling results are shown as blue squares, generic coupling as red diamonds, and their sum as green triangles. All calculations are carried out using “occupation” method in Eq. (6.33), and both estimates use the same ensemble of random numbers.

total estimated potential is also increased in the cross-over region, dominated by the statistical error from the generic coupling estimate. The method used here manages to improve on the generic coupling results significantly, since it does not rely on rare paths from a very large ensemble to capture the behavior in the strong-coupling regime. However, the presented results have a larger statistical error than the simpler generic coupling, but this is perhaps due to a slightly smaller ensemble of paths. There are $N = 10^8$ sample paths in Figure 6.4, versus $N = 10^9$ sample paths in Figure 6.3. This is still under study.

There is yet another way of treating the delta function in terms of restricting \mathcal{T} . If the paths are assumed to start on the surface of the first body, and not enter, then the delta function can be interpreted as a delta function in the path time \mathcal{T} . (Since there is only one \mathcal{T} integral in the path integral, only one of the delta functions can be handled in this manner. The remainder should be accounted for in the spatial integrals.) For a given Brownian bridge \mathbf{B}_k , the times \mathcal{T}_* that it intersects the surfaces, or satisfies $\sigma_2(\mathbf{x}_0 + \sqrt{\mathcal{T}_*}\mathbf{B}_k - \mathbf{R}_2) = 0$ could be found. This has not yet been implemented, but would be much simpler. However, the softened delta function approach may be also be useful in handling other constraints. For example, it may be useful when computing the potential in a complicated geometry. It might be hard to construct paths that touch both surfaces, and yet enter neither from randomly constructing Brownian bridges. This softened style of pinning could allow a broader class of paths to contribute in that case.

CHAPTER VII

CONCLUSION

The goal of this thesis was to develop a general purpose numerical method employing the worldline method to calculate electromagnetic Casimir energies. We have been partially successful in those aims.

Following Bordag *et al.* (1999, 1998), we developed a full vector path integral (2.50) for the EM field. So far it has not been implemented as a numerical method. Instead, we developed an approximate worldline description for the EM field in terms of two independent scalar fields, corresponding to the TE and TM polarizations. Although the decoupled scalars are adapted to a planar geometry, they share some similarities with the potentials in the full vector path integral, and are a useful test case in their own right.

We showed analytically and numerically that the polarization worldline path integrals recover the known expressions for the Casimir–Polder and Casimir energies in planar geometries, at zero and high temperature. Doing so involved regularizing singular TM potentials, and finding analytical solutions to the path integral in certain geometries. The analytical expressions for the path average of the TM potential are essential for numerical computations with this method.

Even with regularized solutions, it was necessary to develop techniques to efficiently sample the worldline path integral. The TE integrand was relatively simple to evaluate, while the TM integrand is much more challenging and still under study. The birth-death method for sampling paths was essential for bringing the statistical errors under control, and the partial averaging method also allowed us to evaluate

the derivatives required for the TM method. The numerical methods we developed are in agreement with the expected analytical results.

The methods that were developed could be used as an (uncontrolled) approximation to the Casimir effect in a general geometry. They will also probably be useful in handling the vector path integral. In cases where path integrals can be analytically solved for open Brownian bridges [such as Dirichlet (3.29) and TM boundary conditions (3.52)], those expressions can be applied locally at each step of the path. At each step, the potential could be computed using a local planar approximation to the exact solution. The local solutions joined together along the path, could form a basis for solving a path integral in general, based on the local approximations throughout the path.

Another possible approach to leveraging the results contained here into a general method is to consider how the two scalar polarizations are coupled. At each point along the path, the EM field could be split into the TE and TM polarizations based on the nearest surface normal. The weights for the polarizations are the components of an auxiliary two component vector that travels along the path. At each step, the terms acquire the appropriate TE or TM potential, and are then coupled together via a rotation matrix where the rotation angle depends on the change in the surface normal.

The worldline method has not yet been generalized to full electromagnetism. However, the worldline has a number of attractive features such as its simple parallelism, and the possibility for superior performance in very complicated geometries. Given the progress thus far, I believe that this method is worth developing further, where it could complement existing methods and may have uses in electromagnetism beyond just Casimir physics.

APPENDIX

DETAILED CALCULATIONS

This appendix collects a couple lengthy, but tedious calculations required in the main text.

A.1. Integrated Renormalized Two-Body Feynman-Kac Formula

The following calculation is required for the renormalized two-body energies for both TE and TM. Since TE and TM mimic each other in the form of their solutions, most of this can proceed in parallel. Only at the end is the exact form of the solution required. The form of the two-body solutions are given in Eqs. (3.31) and (3.60).

The spatial integral over the solution f_{12} in region I is

$$\begin{aligned}
 J_I &= \int_{-\infty}^{d_1} dx_0 (f_{12}(\mathbf{x}_0) - f_{12}^{(0)}) \\
 &= \int_{-\infty}^{d_1} dx_0 e^{-2\sqrt{2(\lambda+\chi_1)}(d_1-x_0)} \frac{r_2 e^{-2\sqrt{2\lambda}d} - r_1}{\sqrt{2(\lambda+\chi_1)}(1 - r_1 r_2 e^{-2\sqrt{2\lambda}d})} \\
 &= \frac{r_2 e^{-2\sqrt{2\lambda}d} - r_1}{4(\lambda+\chi_1)(1 - r_1 r_2 e^{-2\sqrt{2\lambda}d})}. \tag{A.1}
 \end{aligned}$$

The equivalent one-body expressions can be found by setting one of the susceptibilities to zero. The spatial integrals over the other regions are

$$\begin{aligned}
 J_{II} &= \int_{d_1}^{d_2} dx_0 [f_{12}(\mathbf{x}_0) - f_{12}^{(0)}] \\
 &= \int_{d_1}^{d_2} dx_0 \left[\frac{2r_1 r_2 e^{-2\sqrt{2\lambda}d} + r_1 e^{2\sqrt{2\lambda}(d_1-x_0)} + r_2 e^{-2\sqrt{2\lambda}(d_2-x_0)}}{\sqrt{2\lambda}(1 - r_1 r_2 e^{-2\sqrt{2\lambda}d})} \right] \\
 &= \frac{2d r_1 r_2 e^{-2\sqrt{2\lambda}d}}{\sqrt{2\lambda}(1 - r_1 r_2 e^{-2\sqrt{2\lambda}d})} + \frac{(r_1 + r_2)(1 - e^{-2\sqrt{2\lambda}d})}{4\lambda(1 - r_1 r_2 e^{-2\sqrt{2\lambda}d})}, \tag{A.2}
 \end{aligned}$$

and

$$\begin{aligned}
J_{II} &= \int_{d_2}^{\infty} dx_0 (f_{12}(\mathbf{x}_0) - f_{12}^{(0)}) \\
&= \int_{d_2}^{\infty} dx_0 e^{2\sqrt{2(\lambda+\chi_2)}(d_2-x_0)} \frac{(r_1 e^{-2\sqrt{2\lambda}d} - r_2)}{\sqrt{2(\lambda+\chi_2)}(1 - r_1 r_2 e^{-2\sqrt{2\lambda}d})} \quad (\text{A.3})
\end{aligned}$$

$$= \frac{(r_1 e^{-2\sqrt{2\lambda}d} - r_2)}{4(\lambda + \chi_2)(1 - r_1 r_2 e^{-2\sqrt{2\lambda}d})}. \quad (\text{A.4})$$

The total spatial integral for the fully renormalized two-body solution is found by adding together Eqs. (A.1)–(A.4), and subtracting off the one-body integrals. The result is

$$\int_{-\infty}^{\infty} dx_0 \left[(f_{12}(\mathbf{x}_0) - f_{12}^{(0)}) - (f_1(\mathbf{x}_0) - f_1^{(0)}) - (f_2(\mathbf{x}_0) - f_2^{(0)}) \right] \quad (\text{A.5})$$

$$\begin{aligned}
&= \frac{r_2 e^{-2\sqrt{2\lambda}d} - r_1}{4(\lambda + \chi_1)(1 - r_1 r_2 e^{-2\sqrt{2\lambda}d})} + \frac{r_1}{4(\lambda + \chi_1)} - \frac{r_2 e^{-2\sqrt{2\lambda}d}}{4\lambda} \\
&+ \frac{2d r_1 r_2 e^{-2\sqrt{2\lambda}d}}{\sqrt{2\lambda}(1 - r_1 r_2 e^{-2\sqrt{2\lambda}d})} + \frac{(r_1 + r_2)(1 - e^{-2\sqrt{2\lambda}d})}{4\lambda(1 - r_1 r_2 e^{-2\sqrt{2\lambda}d})} \\
&- \frac{(r_1 + r_2)(1 - e^{-2\sqrt{2\lambda}d})}{4\lambda} \\
&+ \frac{r_1 e^{-2\sqrt{2\lambda}d} - r_2}{4(\lambda + \chi_2)(1 - r_1 r_2 e^{-2\sqrt{2\lambda}d})} - \frac{r_1 e^{-2\sqrt{2\lambda}d}}{4\lambda} + \frac{r_2}{4(\lambda + \chi_2)}. \quad (\text{A.6})
\end{aligned}$$

Pairs of common terms can be simplified by using $a/(1-x) - a = ax/(1-x)$, with $a = r_i$ and $x = r_1 r_2 e^{-2\sqrt{2\lambda}d}$.

$$\begin{aligned}
J &= \frac{2d r_1 r_2 e^{-2\sqrt{2\lambda}d}}{\sqrt{2\lambda}(1 - r_1 r_2 e^{-2\sqrt{2\lambda}d})} + \frac{r_2 e^{-2\sqrt{2\lambda}d} - r_1}{4(\lambda + \chi_1)(1 - r_1 r_2 e^{-2\sqrt{2\lambda}d})} + \frac{r_1}{4(\lambda + \chi_1)} \\
&+ \frac{(r_1 + r_2)(1 - e^{-2\sqrt{2\lambda}d})}{4\lambda(1 - r_1 r_2 e^{-2\sqrt{2\lambda}d})} - \frac{(r_1 + r_2)}{4\lambda} + \frac{r_1 e^{-2\sqrt{2\lambda}d} - r_2}{4(\lambda + \chi_2)(1 - r_1 r_2 e^{-2\sqrt{2\lambda}d})} + \frac{r_2}{4(\lambda + \chi_2)}. \quad (\text{A.7})
\end{aligned}$$

The exponential pieces are common to all terms and can be factored out. The terms can be grouped by their denominators

$$J = \frac{e^{-2\sqrt{2\lambda}d}}{(1 - r_1 r_2 e^{-2\sqrt{2\lambda}d})} \left[\frac{2d r_1 r_2}{\sqrt{2\lambda}} + \frac{r_2 [1 - (r_1)^2]}{4(\lambda + \chi_1)} + \frac{(r_1 + r_2)[-1 + r_1 r_2]}{4\lambda} + \frac{r_1 [1 - (r_2)^2]}{4(\lambda + \chi_2)} \right]. \quad (\text{A.8})$$

The middle term with denominator λ can then be paired with the terms in $(\lambda + \chi_1)^{-1}$ and $(\lambda + \chi_2)^{-1}$,

$$J = \frac{e^{-2\sqrt{2\lambda}d}}{(1 - r_1 r_2 e^{-2\sqrt{2\lambda}d})} \left[\frac{2d r_1 r_2}{\sqrt{2\lambda}} + r_2 [1 - (r_1)^2] \left(\frac{1}{4(\lambda + \chi_1)} - \frac{1}{4\lambda} \right) + r_1 [1 - (r_2)^2] \left(\frac{1}{4(\lambda + \chi_2)} - \frac{1}{4\lambda} \right) \right] \quad (\text{A.9})$$

After factoring out $r_1 r_2$, the result is

$$J = \frac{r_1 r_2 e^{-2\sqrt{2\lambda}d}}{(1 - r_1 r_2 e^{-2\sqrt{2\lambda}d})} \left[\frac{2d}{\sqrt{2\lambda}} - [r_1^{-1} - (r_1)] \frac{\chi_1}{4\lambda(\lambda + \chi_1)} - [r_2^{-1} - (r_2)] \frac{\chi_2}{4\lambda(\lambda + \chi_2)} \right]. \quad (\text{A.10})$$

At this point, the exact form of the reflection coefficients must be used to proceed any further.

A.1.1. TE Reflection Coefficients

For TE reflection coefficients (3.23), the integrated, renormalized two body solution is

$$J^{(\text{TE})} = \frac{r_1^{(\text{TE})} r_2^{(\text{TE})} e^{-2\sqrt{2\lambda}d}}{(1 - r_1^{(\text{TE})} r_2^{(\text{TE})} e^{-2\sqrt{2\lambda}d})} \left[\frac{2d}{\sqrt{2\lambda}} - \sum_{i=1}^2 \left(\frac{4\sqrt{\lambda}\sqrt{\lambda + \chi_i}}{\lambda - (\lambda + \chi_i)} \frac{\chi_i}{4\lambda(\lambda + \chi_i)} \right) \right] \quad (\text{A.11})$$

$$= \frac{r_1^{(\text{TE})} r_2^{(\text{TE})} e^{-2\sqrt{2\lambda}d}}{\sqrt{2\lambda}(1 - r_1^{(\text{TE})} r_2^{(\text{TE})} e^{-2\sqrt{2\lambda}d})} \left(2d + \frac{\sqrt{2}}{\sqrt{\lambda + \chi_1}} + \frac{\sqrt{2}}{\sqrt{\lambda + \chi_2}} \right). \quad (\text{A.12})$$

This will be used to compute the Casimir energy between two dielectric half-spaces. The extra terms will allow an integration by parts to occur, that considerably simplifies the expressions.

A.1.2. TM Reflection Coefficients

In contrast, for the TM polarization, the $\sqrt{\lambda} \rightarrow e^{2\Xi}\sqrt{\lambda}$, but $\sqrt{\lambda + \chi}$ is unchanged. Note that the post-factor of $\chi_i/[4\lambda(\lambda + \chi_i)]$ in Eq. (A.10) came from the integrating the the exponentials, rather than the reflection coefficients. The TM reflection coefficients are given by Eq. (3.57). After combining $r_i^{(\text{TM})} - 1/r_i^{(\text{TM})}$, the result is

$$J^{(\text{TM})} = \frac{r_1^{(\text{TM})} r_2^{(\text{TM})} e^{-2\sqrt{2\lambda}d}}{(1 - r_1^{(\text{TM})} r_2^{(\text{TM})} e^{-2\sqrt{2\lambda}d})} \left[\frac{2d}{\sqrt{2\lambda}} - \sum_{i=1}^2 \left(\frac{4e^{2\Xi_i}\sqrt{\lambda}\sqrt{\lambda + \chi_i}}{\lambda e^{4\Xi_i} - (\lambda + \chi_i)} \frac{\chi_i}{4\lambda(\lambda + \chi_i)} \right) \right] \quad (\text{A.13})$$

$$= \frac{r_1^{(\text{TM})} r_2^{(\text{TM})} e^{-2\sqrt{2\lambda}d}}{\sqrt{2\lambda}(1 - r_1^{(\text{TM})} r_2^{(\text{TM})} e^{-2\sqrt{2\lambda}d})} \left[2d - \sum_{i=1}^2 \frac{\sqrt{2}e^{2\Xi_i}\chi_i}{\sqrt{\lambda + \chi_i}[\lambda e^{4\Xi_i} - (\lambda + \chi_i)]} \right] \quad (\text{A.14})$$

Again, the extra terms allow an integration by parts to proceed, and for the Lifshitz form of the energy to be recovered.

REFERENCES CITED

- Aehlig, K., H. Dietart, T. Fischbacher, and J. Gerhard (2011), “Casimir forces via worldline numerics: Method improvements and potential engineering applications,” arxiv:1110.5936 [quant-ph] .
- Altland, A., and B. Simons (2011), *Condensed Matter Field Theory*, 2nd ed. (Cambridge University Press).
- Alton, D. J., N. P. Stern, T. Aoki, H. Lee, E. Ostby, K. J. Vahala, and H. J. Kimble (2011), “Strong interactions of single atoms and photons near a dielectric boundary,” Nat. Phys. **7**, 159.
- Asmussen, S., and P. W. Glynn (2007), *Stochastic Simulation* (Springer).
- Barash, Y. U., and V. L. Ginzburg (1975), “Electromagnetic fluctuations in matter and molecular (van-der-Waals) forces between them,” Sov. Phys. Usp. **18**, 305.
- Bechler, A. (1999), “Quantum electrodynamics of the dispersive dielectric medium - a path integral approach,” J. Mod. Opt. **46**, 901–921.
- Bechler, A. (2006), “Path-integral quantization of the electromagnetic field in the Hopfield dielectric beyond dipole approximation,” J. Phys. A: Math. Gen. **39**, 13553.
- Beliakov, G., and Y. Matiyasevich (2013), “A parallel algorithm for calculation of large determinants with high accuracy for GPUs and MPI clusters,” arxiv:1308.1536v2 [cs-DC] .
- Bezerra, V. B., G. L. Klimchitskaya, V. M. Mostepanenko, and C. Romero (2011), “Constraints on non-Newtonian gravity from measuring the Casimir force in a configuration with nanoscale rectangular corrugations,” Phys. Rev. D **83**, 075004.
- Blocki, J., J. Randrup, W. J. Swiatecki, and C. F. Tsang (1977), “Proximity forces,” Ann. Phys. (N. Y.) **105**, 427.
- Bordag, M., K. Kirsten, and D. Vassilevich (1999), “Ground state energy for a penetrable sphere and for a dielectric ball,” Physical Review D **59**, 085011.
- Bordag, M., K. Kirsten, and D. V. Vassilevich (1998), “Path integral quantization of electrostatics in dielectric media,” J. Phys. A: Math. Gen. **31**, 2381.
- Bordag, M., G. L. Klimchitskaya, U. Mohideen, and V. M. Mostapenenko (2009), *Advances in the Casimir Effect* (Oxford).

- Bordag, M., D. Robaschik, and E. Wieczorek (1985), “Quantum field theoretic treatment of the Casimir effect,” *Ann. Phys.* **165**, 192.
- Boyer, T. H. (1968), “Quantum electromagnetic zero-point energy of a conducting spherical shell and the Casimir model for a charged particle,” *Phys. Rev.* **174**, 1765.
- Boyer, T. H. (1974), “Van der Waals forces and zero-point energy for dielectric and permeable materials,” *Phys. Rev. A* **9**, 2078.
- Bressi, G., G. Carugno, R. Onofrio, and G. Ruoso (2002), “Measurement of the Casimir force between parallel metallic surfaces,” *Phys. Rev. Lett.* **88**, 041804.
- Brown, L. S. (1994), *Quantum Field Theory* (Cambridge University Press).
- Buks, E., and M. L. Roukes (2001), “Stiction, adhesion energy, and the Casimir effect in micromechanical systems,” *Phys. Rev. B* **63**, 033402.
- Canaguier-Durand, A., R. Gurout, P. A. Maia Neto, A. Lambrecht, and S. Reynaud (2012), “The Casimir effect in the sphere-plane geometry,” *Int. J. Mod. Phys. Conf. Ser.* **14**, 250.
- Cartier, P., and C. deWitte Morette (2006), *Functional Integration: Actions and Symmetries* (Cambridge University Press).
- Casimir, H. B. G. (1948), “On the attraction between two perfectly conducting plates,” *Proc. K. Ned. Akad. Wet.* **51**, 793.
- Casimir, H. B. G., and D. Polder (1948), “The influence of retardation on the London-van der Waals forces,” *Phys. Rev.* **73**, 360.
- Chan, H. B., V. A. Aksyuk, R. N. Kleiman, D. J. Bishop, and F. Capasso (2001), “Nonlinear micromechanical Casimir oscillator,” *Phys. Rev. Lett.* **87**, 211801.
- Chen, N., and P. Glasserman (2007), “Malliavin greeks without Malliavin calculus,” *Stoch. Proc. and Appl.* **117**, 1689.
- Chen, Y.-J., W. K. Tham, D. E. Krause, D. López, E. Fischbach, and R. S. Decca (2016), “Stronger limits on hypothetical Yukawa interactions in the 30–8000 nm range,” *Phys. Rev. Lett.* **116**, 221102.
- Dalvit, D., P. Milonni, D. Roberts, and F. Rosa, Eds. (2011), *Casimir Physics* (Springer).
- Del Moral, P. (2004), *Feynman–Kac Formulae: Genealogical and Interacting Particle Systems with Applications* (Springer).

- Derjaguin, B. (1934), “Analysis of friction and adhesion, IV. the theory of the adhesion of small particles,” *Kolloid Z.* **69**, 155, (in German).
- Devroye, L. (2003), *Non-Uniform Random Variate Generation* (Springer) available online at <http://www.nrbook.com/devroye>.
- Dimopoulos, S., and A. A. Geraci (2003), “Probing submicron forces by interferometry of Bose–Einstein condensed atoms,” *Phys. Rev. D* **68**, 124021.
- DiNunno, G., B. Øksendal, and F. Proske (2009), *Malliavin Calculus for Levy Processes with Applications to Finance* (Springer).
- Dirac, P. A. M. (1950), “Generalized Hamiltonian dynamics,” *Canad. J. Math.* **2**, 129.
- Dirac, P. A. M. (1964), *Lectures on Quantum Mechanics* (Belfer Graduate School of Science, Yeshiva University).
- Dirac, P. A. M. (1966), *Lectures on Quantum Field Theory* (Belfer Graduate School of Science, Yeshiva University).
- Dung, H. T., L. Knöll, and D.-G. Welsch (1998), “Three-dimensional quantization of the electromagnetic field in dispersive and absorbing inhomogeneous dielectrics,” *Phys. Rev. A* **57**, 3931.
- Durrett, R. (1996), *Stochastic Calculus: A Practical Introduction* (CRC Press).
- Dzyaloshinskii, I. E., E. M. Lifshitz, and L. P. Pitaevskii (1961), “General theory of van der Waals’ forces,” *Sov. Phys. Uspekhi* **73**, 381.
- Dzyaloshinskii, I. E., and L. P. Pitaevskii (1959), “Van der Waals forces in an inhomogenous dielectric,” *Sov. Phys. JETP-USSR* **36**, 1797.
- Elizalde, E. (2008), “Zeta function methods and quantum fluctuations,” *J. Phys. A: Math. Theor.* **41**, 304040.
- Elizalde, E., L. Vanzo, and S. Zerbini (1998), “Zeta-function regularization, the multiplicative anomaly and the Wodzicki residue,” *Comm. Math. Phys.* **194**, 613.
- Emig, T., and R. Büscher (2004), “Towards a theory of molecular forces between deformed media,” *Nuc. Phys. B* **696**, 468.
- Emig, T., N. Graham, R. L. Jaffe, and M. Kardar (2007), “Casimir forces between arbitrary compact objects,” *Phys. Rev. Lett.* **99**, 170403.
- Faddeev, L. D., and V. N. Popov (1967), “Feynman diagrams for the Yang–Mills field,” *Phys. Lett. B* **25**, 29.

- Faddeev, L. D., and A. A. Slavnov (1991), *Gauge fields: An introduction to quantum theory*, 2nd ed. (Addison-Wesley).
- Feynman, R. P. (1948), “Space-time approach to non-relativistic quantum mechanics,” *Rev. Mod. Phys.* **20**, 367.
- Feynman, R. P. (1950), “Mathematical formulation of the quantum theory of electromagnetic interaction,” *Phys. Rev.* **80**, 440.
- Feynman, R. P., and A. R. Hibbs (1965), *Quantum Mechanics and Path Integrals* (McGraw-Hill).
- Folman, R., P. Krüger, D. Cassettari, B. Hessmo, T. Maier, and J. Schmiedmayer (2000), “Controlling cold atoms using nanofabricated surfaces: Atom chips,” *Phys. Rev. Lett.* **84**, 4749.
- Fosco, C. D., F. C. Lombardo, and F. D. Mazzitelli (2010), “Neumann Casimir effect: A singular boundary-interaction approach,” *Phys. Lett. B* **690**, 189.
- Gardiner, C. W. (2009), *Stochastic Methods*, 4th ed. (Springer).
- Gardiner, C. W., and P. Zoller (2004), *Quantum Noise*, 3rd ed. (Springer).
- Garvels, M. J. J. (2000), *The Splitting Method in Rare Event Simulation*, Ph.D. thesis (University of Twente).
- Genet, C., A. Lambrecht, and S. Reynaud (2003), “Casimir force and the quantum theory of lossy optical cavities,” *Phys. Rev. A* **67**, 043811.
- Geraci, A. A., and H. Goldman (2015), “Sensing short range forces with a nanosphere matter-wave interferometer,” *Phys. Rev. D* **92**, 062002.
- Gies, H., and K. Klingmüller (2006a), “Quantum energies with worldline numerics,” *J. Phys. A:Math. Gen* **39**, 6415.
- Gies, H., and K. Klingmüller (2006b), “Worldline algorithms for Casimir configurations,” *Phys. Rev. D* **74**, 045002.
- Gies, H., K. Langfeld, and L. Moyaerts (2003), “Casimir forces on the worldline,” *J. High Energy Phys.* **06**, 018.
- Gies, H., J. Sanchez-Guillen, and R. A. Vásquez (2005), “Quantum effective actions from nonperturbative worldline dynamics,” *J. High Energy Phys.* **0508**, 067.
- Glasserman, P. (2004), *Monte Carlo Methods in Financial Engineering* (Springer).
- Glasserman, P., P. Heidelberger, P. Shahabuddin, and T. Zajic (1999), “Multilevel splitting for estimating rare event probabilities,” *Ops. Res.* **47**, 585.

- Glauber, R. J., and M. Lewenstein (1991), “Quantum optics of dielectric media,” *Phys. Rev. A* **1**, 467.
- Goban, A., C.-L. Hung, S.-P. Yu, J. D. Hood, J. A. Muniz, H. J. Lee, M. J. Martin, A. C. McClung, K. S. Choi, D. E. Chang, O. Painter, and J. Kimble (2014), “Atom-light interactions in photonic crystals,” *Nature Communications* **5**, 3808.
- Gutzwiller, M. C. (1990), *Chaos in Classical and Quantum Mechanics* (Springer).
- Harber, D. M., J. M. Obrecht, J. M. McGuirk, and E. A. Cornell (2005), “Measurement of the Casimir–Polder force through center-of-mass oscillations of a Bose–Einstein condensate,” *Phys. Rev. A* **72**, 033610.
- Hooghiemstra, G. (2002), “On explicit occupation time distributions for Brownian processes,” *Statistics & Probability Letters* **56**, 405.
- Hörmander, L. (1983), *The Analysis of Linear Partial Differential Operators I: Distribution Theory and Fourier Analysis* (Springer).
- Hung, C.-L., S. M. Meenehan, D. E. Chang, O. Painter, and H. J. Kimble (2013), “Trapped atoms in one-dimensional photonic crystals,” *New J. Phys.* **15**, 083026.
- Huttner, B., and S. M. Barnett (1992), “Quantization of the electromagnetic field in dielectrics,” *Phys. Rev. A* **46**, 4306.
- Iannuzzi, D., and F. Capasso (2003), “Comment on “repulsive Casimir forces”,” *Phys. Rev. Lett.* **91**, 029101.
- Israelachvili, J. N. (2011), *Intermolecular and Surface Forces* (Academic Press).
- Jacobs, K. (2010), “Wave-function Monte Carlo method for simulating conditional master equations,” *Phys. Rev. A* **81**, 042106.
- Jaffe, R. L. (2005), “Casimir effect and the quantum vacuum,” *Phys. Rev. D* **72**, 021301(R).
- Johnson, S. G. (2011), “Numerical methods for calculating Casimir interactions,” in *Casimir Physics*, edited by D. Dalvit, P. Milonni, D. Roberts, and F. Rosa, Chap. 6 (Springer) p. 175.
- Kac, M. (1949), “On distributions of certain Wiener functionals,” *Trans. Amer. Math. Soc.* **64** (1), 1.
- van Kampen, N. G., B. R. A. Nijboer, and K. Schram (1968), “On the macroscopic theory of van der Waals forces,” *Phys. Lett.* **26A**, 307.

- Karatzas, I., and S. E. Shreve (1991), *Brownian Motion and Stochastic Calculus* (Springer).
- Kenneth, O., and I. Klich (2006), “Opposites attract: A theorem about the Casimir force,” *Phys. Rev. Lett.* **97**, 160401.
- Kenneth, O., I. Klich, A. Mann, and M. Revzen (2002), “Repulsive Casimir forces,” *Phys. Rev. Lett.* **89**, 033001.
- Kimble, H. J. (2008), “The quantum internet,” *Nature* **453**, 1023.
- Kleinert, H. (2012), *Path Integrals in Quantum Mechanics, Statistics, Polymer Physics and Financial Markets*, 5th ed. (World Scientific).
- Klingmüller, K., and H. Gies (2008), “Geothermal Casimir phenomena,” *J. Phys. A:Math. Theor.* **41**, 164042.
- Knöll, L., W. Vogel, and D. G. Welsch (1987), “Action of passive, lossless optical systems in quantum optics,” *Phys. Rev. A* **36**, 3803.
- Kohatsu-Higa, A., and M. Montero (2003), “An application of Malliavin calculus to finance,” *Physica A* **320**, 548, (Also see preprint at <http://www.ritsumei.ac.jp/%7Ekhts00/papers/Malliavin.pdf>).
- Kohatsu-Higa, A., and M. Montero (2004), “Handbook of computational and numerical methods in finance,” Chap. Malliavin Calculus in Finance (Springer) p. 111.
- Kubo, R. (1957), “Statistical-mechanical theory of irreversible processes. I. general theory and simple applications to magnetic and conduction problems,” *J. Phys. Soc. Jpn.* **12**, 570.
- Lambrecht, A., A. Canguier-Durand, R. Guérout, and S. Reynaud (2011), “Casimir effect in the scattering approach: Correlations between material properties, temperature and geometry,” in *Casimir Physics*, edited by D. Dalvit, P. Milonni, D. Roberts, and F. Rosa, Chap. 4 (Springer) p. 97.
- Lambrecht, A., P. A. Maia Neto, and S. Reynaud (2006), “The Casimir effect within scattering theory,” *New J. Phys.* **8**, 243.
- Lamoreaux, S. K. (1997), “Demonstration of the Casimir force in the 0.6 to 6 μm range,” *Phys. Rev. Lett.* **78**, 5.
- Lamoreaux, S. K. (2011), “Progress in experimental measurements of the surface-surface Casimir force: Electrostatic calibrations and limitations to accuracy,” in *Casimir Physics*, edited by D. Dalvit, P. Milonni, D. Roberts, and F. Rosa, Chap. 7 (Springer) p. 219.

- Levin, M., A. P. McCauley, A. W. Rodriguez, M. T. H. Reid, and S. G. Johnson (2010), “Casimir repulsion between metallic objects in vacuum,” *Phys. Rev. Lett.* **105**, 090403.
- Lew, J. S. (1975), “On some relations between the Laplace and Mellin-transforms,” *IBM Journal of Research and Development* **19**, 582.
- Li, H., and M. Kardar (1991), “Fluctuation-induced forces between rough surfaces,” *Phys. Rev. Lett.* **67**, 3275.
- Lifshitz, E. M. (1956), “The theory of molecular attractive forces between solids,” *Soviet Physics JETP* **2**, 73.
- Lin, Y., I. Teper, C. Chin, and V. Vuletić (2004), “Impact of the Casimir–Polder potential and Johnson noise on Bose–Einstein condensate stability near surfaces,” *Phys. Rev. Lett.* **92**, 050404.
- London, F. (1930), “Zur theorie und systematik der molekularkräfte,” *Z. Phys. Chem. B* **11**, 222, (in German).
- Lonij, V. P. A., W. F. Holmgren, and A. D. Cronin (2009), “Magic ratio of window width to grating period for van der Waals potential measurements using material gratings,” *Phys. Rev. A* **80**, 062904.
- Mackrory, J. B., T. Bhattacharya, and D. A. Steck (2016), “Worldline approach for numerical computation of electromagnetic Casimir energies. I. scalar field coupled to magnetodielectric media,” *Phys. Rev. A* **94**, 042508.
- Maggs, A. C., and R. Everaers (2006), “Simulating nanoscale dielectric response,” *Phys. Rev. Lett.* **96**, 230603.
- Maia Neto, P. A., A. Lambrecht, and S. Reynaud (2008), “Casimir energy between a plane and a sphere in electromagnetic vacuum,” *Phys. Rev. A* **78**, 012115.
- Malliavin, P., and A. Thalmaier (2006), *Stochastic Calculus of Variations in Mathematical Finance* (Springer).
- Mandl, F., and G. Shaw (2010), *Quantum Field Theory*, 2nd ed. (Wiley).
- Mazur, D., and J. S. Heyl (2014), “Parallel worldline numerics: Implementation and error analysis,” arxiv:1407.7486v1 [hep-th] .
- McKenzie-Smith, J. J., and D. J. Toms (1998), “ ζ -function regularization, the multiplicative anomaly, and finite temperature quantum field theory,” *Phys. Rev. D* **58**, 105001.
- McKeon, D. G. C., and A. Rebhan (1993), “Thermal Green’s functions from quantum-mechanical path integrals,” *Phys. Rev. D* **47**, 5487.

- Milonni, P. W. (1994), *The Quantum Vacuum: An Introduction to Quantum Electrodynamics* (Academic Press).
- Milton, K. A. (2001), *The Casimir Effect: Physical Manifestations of Zero-Point Energy* (World Scientific Publishing).
- Milton, K. A., E. K. Abalo, P. Parashar, N. Pourtolami, I. Brevik, and S. A. Ellingsen (2011), “Casimir–Polder repulsion near edges: Wedge apex and a screen with an aperture,” *Phys. Rev. A* **83**, 062507.
- Milton, K. A., L. L. DeRaad, and J. Schwinger (1978), “Casimir self-stress on a perfectly conducting spherical shell,” *Ann. Phys.* **115**, 388.
- Milton, K. A., P. Parashar, N. Pourtolami, and I. Brevik (2012), “Casimir–Polder repulsion: Polarizable atoms, cylinders, spheres, and ellipsoids,” *Phys. Rev. D* **85**, 025008.
- Mohideen, U., and A. Roy (1998), “Precision measurement of the Casimir force from 0.1 to 0.9 μm ,” *Phys. Rev. Lett.* **81**, 4549.
- Munday, J. N., F. Federico Capasso, and V. A. Parsegian (2009), “Measured long-range repulsive Casimir–Lifshitz forces,” *Nature* **457**, 170.
- Nisbet, A. (1955), “Hertzian electromagnetic potentials and associated gauge transformations,” *Proc. R. Soc. Lond. A* **231**, 250.
- Nisbet, A. (1957), “Electromagnetic potentials in a heterogeneous non-conducting medium,” *Proc. R. Soc. Lond. A* **240**, 375.
- Nualart, D. (2006), *The Malliavin Calculus and Related Topics* (Springer).
- Obrecht, J. M., R. J. Wild, M. Antezza, L. P. Pitaevskii, S. Stringari, and E. A. Cornell (2007), “Measurement of temperature dependence of the Casimir–Polder force,” *Phys. Rev. Lett.* **98**, 063201.
- Parsegian, V. A. (2006), *Van der Waals Forces* (Cambridge).
- Pasquali, S., F. Nitti, and A. C. Maggs (2008), “Numerical methods for fluctuation-driven interactions between dielectrics,” *Phys. Rev. E* **77**, 016705.
- Pendry, J. B., A. J. Holden, D. J. Robbins, and W. J. Stewart (1999), “Magnetism from conductors and enhanced nonlinear phenomena,” *IEEE Transactions on Microwave Theory and Techniques* **47**, 2075.
- Perreault, J. D., and A. D. Cronin (2005), “Observation of atom wave phase shifts induced by van der Waals atom-surface interactions,” *Phys. Rev. Lett.* **95**, 133201.

- Peskin, M., and D. Schroeder (1995), *An Introduction to Quantum Field Theory* (Westview).
- Philbin, T. G. (2010), “Canonical quantization of macroscopic electromagnetism,” *New J. Phys.* **12** (12), 123008.
- Pirozhenko, I. G., and A. Lambrecht (2008), “Casimir repulsion and metamaterials,” *J. Phys. A: Math. Theor.* **41** (16), 164015.
- Press, W. H., B. P. Flannery, S. A. Teukolsky, and W. T. Vetterling (1990), *Numerical Recipes in Fortran*, 1st ed. (Cambridge University Press).
- Rahi, S. J., T. Emig, N. Graham, R. L. Jaffe, and M. Kardar (2009), “Scattering theory approach to electrodynamic Casimir forces,” *Phys. Rev. D* **80**, 085201.
- Rahi, S. J., T. Emig, and R. L. Jaffe (2011), “Geometry and material effects in Casimir physics-Scattering theory,” in *Casimir Physics*, edited by D. Dalvit, P. Milonni, D. Roberts, and F. Rosa, Chap. 5 (Springer) p. 129.
- Rahi, S. J., M. Kardar, and T. Emig (2010), “Constraints on stable equilibria with fluctuation-induced (Casimir) forces,” *Phys. Rev. Lett.* **105**, 070404.
- Reid, M. T. H., A. W. Rodriguez, J. White, and S. G. Johnson (2009), “Efficient computation of Casimir interactions between arbitrary 3D objects,” *Phys. Rev. Lett.* **103**, 040401.
- Reid, M. T. H., J. White, and S. G. Johnson (2011), “Computation of Casimir interactions between arbitrary three-dimensional objects with arbitrary material properties,” *Phys. Rev. A* **84**, 010503(R).
- Reid, M. T. H., J. White, and S. G. Johnson (2013), “Fluctuating surface currents: An algorithm for efficient prediction of Casimir interactions among arbitrary materials in arbitrary geometries,” *Phys. Rev. A* **88**, 022514.
- Rodriguez, A., M. Ibanescu, D. Iannuzzi, F. Capasso, J. D. Joannopoulos, and S. G. Johnson (2007a), “Computation and visualization of Casimir forces in arbitrary geometries: Nonmonotonic lateral-wall forces and the failure of the proximity force approximation,” *Phys. Rev. Lett.* **99**, 080401.
- Rodriguez, A., M. Ibanescu, D. Iannuzzi, J. D. Joannopoulos, and S. G. Johnson (2007b), “Virtual photons in imaginary time: Computing exact Casimir forces via standard numerical electromagnetism techniques,” *Phys. Rev. A* **76**, 032106.
- Rodriguez, A. W., A. P. McCauley, J. D. Joannopoulos, and S. G. Johnson (2009), “Casimir forces in the time domain: Theory,” *Phys. Rev. A* **80**, 012115.

- Rodriguez, A. W., A. P. McCauley, D. Woolf, F. Capasso, J. D. Joannopoulos, and S. G. Johnson (2010), “Nontouching nanoparticle dyclusters bound by repulsive and attractive Casimir forces,” *Phys. Rev. Lett.* **104**, 160402.
- Rodriguez, A. W., M. T. H. Reid, F. Intravaia, A. Woolf, D. A. R. Dalvit, F. Capasso, and S. G. Johnson (2013), “Geometry-induced Casimir suspension of oblate bodies in fluids,” *Phys. Rev. Lett.* **111**, 180402.
- Rosa, F. S. S., D. A. R. Dalvit, and P. W. Milonni (2008), “Casimir–Lifshitz theory and metamaterials,” *Phys. Rev. Lett.* **100**, 183602.
- Rosa, F. S. S., D. A. R. Dalvit, and P. W. Milonni (2010), “Electromagnetic energy, absorption, and Casimir forces: Uniform dielectric media in thermal equilibrium,” *Phys. Rev. A* **81**, 033812.
- Sabisky, E. S., and C. H. Anderson (1973), “Verification of the Lifshitz theory of the van der Waals potential using liquid-helium films,” *Phys. Rev.* **7**, 790.
- Sakurai, J. (1994), *Modern Quantum Mechanics* (Addison Wesley Longman) edited by S. F. Tan.
- Salem, R., Y. Japha, C. J., B. Hadad, M. Keil, K. A. Milton, and R. Folman (2010), “Nanowire atomchip traps for sub-micron atom-surface distances,” *New J. Phys.* **12**, 023039.
- Scardicchio, A., and R. L. Jaffe (2005), “Casimir effects: an optical approach I. foundations and examples,” *Nuc. Phys. B* **704**, 552.
- Scardicchio, A., and R. L. Jaffe (2006), “Casimir effects: An optical approach II. local observables and thermal corrections,” *Nuc. Phys. B* **743**, 249.
- Schaden, M. (2009a), “Dependence of the direction of the Casimir force on the shape of the boundary,” *Phys. Rev. Lett.* **102**, 060402.
- Schaden, M. (2009b), “Numerical and semiclassical analysis of some generalized Casimir pistons,” *Phys. Rev. A* **79**, 052105.
- Schaden, M., and L. Spruch (1998), “Infinity-free semiclassical evaluation of Casimir effects,” *Phys. Rev. A* **58**, 935.
- Schäfer, M., I. Huet, and H. Gies (2012), “Energy-momentum tensors with worldline numerics,” *Int. J. Mod. Phys. Conf. Ser.* **14**, 511.
- Schäfer, M., I. Huet, and H. Gies (2016), “Worldline numerics for energy-momentum tensors in Casimir geometries,” *J. Phys. A* **49**, 135402.
- Scheel, S., L. Knöll, and D.-G. Welsch (1998), “QED commutation relations for inhomogeneous Kramers–Kronig dielectrics,” *Phys. Rev. A* **58**, 700.

- Schmidt, M. G., and C. Schubert (1995), “Multiloop calculation in QED by superparticle path integrals,” Nucl. Phys. B **39B**, 306.
- Schneider, S., A. Kasper, C. vom Hagen, M. Bartenstein, B. Engeser, T. Schumm, I. Bar-Joseph, R. Folman, L. Feenstra, and J. Schmiedmayer (2003), “Bose–Einstein condensation in a simple microtrap,” Phys. Rev. A **67**, 023612.
- Schubert, C. (2001), “Perturbative quantum field theory in the string inspired formalism,” Phys. Rept. **355**, 75.
- Schwinger, J. (1992), “Casimir energy for dielectrics,” Proc. Natl. Acad. Sci. USA **89**, 4091.
- Schwinger, J., L. DeRaad, and K. A. Milton (1978), “Casimir effect in dielectrics,” Ann. Phys. **115**, 1.
- Serry, F. M., D. Walliser, and G. J. Maclay (1998), “The role of the Casimir effect in the static deflection and stiction of membrane strips in microelectromechanical systems (MEMS),” J. Applied Physics **84**, 2501.
- Sorrentino, F., A. Alberti, G. Ferrari, V. V. Ivanov, N. Poli, M. Schioppo, and G. M. Tino (2009), “Quantum sensor for atom-surface interactions below $10\ \mu\text{m}$,” Phys. Rev. A **79**, 013409.
- Srednicki, M. (2008), *Quantum Field Theory* (Cambridge).
- Steck, D. A. (2015), “Quantum and atom optics,” Available online at <http://steck.us/teaching/> (revision 2.1.2, 12 August 2015).
- Strassler, M. J. (1992), “Field theory without Feynman diagrams: One-loop effective actions,” Nucl. Phys. B **385**, 145.
- Sukenik, C. I., M. G. Boshier, D. Cho, V. Sandoghdar, and E. A. Hinds (1993), “Measurement of the Casimir–Polder force,” Phys. Rev. Lett. **70**, 560.
- Sushkov, A. O., W. J. Kim, D. A. R. Dalvit, and S. K. Lamoreaux (2011a), “New experimental limits on non-Newtonian forces in the micrometer range,” Phys. Rev. Lett. **107**, 171101.
- Sushkov, A. O., W. J. Kim, D. A. R. Dalvit, and S. K. Lamoreaux (2011b), “Observation of the thermal Casimir force,” Nat. Phys. **7**, 230.
- Tas, N., T. Sonnenberg, H. Jansen, L. R., and M. Elwenspoek (1996), “Stiction in surface micromachining,” J. Micromech. Microeng. **6**, 385.
- Tip, A., L. Knöll, S. Scheel, and D.-G. Welsch (2001), “Equivalence of the Langevin and auxiliary-field quantization methods for absorbing dielectrics,” Phys. Rev. A **63**, 043806.

- Vassilevich, D. V. (2003), “Heat kernel expansion: user’s manual,” Phys. Rept. **388**, 279.
- van der Waals, J. D. (1873), *On the Continuity of the Gas and Liquid State*, Ph.D. thesis (Leiden).
- Weber, A., and H. Gies (2009), “Interplay between geometry and temperature for inclined Casimir plates,” Phys. Rev. D. **80**, 065033.
- Weber, A., and H. Gies (2010a), “Geothermal Casimir phenomena for the sphere-plate and cylinder-plate configurations,” Phys. Rev. D **82**, 125019.
- Weber, A., and H. Gies (2010b), “Nonmonotonic thermal Casimir force from geometry-temperature interplay,” Phys. Rev. Lett. **105**, 040403.
- Weinberg, S. (1996), *The Quantum Theory of Fields. Volume II: Modern Applications* (Cambridge University Press).
- Yannopoulos, V., and N. V. Vitanov (2009), “First-principles study of Casimir repulsion in metamaterials,” Phys. Rev. Lett. **103**, 120401.
- Zhou, F., and L. Spruch (1995), “van der Waals and retardation(Casimir) interactions of an electron or an atom with multilayered walls,” Phys. Rev. A **52**, 297.
- van Zwol, P. J., V. B. Svetovoy, and G. Palasantzas (2011), “Characterization of optical properties and surface roughness profiles: The Casimir force between real materials,” in *Casimir Physics*, edited by D. Dalvit, P. Milonni, D. Roberts, and F. Rosa, Chap. 10 (Springer) p. 311